Titre: Title:	Accelerating Electromagnetic Transient Simulations of Large-Scale Multiterminal High Voltage Direct Current Systems
Auteur: Author:	Ahmad Allabadi
Date:	2025
Type:	Mémoire ou thèse / Dissertation or Thesis
Référence: Citation:	Allabadi, A. (2025). Accelerating Electromagnetic Transient Simulations of Large-Scale Multiterminal High Voltage Direct Current Systems [Ph.D. thesis, Polytechnique Montréal]. PolyPublie. https://publications.polymtl.ca/69361/

URL de PolyPublie: PolyPublie URL:	https://publications.polymtl.ca/69361/
Directeurs de recherche: Advisors:	Jean Mahseredjian, Ilhan Kocar, & Tarek Ould-Bachir
Programme: Program:	Génie électrique

POLYTECHNIQUE MONTRÉAL

affiliée à l'Université de Montréal

Accelerating Electromagnetic Transient Simulations of Large-Scale Multiterminal High Voltage Direct Current Systems

AHMAD ALLABADI

Département de génie électrique

Thèse présentée en vue de l'obtention du diplôme de *Philosophiæ Doctor*

Génie électrique

Octobre 2025

POLYTECHNIQUE MONTRÉAL

affiliée à l'Université de Montréal

Cette thèse intitulée :

Accelerating Electromagnetic Transient Simulations of Large-Scale Multiterminal High Voltage Direct Current Systems

présentée par **Ahmad ALLABADI**

en vue de l'obtention du diplôme de *Philosophiæ Doctor*

a été dûment acceptée par le jury d'examen constitué de :

Antoine LESAGE-LANDRY, président
Jean MAHSEREDJIAN, membre et directeur de recherche
Ilhan KOCAR, membre et codirecteur de recherche
Tarek OULD-BACHIR, membre et codirecteur de recherche
Sébastien DENNETIÈRE, membre
Reza IRAVANI, membre externe

DEDICATION

To my family,

whose unwavering support, love, and encouragement

made this journey possible.

ACKNOWLEDGEMENTS

I would first like to express my deepest gratitude to my supervisor, Prof. Jean Mahseredjian, for his unwavering guidance, trust, and patience throughout this journey. His insight and mentorship shaped not only this dissertation but also the way I think as a researcher and engineer.

I am also sincerely thankful to Prof. Ilhan Kocar and Dr. Tarek Ould-Bachir for their generous support and involvement as co-directors. I would like to extend a special acknowledgment to Dr. Tarek, whose early guidance and close involvement were instrumental in setting me on the right path when I needed it most.

My heartfelt appreciation goes to Dr. Keijo Jacob, whose support throughout my entire doctoral journey has meant more than words can say. His encouragement, thoughtful listening, and genuine belief in my work and potential gave me strength at every stage. I am deeply grateful.

I would also like to thank Dr. Sébastien Dennetière for his ongoing collaboration, valuable feedback, and tireless help throughout my work. His technical insight and availability always made a difference.

I also wish to thank Prof. Reza Iravani and Dr. Antoine Lesage-Landry for their role as members of my examination committee and for taking the time to engage thoughtfully with my work.

Special thanks go to Dr. Hani Saad and Dr. Anton Stepanov, whose dissertations I encountered early in my research. Their work helped orient my understanding and gave me direction at a time when everything was still new. I am also thankful to Dr. Mohammed Naidjate for his support and encouragement during key moments of my Ph.D.

I owe many thanks to my colleagues and friends. Juan Antonio deserves a very special mention as a true companion throughout this journey, sharing the ups and downs and always pushing forward together. I also warmly thank Sayed Armin, Emmanuel François, Mohammad Jafari, Kouamé N'Zi, and Anoosh Dini for their friendship, collaboration, and support, which made this path both productive and memorable. Finally, I would also like to express my heartfelt thanks to my sister and colleague, Afaf, for her endless support and help, both personally and professionally. Her encouragement was a constant source of strength throughout my Ph.D.

RÉSUMÉ

L'intégration croissante des sources d'énergie renouvelable, ainsi que le développement rapide des systèmes de transport d'électricité en courant continu haute tension (HVDC) et des réseaux multiterminaux en courant continu (MTDC), ont introduit une complexité importante tant sur le plan de la modélisation que sur celui du calcul dans l'analyse des réseaux électriques. La simulation de ces systèmes à grande échelle, à l'aide d'outils de simulation des transitoires électromagnétiques (EMT), est essentielle pour garantir un fonctionnement fiable, la validation des systèmes de contrôle et une intégration sécurisée au réseau. Toutefois, les plateformes EMT traditionnelles peinent à gérer efficacement l'augmentation de la taille des systèmes, la présence de nombreux composants non linéaires et les exigences de modélisation détaillée des convertisseurs. De plus, le processus d'initialisation à l'état stationnaire demeure un goulot d'étranglement majeur : il est souvent fastidieux, numériquement instable et coûteux en ressources de calcul, en particulier pour les systèmes intégrant des systèmes de contrôle complexes ou des composants de type boîte noire.

Pour répondre à ces limitations, cette thèse propose des techniques de simulation avancées, spécialement conçues pour accélérer les simulations EMT et améliorer le processus d'initialisation dans les réseaux MTDC à grande échelle. Tout d'abord, avant d'aborder l'initialisation EMT, une nouvelle méthode hybride de calcul de flux de puissance AC–DC est proposée. Cette méthode est adaptée à des modèles de simulation MTDC complexes, prenant en charge une diversité de stratégies de commande des convertisseurs et dépassant les limitations des approches classiques. Elle offre également une grande flexibilité, ce qui lui permet de s'adapter aux nouveaux modèles de systèmes de contrôle sans modifier l'algorithme. Sur cette base, une méthodologie d'initialisation unifiée, appelée méthode de l'Interface de Découplage (DI), est développée pour rationaliser l'initialisation EMT. En exploitant les résultats du calcul de flux de puissance pour initialiser les systèmes de contrôle sans nécessiter d'accès interne, la méthode DI permet une convergence rapide et une transition stable vers la simulation temporelle. Les évaluations sur bancs d'essai confirment sa supériorité par rapport aux méthodes d'initialisation existantes. De plus, cette méthode est étendue avec succès aux environnements de simulation en temps réel, où elle permet une convergence accélérée, réduit les transitoires liés à l'initialisation et protège les composants sensibles lors des tests Hardware-in-the-Loop (HIL).

Consciente que les parcs éoliens basés sur des générateurs asynchrones à double alimentation (DFIG) représentent souvent une source majeure de retard lors de l'initialisation, la thèse introduit une méthode spécifique appelée Interface de Découplage Hybride (HDI), conçue pour ces systèmes. En découplant partiellement et en initialisant sélectivement les boucles de systèmes de contrôle critiques, la méthode HDI réduit considérablement les délais d'initialisation sans nuire à la précision. Son efficacité est démontrée sur des modèles de parcs éoliens DFIG, aussi bien agrégés que détaillés.

Par ailleurs, afin de surmonter la complexité intrinsèque des simulations EMT à grande échelle, cette thèse explore des techniques d'accélération avancées applicables aux simulations EMT génériques. Les méthodes sont évaluées en termes de faisabilité et de fidélité, aussi bien pour des systèmes HVDC de petite que de grande taille. Trois approches sont systématiquement étudiées : la parallélisation basée sur les lignes de transmission (TLP), la parallélisation des systèmes de contrôle (CtrlP) et les solveurs séquentiels optimisés (OSeqCtrl). Chacune de ces méthodes, évaluée individuellement et en configurations hybrides, montre des gains de calcul substantiels, avec des facteurs d'accélération supérieurs à 20 par rapport aux approches EMT séquentielles classiques.

En résumé, cette thèse propose un ensemble cohérent de méthodes qui améliorent les performances de simulation EMT à toutes les étapes du flux de modélisation, en introduisant des formulations robustes de calcul de flux de puissance AC–DC, un ensemble de techniques d'initialisation efficaces, ainsi que des méthodes d'accélération évolutives. Ensemble, ces avancées permettent des simulations EMT plus rapides, plus fiables et plus extensibles, contribuant à la planification, à l'analyse et aux essais en temps réel des réseaux électriques modernes.

ABSTRACT

The increasing integration of renewable energy sources, alongside the rapid development of High Voltage Direct Current (HVDC) systems and Multi-Terminal DC (MTDC) networks, has introduced significant modeling and computational complexity in power system analysis. Simulating these large-scale, control-intensive systems using Electromagnetic Transient (EMT) tools is essential for reliable operation, control validation, and secure grid integration. However, traditional EMT simulation platforms struggle to efficiently manage growing system size, extensive nonlinear components, and the detailed modeling required for power converters. In addition, the steady-state initialization process remains a major bottleneck, often cumbersome, numerically unstable, and computationally demanding, especially in systems containing complex control hierarchies or black-box models.

To address these limitations, this dissertation introduces advanced simulation techniques specifically designed to accelerate EMT simulations and enhance the initialization process for large-scale MTDC networks. First, prior to engaging in EMT initialization, a novel hybrid AC–DC load-flow technique is proposed. This method is tailored for sophisticated MTDC simulation models, accommodating diverse converter control strategies and extending beyond the limitations of conventional AC–DC load-flow approaches. Its flexibility also allows adaptation to emerging control models without changing the algorithm.

Building upon this, a unified initialization methodology called the Decoupling Interface (DI) method is proposed to streamline EMT initialization. By leveraging load-flow results to initialize control systems without requiring internal access, the DI method achieves rapid convergence and stable transitions to time-domain simulation. Benchmark evaluations confirm its superiority over existing initialization methods. Furthermore, the method is successfully extended to real-time simulation environments, where it ensures faster convergence, reduces initialization-induced transients, and protects sensitive grid components during Hardware-in-the-Loop (HIL) testing.

Recognizing that Doubly-Fed Induction Generator (DFIG)-based wind parks frequently cause prolonged initialization delays, the dissertation introduces a specialized Hybrid Decoupling Interface (HDI) method tailored to these systems. The HDI approach significantly shortens initialization time without compromising accuracy by partially decoupling and initializing critical

control loops. Its effectiveness is demonstrated on both aggregated and detailed DFIG wind park models.

Furthermore, to overcome the inherent computational complexity of large-scale EMT simulations, this dissertation investigates advanced acceleration techniques applicable to generic EMT studies. The methods are evaluated in terms of their feasibility and fidelity for accelerating both small- and large-scale HVDC systems. Transmission Line-based Parallelization (TLP), control system parallelization (CtrlP), and Optimized Sequential Control Solvers (OSeqCtrl) are systematically explored. Each technique is assessed individually and in hybrid configurations, demonstrating substantial computational gains, with acceleration factors exceeding 20 times compared to traditional serial EMT simulation approaches.

In summary, this dissertation contributes a cohesive set of methods that improve EMT simulation performance across the whole modeling workflow, introducing robust AC–DC load-flow formulations, a set of initialization techniques, and scalable acceleration methods. Collectively, these developments enable faster, more reliable, and more scalable EMT simulations, supporting the planning, analysis, and real-time testing of modern power systems.

TABLE OF CONTENTS

LIST OF TABLES

LIST OF FIGURES

LISTE OF SYMBOLS AND ABBREVIATIONS

AC	Alternating Current
AEM	Arm Equivalent Model
AVM	Average Value Model
BTF	Block Triangular Factorization
CBA	Capacitor Balancing Algorithm
CCC	Capacitor Commutated Converter
CM	The Compensation Method
CSCs	Current Source Converters
DC	Direct Current
DCC	Diode Clamped Converter
DCCB	DC Circuit Breaker
DEM	Detailed Equivalent Model
DFIGs	Doubly-Fed Induction Generator
DI	Decoupling Interface
DLL	Dynamic Linked Library
DM	Detailed Model
DP	Dynamic Phasor
DAB	Dual Active Bridge
EEM	Enhanced Equivalent Model
EIAS	External Interfacing auxiliary source
EMT	Electromagnetic Transient
FDNE	Frequency-Dependent Network Equivalent
FMI	Functional Mockup Interface
FMU	Functional Mock-up Unit
GFL-VSC	Grid Following VSC
GFM-VSC	Grid-forming VSC
GSC	Grid Side Control

HDI	Hybrid Decoupling Interface
HFE	High-Frequency Equivalent
HIL	Hardware-in-the-Loop
HPF	High-Pass Filter
HVDC	High Voltage Direct Current
IAS	Interfacing Auxiliary Source
IBR	Inverter-Based Resource
IGS	Islanded Grid Subsystem
IIAS	Internal Interfacing auxiliary source
ISS	Initialized Subsystems
KVL	Kirchhoff's Voltage Law
LCC	Line Commutated Converter
LF	Load-Flow
LFE	Low-Frequency Equivalents
LFSI	Load-Flow and Source Initialization
LS	Limited Sensitivity
MANA	Modified Augmented Nodal Analysis
MATE	Multi-Area Thevenin Equivalent
MMC	Modular Multilevel Converter
MTDC	Multi-Terminal Direct Current
MVAR	Megavolt Ampere Reactive
MW	Megawatt
NIJ	Non-Iterative Jacobian
NLC	Nearest Level Control
OCISS	Outer Control Initialization in Steady-State
OPF	Optimal Power Flow
OSeqCtrl	Optimized Sequential Control solver
PLL	Phase-Locked Loop

pu	Per-Unit
RSC	Rotor Side Control
SCIF	Squirrel Cage Induction Generator
SFP	Shifted Frequency Phasor
SM	Sub Module
SO	Sensitive Operation
SS	Steady-State
TDIS	Time-Domain Initialized Subsystem
TDM	Traditional Detailed Model
TEA	Thevenin Equivalent Approach
TLP	Transmission Line-Based Parallelization
TS	Transient Stability
VSC	Voltage Source Converter
VTS	Variable Time-Step
WP	Wind Park
WPC	Wind Park controller
WRIG	Wound Rotor Induction Generator

CHAPTER 1 INTRODUCTION

1.1 Context and motivation

The global transition toward cleaner energy has driven significant integration of renewable energy resources into modern power systems. This shift presents complex challenges for planning, operation, and protection, particularly as large-scale renewable generation, such as offshore wind and solar farms, is increasingly located far from major consumption centers [1-3]. High Voltage Direct Current (HVDC) technology, especially based on Voltage Source Converters (VSCs), has emerged as a key enabler of such long-distance power transfer. Its ability to interconnect asynchronous grids, support flexible power flow, and accommodate various control strategies has led to the development of Multi-Terminal DC (MTDC) systems [4].

However, the sophistication and scale of MTDC grids introduce critical challenges in terms of system modeling, simulation, and analysis. These systems involve a wide variety of converter types, control modes, and dynamic interactions. These interactions have a very wide range of frequencies. Consequently, Electromagnetic Transient (EMT) simulation has become an indispensable tool for analyzing MTDC systems, particularly for studying fast transients, control behavior, and fault response [5].

Despite their accuracy, EMT simulations are computationally demanding due to the small time-steps required and the complexity of the system dynamics [6-8]. The challenge intensifies with increasing network size, model fidelity, and the presence of inverter-based resources (IBRs) with nonlinear control structures. In addition, preparing EMT simulations for execution, especially the process of steady-state initialization, is often time-consuming and prone to instability, particularly in large-scale systems and complex controls [9, 10]. In real-time applications, such as Hardware-in-the-Loop (HIL) testing, the demand for fast and stable initialization becomes even more critical [11].

To address these challenges, new methodologies are needed to enhance the efficiency and robustness of EMT simulations. Specifically, methods are required that can:

- Provide a compact solution for initializing complex MTDC systems that:
    - Accurately initialize MTDC components without relying on full model transparency.
    - Improve startup stability and mitigate initialization failures.
    - Ensure fast startup in both offline and real-time environments.
- Discover various accelerations of EMT simulation and reduce computational burdens through efficient simulation techniques.

This dissertation is dedicated to investigating such methods, aiming to improve the practicality and scalability of EMT simulations for future power systems.

MTDC structure and terminology.

1.2 MTDC systems: definitions, structures, and project landscape

An MTDC (multi-terminal high-voltage direct current) system [12, 13] is a specific type of high-voltage DC network used for large-scale electric power transmission. It consists of more than two converter stations connected to a shared DC network, and is typically deployed to enable long-distance power transfer, asynchronous interconnection, or integration of dispersed renewable energy sources, such as offshore wind farms.

1.2.1 Categories of HVDC schemes

Practical HVDC schemes can be broadly categorized into (i) point-to-point links, (ii) back-to-back AC–AC converters, and (iii) DC–DC interconnections, as illustrated in Figure 1.1. Point-to-point links are the classical and most widespread configuration, widely used for bulk power transfer over long distances, including submarine and overhead applications. Back-to-back converters, by contrast, do not require a DC transmission line; instead, they connect two asynchronous AC systems through a shared DC link within the same station, making them particularly attractive for cross-border or regional interconnections. DC–DC interconnections are an emerging category, enabled by VSCs, that allow coupling between distinct HVDC grids or between networks operating at different voltage levels. Collectively, these configurations provide the foundation for long-distance power transfer, asynchronous interconnection, and enhanced controllability beyond conventional AC stability limits.

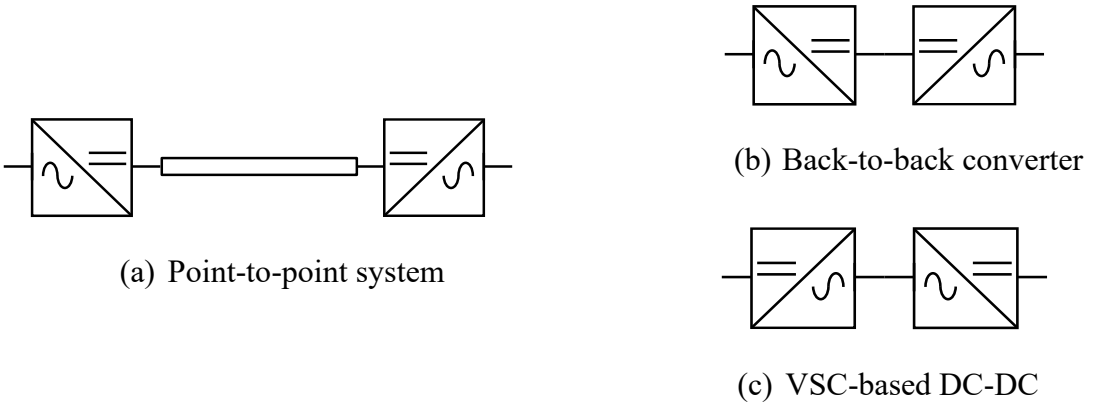

(a) Point-to-point system

(b) Back-to-back converter

(c) VSC-based DC-DC

Figure 1.1 Typical HVDC configurations.

1.2.2 DC network structure and pole arrangements

Figure 1.2 illustrates the monopolar arrangements used in practical HVDC and MTDC systems. The symmetrical monopolar configuration, shown in Figure 1.2.(a), consists of two conductors operated at equal positive and negative voltages with respect to ground ($\pm V_{dc}/2$). This arrangement has no intentional return path and is commonly used in VSC-based submarine cable projects, where the elimination of ground current and reduced insulation stress is advantageous. Notable examples include the BorWin1 offshore wind connection in Germany [14] and the recently commissioned Greenlink interconnector [15] between the UK and Ireland.

The bipolar configurations, shown in Figure 1.2.(b) and Figure 1.2(c), operates with two poles at $\pm V_{dc}$ referenced to ground. Under normal conditions, the positive- and negative-pole currents are equal and opposite, so no ground current flows. If one pole is lost, the system can continue in monopolar (unbalanced) operation, where the remaining pole transfers power through a return path. Two return path options are typically considered. In the first case, shown in Figure 1.2.(b), a ground or sea return is used, which is cost-effective and historically dominant in long-distance overhead LCC projects such as the Québec–New England link [4] and the Xiangjiaba–Shanghai interconnection [15] in China. Alternatively, a dedicated metallic return (DMR) conductor can be employed to avoid ground currents, shown in Figure 1.2.(c), an example of a real project is Kimal Lo Aguirre in Chile[16].

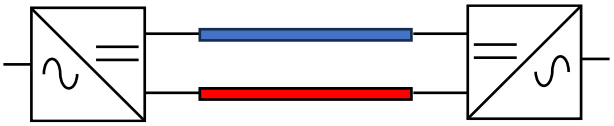

(a) Symmetrical monopolar

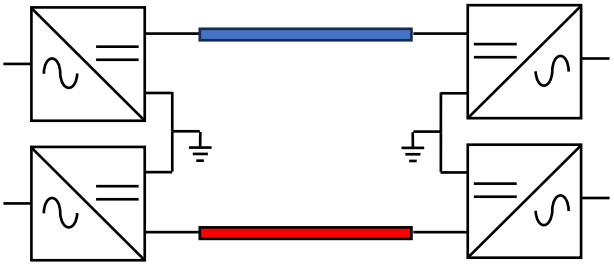

(b) Bipolar with ground return

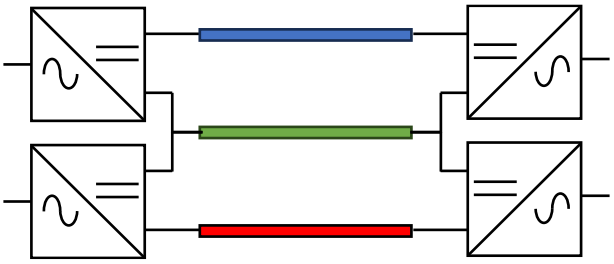

(c) Bipolar with DMR

Figure 1.2 Typical HVDC pole configurations.

1.2.3 Status and trends

Early MTDC deployments were few and mainly LCC-based. Flagship examples include the Québec–New England [4] scheme, which was upgraded to a multiterminal bipole (±450 kV, ~1,480 km) in 1990, and India's North-East Agra system (±800 kV) [4], built with two rectifier stations and one inverter station in a double-bipolar arrangement since 2015.

By contrast, today's operational VSC-based DC grids are concentrated in China. Notable MTDC systems are Nan'ao [15] (in service since 2013; MMC, three terminals; ±160 kV), Zhoushan [15] (since 2014; five terminals; ±200 kV; DC circuit breakers added in 2016), and the large-scale Zhangbei grid [15] (commissioned 2021; ±500 kV; four terminals; 16 hybrid DCCBs). China has also piloted hybrid LCC/VSC at Wudongde [15] (commissioned 2021; LCC with MMC blocks).

In Europe and the North Sea basin, momentum is shifting from point-to-point links toward scalable MTDC. Current programs include Bornholm Energy Island [17] (two HVDC links by 2030; possible multi-vendor), Germany's DC hubs [18] (common MTDC specs by four TSOs with execution targeted for 2028–2034), France's GiLa [19] (two ±320 kV symmetrical monopoles with

an offshore wind tap), and the Ultranet [15] ±380 kV/2 GW bipolar. The UK roadmap similarly foresees multiple 2 GW/525 kV schemes and has launched the Aquila interoperability program [20]. The U.S. Department of Energy's Atlantic study [20] proposes a meshed offshore HVDC grid to integrate ~30 GW by 2030.

This accelerating build-out explains the launch of the interOPERA initiative [21], which targets "interoperability by design" for multi-vendor, grid-forming MTDC: establishing functional frameworks and procurement models, delivering a real-time demonstrator, and de-risking pilot tenders as early as 2027. The program explicitly addresses the gap between today's single-vendor point-to-point practice and the scalable, multi-terminal offshore grids needed to meet EU objectives for 300–450 GW of offshore wind by 2050.

1.3 Overview of MTDC components and their models.

Modern MTDC grids extend point-to-point HVDC into networks that interconnect multiple converters over shared DC buses. This section summarizes the main MTDC building blocks and the modeling choices adopted in this dissertation for AC–DC load-flow (LF), initialization, and EMT studies.

- DC transmission lines/cables: These lines or cables form the physical medium for power transfer between terminals. They can be overhead lines or submarine/underground cables, depending on geography and voltage level, and are often modeled using wideband frequency-dependent line models in EMT environments [22].
- DC Circuit Breakers (DCCBs): DCCBs enable fault isolation and network reconfiguration in DC grids. Their fast interruption capability is essential for the protection of MTDC systems, especially in meshed or multiterminal topologies. Various technologies exist, such as mechanical, hybrid, and solid-state breakers, each with different interruption times and current ratings [3, 8].
- DC-DC converters: In some configurations, DC-DC converters are used to interface separate DC voltage levels or provide galvanic isolation between sub-grids. They enable hierarchical or zonal operation in large-scale DC systems [23, 24].
- Supervisory control systems: Centralized or distributed control and monitoring platforms manage power flow, enforce operational limits, and coordinate between converters. They play an increasingly critical role in real-time optimization and fault recovery [25].

A representative MTDC layout is shown in Figure 1.3, highlighting the presence of various system components including VSC stations, DC lines, and protection and control equipment. Among all MTDC components, power converters and IBRs constitute the dominant share of computational burden in EMT simulations. Consequently, they are the primary focus of the acceleration strategies investigated in this research. The following subsections describe them and their modelling in detail.

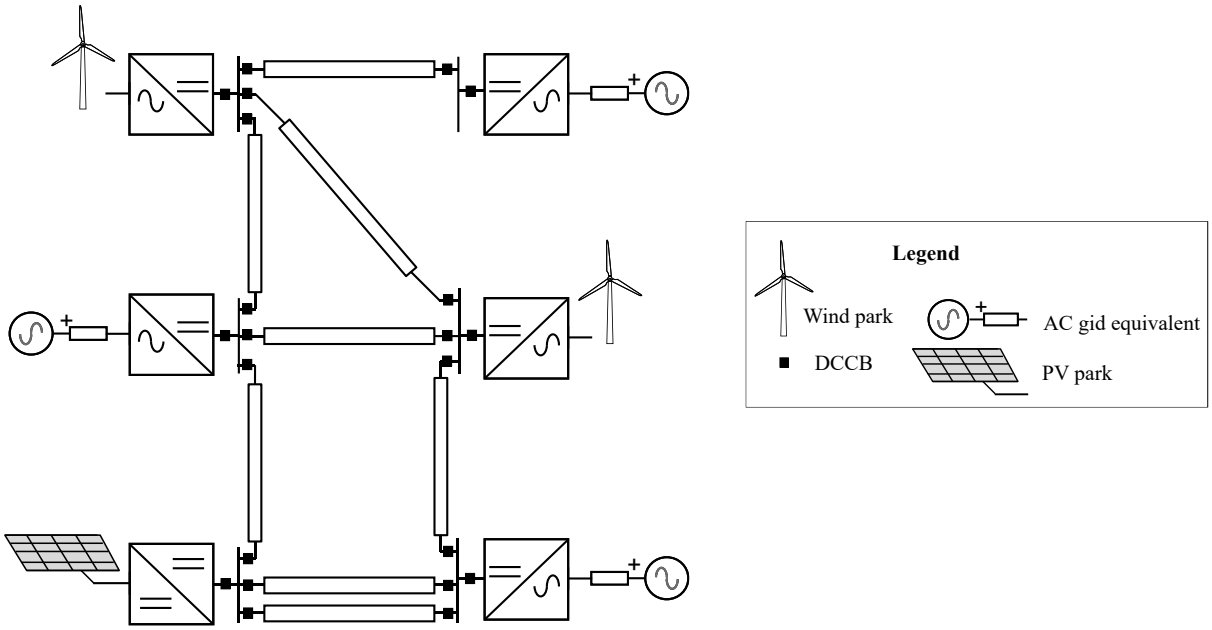

Figure 1.3 Example of a meshed MTDC network.

1.3.1 IBRs

Renewable energy sources, primarily wind parks (WPs) and photovoltaic (PV) systems, constitute the majority of generation assets integrated into modern MTDC networks. Unlike conventional synchronous generators, these resources interface with the grid through power electronics-based inverters, commonly known as IBRs. Due to their nonlinear control systems, switching behavior, and detailed internal dynamics, IBRs pose substantial modeling and computational challenges in EMT simulations.

In the context of WPs, wind turbines are based on several types of technologies, categorized into four main types depending on the generator architecture and the control approach employed [26].

A Type I wind turbine uses a Squirrel Cage Induction Generator (SCIG) directly connected to the grid via a transformer. Soft starters are employed to mitigate inrush currents during startup and synchronization. The operating speed of Type I turbines is fixed and determined by the gearbox

and the number of pole pairs in the generator. Although this design is simple, robust, and cost-effective, it suffers from suboptimal energy extraction efficiency, especially at varying wind speeds. Reactive power compensation is typically required through external capacitor banks. Some enhanced configurations implement dual-winding or dual-generator setups to slightly improve performance at different wind speeds.

Type II turbines employ a Wound Rotor Induction Generator (WRIG) with an externally connected variable resistor inserted in the rotor circuit. The external resistance, controlled through a DC chopper, allows for limited variable-speed operation by modifying the machine's torque-speed characteristic, typically providing about 10% speed variability above synchronous speed. This arrangement eliminates the need for slip rings by mounting the resistor on the shaft and optically controlling it. However, the design still requires external capacitors for reactive power support, and the additional rotor losses associated with the external resistance limit the achievable speed range.

Type III turbines are based on the DFIG concept. In this configuration, the stator is connected directly to the grid, while the rotor is interfaced through a partial-scale back-to-back converter operating at approximately 30–35% of the generator’s rated power. This structure allows independent control of active and reactive power by regulating the d–q components of the rotor current via vector control strategies. Type III turbines have historically dominated large-scale wind farm installations, thanks to their favorable balance between cost, flexibility, and grid support capabilities. While they remain widely deployed, especially in existing onshore fleets, recent large-scale offshore and some onshore projects increasingly adopt Type IV turbines to meet more stringent grid code and performance requirements [27].

Type IV turbines utilize a full-scale power converter that decouples the generator completely from the grid. These designs can incorporate various types of generators, including SCIGs, WRIGs, or Permanent Magnet Synchronous Generators (PMSGs). By interfacing through full-rated converters, Type IV turbines offer wide operational speed ranges, enabling maximum power extraction across a broad spectrum of wind conditions. They also provide complete decoupling of active and reactive power control from the grid, making them ideal for weak-grid or islanded operation. Despite their higher cost, Type IV turbines are gaining increased adoption due to their superior flexibility, potential for gearless designs, and enhanced grid support functionalities.

In practical MTDC designs, wind parks typically consist of Type III or Type IV wind turbines. Therefore, in MTDC studies, the focus should be exclusively on these two types. On the other hand, photovoltaic (PV) systems can be integrated into MTDC networks through two main approaches: (i) direct DC injection into the MTDC grid via appropriate DC-DC converters, or (ii) AC coupling, where DC power is first converted to AC through a DC-AC inverter and then interfaced with the MTDC network using an AC–DC converter.

In practical MTDC deployments, wind farms are primarily Type III or Type IV. Accordingly, this dissertation focuses on these two types in MTDC studies. For example, the Nan'ao VSC-MTDC project in China integrates DFIG-based wind farms (Type III) [28], In contrast, large Type-IV (PMSG/full-converter) fleets are deployed in recent MTDC systems, such as the Zhangbei region [29]). Both turbine types are therefore relevant to MTDC operation and EMT studies.

Photovoltaic (PV) plants can connect to MTDC networks in two ways: direct DC injection or AC coupling. Direct injection uses a high-power DC-DC stage to elevate the PV system's medium-voltage DC output to the MTDC transmission level. While this approach reduces the number of conversion stages, it demands advanced features such as galvanic isolation, bidirectional power control, and coordinated DC fault management. At present, no commercial MTDC project has deployed MMC-based DC-DC converters, which remain at TRL 4–6 and are limited to prototype and pilot demonstrations[23]. Accordingly, this dissertation models PV and wind farm connections using the established AC-coupled architecture.

1.3.2 Power converters

1.3.2.1 AC/DC converters

AC/DC converters are fundamental to HVDC and MTDC systems, serving as the interface between the AC grid and the DC network. These converters fall into two primary categories: Current Source Converters (CSCs) and VSCs, each offering distinct operational characteristics and modeling challenges for EMT simulations.

CSC is the earliest large-scale HVDC system that employed thyristor-based CSCs, particularly the Line Commutated Converter (LCC) topology. A notable example is the 320 MW, 80 kV HVDC link commissioned in New Brunswick, Canada, in 1972 [30]. LCCs operate using 12-pulse configurations composed of dual six-pulse bridges and rely heavily on strong AC systems for

proper commutation. Their performance is constrained by issues such as commutation failures, harmonic distortion, and the requirement for extensive reactive power compensation and filtering [31-33]. Figure 1.4.(a) illustrates the typical LCC structure.

CSC is the earliest large-scale HVDC technology, employing thyristor-based converters, particularly the Line Commutated Converter (LCC) topology. One landmark project is the Eel River Converter Station in New Brunswick, Canada, commissioned in 1972 [30], which was the world's first fully thyristor-based commercial HVDC back-to-back link. With a capacity of 320 MW at ±80 kV, it demonstrated the feasibility of large-scale solid-state HVDC transmission and earned recognition as an IEEE Milestone for its pioneering role. Another prominent example is the Hydro-Québec–New York interconnection via the Châteauguay HVDC back-to-back station, commissioned in the early 1980s [4]. This installation consists of two 500 MW LCC units (1,000 MW total) operating at ±140 kV, enabling substantial cross-border power exchange while providing asynchronous interconnection between the Québec and New York grids. Importantly, the first operational MTDC project was also realized with LCC technology: the Québec–New England interconnection, commissioned in 1992, which formed a three-terminal ±450 kV scheme linking Radisson, Nicolet, and Sandy Pond [4, 34].

Both point-to-point and multi-terminal projects illustrate the scalability of LCC technology, from early proof-of-concept implementations to gigawatt-scale interconnections.

Capacitor Commutated Converters (CCC), shown in Figure 1.4.(b), were later introduced to address some of the limitations of conventional LCCs, particularly in weak-grid environments where commutation failures are more likely. CCCs incorporate series-connected commutation capacitors between the converter valves and the converter transformer, which improve commutation by providing leading reactive power, reduce the need for large reactive power compensation banks, and enhance dynamic performance [35]. This topology was pioneered in the 1990s and deployed in several projects, such as the 500 MW Garabi HVDC interconnection between Argentina and Brazil, commissioned in 1999 [4]. However, despite these improvements, both LCC and CCC remain limited in terms of control flexibility and fault ride-through capabilities, making them less suitable for meshed MTDC applications.

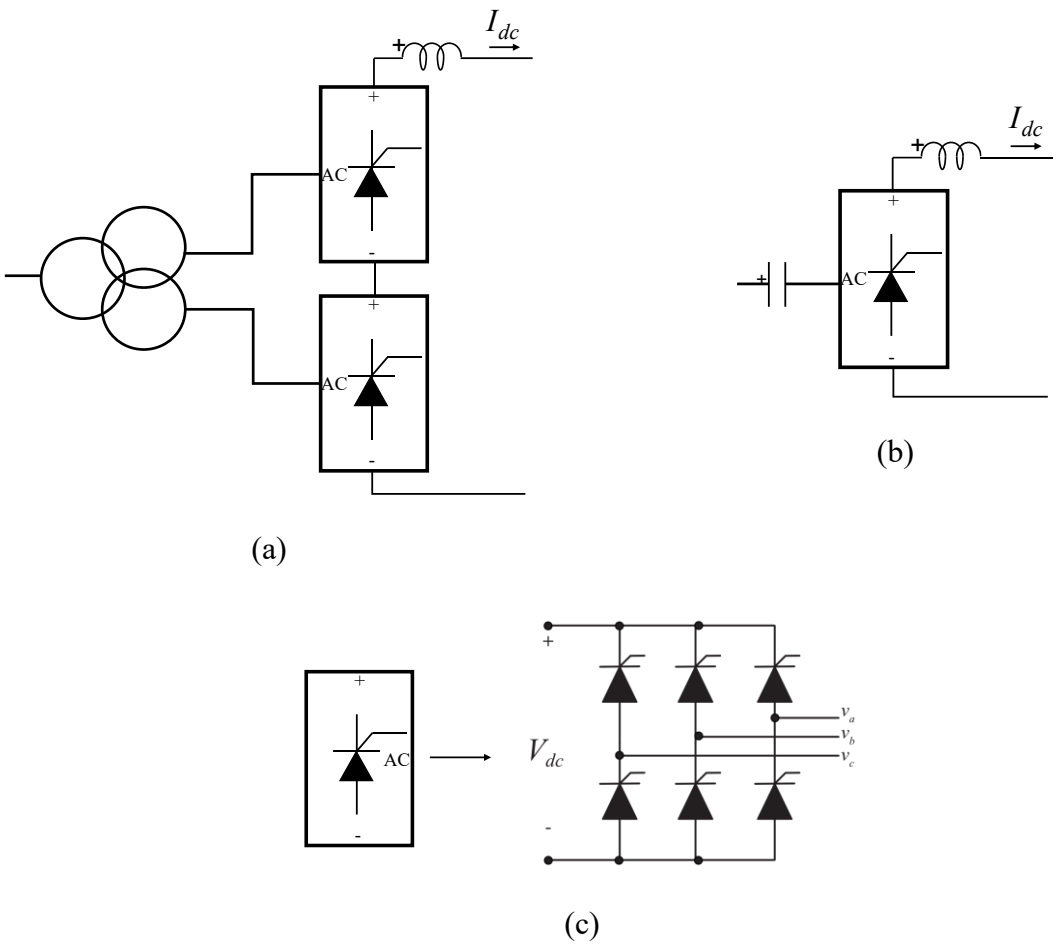

Figure 1.4 Current-source converter types: (a) LCC, (b) CCC, (c) thyristor bridge.

Modern HVDC projects increasingly favor VSCs due to their ability to independently control active and reactive powers, operate in weak or passive grids, and provide black-start capability [36-39]. The simplest form, the two-level VSC (Figure 1.5), uses fully controllable semiconductor switches with antiparallel diodes. However, due to high switching losses, electromagnetic interference, and limited voltage scalability, two-level topologies are not widely used in high-power applications [3].

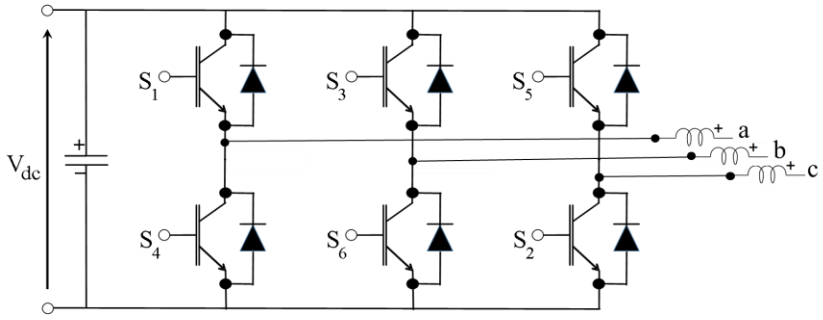

Figure 1.5 The basic structure of a two-level VSC

To overcome these limitations, multilevel topologies such as the Modular Multilevel Converter (MMC) and the Diode Clamped Converter (DCC) have been introduced [3]. MMCs, in particular, offer improved waveform quality, scalability, and reduced filtering needs. Each MMC arm is composed of several submodules (SMs), typically implemented using half-bridge or full-bridge configurations, as shown in Figure 1.6.

The MMC synthesizes AC waveforms by inserting or bypassing SMs, which allows for fine voltage resolution and low harmonic distortion. The SM capacitors maintain DC voltage stiffness, while the arm inductors manage circulating and fault currents [40, 41]. Half-bridge SMs are favored due to their simplicity and efficiency, though full-bridge SMs offer fault-blocking capability at the cost of increased complexity [42, 43].

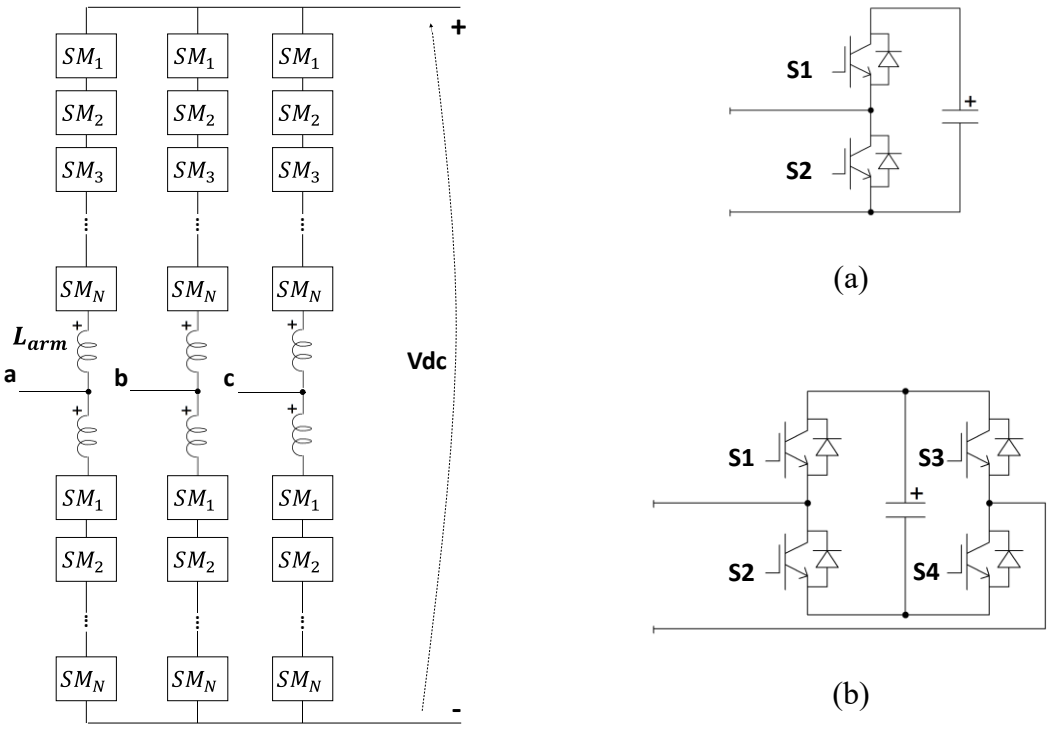

Figure 1.6 Generic MMC circuit for N+1 levels: (a) half-bridge, (b) full-bridge SM.

As MTDC systems scale in size and complexity, accurate modeling and efficient simulation of these AC/DC converters become crucial for system-level EMT analysis. Section 1.4 discusses various MMC modeling approaches tailored to balance accuracy and computational performance in such simulations.

1.3.2.2 DC/DC converter

In MTDC networks, DC/DC converters are essential for adapting voltage levels, providing galvanic isolation, and enhancing operational flexibility. One prominent high-power implementation is the MMC-based DC/DC converter, which comprises two MMCs interconnected via an AC link. Each MMC functions as a voltage source converter, and the overall system facilitates controlled, bidirectional power transfer between two DC grids. This architecture is well-suited for large-scale, high-voltage applications and is increasingly explored for meshed MTDC grids. However, MMC-based HVDC DC–DC converters are still at the R&D stage (TRL 4–6) [23], with development limited to laboratory prototypes and pilot tests, and no utility-scale deployment to date.

Another noteworthy topology is the Dual Active Bridge (DAB) converter, which consists of two H-bridge inverters connected via a high-frequency transformer. DABs offer several advantages, including bidirectional power flow, galvanic isolation, and the ability to step voltages up or down. The use of high-frequency AC significantly reduces transformer size, making DABs attractive for compact and modular power conversion, particularly in medium-voltage DC systems, energy storage interfaces, and emerging DC microgrid applications. Although established at lower power levels, DAB converters for high-power MTDC applications are also considered to be at low TRL (4–5) [23], and their extension to transmission-scale networks remains a promising research direction.

1.4 Converter modeling approaches

Although various converter types can be employed in MTDC systems, as outlined above, this section focuses exclusively on the MMC, given its widespread adoption and the inherent modeling challenges it presents. MMCs are central to VSC-based MTDC networks due to their scalable architecture, superior waveform quality, and operational flexibility. However, their complex internal structure, comprising hundreds of submodules (SMs), nonlinear switching elements, and multi-layered control systems, creates significant computational challenges for EMT simulation. To address these issues, a range of modeling strategies has been developed, classified according to their level of detail and intended application.

CIGRE technical brochure classifies MMC models into seven distinct types, shown in Figure 1.7. Each is suited for different EMT study objectives [2, 4]:

- Type 1, Full Physics-Based Models: Include full electromagnetic and semiconductor-level modeling. Though highly accurate, they are impractical for power system simulations due to their computational demands.
- Type 2, Full Detailed Models: Represent each switch and nonlinear behavior. Used as benchmark references or for internal fault studies, these require very small time-steps and nonlinear solvers [40].
- Type 3, Switchable Resistance Models: Replace switches with two-value resistors, offering reduced complexity while maintaining switch logic. However, both Type 2 and Type 3 models are generally not practical for large system studies, except in cases where converters have a low number of switches, such as LCC converters [44].

- Type 4, Detailed Equivalent Models: Substitute SMs with equivalent blocks or small admittance subsystems [40, 45-48], often coupled via dependent sources. Advanced versions incorporate node reduction and optimized solver techniques [49, 50].
- Type 5, Average Value Models (AVM): Neglect switching details and model converter behavior with controlled voltage/current sources[6, 7, 40]. Arm Equivalent Models (AEM) simplify SM groups into capacitive equivalents [40, 51], and some include blocking state and capacitor ripple effects [52-56].
- Type 6, Phasor Models: Abstracted from AVM, these models facilitate control design and system-level interactions [2].
- Type 7, RMS Load-Flow Models: Serve as static models for initializing EMT systems using steady-state power flow results [2].

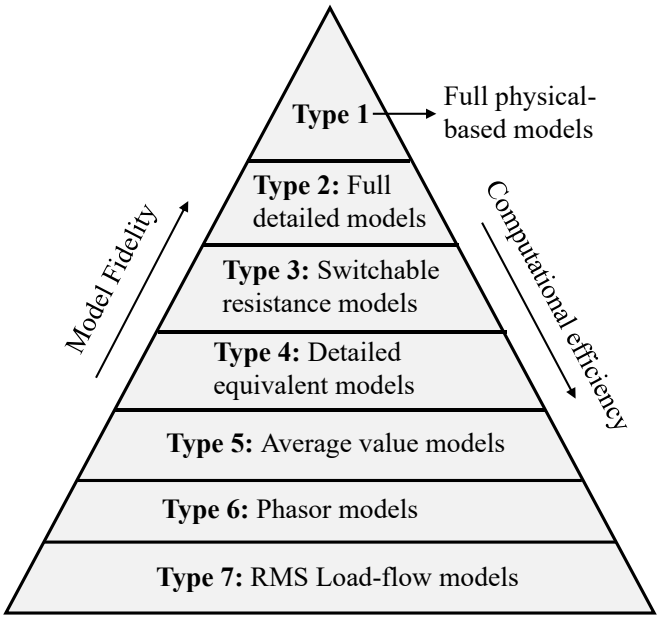

Figure 1.7 MMC modeling hierarchy for EMT simulations [2]

Table 1.1 Summary of MMC models for EMT studies.

CIGRE Technical Brochure [2]		Other names across the literature
Type 2: Full Detailed Models		• Model 1: Detailed IGBT-Based Model [40]. • Detailed Model (DM) [6]. • Traditional Detailed Model (TDM) [57].
Type 3: Switchable Resistance Models		-
Type 4: Detailed Equivalent Models		• Model 2: Equivalent Circuit-Based Model [40]. • Detailed Equivalent Model (DEM) [57]. • Accelerated SM level model [58]. • Enhanced Equivalent Model (EEM) [59].
Type 5: Average Value Models	Arm level	• Model 3: MMC Arm Switching Function [40]. • Accelerated Model [57]. • AEM [51]. • Continuous model [60].
	Converter level	• Model 4: AVM [40]. • Average Model [58].

The choice of the MMC model depends heavily on the simulation objective. For example, detailed models (Types 1–2) are best suited for converter design and SM-level studies, while simplified models (Types 5–7) are more appropriate for system-level analysis where computational efficiency is critical. Type 4 models often serve as a middle ground, balancing fidelity and performance. Enhanced AVMs and AEMs have emerged as practical options for large-scale EMT studies, offering key dynamic features without the burden of full switch-level representation. Table 1.1 Summarizes these models and their common aliases across the literature.

1.5 Control systems in MTDC grids

Control systems are fundamental to the stable and efficient operation of MTDC grids. These systems coordinate the behavior of AC/DC converters, regulate voltage and power flows, and ensure proper interaction with connected AC networks. Control strategies vary depending on system configuration, operational objectives, and converter technologies. The control systems are divided into two categories; system level and control levels as explained below.

1.5.1 System level

At the system level, MTDC grids rely on DC voltage regulation schemes to balance power among converters and maintain voltage stability. The three main approaches are:

- Master-Slave Control: A single converter (master) regulates the DC voltage, while other stations inject or absorb power based on active power control. This method is simple but less robust to converter outages [61].
- Voltage Margin Control: A decentralized variant of master-slave control, where multiple converters are equipped to regulate voltage, but only one operates as the voltage controller at a time based on voltage deviation [62].
- Droop Control: A decentralized control method where multiple converters share the voltage regulation task proportionally, enabling redundancy and scalability [63, 64]. This approach is especially beneficial for meshed and large-scale systems.

In addition to voltage regulation, MTDC systems may implement optimal power flow (OPF) strategies, power oscillation damping, and fault ride-through. OPF-based controls combine economic dispatch and dynamic constraints to optimize setpoints [65, 66]. While damping controllers contribute to system stability under low-frequency oscillations [67-69].

1.5.2 Converter level

At the converter level [70], control systems are typically organized into hierarchical layers, as illustrated in Figure 1.8. Although there are other control hierarchies, cascaded control will be used in this research as it is more common and simpler for coordination.

Here, there are two control levels, upper and lower levels. The upper level contains outer and inner controls. The outer control governs system-level objectives such as power flow, DC voltage, and

AC frequency. The inner current control loops offer fast regulation of d-q axis components. The lower-level controllers manage internal converter dynamics and include:

- Modulation schemes, such as Nearest Level Control (NLC), Phase Shift PWM, and Phase Disposition PWM [2]
- Capacitor Balancing Algorithms (CBA) to maintain uniform capacitor voltage across submodules [8, 71, 72]
- Circulating Current Suppression to minimize negative-sequence currents caused by arm imbalance [73].

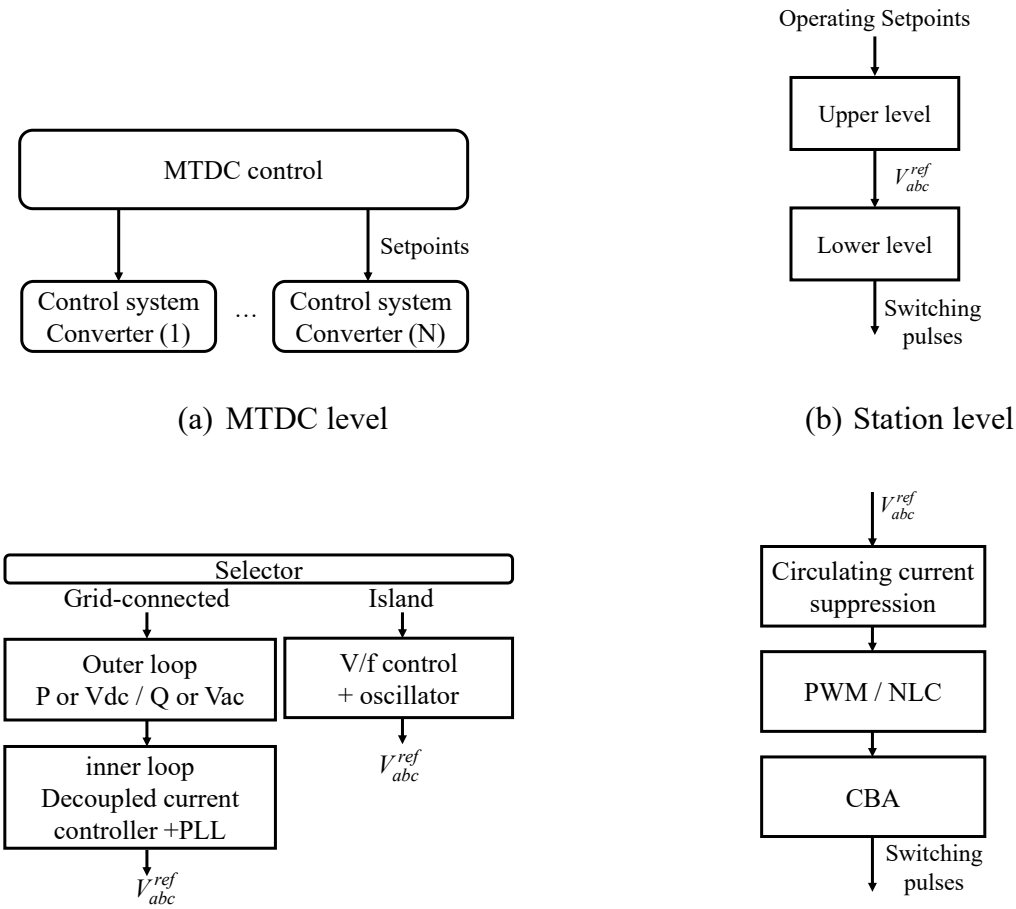

(a) MTDC level (b) Station level

(c) Upper level (c) Lower level

Figure 1.8 MMC control hierarchy.

Proper coordination between control layers is critical to ensure the converter's safe and stable operation. Discrepancies in timing or tuning between these loops can result in internal voltage instability or excessive switching loss. Moreover, the choice of control structure significantly

impacts the behavior of EMT simulations, influencing model convergence, simulation time, and numerical stability.

In summary, MTDC control systems span multiple layers of complexity and functionality. Accurate modeling of these systems in EMT simulations is essential to capture their dynamic performance and evaluate their impact under both steady-state and fault conditions.

1.6 Overview of existing acceleration methods

The computational demands of EMT simulations have spurred extensive research into acceleration techniques aimed at improving simulation efficiency without compromising accuracy. These techniques can be broadly categorized into three main classes: system equivalencing, simulation strategies, and hardware acceleration.

1.6.1 System equivalencing

System equivalencing reduces the size of the simulated network by separating it into an internal and an external system. The internal system, typically the focus of analysis, is modeled in full EMT detail, while the external system is replaced by a simplified equivalent model. Three main types of equivalents are commonly used:

- High-Frequency Equivalents (HFE): Designed to capture fast transients, often using Frequency-Dependent Network Equivalents (FDNEs) or rational functions [74-81].
- Low-Frequency Equivalents (LFE): Focus on electromechanical oscillations (0–2 Hz) and are often used with coherency-based methods or measurement-driven models [77].
- Wideband Equivalents: Combine both high and low-frequency behaviors to ensure fidelity across a broader spectrum [82].

While these techniques can significantly reduce the simulation domain and computational load, they also present notable limitations for large-scale EMT studies of MTDC and converter-dominated grids. Frequency-domain equivalents often fail to represent non-simultaneous disturbances accurately unless re-derived for each operating condition, making them less practical for multi-scenario studies [83]. In systems with high penetration of IBRs, equivalencing may omit critical converter–grid interaction modes or rely on aggregated models that under-represent dynamic behavior under varying grid strengths [84]. Furthermore, hybrid EMT–phasor simulations

that employ network equivalents can still struggle to capture all dynamic interactions across operating scenarios, particularly in weak-grid or highly meshed conditions.

Given these limitations, this dissertation instead focuses on acceleration methods that retain the full EMT representation of the studied network, ensuring all converter–grid dynamics are preserved, while achieving computational speed-up through parallelization and optimized solver strategies.

1.6.2 Hardware-based acceleration

Exploiting modern computational hardware is another cornerstone of acceleration. This includes both multicore CPUs, FPGAs, and GPUs.

1.6.2.1 Multicore CPU parallelization

A range of techniques has been proposed to accelerate EMT simulations by leveraging multicore CPU architectures. These methods primarily differ in how they achieve subsystem decoupling and parallelism, and can broadly be categorized into algebraic, physical, and modular approaches.

Algebraic partitioning techniques, such as Node Splitting [85] and the Multi-Area Thévenin Equivalent (MATE) method [86-88], divide the network into electrically bounded subdomains. These subdomains are then solved in parallel, with equivalent sources used to preserve interface conditions and ensure convergence. However, it has been recently demonstrated that MATE is actually a method preceded and included into the Compensation method (CM) [89].

In CM, tightly coupled subsystems are artificially decoupled by removing selected network couplings and injecting compensation currents or voltages to represent the removed interactions. These compensation terms are updated iteratively until the coupled solution is recovered. This algebraic approach enables parallelism even when natural separation is absent. Recent developments, such as the iterative nonlinear CM [90], extended the method to handle strong nonlinearities and has been validated in real-time environments, including HIL testing of HVDC and distribution networks with both LCC and VSC converters.

Physical decoupling approaches exploit the natural propagation delays of transmission lines. Transmission Line-Based Parallelization (TLP) is a notable example, where the inherent delay between sending and receiving ends enables parallel computation without introducing numerical inaccuracies. This principle is leveraged in multiple implementations. One such method, detailed

in [91], applies Block Triangular Factorization (BTF) to isolate independent sub-networks. These are then solved using a parallelized sparse matrix solver (KLU), enhanced with pivot validity testing and partial refactorization, making it especially effective for nonlinear and time-varying systems in multi-core CPU environments, all without requiring user intervention. Co-simulation approaches offer another variant of transmission-line-based parallelism. For example, [92] assigns subsystems connected via transmission lines to different simulation instances, which may use distinct solvers or time steps. This allows for distributed or multi-threaded execution, increasing flexibility and efficiency.

Beyond system-level decomposition, modular component-level parallelization also offers significant speedups. Dynamic Linked Library (DLL)-Based Modular Parallelization [93] is frequently used in MMC simulations, where identical or similar control loops, such as those for converter arms or turbine modules, are executed concurrently across threads via dynamic linking, enabling scalable performance.

1.6.2.2 FPGA Acceleration:

Field-Programmable Gate Arrays (FPGAs) have also been widely explored for EMT and MTDC simulations. Their main advantage lies in deterministic, low-latency parallelism achieved through hardware-level execution of numerical kernels. Unlike CPUs and GPUs, which rely on instruction scheduling, FPGAs map simulation tasks directly to reconfigurable logic, enabling cycle-accurate updates of state variables and precise emulation of switching events. Several EMT solvers for MMC stations and MTDC grids have been implemented on FPGA platforms [94-96], demonstrating real-time execution capability even for detailed submodule-level models. FPGAs are also frequently used in HIL setups, where the tight timing requirements of power electronic devices (e.g., IGBTs, MMC submodules) exceed the responsiveness of software-only solutions.

Despite these strengths, FPGA-based acceleration also faces significant challenges. Many FPGA-based EMT implementations rely on fixed-point or single-precision arithmetic, which narrows the dynamic range and introduces quantization errors; double-precision or adaptive mixed-precision schemes are required for accuracy, but at the expense of greater resource consumption [97]. In addition, the limited on-chip logic and memory of FPGAs restrict the size of models that can be implemented and often necessitate simplified device representations or hybrid CPU–FPGA partitioning to offload part of the computation [95]. Finally, FPGA development typically requires

HDL coding and careful hardware–software integration, while communication bottlenecks (e.g., PCIe latency in CPU–FPGA platforms) further reduce flexibility for frequent model modifications [95].

1.6.2.3 GPU Acceleration

GPUs enable fine-grained parallelization, which is particularly suited for repetitive matrix operations in EMT simulations. Applications include large wind parks [98, 99] and detailed converter models. Building on this capability, more advanced frameworks have emerged that combine domain partitioning with GPU acceleration. One example is hybrid CPU-GPU co-simulation techniques, where different portions of the system are mapped to appropriate computing resources. For instance, Shifted Frequency Phasor (SFP) methods have been used for MMCs on GPUs with significant performance gains [100]. In [101] it has been, however, demonstrated that dynamic phasor type methods (includes SFP) may actually suffer from performance issues when compared to more robust EMT type methods. The dynamic phasor type methods also introduce significant and unnecessary complexity in modeling.

In addition, GPU-based EMT approaches face several important limitations. Their performance can be strongly affected by CPU–GPU data transfer overhead, since PCIe communication is much slower than on-device memory and must be carefully minimized. They are also constrained by the limited global memory available on GPUs, which prevents caching all required matrices and leads to performance degradation as model size increases [102].

1.6.3 Simulation Techniques

Several simulation strategies have been proposed to increase computational efficiency through intelligent algorithm design and solver adaptation:

- Variable Time-Step (VTS): Adapts the simulation time-step based on the transient intensity, allowing longer steps during quasi-steady periods [103].
- Adaptive modeling: For example, using a simplified MMC model (e.g., AVM or DEM) during startup before switching to a detailed model as proposed in [104].
- Co-Simulation: Capitalizes on the natural decoupling between subsystems, especially across long transmission lines, to allow parallel or staged simulation. Three main approaches exist:
    - Multistep co-simulation: Different subsystems run with varying time steps to match local dynamics [105-107].
    - Multi-domain co-simulation: Combines EMT with Transient Stability (TS) or Dynamic Phasor (DP) domains to optimize both speed and accuracy [108, 109].
    - Hybrid co-simulation: Mixes multistep and domain-splitting strategies, sometimes in combination with parallel computing [92, 110].
- Fast initialization techniques: Target to reduce or eliminate the lengthy delays associated with settling startup transients by pre-loading steady-state conditions or implementing targeted initialization strategies [5, 8, 104, 111-113]. Given their complexity and critical role in EMT simulation, these techniques are discussed in detail in the following subsection.

1.6.4 Simulation initialization

Accurate EMT simulations require a reliable, steady-state starting point to correctly capture the dynamic behavior of power system components. One basic approach is to start the time-domain simulation from zero initial conditions and allow the system to settle naturally. While this method might be feasible for simple circuits, it becomes impractical for realistic power system models. Not only is the required simulation time excessive, but such an approach often fails to reach the correct operating point. Instead, it may suffer from prolonged transient behavior, mismatched steady-state trajectories, activation of protection systems, or undesired magnetic saturation.

Several initialization methods have been proposed to address these challenges:

- Phasor-based initialization: This group of methods employs a phasor solution to obtain the system's nominal frequency solution [114]. While simple and computationally light, it performs poorly when nonlinearities, such as switching behavior in IGBTs, or intricate control configurations are involved.
- EMT-based boundary value approaches: These methods reformulate the initialization as a two-point boundary value problem solved directly within the EMT platform [115-118]. Despite their generality, they tend to be computationally expensive, may suffer from convergence issues, and may not always guarantee a physically meaningful steady-state, especially in stiff or ill-conditioned systems.
- Load-Flow (LF) based initialization: More recent strategies rely on conventional load-flow engines to find the operating point of both the electrical network and embedded dynamic models. This includes initializing auxiliary control blocks such as governors, exciters, or converter controllers using steady-state operating points [5, 119]. The approach is particularly useful when models are transparent and modular.

Apart from conventional power system models, the need for a robust initialization strategy becomes even more critical in the context of HVDC systems and IBRs. Their sophisticated architectures and tightly integrated control loops render conventional initialization approaches virtually infeasible. In such systems, a well-structured initialization scheme is essential to ensure numerical stability, simulation accuracy, and computational efficiency [5, 120-122].

Building on the load-flow-based initialization approach, further advancements have extended the method by following the LF solution with a steady-state comprehensive solution of all control system equations of an IBR. This enables comprehensive initialization of electrical, mechanical, and control subsystems before starting the time-domain simulation. These enhanced methods have been successfully applied to MMC models [111], photovoltaic (PV) systems [113], and full-scale converter-based parks [112]. However, their effectiveness typically hinges on full access to internal model parameters and control logic, an assumption that often does not hold in the case of commercial or proprietary black-box models.

1.7 Problem statement and research gaps

EMT simulations, although essential for detailed analysis of MTDC systems, are computationally demanding, especially as networks scale up and incorporate increasingly complex control schemes. A primary challenge is achieving rapid and stable initialization, which is critical for both simulation accuracy and computational efficiency. Existing initialization methodologies frequently encounter convergence issues or excessive computation times, particularly in large-scale MTDC systems featuring diverse technologies, intricate control designs, or black-box and grey-box modules. Moreover, initialization techniques available in the literature are typically model-specific, lacking unified or generalized frameworks suitable for different converter technologies and configurations. Additionally, there is a notable scarcity of studies specifically addressing initialization methods for real-time simulations.

Among existing initialization methods, those based on load-flow solutions have shown the greatest promise. However, since MTDC systems encompass both AC and DC sub-networks, an integrated AC–DC load-flow solution becomes essential to accurately determine the operating point prior to initialization. Unfortunately, most EMT simulation platforms do not provide robust or flexible solvers for AC–DC load-flow analysis. This limitation poses a significant barrier to effective initialization, especially in hybrid systems featuring complex converter control strategies such as multiple DC voltage regulators, adaptive droop characteristics, or a combination of V_{dc} and droop converters. The lack of dedicated and generalized load-flow methods for unbalanced AC–DC systems (i.e., MTDC networks operating with a DC pole out of service, where the system reverts to monopolar operation with metallic or ground return) further exacerbates this challenge, leaving a critical gap in the modeling and simulation workflow for modern MTDC networks.

Overall, while equivalencing, hardware acceleration, and simulation-strategy methods have demonstrated speedups in various EMT contexts, their applicability to large-scale MTDC studies remains insufficiently characterized. Strong AC/DC couplings, stiff converter dynamics, and interacting voltage-control loops can limit effective decomposition and reduce parallel efficiency. Co-simulation may introduce causality issues, latency, and energy-balance errors, unless power-consistent interface schemes are carefully employed. Although significant parallel speedups have been reported in the literature, many such demonstrations are based on highly detailed component-level models that are not typically used in system-level MTDC studies. As a result, these findings

may not translate directly to realistic MTDC applications involving multiple converters and coordinated control systems. Solver-level optimizations, such as sparse matrix reordering, block factorization, and controller re-sequencing, can improve simulation efficiency but have not been systematically benchmarked for robustness under large disturbances. Standardized MTDC-oriented benchmarks that jointly evaluate speedup and waveform fidelity, particularly for converter–grid interactions, remain scarce. These gaps, combined with the central importance of fast and reliable initialization, motivate the problem statement and methods developed next.

In summary, this dissertation explicitly addresses the following critical research gaps:

- Lack of robust, unified initialization methods suitable for EMT simulations, particularly accommodating black-box and grey-box MTDC system models.
- Insufficient AC–DC load-flow methodologies that can accurately support steady-state initialization of complex MTDC systems involving diverse control strategies.
- Limited exploration and validation of existing computational acceleration techniques specifically tailored to MTDC networks. In addition, an absence of comprehensive evaluations of hybrid acceleration approaches that integrate multiple techniques, potentially leading to significant simulation speed improvements.

This dissertation aims to bridge these research gaps by proposing novel methodologies to enhance the initialization, computational efficiency, robustness, and scalability of EMT simulations for complex MTDC systems.

1.8 Contributions

This dissertation addresses key challenges in the EMT simulation of large-scale hybrid AC–DC systems, with a particular emphasis on MTDC networks. The overarching objective is to accelerate EMT simulations of MTDC systems. The contributions are organized into two primary focus areas: simulation initialization and computational acceleration.

The first area, simulation initialization, aims to enhance simulation efficiency by reducing or eliminating the time typically wasted during the steady-state setup phase. The second area, computational acceleration, focuses on significantly increasing simulation speed through optimized methods and parallel execution strategies.

A suite of novel techniques is developed to improve EMT simulation efficiency, robustness, and compatibility with black-box converter models. The main contributions of this dissertation are summarized as follows.

1. **AC–DC load-flow for hybrid MTDC systems**

A novel hybrid AC–DC load-flow methodology is proposed to facilitate EMT simulation of MTDC systems with detailed control requirements. The approach integrates a Newton-based solver for the AC network with a fixed-point solver for the DC side, enabling accurate power flow calculations across AC–DC converter stations. It supports a wide range of control modes, including P-, Vdc-, V/f-, Pdc-droop, Vdc-droop, multi-droop, and emerging control strategies, thus accommodating diverse control configurations. The method addresses key challenges in existing AC–DC load-flow approaches. Importantly, its results can be directly used for steady-state initialization in time-domain EMT simulations.

2. **Initialization of Grid Forming-VSCs (GFM-VSCs)**

A robust initialization strategy is developed for GFM-VSCs, enabling complete steady-state initialization of their control systems. Two complementary methods are introduced. The first extends an existing load-flow-based initialization approach and is suitable for white-box models, as it relies on access to control parameters. The second is a time-domain technique based on subsystem decoupling, referred to as the Decoupling Interface. This method enables the initialization of isolated AC grids interconnected through GFM-VSCs, a scenario in which conventional methods often fail. Notably, it is compatible with black-box models.

3. **Unified initialization of MTDC systems**

Unlike existing methods, this contribution focuses on a system-level initialization. This contribution presents a generalized initialization framework based on the DI method presented for GFM-VSCs, applicable to hybrid AC–DC systems and black-box models. The proposed method is validated on various MTDC benchmarks and shown to handle diverse converter types and system configurations.

4. **Real-time extension of DI initialization**

To address the needs of HIL and real-time applications, the DI method is extended to real-time simulation environments. The strategy leverages subsystem decoupling to suppress transients and reduce startup delays. A real-time test on a modified CIGRE benchmark demonstrates significantly faster initialization compared to traditional approaches.

5. **Hybrid initialization strategy for DFIG wind parks**

In the previous contributions on unified DI initialization [11], DFIG-WPs were the bottleneck for initializing the entire MTDC system. A new initialization technique is proposed for DFIG-WP models. The approach combines internal application of DI blocks with targeted steady-state initialization of critical control segments. This significantly reduces initialization time while preserving accuracy and stability.

6. **Acceleration techniques for EMT simulation**

This dissertation evaluates and proposes several acceleration strategies for MTDC simulation. These include:

- Transmission line-based parallelization (TLP), which exploits propagation delays to parallelize network segments.
- Control system parallelization (CtrlP), which distributes the solution of control equations across CPUs.
- Optimized sequential control solvers (OSeqCtrl), which reduce solver delays without compromising accuracy.

A hybrid strategy combining these methods is demonstrated to achieve over 20 times simulation speedup in large-scale MTDC systems.

1.9 Thesis outline

This dissertation is organized into seven chapters:

CHAPTER 1 introduces the research context, summarizes key literature, and outlines the main contributions.

CHAPTER 2 presents a new hybrid load-flow methodology for MTDC systems, detailing the formulation and verification of the proposed AC–DC LF solvers.

CHAPTER 3 introduces an initialization framework for GFM-VSCs and discusses techniques for outer control initialization and time-domain recoupling.

CHAPTER 4 extends the DI-based initialization framework to broader MTDC configurations, including real-time simulations. A unified and scalable methodology is developed and validated on CIGRE test systems.

CHAPTER 5 proposes a hybrid initialization strategy for wind parks with DFIGs, addressing the bottlenecks in convergence time through selective steady-state and decoupling techniques.

CHAPTER 6 investigates several acceleration techniques for EMT simulation. The feasibility and performance of each method are assessed through benchmark systems, including the InterOPERA MTDC network.

CHAPTER 7 concludes the dissertation and outlines future directions for research.

CHAPTER 2 HYBRID AC–DC LOAD-FLOW ALGORITHM FOR MTDC MODELS

2.1 Introduction and background

MTDC systems integrate alternating current (AC) and direct current (DC) networks, making accurate LF analysis essential for system planning, operation, and stability assessment [123-125]. Beyond these conventional applications, LF solutions also play a crucial role in initializing EMT simulations, ensuring stable startup while mitigating numerical instabilities [9, 11, 111, 126]. Despite its importance, unbalanced AC–DC LF analysis remains insufficiently addressed within EMT platforms. While AC LF tools are widely available, most EMT simulators lack dedicated AC–DC LF solvers, highlighting a critical gap in current methodologies. Furthermore, the increasing complexity of converter control strategies, such as DC Droop and GFM controls, necessitates flexible LF approaches that can accommodate diverse control modes.

The Modified Augmented Nodal Analysis (MANA) structure has proven effective for formulating and solving conventional LF problems using Newton's method, initially proposed in [5, 127, 128] and further developed in [123, 124]. It has also been extended to microgrid applications [129] and multifrequency LF analysis [130]. Additionally, a MANA-based formulation for DC distribution networks has been proposed in [131].

AC–DC LF methods can be broadly classified into sequential methods [132, 133] and direct methods [133-135]. Sequential methods solve AC and DC LF separately, iterating between them until convergence. They offer ease of implementation and can readily incorporate different control modes. In contrast, direct methods provide faster convergence but may introduce modeling complexities, especially when integrating advanced control strategies.

A key trend in recent AC–DC LF research is simplicity: many studies leverage existing AC LF solvers within EMT environments by representing the DC grid with AC-equivalent circuits. Both sequential [136] and direct methods [135] use this idea, but they typically do not embed DC-voltage droop laws and often struggle when multiple converters regulate V_{dc} simultaneously. In contrast, [134] propose a unified Newton–Raphson AC–DC power-flow that treats the DC grid as AC-equivalent and permits multiple converters to regulate DC voltage concurrently. However, their formulation does not explicitly model DC-voltage droop control, the DC regulation is enforced via

voltage-control constraints rather than droop sharing, which limits direct applicability to MTDC schemes that rely on droop for power-sharing and redundancy.

Overall, there is an inherent trade-off between simplicity and flexibility. While simpler methodologies enhance compatibility with existing solvers, they may limit algorithm adaptability, making it more challenging to model evolving and diverse control strategies.

This chapter introduces a new hybrid approach for unbalanced AC–DC LF analysis, combining a Newton-based MANA AC LF engine [5, 127, 128] with a complementary fixed-point algorithm to model various MTDC components. Here, unbalanced AC–DC load-flow refers to the operating condition where one pole of a bipolar HVDC system is lost or intentionally grounded, forcing monopolar operation with either metallic or ground return. The proposed method incorporates adapted constraints, enabling seamless representation of multiple converter control strategies, including DC Droop and multi-droop control [137], while addressing limitations of previous research. It is directly adaptable to any EMT-type solver with multiphase load-flow capability, which is a unique advantage. It is generic and is applied externally, by scripting, without accessing or modifying the existing LF program.

The proposed approach is demonstrated on the InterOPERA test system [138], with results verified through time-domain EMT simulations. Furthermore, the LF solutions are used to initialize EMT simulations via the DI method [9], which is explained later in CHAPTER 4, bridging the gap between steady-state analysis and dynamic EMT modeling.

2.2 The proposed hybrid AC–DC load-flow methodology

This research proposes a sequential hybrid algorithm to perform AC–DC LF analyses for MTDC systems. The hybrid methodology involves decoupling the AC and DC sides of power converters, representing each side by equivalent LF buses, as illustrated in Figure 2.1 . The AC and DC LFs are conducted separately, i.e., decoupled AC and DC LFs, and the fixed-point algorithm updates the AC and DC constraints for the next iteration.

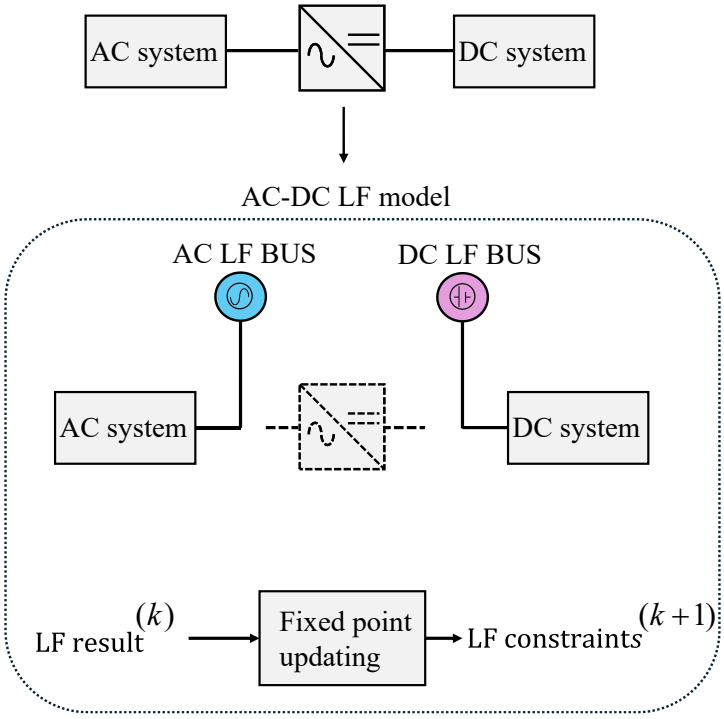

Figure 2.1 The proposed hybrid AC–DC LF schematics.

Figure 2.2 shows a high-level overview of the proposed algorithm. It comprises two primary computational methods: Newton's iterative method and the fixed-point method. Newton's method, implemented via a matrix-based method (MANA), efficiently handles complex and computationally intensive tasks. It is used directly from the EMTP® software. Meanwhile, simpler calculations, such as the coupling equations between AC and DC buses and the updating of dependent constraints, are performed using a fixed-point iteration method, facilitating computational simplicity and method flexibility.

The overall procedure involves nested iterations, with the master loop including both Newton's and fixed-point parts. In the Newton's method part, the decoupled AC and DC LFs are performed in a sub-loop, exploiting the efficiency provided by the existing MANA-based solver.

The fixed-point part solves the AC–DC coupling equation to ensure consistency between the decoupled AC and DC LF solutions. Moreover, this part includes an optional step to update discretized variables for more advanced controls. Iterative convergence of the coupled AC–DC system is pursued until a steady-state solution is achieved. The following section details the decoupled AC and DC LFs, while Section 2.4 outlines the specifics of the fixed-point iteration process.

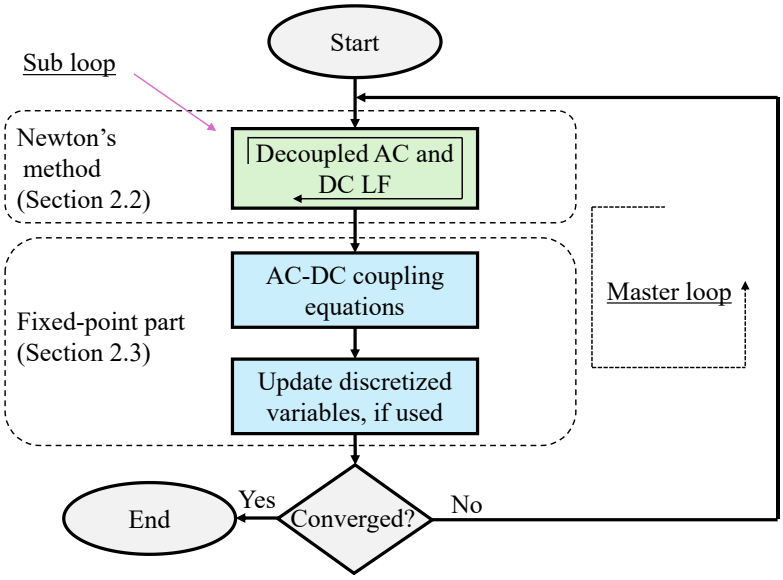

Figure 2.2 Overview of the hybrid AC–DC load-flow process.

2.3 Decoupled AC and DC LFs

The decoupled AC and DC LF formulation is obtained by substituting the power converter with two independent LF buses: an AC LF bus and a DC LF bus, as illustrated in Figure 2.3. At this stage, solving the AC and DC subsystems separately does not yet yield the complete AC–DC LF solution, but it provides the foundation for the subsequent coupled formulation.

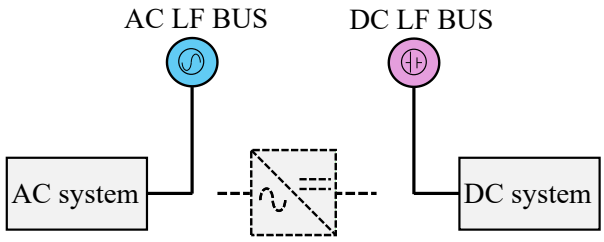

Figure 2.3 Decoupled AC and DC LF schematic.

2.3.1 Decoupled AC LF constraints

The AC LF computation leverages a multiphase LF algorithm based on MANA as presented in [5, 127, 128]. The AC-side representation of power converters employs standard LF bus types (*slack*, *PV*, and *PQ*), which are selected according to the respective control mode. Table 2.1 provides detailed guidance on selecting LF bus types for various converter control scenarios. The "Main

control mode" refers to the primary active-power or DC-side objective (e.g., V_{dc}, P_{dc}, P_{ac}, or droop control).

Table 2.1 LF modelling for power converter's AC side.

Grid component	Main control mode	Other control options	LF model
VSC	V_{dc}	AC voltage	*PV*
		Reactive power	*PQ*
	GFM	-	*Slack*
	Vdc-Droop	AC voltage	*PV*
		Reactive power	*PQ*
	Pdc-Droop	AC voltage	*PV*
		Reactive power	*PQ*
	P_{dc} or P_{ac}	AC voltage	*PV*
		Reactive power	*PQ*
Wind Park	AC voltage	-	*PV*
	Reactive power		*PQ*
	Power factor		
	Q\V droop		
PV Park	AC voltage	-	*PV*
	Reactive power		*PQ*
	Power factor		
	Q\V droop		

2.3.2 Decoupled DC LF constraints and derivation

Under steady-state conditions, DC systems can be represented analogously to AC systems operating at zero frequency. Consequently, standard AC LF tools available within EMT simulators can be utilized, provided modifications to the constraints are introduced. Specifically, three DC LF constraints are introduced: DC voltage (*Vdc-LF*), DC power (*Pdc-LF*), and DC droop control (*Ddc-LF*). These constraints effectively represent various DC-side converter control modes, as summarized in Table 2.2, and serve as the foundation for advanced control strategies discussed in subsequent sections.

Table 2.2 LF modelling for the power converter's DC side.

Grid component	Main control mode	Other control options	LF model
VSC	GFM	-	*Pdc-LF*
	V_{dc}	AC voltage	*Vdc-LF*
		Reactive power	
	Vdc-Droop	AC voltage	*Ddc-LF*
		Reactive power	
	P_{dc} or P_{ac}	AC voltage	*Pdc-LF*
		Reactive power	
	Pdc-Droop	AC voltage	*Ddc-LF*
		Reactive power	
DC-DC converters	DC transformer	Ideal transformer	
	Back-to-back VSCs	Each VSC will be modelled individually.	
PV arrays	MPPT	-	*Pdc-LF*

For practicality and intuitive physical interpretation, V_{dc} is associated with the real part of the peak line-to-line voltage, as shown in Figure 2.4. Where the DC terminals are represented, for example, by phases A and B, abandoning the third phase (phase C). Therefore, V_{dc} can be represented mathematically as:

$$V_{dc} = \sqrt{2} \times \mathbb{R}\left(\vec{V}_{ac}\right) \tag{0.1}$$

where $\vec{V}_{ac}$ represents the line-to-line AC voltage phasor in RMS. Extracting the real side, V_{dc} can be written as:

$$V_{dc} = \sqrt{2}\left|\vec{V}_{ac}\right| \times \cos\left(\delta\right) \tag{0.2}$$

where δ is the angle of $\vec{V}_{ac}$ as shown in Figure 2.4. This voltage phasor can be set as a reference; therefore, δ is set to 0.

$$V_{dc} = \sqrt{2}\left|\vec{V}_{ac}\right| \tag{0.3}$$

The equivalent value of V_{dc} is introduced into the conventional AC LF problem as conventional *Slack* bus constraints, i.e, voltage magnitude and angle. The equivalent voltage magnitude is found using (0.2) and the angle, δ, is set to 0.

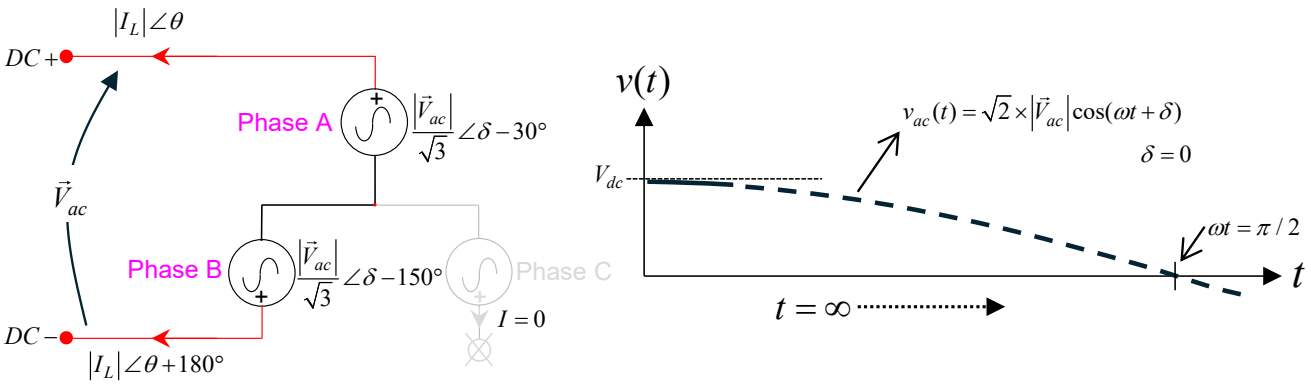

(a) (b)

Figure 2.4 DC system realization using an AC system: (a) schematic, (b) waveforms.

Furthermore, AC parameters are converted into DC equivalents via appropriate scaling factors:

$$\begin{aligned} I_{dc} &= \sqrt{2}\mathbb{R}\left(\vec{I}_L\right) \\ &= \sqrt{2}\left|\vec{I}_L\right|\cos(\theta) \end{aligned} \tag{0.4}$$

where I_L and θ are the line AC current phasor in RMS and its angle, respectively. For power conversions, P_{dc} can be expressed as:

$$P_{dc} = V_{dc} I_{dc} \tag{0.5}$$

Therefore, it can be rewritten using (0.3) and (0.4) as:

$$\begin{aligned} P_{dc} &= \left(\sqrt{2}\left|\vec{V}_{ac}\right|\right)\left(\sqrt{2}\left|\vec{I}_L\right|\cos(\theta)\right) \\ &= 2\left|\vec{V}_{ac}\right|\left|\vec{I}_L\right|\cos(\theta) \end{aligned} \tag{0.6}$$

On the other side, referring to Figure 2.4, as we abandon a one-phase out of the three phases, the total AC power can be found as:

$$P_{ac} = \left|\vec{V}_{ac}\right|\left|\vec{I}_L\right|\cos(\theta) \tag{0.7}$$

Therefore, by comparing (0.6) and (0.7), the relation between the P_{dc} and P_{ac} is given by:

$$P_{dc} = 2P_{ac} \tag{0.8}$$

Thus, the DC power constraint (*Pdc-LF*) can be equivalently represented using an adapted *PQ* bus, with reactive power set to zero.

For DC-droop control, they are typically realized as either *Vdc-Droop* or *Pdc-Droop* (illustrated in Figure 2.5.(a) and Figure 2.5.(b)). *Pdc-Droop* is usually added to converters with V_{dc} control to coordinate their roles. Similarly, *Vdc-Droop* branch is added to converters with P_{dc} control.

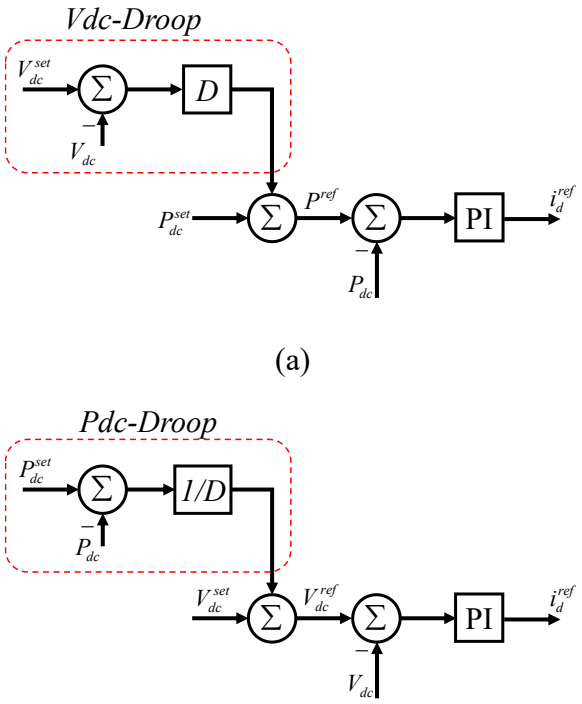

Figure 2.5 The outer control schematic of: (a) *Vdc-Droop* control, (b) *Pdc-Droop* control.

The steady-state representations of these two types are identical and can be expressed as:

$$P_{dc} = P_{dc}^{set} + D\left(V_{dc}^{set} - V_{dc}\right) \tag{0.9}$$

Where P_{dc}^{set} and V_{dc}^{set} are the setpoints, and D represents the droop coefficient, which defines the slope of the linear relationship between the P_{dc} and V_{dc} as illustrated in Figure 2.6. Since all of P_{dc}^{set}. V_{dc}^{set}, and D are constants, (0.9) can be rewritten by aggregating all constant terms together in a single combined constant term as

$$\begin{aligned} P_{dc} &= \left(P_{dc}^{set} + DV_{dc}^{set}\right) - DV_{dc} \\ &= P_{combined}^{set} - DV_{dc} \end{aligned} \tag{0.10}$$

where

$$P_{combined}^{set} = P_{dc}^{set} + DV_{dc}^{set} \tag{0.11}$$

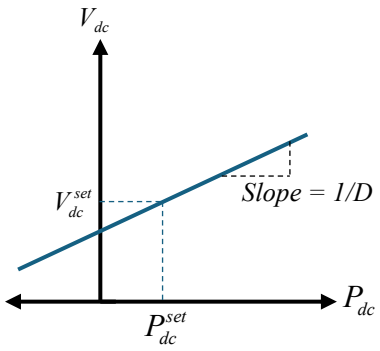

Figure 2.6 DC-Droop characteristics.

As clear from (0.10), the resulting P_{dc} has two parts: a fixed power represented by $P_{combined}^{set}$, and a linearly dependent part on V_{dc} represented by *-D*. Therefore, the *Ddc-LF* can be modeled straightforwardly as a combination of a fixed-power constraint with a fixed-current load on one node.

2.3.3 Decoupled AC and DC LF procedure

As illustrated in Figure 2.7, equivalent basic LF bus constraints are given for each side of the power converters as well as at the PCC of IBRs. The selection is based on Table 2.1 and Table 2.2. A detailed algorithm for implementing the AC and the DC LF is illustrated in Figure 2.8. For the AC LF part, it is a straightforward procedure where the multiphase MANA-based LF solver described in [5, 127, 128] is used directly to compute the solution using Newton's iterative method.

On the other hand, the DC LF looks similar but with an interface to convert the constraints to equivalent AC ones using scaling factors, then converting the results back from the AC results to their DC equivalent. The scaling factors can be applied automatically using a scripting language available within EMT software. Both the AC and DC LFs are computed simultaneously, i.e., they are computed together in a single MANA as a single decoupled system.

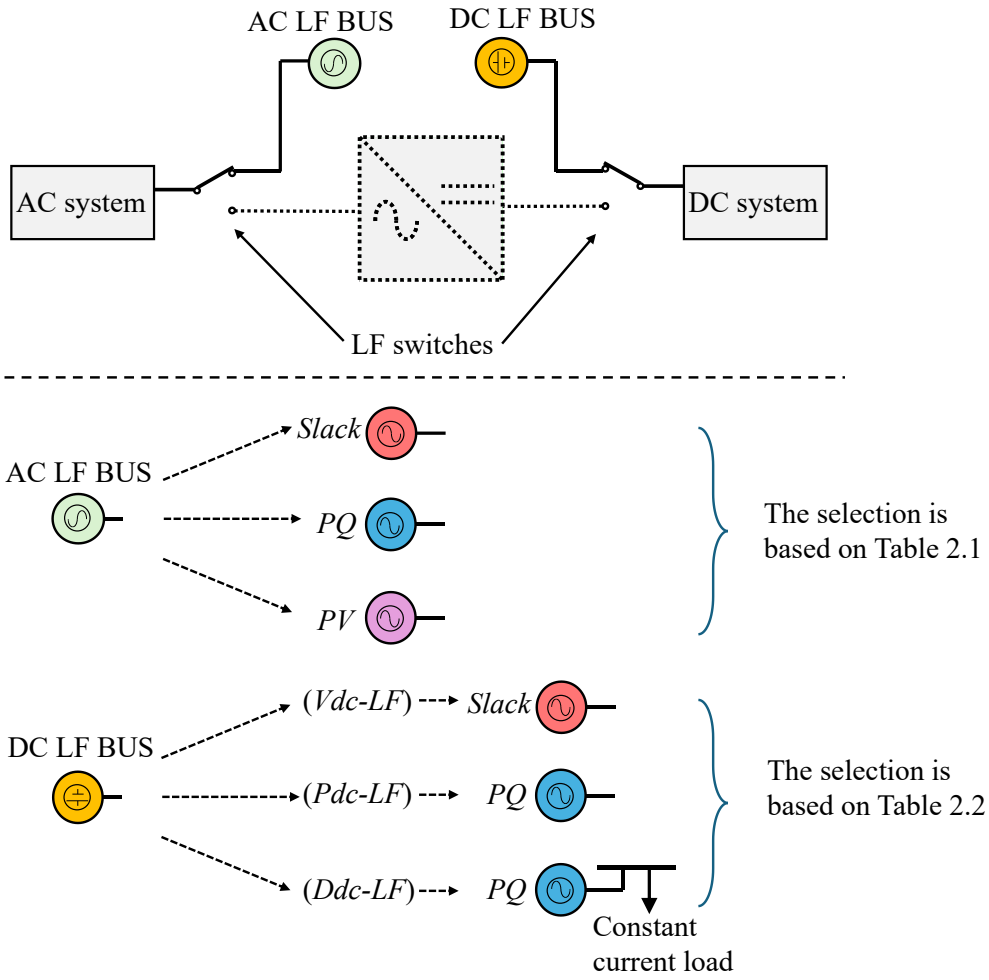

Figure 2.7 Decoupled AC and DC LF implementation.

Finally, for EMT tools that do not support multi-frequency LF analysis, i.e., those unable to set LF bus frequencies to zero, or close to zero, DC lines can be replaced with equivalent resistances. This inherently eliminates the reactive power component associated with DC transmission, ensuring that the load-flow solution remains physically consistent with the steady-state DC network behavior. As a result, DC-LF can be performed at the nominal AC system frequency (e.g., 50 or 60 Hz) while maintaining accuracy through the same derived transformation factors in (0.3), (0.4), and (0.8), without requiring modifications to the solver's internal formulation.

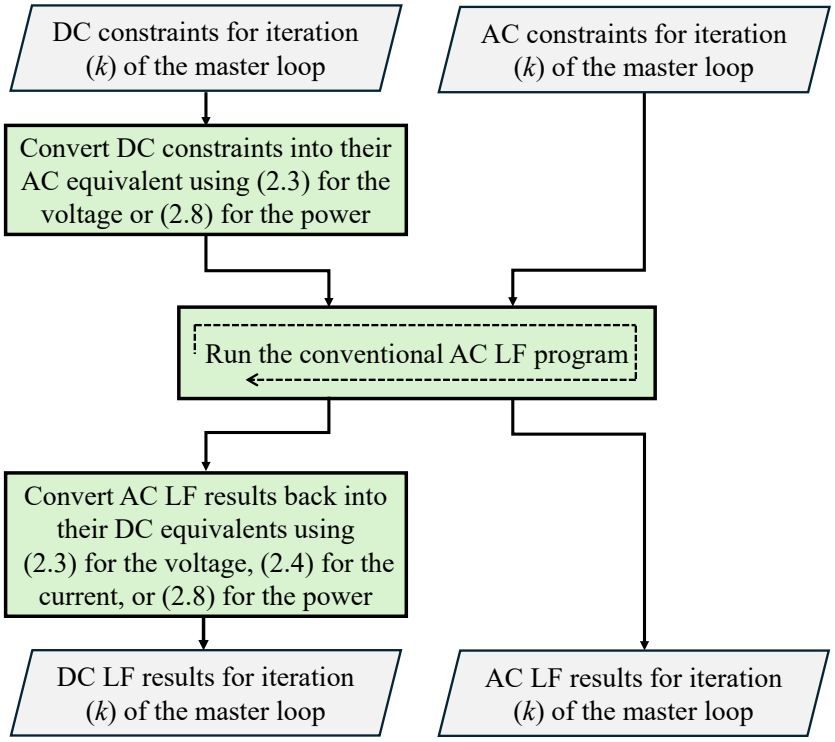

Figure 2.8 Decoupled AC and DC LF procedure.

2.4 The Fixed-point part

The synchronization and coherence between AC and DC calculations within the proposed hybrid LF algorithm are ensured through updating procedures implemented via fixed-point iterations. This iterative method was chosen for its simplicity and stable convergence behavior when applied to the coupled AC–DC problem, enabling straightforward coordination between the two domains. Another advantage is that it can be externally added with scripts to any existing software.

2.4.1 AC–DC coupling equations

The AC–DC coupling equations establish a direct connection between AC and DC LF buses through power converters. Depending on the converter's primary control mode, either the AC or DC constraints are updated for the subsequent iteration $(k+1)$. Specifically, if the primary control is situated on the DC side, the AC side constraints are dependent on the DC side, therefore the dependent constraint should be updated here accordingly, and vice versa.

For example, in a GFM-MMC, where control primarily occurs on the AC side, the corresponding DC side constraint (P_{dc}) is dependent on P_{ac}. Therefore, P_{dc} should be updated by adding converter losses to the calculation in the current iteration:

$$P_{dc}^{ref(k+1)} = P_{ac}^{(k)} + P_{loss}^{(k)} \tag{0.12}$$

A where $P_{dc}^{ref(k+1)}$ is the P_{dc} constraint for the $(k+1)$ iteration of the master loop. Alternatively, if the control is primarily on the DC side, the AC side should be updated accordingly using:

$$P_{ac}^{ref(k+1)} = P_{dc}^{(k)} - P_{loss}^{(k)} \tag{0.13}$$

The calculation of converter losses depends on the specific converter model utilized. For the MMC, most EMT models used for large-scale systems are either Model 3 or Model 4 in [40]. Therefore, in these models, MMC losses at iteration (k) are expressed using [43, 139]:

$$P_{losses}^{(k)} = \underbrace{\frac{3R_{arm}}{2}\left|\vec{I}_L^{(k)}\right|^2 + \frac{2R_{arm}}{3}\left(I_{dc}^{(k)}\right)^2}_{Conduction\,losses} + \underbrace{P_{loss,XFMR}^{(k)}}_{Transformer\,losses} \tag{0.14}$$

where R_{arm} is the total arm resistance and $P_{loss,XFMR}^{(k)}$ is the transformer losses at iteration (k).

Other losses can also be incorporated into (0.14) to suit the level of detail required for a given LF application. For example, additional components such as arm reactor losses and switching losses of power electronic devices may be included. Standardized formulations for these losses are provided in [140], which can be added to (0.14) for more comprehensive modeling. The selection of which losses to represent depends on the desired modeling accuracy and the target application.

Another option is to use an approximated model, such as the quadratic models used in [134]:

$$P_{losses}^{(k)} = a + b\left|\vec{I}_L^{(k)}\right| + a\left|\vec{I}_L^{(k)}\right|^2 \tag{0.15}$$

where *a, b,* and *c* are the coefficients for this model. Typical values for the coefficients are often used to represent this model. In this chapter, the loss model in (0.14) is used for the LF calculations.

2.4.2 Update discretized variables

Due to the increasing sophistication and variability of converter control strategies, representing converters through standard LF constraints can become challenging. To address this complexity,

more intricate control modes are linearized and converted into basic AC or DC LF models, updating discretized variables as required.

This dissertation demonstrates a practical implementation using a DC-droop control strategy with multi-droop coefficients, proposed in [137]. A generic characteristic is illustrated in Figure 2.9.

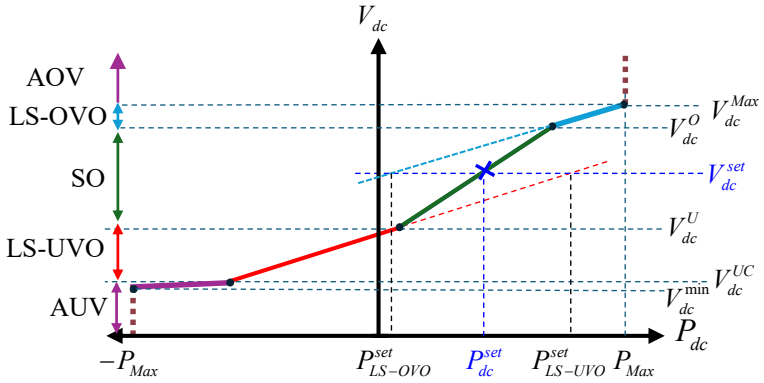

AOV: Abnormal Overvoltage
LS-OVO: Limited sensitivity-Overvoltage Operation
SO: Sensitive Operation
LS-UVO: Limited sensitivity-Undervoltage Operation
AUV: Abnormal Undervoltage

Figure 2.9 Multi-droop characteristic [137].

This multi-droop control mechanism dynamically adjusts the droop coefficient based on the measured V_{dc}, altering droop sensitivity according to the instantaneous DC voltage level.

As depicted in Figure 2.9 and detailed in [137], the multi-droop characteristic is segmented into three operational regions:

- **Sensitive Operation (SO):** The primary operational zone characterized by the highest sensitivity and steepest slope.
- **Limited Sensitivity (LS):** Regions adjacent to SO, with reduced droop sensitivity for V_{dc} DC voltages significantly above or below the normal operational range.
- **Fixed Power Mode:** Activated when P_{dc} reaches predetermined upper or lower operational limits, thereby maintaining fixed power output.

To accurately represent these control strategies within the load-flow framework, corresponding *Ddc-LF* are defined separately for each operational segment, as summarized in Table 2.3.

Therefore, the droop coefficient is defined as a piecewise function that updates its discretized value through the master loop, as shown in Figure 2.2.

Table 2.3 Piecewise realization of the multidroop characteristic in Figure 2.9.

***Ddc-LF* settings**			**Range**
D	**Power setpoint**	**Voltage setpoint**	
D_{SO}	P_{dc}^{set}	V_{dc}^{set}	$V_{dc}^{O} > V_{dc} > V_{dc}^{U}$
D_{LS-OVO}	P_{LS-OVO}^{set}	V_{dc}^{set}	$V_{dc}^{Max} > V_{dc} > V_{dc}^{O}$
0	P_{Max}	V_{dc}^{set}	$V_{dc} \geq V_{dc}^{Max}$
D_{LS-UVO}	P_{LS-UVO}^{set}	V_{dc}^{set}	$V_{dc}^{U} > V_{dc} > V_{dc}^{UC}$
D_{AUV}	P_{AUV}^{set}	V_{dc}^{set}	$V_{dc}^{UC} > V_{dc} > V_{dc}^{\min}$
0	$-P_{Max}$	V_{dc}^{set}	$V_{dc}^{\min} \geq V_{dc}$

2.4.3 Fixed-point procedure

As shown in Figure 2.10, the results of AC and DC LFs are first obtained for the current iteration (k), then used to calculate updated values for the dependent constraints for the next iteration (k+1). If applicable, the discretized constraints are also updated for the next iteration, and the process repeats until convergence.

Convergence is determined by monitoring either the variation in AC/DC LF results or the change in dependent setpoints across iterations. The algorithm terminates when these variations between iterations fall below a predefined threshold. A maximum number of iterations is also specified to prevent endless looping in case the convergence criterion is not met, thereby ensuring numerical stability of the procedure.

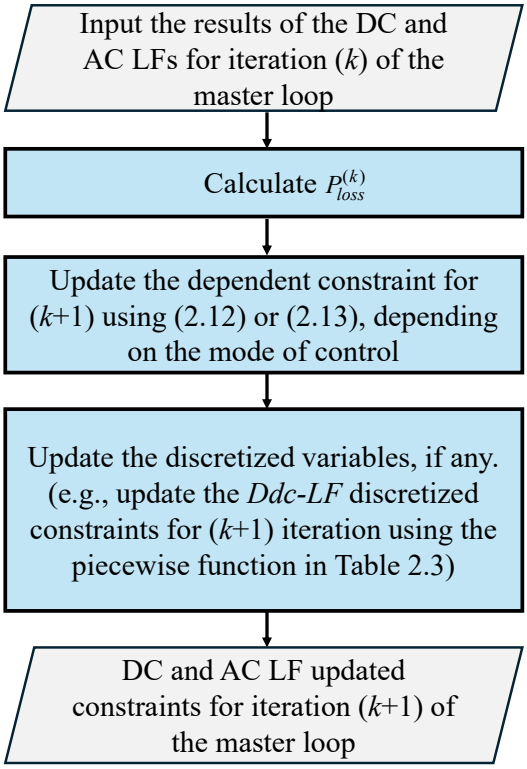

Figure 2.10 Fixed-point implementation flowchart.

2.5 Test cases

This section assesses the effectiveness of the proposed AC–DC LF methodology using the InterOPERA system[138]. Developed as a European-funded benchmark, InterOPERA aims to ensure interoperability among multi-vendor HVDC grids while facilitating the integration of renewable energy sources. For this study, InterOPERA Variant 1, referred to as the "Meshed offshore grid for wind export"[138], is used as the reference system for comparative analysis. The AC–DC LF algorithm is evaluated under various scenarios, including MTDC system operation in unbalanced conditions.

As depicted in Figure 2.11, the system consists of five MMC bipolar stations interconnected within a meshed DC network. This infrastructure is designed to efficiently collect and transmit power from offshore renewable sources to onshore receiving stations. It serves as a representative testbed for evaluating the effectiveness of LF algorithms in large-scale MTDC networks across a range of operating scenarios.

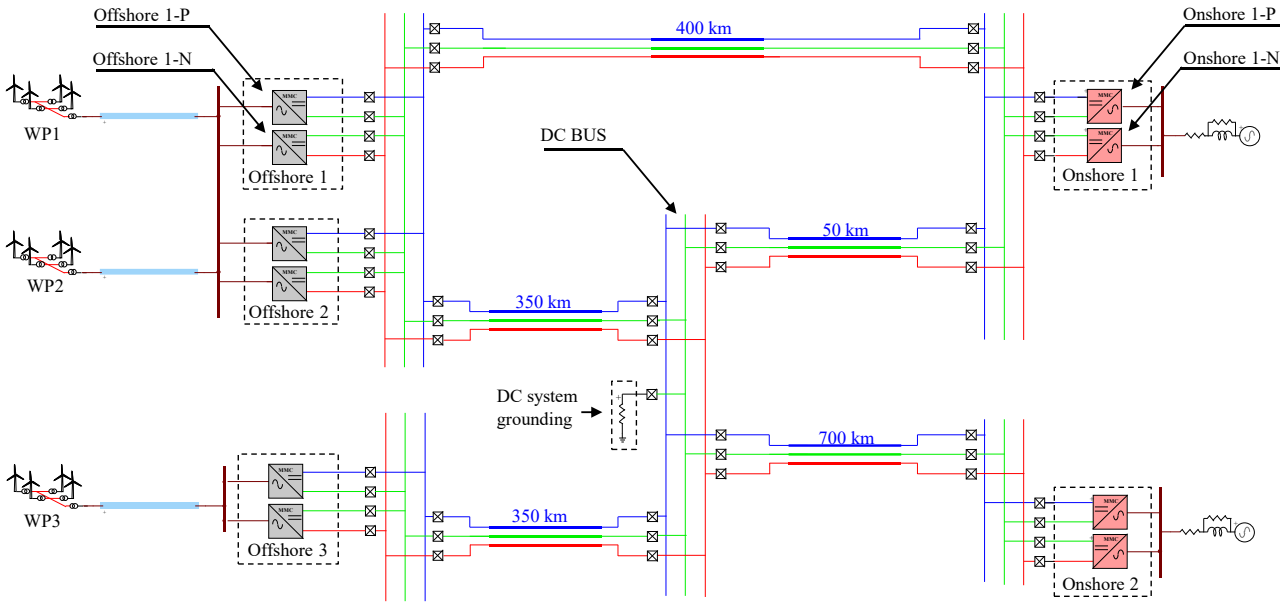

Figure 2.11 InterOPERA's variant 1 test system schematic.

2.5.1 EMT model description of InterOPERA

The Offshore VSC stations operate under V/f control [141], while the onshore stations implement multi-droop control [137], is configured as shown in Figure 2.12. The droop coefficients, defined in per-unit (pu) relative to a 525 kV and 1000 MW base, include a sensitive operation mode at 10 pu and a limited sensitivity mode at 25 pu. In addition to multi-droop regulation, onshore stations apply secondary control to regulate reactive power with the reference set to zero.

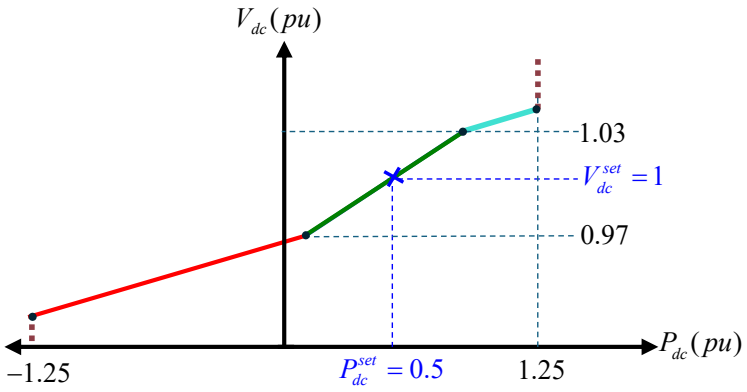

Figure 2.12 Multi-droop control settings for all onshore stations.

All MMC stations are modeled with a generic 401-level half-bridge MMC (Model 3) [40]. Each pole is rated 1000 MVA (i.e., 2000 MVA per station) with an overload capability up to 1.25 pu. Wind parks can be modelled by either DFIG or full-scale models; the latter is selected for this

chapter. Wind-park operating points are set for testing purposes as follows: each turbine is rated 16.67 MVA and produces 15 MW active power. WP1 comprises 67 turbines; WP2 and WP3 comprise 40 and 47 turbines, respectively. All wind parks operate in reactive-power control with the reference set to zero.

Table 2.4 consolidates the component data (line models, converter ratings and controls, wind-park aggregation, and load representations) used in the simulations. While some of these details (e.g., EMT cable or converter models) are not directly required for solving the LF equations, they are included here to provide a consistent description of the complete InterOPERA test system EMT model. This ensures that the LF formulation can be directly mapped to the EMT implementation used later in the study.

Table 2.4 Model types used in InterOpera variant 1

Aspect		**Details**
Load-flow	Number of AC LF buses	15
	Number of DC LF buses	10
	Convergence tolerance for AC–DC LF (pu)	0.00001
Time-domain simulation details (for LF validation)	Simulation interval (s)	10
	Time-step (μs)	50
Component model	MMC	Generic 401-level, half-bridge, AVM, (Model 4) [40]
		Offshore stations operate in V/f control mode [141]
		Onshore stations operate in DC adaptive Droop control mode [137], the parameters are plotted in Figure 2.12
	Wind parks	Generic aggregated full-scale converter wind park model.

2.5.2 LF implementation in EMT software

The proposed DC load-flow formulation can be implemented in any EMT-type program. In this work, the implementation is carried out in EMTP®, where each DC bus is represented by two phases: phase A and phase B correspond to the positive and negative DC terminals, respectively. The unused phase terminal (phase C) is grounded through a high-value dummy resistance (e.g., 1000 MΩ) to maintain compatibility with the AC bus representation.

As shown in Figure 2.13, the *Pdc-LF* bus is implemented in EMTP® by using a conventional *PQ-LF* bus. The unused phase terminal is grounded through a dummy resistor, while the positive and negative terminals enforce the DC power injection obtained from the LF solution.

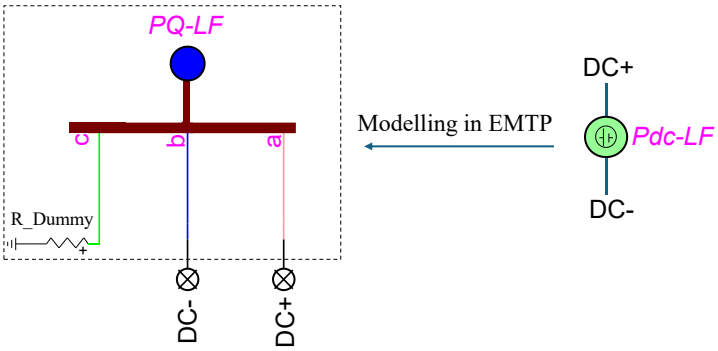

Figure 2.13 *Pdc-LF* implementation in EMTP®.

Similarly, Figure 2.14 shows the implementation of a *Vdc-LF* bus, where the LF *slack* bus is used instead of a *PQ-LF* bus, as described in Section 2.3.3. This allows the DC voltage to be fixed at the LF solution value, while the current adjusts accordingly.

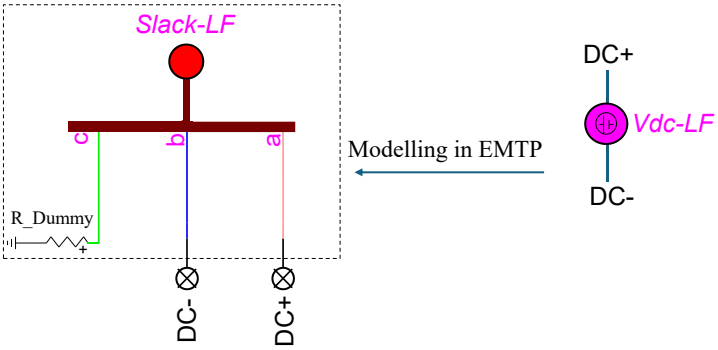

Figure 2.14 *Vdc-LF* implementation in EMTP®.

For the *Ddc-LF* bus, the implementation follows the formulation in Section 2.3.3 and Equation (0.10). As shown in Figure 2.15, it is realized by combining a *Pdc-LF* bus with a constant current load that reflects the droop characteristic. Since conventional LF programs require at least one slack bus in the system, a *Vdc-LF* bus (which contains a *slack*) with a high dummy resistance (e.g., 1000 MΩ) is connected. This ensures proper initialization in cases where only droop-controlled buses exist (e.g., in the InterOPERA system).

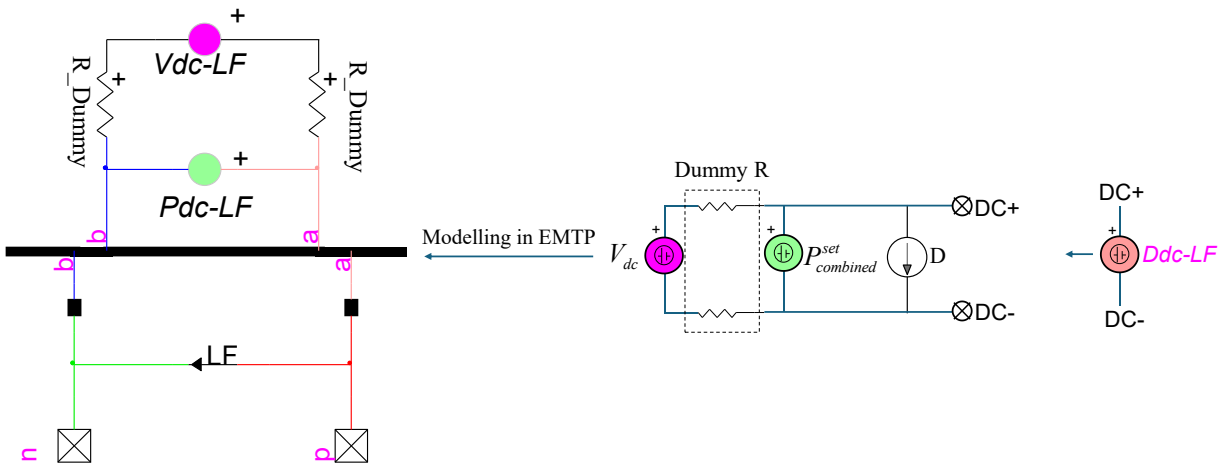

Figure 2.15 *Ddc-LF* implementation in EMTP®.

Each converter is assigned two LF buses, one on the AC side and one on the DC side, as shown in Figure 2.16. The DC LF bus is defined between the pole and the neutral terminal, which allows the representation of monopole and bipolar configurations. Consequently, a bipolar station is associated with two AC LF buses and two DC LF buses, enabling the LF solution to account for possible unbalanced operating conditions between the poles.

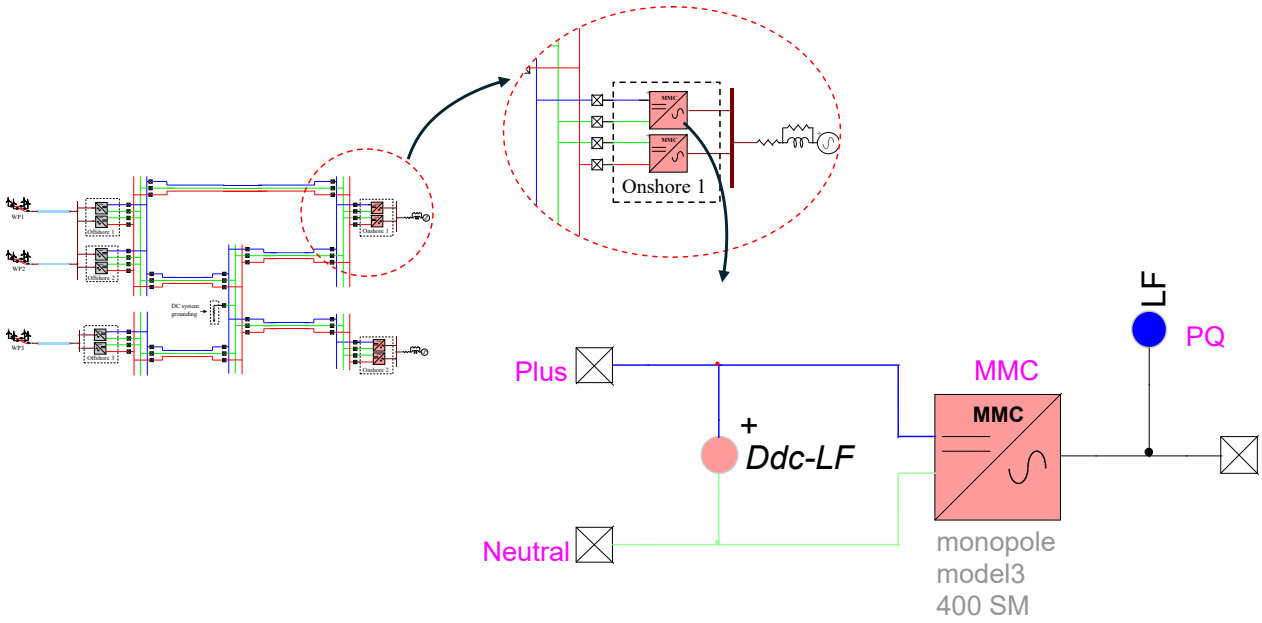

Figure 2.16 AC–DC LF implementation in EMTP®.

2.5.3 Scenarios and Results

The AC–DC LF analysis is conducted across two sets of test cases: the first set (Section 2.5.3.1) examines the InterOPERA system under different operational conditions, while the second set (Section 2.5.3.2) evaluates a modified version designed to assess cases with multiple *Vdc-LF* constraints, which present challenges for conventional AC–DC LF algorithms [134].

2.5.3.1 InterOPERA scenarios

Scenario 1: Balanced system

In this scenario, all converter poles are operational, ensuring a balanced DC network. The proposed AC–DC LF algorithm successfully converges within two master iterations. Figure 2.17 shows a screenshot of EMTP® with AC–DC LF results, including DC bus voltages, pole currents, and power injections. In the figure, the quantities Vdc_plus, Vdc_neg, and Vdc_n correspond to the V_{dc} with reference to the ground measured at the positive pole, negative pole, and neutral node, respectively. Similarly, for the DC current of cables. As observed, all DC neutral data; voltage and currents are zeros, confirming that the MTDC is the neutral voltages and currents are balanced. Detailed data are presented in Table 2.5 for converters and IBRs. Here, all data reflect the AC and DC LF buses, i.e., the measurements are taken at the PCC. Since the system is perfectly balanced, only one converter pole per station is shown. Finally, to check the Onshore multidrop operating point, Figure 2.18 illustrates the operating point mapping of onshore converters on the multidrop characteristic. As shown, all onshore stations operate in the SO mode (operation modes are defined in Section 2.4.2), i.e., operating within the green segment. The complete simulation setup for this case is provided in the file *Chapter 2/Scenario1.ecf*, included in the supplementary material.

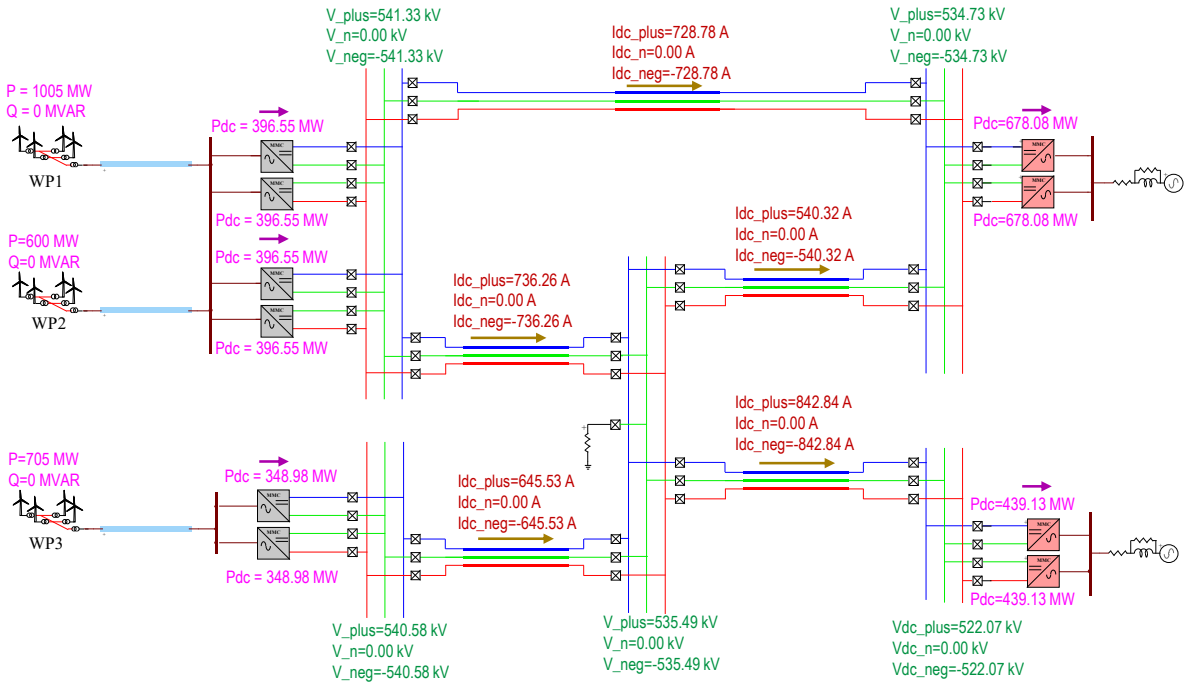

Figure 2.17 A screenshot of EMTP® with AC–DC results of Scenario 1

Table 2.5 AC–DC LF results for scenario 1, balanced system.

MTDC Component	**Scenario 1 (pu)**				
	P_{dc}	V_{dc} (Pole-to-neutral)	I_{dc}	P_{ac}	Q
Offshore1 station	0.397	1.031	0.385	-0.398	0.000
Offshore2 station	0.397	1.031	0.385	-0.398	0.000
Offshore3 station	0.349	1.030	0.339	-0.350	0.000
Onshore1 station	-0.678	1.018	-0.666	0.674	0.000
Onshore2 station	-0.439	0.994	-0.442	0.437	0.000
WP1	-	-	-	1.005	0.000
WP2	-	-	-	0.600	0.000
WP3	-	-	-	0.705	0.000

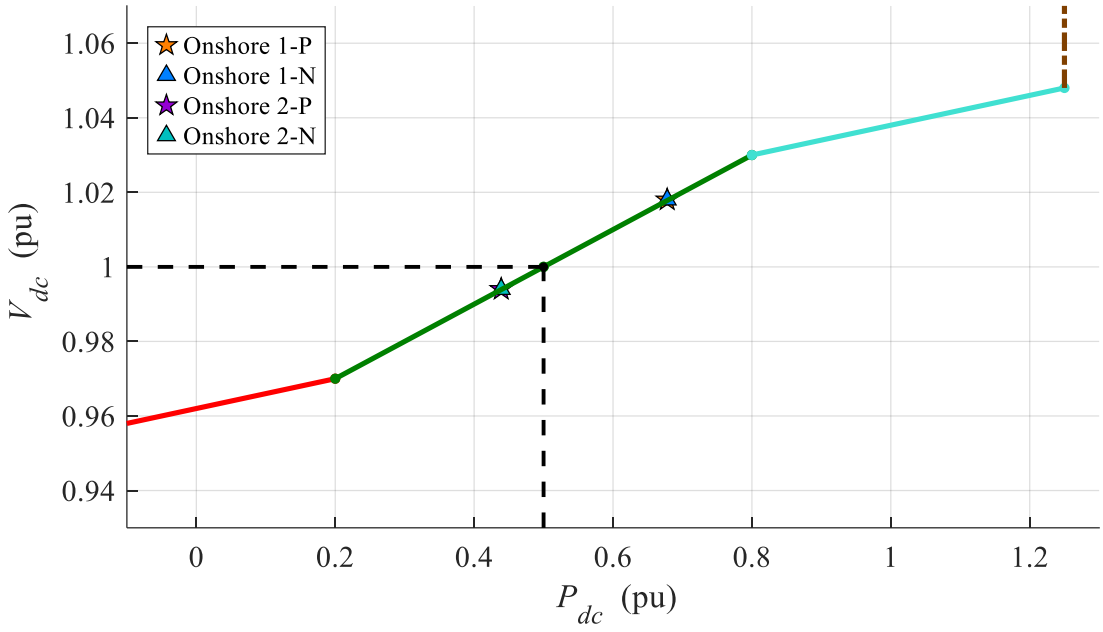

Figure 2.18 Operating points mapping for the onshore stations of Scenario 1

Scenario 2: Single pole disconnection

To evaluate the algorithm under unbalanced conditions, the negative pole of Offshore 2 is disconnected. This contingency requires five master iterations before convergence is achieved, compared to two in the balanced case. Figure 2.19 shows the EMTP® screenshot with AC–DC LF results, while Table 2.6 summarizes the corresponding numerical values for all converters and IBRs. As expected, the pole disconnection introduces an asymmetry between the positive and negative poles of Offshore 2, which is directly reflected in the bus voltages, pole currents, and power injections. The complete simulation setup for this case is provided in the file *Chapter 2/Scenario2.ecf*, included in the supplementary material.

The operating points of the onshore stations are shown in Figure 2.20. Notably, Onshore1-P transitions from SO mode to LS-OVO mode to mitigate excessive voltage rise, while the remaining onshore poles maintain their operation in SO mode (see Section 2.4.2 for mode definitions). This demonstrates that the proposed AC–DC LF algorithm is capable of capturing both the imbalance in pole operation and the associated control mode transitions required for stable system behavior.

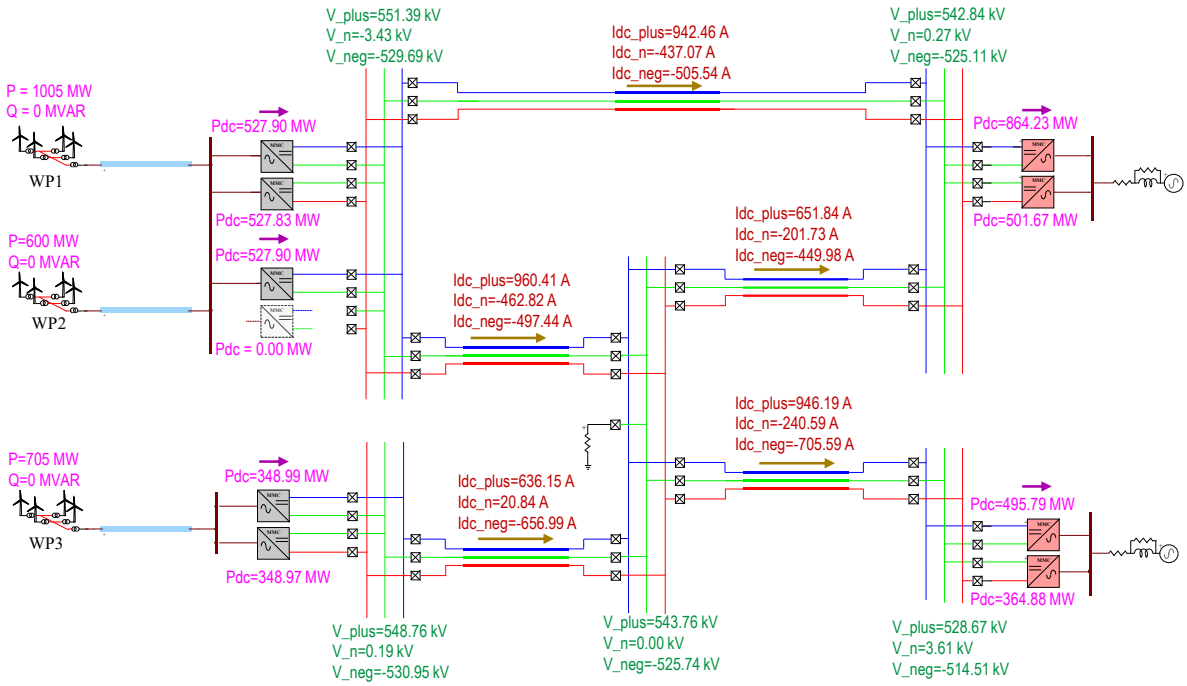

Figure 2.19 A screenshot of EMTP® with AC–DC results of Scenario 2

Table 2.6 AC–DC LF results for Scenario 2

MTDC Component	Scenario 2 (pu)				
	P_{dc}	V_{dc} (Pole-to-neutral)	I_{dc}	P_{ac}	Q
Offshore1-P	0.528	1.057	0.500	-0.531	0.000
Offshore1-N	0.528	1.002	0.527	-0.531	0.000
Offshore2-P	0.528	1.057	0.500	-0.531	0.000
Offshore2-N	-	-	-	-	-
Offshore3-P	0.349	1.045	0.334	-0.350	0.000
Offshore3-N	0.349	1.012	0.345	-0.350	0.000
Onshore1-P	-0.864	1.033	-0.837	0.857	0.000
Onshore1-N	-0.502	1.000	-0.502	0.499	0.000
Onshore2-P	-0.496	1.000	-0.496	0.493	0.000
Onshore2-N	-0.365	0.986	-0.370	0.364	0.000
WP1	-	-	-	1.005	0.000
WP2	-	-	-	0.600	0.000
WP3	-	-	-	0.705	0.000

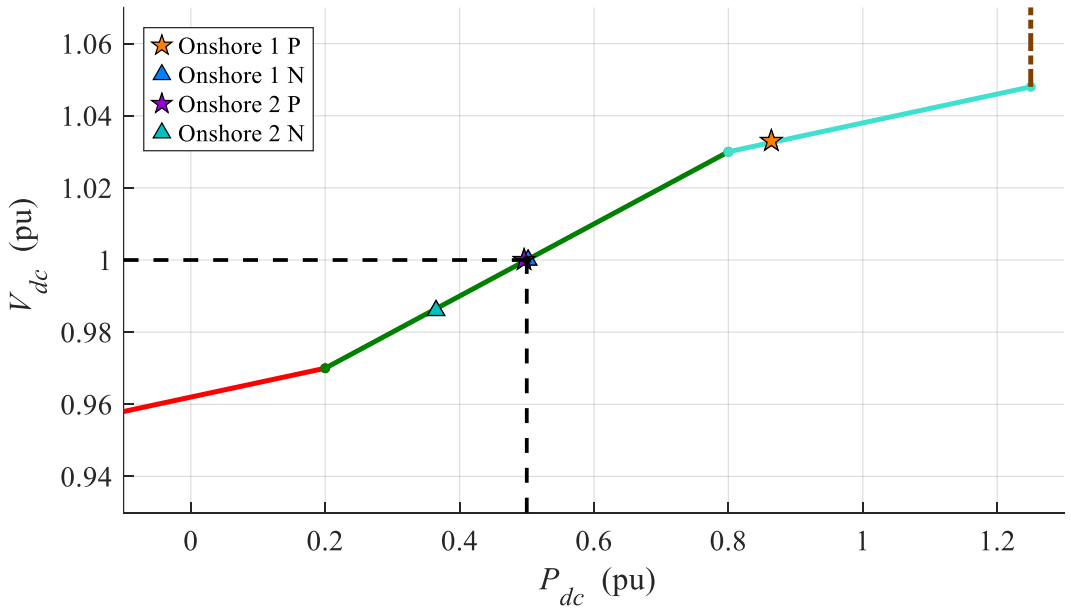

Figure 2.20 Operating points mapping for the onshore stations of Scenario 2

Scenario 3: Multiple Pole Disconnections

A more severe unbalanced condition is simulated by disconnecting the negative poles of Offshore 1 and Offshore 2 simultaneously. Under this contingency, the proposed AC–DC LF algorithm converges in five master iterations. Figure 2.21 shows the EMTP® snapshot with AC–DC LF results, while Table 2.7 summarizes the corresponding numerical values. The results reveal significant asymmetry in bus voltages and pole currents, reflecting the increased stress imposed on the onshore stations. The complete simulation setup for this case is provided in the file *Chapter 2/Scenario3.ecf*, included in the supplementary material.

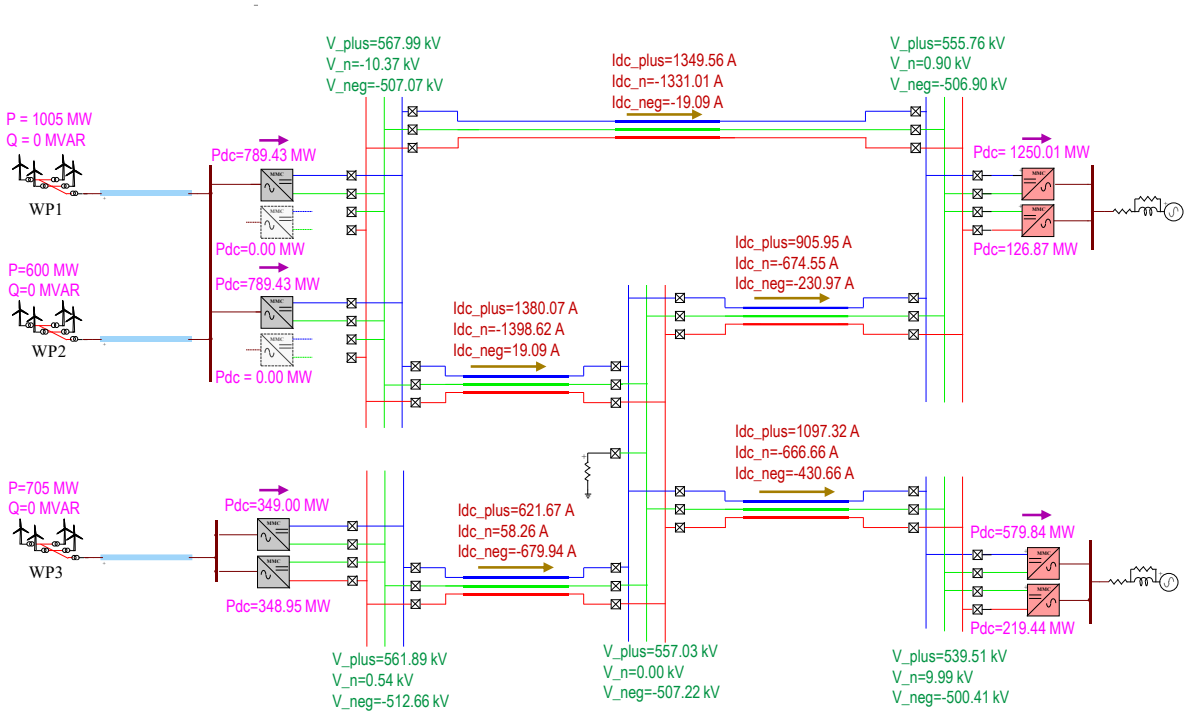

Figure 2.21 A screenshot of EMTP® with AC–DC results of Scenario 3

In particular, Onshore1-P reaches its power transfer limit and shifts into AOV mode, capping its DC power injection at P_{Max} (1.25 pu) to prevent converter overloading. At the same time, Onshore1-N transitions into LS-UVO mode to counteract voltage reduction, thereby maintaining operational stability. The operating points of the onshore stations are depicted in Figure 2.22, confirming the combined occurrence of AOV and LS-UVO modes under this highly unbalanced condition.

These results demonstrate that the proposed algorithm is able to capture both the limiting behavior of converters under overload conditions and the corrective control actions required to preserve the stability of the MTDC system during severe contingencies.

Table 2.7 AC–DC LF results for Scenario 3

MTDC Component	Scenario 3 (pu)				
	P_{dc}	V_{dc} (Pole-to-neutral)	I_{dc}	P_{ac}	Q
Offshore1-P	0.789	1.102	0.717	-0.797	0.000
Offshore1-N	-	-	-	-	-
Offshore2-P	0.789	1.102	0.717	-0.797	0.000
Offshore2-N	-	-	-	-	-
Offshore3-P	0.349	1.069	0.326	-0.350	0.000
Offshore3-N	0.349	0.978	0.357	-0.350	0.000
Onshore1-P	-1.250	1.057	-1.184	1.235	0.000
Onshore1-N	-0.127	0.967	-0.131	0.127	0.000
Onshore2-P	-0.580	1.008	-0.575	0.577	0.000
Onshore2-N	-0.219	0.972	-0.226	0.219	0.000
WP1	-	-	-	1.005	0.000
WP2	-	-	-	0.600	0.000
WP3	-	-	-	0.705	0.000

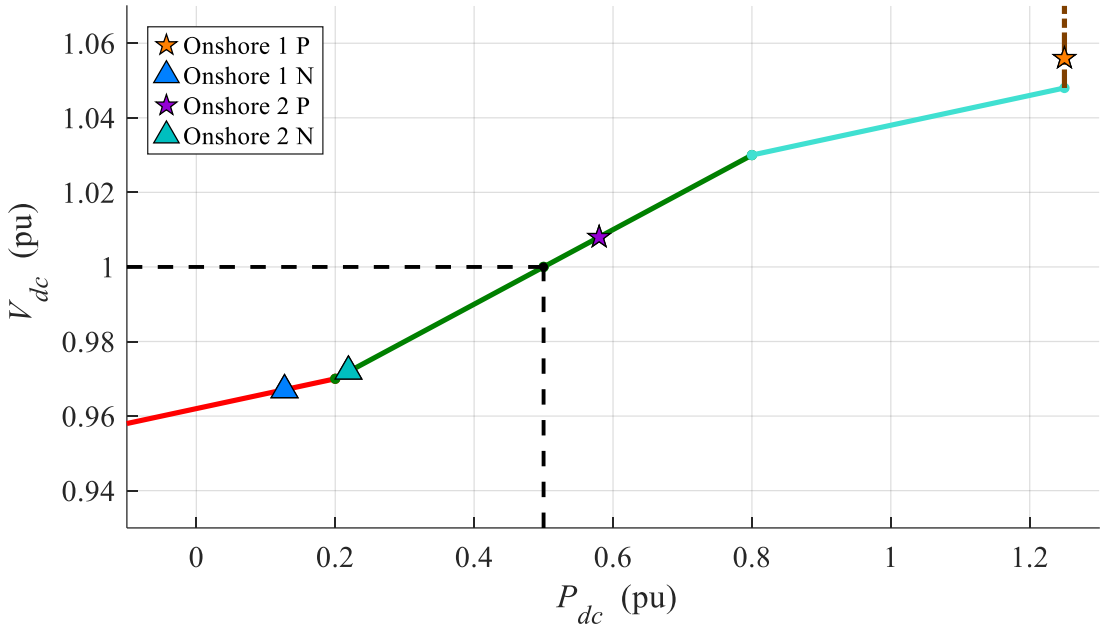

Figure 2.22 Operating points mapping for the onshore stations of Scenario 3

2.5.3.2 Modified InterOPERA Scenarios

Existing studies [134] emphasize the need for an AC–DC LF methodology capable of addressing multiple *Vdc-LF* constraints within a single DC network, an issue that challenges many conventional AC–DC LF approaches. To explore this further, two additional test scenarios are introduced.

Scenario 4: Multiple *Vdc-LF* Constraints

This scenario assesses the capability of the proposed AC–DC LF approach to manage multiple *Vdc-LF* constraints concurrently. The modified InterOPERA system replaces both onshore stations with Vdc-controlled MMCs. The algorithm successfully converges within three master iterations.

Figure 2.23 shows an EMTP snapshot of the AC–DC LF results under this scenario, while Table 2.8 summarizes the corresponding numerical values. The results demonstrate consistent enforcement of the dual *Vdc–LF* constraints, confirming that the algorithm can maintain convergence and system stability even when multiple converters impose DC-voltage control simultaneously. The complete simulation setup for this case is provided in the file *Chapter 2/Scenario4.ecf*, included in the supplementary material.

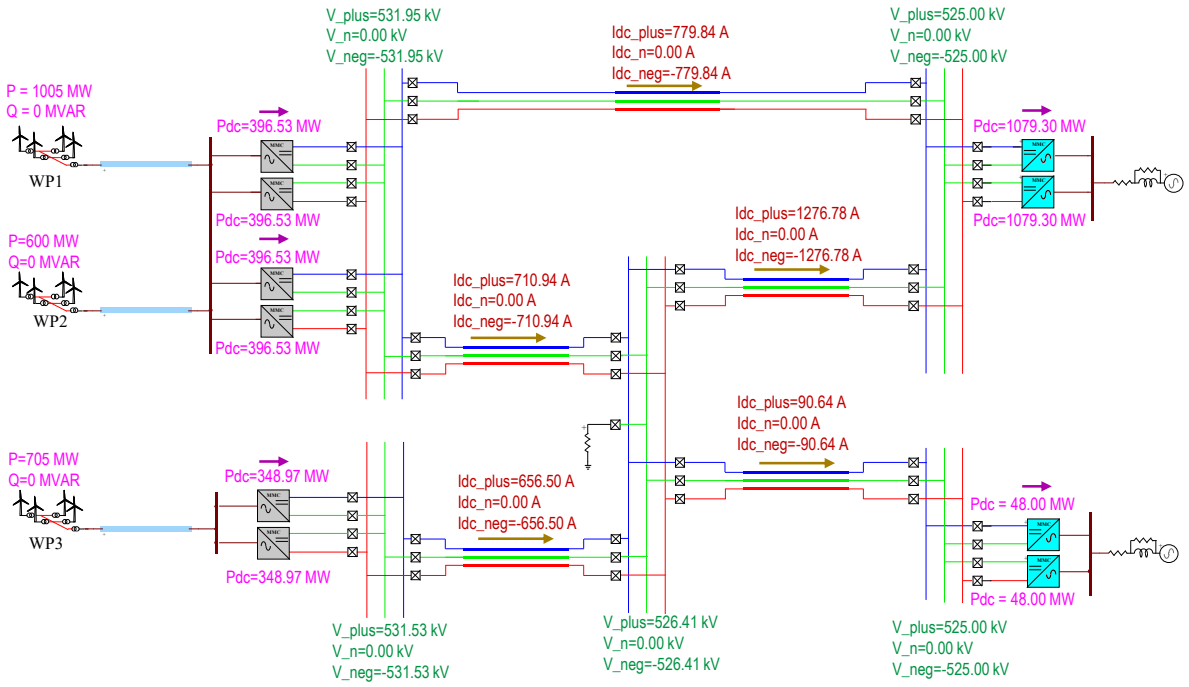

Figure 2.23 A screenshot of EMTP® with AC–DC results of Scenario 4

Table 2.8 AC–DC LF results for scenarios 4-5

MTDC Component	Scenario 4 (pu)				Scenario 5 (pu)			
	P_{dc}	V_{dc}	P_{ac}	Q	P_{dc}	V_{dc}	P_{ac}	Q
Offshore1	0.397	1.013	-0.398	0.000	0.397	1.013	-0.398	0.000
Offshore2	0.397	1.013	-0.398	0.000	0.397	1.013	-0.398	0.000
Offshore3	0.349	1.012	-0.350	0.000	0.349	1.011	-0.350	0.000
Onshore1	-1.079	1.000	1.068	0.000	-0.795	1.000	0.789	0.000
Onshore2	-0.048	1.000	0.048	0.000	-0.327	0.983	0.327	0.000
WP1	-	-	1.005	0.000	-	-	1.005	0.000
WP2	-	-	0.600	0.000	-	-	0.600	0.000
WP3	-	-	0.705	0.000	-	-	0.705	0.000

Scenario 5: Combination of *Ddc-LF* and *Vdc-LF* constraints

This scenario further evaluates the proposed AC–DC LF approach under a mix of DC droop and voltage-controlled converters within the same DC network. Specifically, Onshore1 is replaced with a Vdc-controlled MMC, while Onshore2 remains under multi-droop control. These tests are

maintained as balanced cases for clarity, though the method is also capable of addressing unbalanced operating conditions.

Figure 2.24 provides an EMTP snapshot of the AC–DC LF results for this scenario, while Table 2.8 summarizes the corresponding numerical values. The results confirm that the algorithm can consistently enforce heterogeneous control constraints across multiple converters and maintain stable operation. This demonstrates the flexibility of the proposed approach in handling mixed DC control strategies within large-scale MTDC systems. The complete simulation setup for this case is provided in the file "*Chapter 2/Scenario5.ecf*", included in the supplementary material.

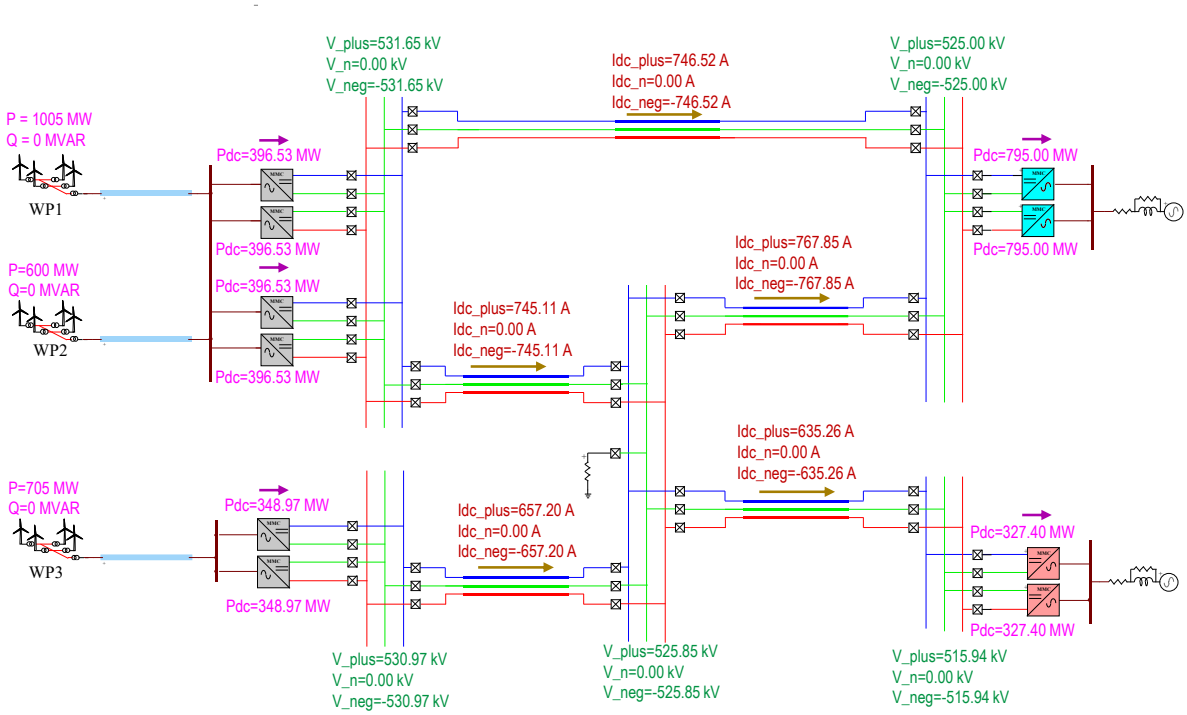

Figure 2.24 A screenshot of EMTP® with AC–DC results of Scenario 5

2.6 Verification through time-domain simulation

To verify the AC–DC LF results, a time domain simulation is conducted to compare the steady-state results with those obtained in Table 2.6 and Table 2.8. For an efficient and healthy simulation, the computed solutions are used for initializing the EMT simulations via the DI method [9] which is presented in CHAPTER 4. The system is modeled in EMTP® software [5] using the component models and configurations detailed in Table 2.4. The DI-based initialization is performed at a recoupling time of t = 0.3 s.

Figure 2.25 presents time-domain responses of onshore stations for scenarios 1-3, depicting variations in V_{dc} and P_{ac} across different scenarios. The results demonstrate a strong correlation between the AC–DC LF calculations and time-domain simulations, validating the accuracy and reliability of the proposed approach.

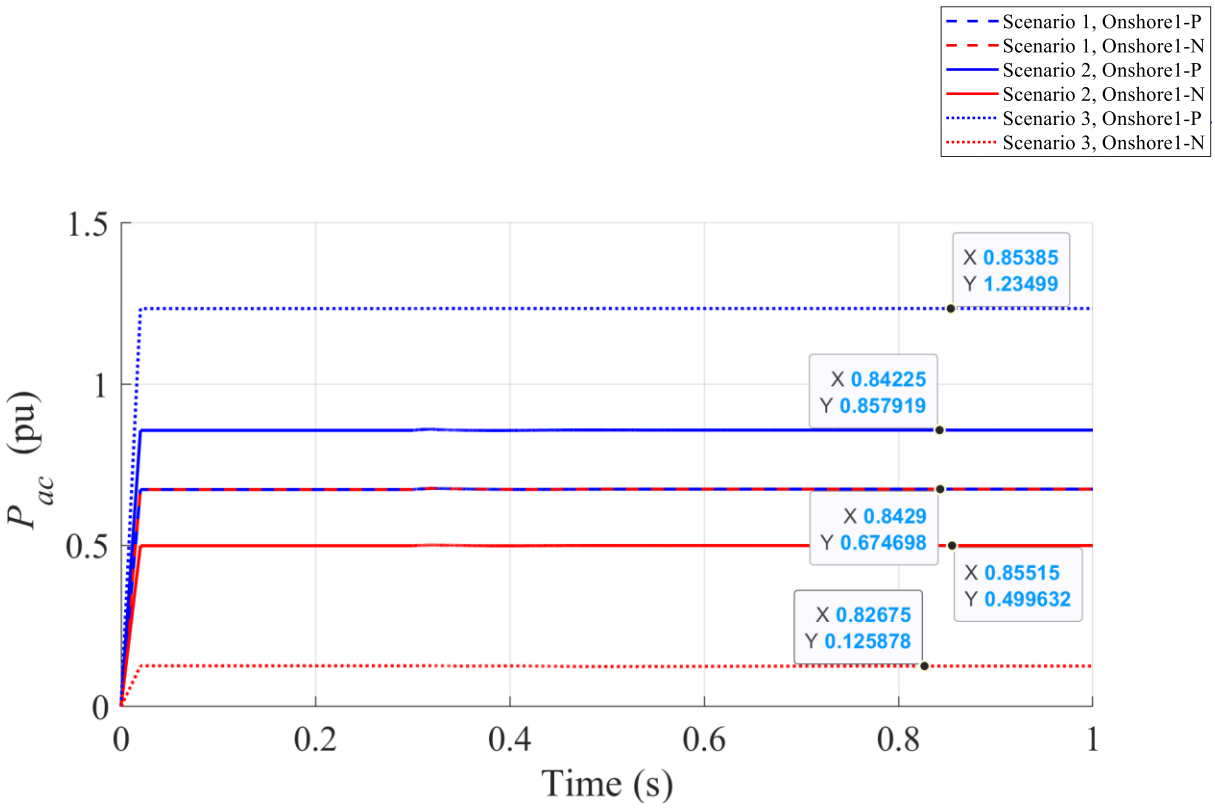

(a)

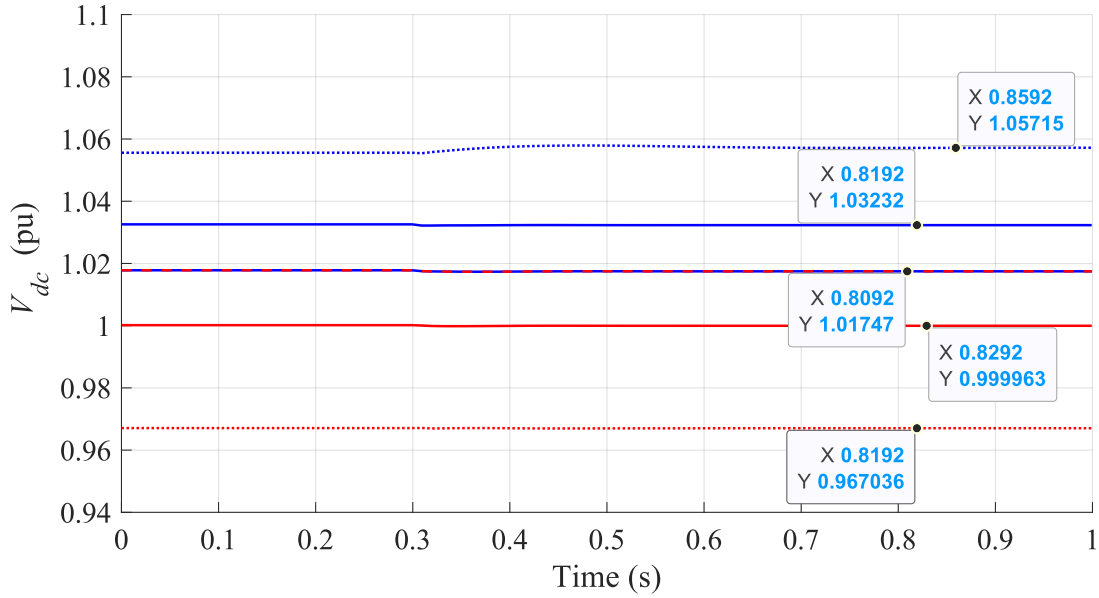

(b)

Figure 2.25 Time-domain validation of Onshore 1 under different scenarios.

For the modified InterOPERA system in Scenarios 4 and 5, the same validation procedure is applied to ensure consistency between the AC–DC LF results and time-domain simulations. Figure 2.26 illustrates the time-domain responses of all Onshore converters under these scenarios. Since the DC network remains balanced, the behavior of the positive and negative pole converters is symmetrical, allowing for a single representative converter per station to be plotted.

The steady-state operating points obtained from the time-domain simulation show excellent agreement with the AC–DC LF results presented in Table 2.5-Table 2.8, thereby confirming the accuracy and consistency of the proposed methodology. This consistency across scenarios highlights the capability of the AC–DC LF framework to accurately reproduce the dynamic behavior of the system while maintaining fidelity to the underlying steady-state conditions.

2.6.1 Conclusion

This chapter introduced a novel unbalanced AC–DC load-flow method designed for EMT simulations, leveraging the MANA-based conventional AC load-flow solver within a sequential framework. Newton's method is applied to both AC and DC networks, while a fixed-point iteration ensures stable coupling. The method seamlessly integrates various converter control modes, such as DC droop and multi-droop control, without requiring structural modifications to the MANA-based solver.

The proposed approach was validated on the InterOPERA Variant 1 system across three different scenarios, demonstrating its accuracy under diverse operating conditions. Additionally, time-domain validation confirmed its capability to provide reliable initial conditions for large-scale MTDC systems, reinforcing its practicality for unbalanced AC–DC studies within EMT environments.

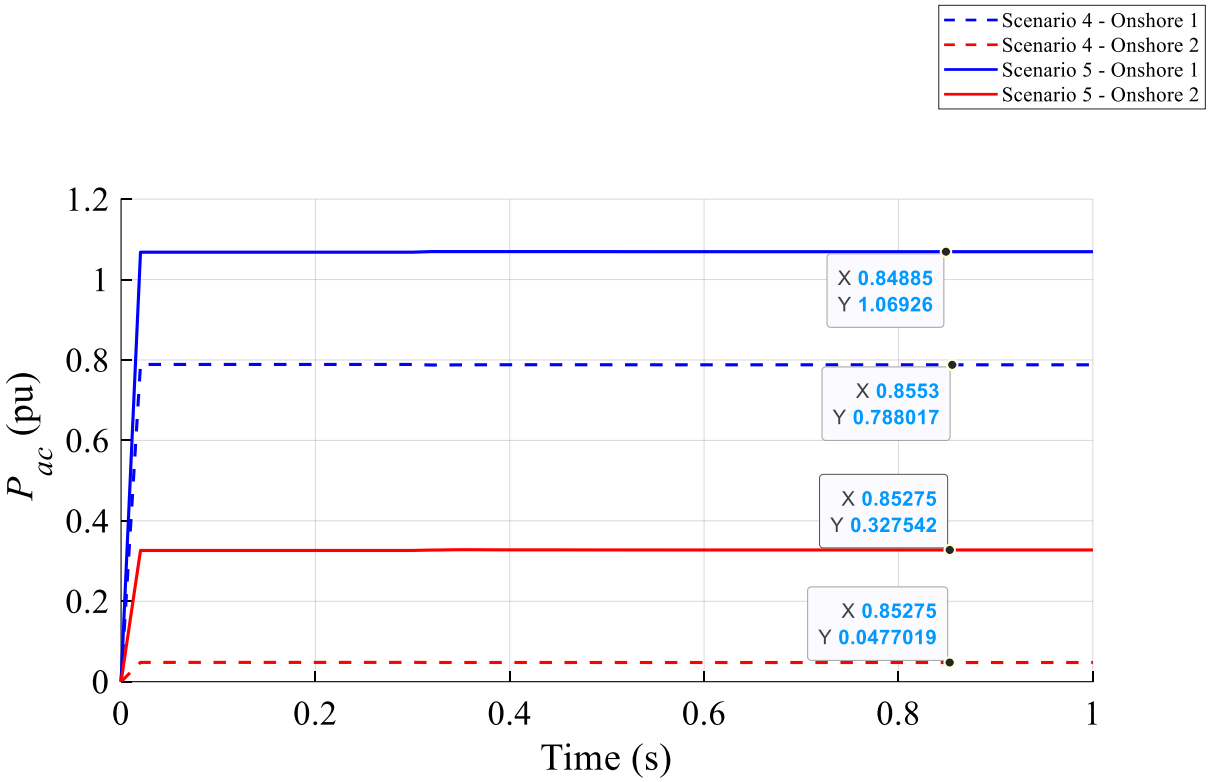

(a)

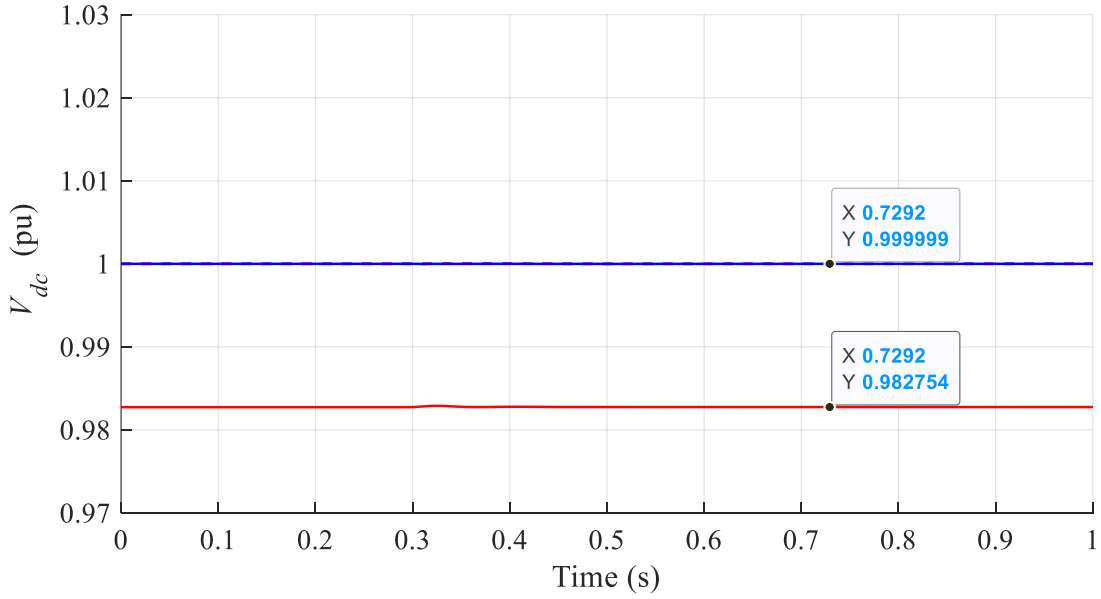

(b)

Figure 2.26 Time-domain validation of onshore stations under Scenarios 4 and 5.

CHAPTER 3 INITIALIZING GFM-VSC MODEL IN MTDC SIMULATION

3.1 Introduction and background

Efficient and accurate initialization methods are essential for ensuring the stability and computational efficiency of MTDC system simulations. EMT tools provide detailed representations of MTDC networks but often face significant computational challenges due to the complexity of modeling advanced converter controls and IBRs.

LF-based initialization techniques are generally effective for conventional AC systems and their control, such as governors and exciters [5, 142]. However, it might become complicated when applied to power electronic converters with complex control mechanisms. The intricate interactions among converter controls and system components can lead to extended initialization times or failure to converge, particularly in large-scale networks [9].

When an islanded AC system is integrated with a grid-forming voltage source converter (GFM-VSC), conventional LF-based initialization methods become inadequate. This is because GFM-VSCs rely on sophisticated control strategies that involve a large number of internal state variables, while also coupling their operation to the DC side of the converter. These additional constraints go beyond the assumptions of standard LF formulations, making it difficult to obtain a consistent steady-state solution using conventional methods. GFM-VSCs are widely used not only in MTDC applications but also in offshore wind farms connected via HVDC transmission, where they provide grid-forming capability and system support. Without a robust initialization process, EMT simulations may fail to converge or produce unstable and unrealistic results.

Full control initialization of GFM-VSCs is possible, as demonstrated in [111], where MMC models are initialized in depth by solving all power and control system equations in steady-state. However, this approach relies on complete knowledge of model parameters and detailed internal representations. When dealing with black-box or grey-box models, where full access to system details is unavailable, implementing such an approach becomes challenging.

This chapter provides an overview of LF-based initialization processes and highlights their challenges when applied to GFM-VSCs. To address these limitations, two advanced initialization methods are proposed: Outer Control Initialization in Steady-State (OCISS) and Decoupling

Interface (DI). Both methods significantly reduce initialization time while ensuring stable and accurate system behavior in EMT simulations.

3.2 Overview of load-flow-based initialization

LF-based initialization is a widely used technique for determining the steady-state operating point of power systems. It comprises three primary steps shown in Figure 3.1.

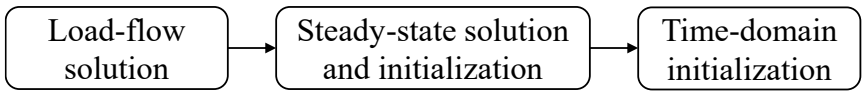

Figure 3.1 LF-based initialization process.

3.2.1 Load-flow solution

The first step involves finding LF solution for the simulation model. MTDC has AC and DC systems, which require implementing AC–DC LF. All details about this step are presented in Chapter 2. LF results give insight into the steady-state operating point of LF buses. Therefore, for expanding the solution for components other than LF buses, further steady-state analysis is required.

3.2.2 Steady-state analysis and component initialization

Using the LF solution results, steady-state analysis determines the remaining electrical quantities across the system, such as voltages, currents, and power phasors. This step covers all components not directly included in the LF solution, including passive elements (e.g., lines, cables, transformers) and conventional rotating machines with their associated controls, which are directly initialized. To initialize the EMT model, all power system components, including sources, loads, and passive devices, are replaced by their lumped equivalent representations derived from the solved LF operating point. In other words, the LF constraints are no longer enforced (explicitly) during the EMT simulation; instead, they are translated into physical equivalents that ensure the system starts from the correct steady-state conditions.

For example, generator buses are typically initialized using equivalent source models that replicate the power injections obtained from the LF results. These models can take the form of current sources or voltage sources with internal impedance, depending on the simulation setup. Similarly, load buses are represented using fixed admittances or equivalent current injections. These

substitutions collectively ensure that the EMT simulation begins from a physically consistent and electrically balanced steady-state operating point.

3.2.3 Time-domain initialization

Some components in EMT simulations, particularly power converters, IBRs, and systems governed by advanced control schemes, require additional attention during initialization. Unlike passive network elements that can be directly initialized from load-flow results, these devices rely on dynamic control systems whose steady-state behavior depends on the correct adjustment of internal variables such as integrator states, reference signals, and limit indicators. Both the electrical quantities and the internal control states must be reconciled in steady state before the time-domain simulation begins.

In this work, the term complex control refers to control architectures that contain several interacting regulation loops, typically current, voltage, and power controllers, together with nonlinear elements, limiters, or mode-switching logic. These interactions create strong couplings between electrical and control variables, which means that the internal controller states depend on network conditions. Their steady-state values cannot be directly assigned from load-flow results and must instead be adjusted to obtain a stable starting condition.

Such controllers differ from conventional ones, such as exciters and governors, whose steady-state references can be explicitly derived from load-flow quantities. For converters, multiple control objectives act simultaneously, and the active limits or priority modes may change depending on the operating point. If these internal states are not properly aligned at the start of the simulation, the converter may begin from inconsistent electrical and control conditions, producing transients that delay convergence or destabilize the network.

Time-domain initialization techniques are therefore applied as a necessary extension of load-flow-based initialization. They provide a gradual transition between the operating point obtained from the load-flow analysis and the dynamic simulation by allowing converter controls to settle into their steady-state conditions before the main EMT run. These strategies are often applied locally to specific subsystems, hereafter referred to as time-domain initialized subsystems (TDISs). This approach ensures that both the network and the control systems start from physically consistent conditions and that the simulation proceeds without unnecessary transients.

One widely used implementation is the Load-Flow and Source Initialization (LFSI) technique. As illustrated in Figure 3.2, LFSI imposes auxiliary voltage sources at the terminals of power converters and IBRs during the startup phase of the simulation. These sources temporarily force the terminal conditions to match the load-flow results, ensuring that the voltage phasors seen by the control systems are consistent with their expected operating points. This controlled approach allows converters, especially those in wind parks or other converter-dense systems, to ramp up their control actions gradually, avoiding abrupt transients or power swings that could disturb the surrounding network. Once the system stabilizes, the auxiliary sources are smoothly removed, enabling a seamless transition to full dynamic simulation.

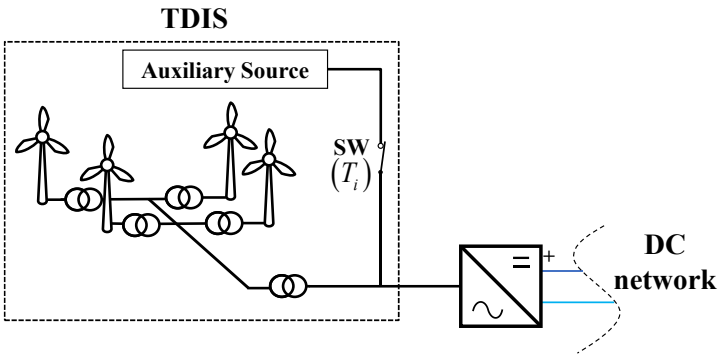

Figure 3.2 Time-domain initialization for a wind park.

3.2.4 Special initialization challenge in GFM-VSC

While LFSI proves effective for initializing many power electronic systems, it introduces conflicts when applied to GFM-VSCs interfacing with islanded AC grids. The issue arises because LFSI enforces steady-state conditions by temporarily imposing auxiliary voltage sources at converter terminals. While this ensures an initial match with LF results, it disrupts the natural operation of GFM-VSCs.

As shown in Figure 3.3, when GFM-VSC is connected directly with an auxiliary source with LF phasors, the AC voltage seen by GFM-VSC will be dictated by the voltage, frequency and angle of the auxiliary voltage source. Referring to Figure 3.3, the GFM-VSC measures the AC voltage magnitude, $|V_{ac}|$, from the auxiliary source rather than the actual system values. Because the auxiliary source is set to match the control setpoint, the error signal (e) is zero, leading to an incorrect initialization of the converter's internal variables. As a result, referring to Figure 3.3, the

reference direct-axis voltage E_d^{ref} is determined by both the integrator's initial condition and the auxiliary source voltage:

$$E_d^{ref} = K_i h + \left|V_{ac}^{set}\right| \tag{0.16}$$

where h is the initial condition of the integrator.

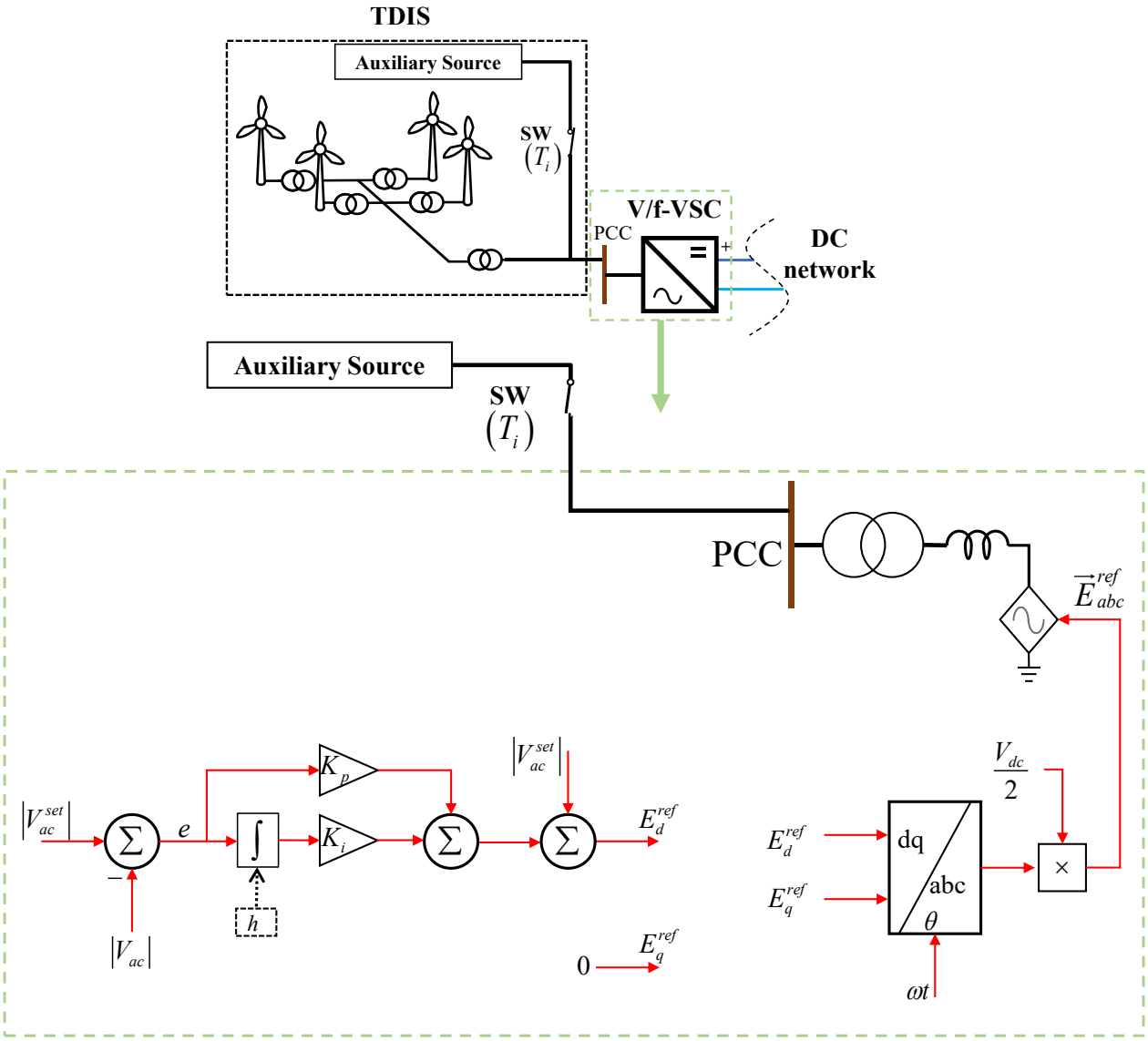

Figure 3.3 V/f-VSC schematic using LFSI for a neighboring IBR.

If the integrator is not initialized, meaning its initial condition is set to zero, E_d^{ref} will be incorrectly assigned the magnitude of the auxiliary source voltage. Consequently, the corresponding reference output voltage E_{abc}^{ref} also becomes inaccurate. Since the active and reactive powers delivered by

the GFM-VSC are directly dependent on E_{abc}^{ref}, the converter will operate at an incorrect steady-state condition. This mismatch creates a conflict between LFSI and the actual control response. When the auxiliary source is removed after time T_i, the GFM-VSC and the wind park will no longer share the same operating point, causing a long transient period before reaching steady-state.

Two methods are proposed below for improving the time-domain initialization step. The first method is outer control system initialization in steady-state (OCISS) involves initializing the main PI controllers of GFM-VSC control by performing steady-state analysis. The second is a generic method called DI. In both methods, all non-initialized converter control variables are rapidly and automatically self-initialized through time-domain computations due to forcing from the steady-state solution.

3.3 Outer control initialization by steady-state analysis

To resolve conflicts in time-domain initialization, OCISS is proposed as a method for determining the initial conditions of the PI controllers in GFM-VSCs. This method does not replace LFSI but complements it by ensuring that the control system starts from a physically consistent steady-state condition. The required inputs for this initialization step include LF results and GFM-VSC model parameters.

Figure 3.4 illustrates the AC-side representation of a GFM-MMC modelled using an AVM in pu quantities, the full model derivation is presented in [40]. In this representation:

- E_{abc}^{ref} denotes the internal voltage of the GFM-VSC
- $\vec{I}_{ac}$ is the AC current phasor
- $\vec{Z}_{tr}$ and $jX_{Larm}/2$ represent the transformer and arm inductance impedances, respectively

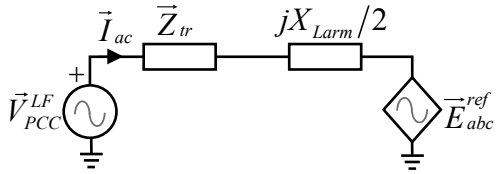

Figure 3.4 AC-side phasor representation of GFM-MMC via its AVM.

By applying Kirchhoff's Voltage Law (KVL), the following equation is obtained:

$$\vec{V}_{PCC}^{LF} - \vec{I}_{ac}\left(\vec{Z}_{tr} + jX_{Larm}/2\right) = \vec{E}_{abc}^{ref} \tag{0.17}$$

From Figure 3.3, the internal voltage phasor can be expressed as:

$$\vec{E}_{abc}^{ref} = \left(E_d^{ref} + jE_q^{ref}\right)\frac{V_{dc}}{2} \tag{0.18}$$

Since E_q^{ref} is always zero, by substituting (0.16) into (0.18) yields:

$$\vec{E}_{abc}^{ref} = \left(K_i h + \left|V_{ac}^{set}\right|\right)\frac{V_{dc}}{2} \tag{0.19}$$

By substituting (0.17) into (0.19), $\vec{E}_{abc}^{ref}$ can be eliminated, then the variable *h* can be expressed as:

$$h = \frac{1}{K_i}\left\{\frac{2}{V_{dc}}\left[\vec{V}_{PCC}^{LF} - \vec{I}_{ac}\left(\vec{Z}_{tr} + \frac{jX_{Larm}}{2}\right)\right] - \left|V_{ac}^{set}\right|\right\} \tag{0.20}$$

By using this equation, *h* can be directly calculated from LF voltage and current phasors. This *h* is used to initialize the integrator in Figure 3.3. Therefore, the GFM is correctly initialized, and if a neighboring TDIS with an auxiliary source is connected directly with this GFM, such as a wind park, the auxiliary source won't cause the initialization conflict explained in section 3.2.4, ensuring that the GFM-VSC starts from the appropriate steady-state condition when the EMT simulation begins.

To give an example for the implementation in any EMT software, Figure 3.5 present the control schematic of V/F-MMC in EMTP®. The initial condition value calculated using (0.20) is assigned to the Reset_Value of the PI controller. This value is forced just at the first time-point by assigning the reset interval "Reset_Int" to this condition (t==0), which will return True only at the first time-point.

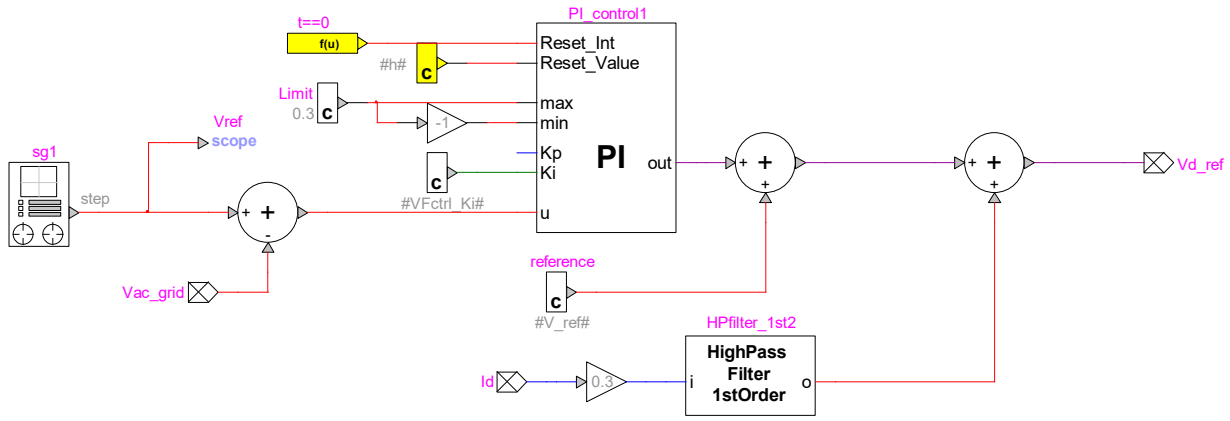

Figure 3.5 Implemnting OCSI in EMTP®.

3.4 Time-domain initialization using decoupling interface

The DI method is introduced as an alternative approach to replace the auxiliary voltage source traditionally used in GFM-VSC time-domain initialization. This method is specifically designed to eliminate startup control conflicts and minimize interactions between the islanded grid subsystem (IGS) and the GFM-VSC, facilitating a more stable initialization process.

A high-level overview of the DI approach is depicted in Figure 3.6. The procedure begins by isolating the IGS from its corresponding GFM-VSC through the introduction of interfacing auxiliary sources (IASs). Once decoupled, the system undergoes time-domain simulation until it reaches steady-state conditions.

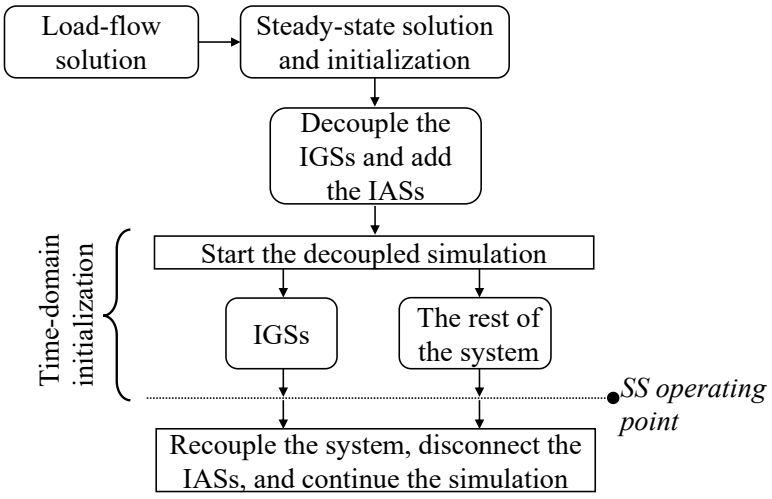

Figure 3.6 The DI initialization method.

After achieving steady-state, the system is seamlessly reintegrated by removing the IASs and reconnecting the IGS, ensuring smooth initialization. To enhance automation and reduce user intervention, IASs can be embedded within simulation models.

3.4.1 System decoupling

During the decoupling phase, all IGSs are disconnected from their respective GFM-VSCs, as illustrated in Figure 3.7. This step involves the addition of two auxiliary sources:

- Equivalent Auxiliary Source: A standalone source that replicates the steady-state behavior of the IGS by maintaining the same active (P) and reactive (Q) powers as determined in the LF solution. Since the GFM-VSC regulates V_{ac} and the frequency, this source is typically implemented as an AC current source to achieve accurate steady-state values for P and Q.
- Replicating Auxiliary Source: This source emulates the GFM-VSC's AC-side behavior to allow the IGS to initialize independently. It is designed as a dependent source that replicates the AC voltage waveforms observed at the PCC, ensuring a consistent transition.

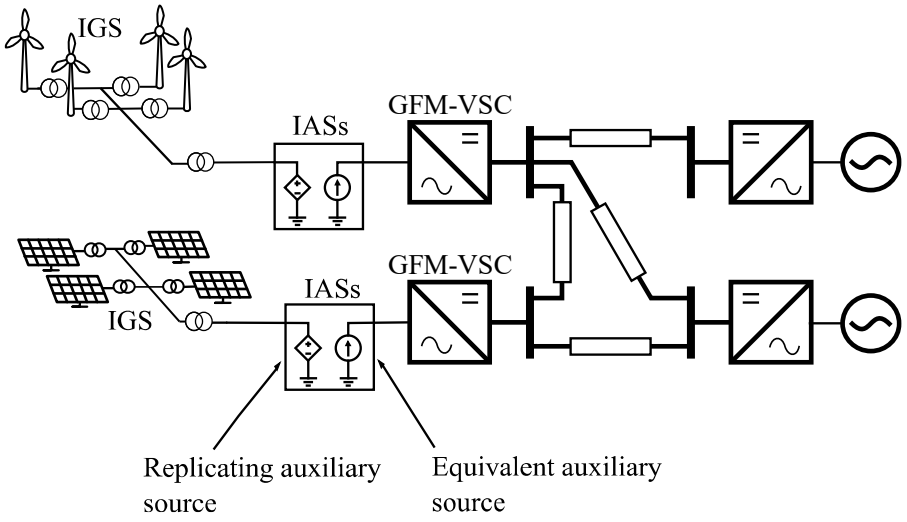

Figure 3.7 The DI initialization setup.

3.4.2 Decoupled simulation and recoupling

After decoupling, time-domain simulation is executed, where both the IGS and the GFM-VSC are initialized separately. Once these subsystems achieve their steady-state operating points within a predefined tolerance, the recoupling process is initiated. At this stage, the IASs are removed, and the original MTDC network is fully restored. This structured approach ensures that the GFM-VSC

and IGS reach stable conditions before complete system integration, mitigating transients and ensuring a smooth simulation startup.

3.4.3 The DI method implementation in EMT tools

The DI method can be implemented in any EMT simulation tool using auxiliary sources and switching devices. In this work, the method was realized in EMTP® software [5] by creating a DI block that decouples an IGS from its corresponding GFM, inserts the auxiliary sources, and then performs recoupling during time-domain simulation. The structure of this block is illustrated in Figure 3.8.

At the start of the simulation, the switch *SW_recoupling* is open, thereby decoupling the IGS from the GFM. Once the system reaches steady-state, this switch closes at the predefined instant T_i, which is chosen manually based on prior knowledge of the settling time required for the GFM to reach steady state. In practice, this value can also be determined automatically by monitoring the settling behavior of the GFM. This operation re-establishes the connection between the IGS and the GFM. At the same time, the auxiliary sources are disconnected using switches such as "*SW_disconnect"*. In the case of the "*Replicating_Aux_Source"* source, which is a dependent current source, explicit disconnection switches are not required. Instead, this source is configured to automatically stop at T_i.

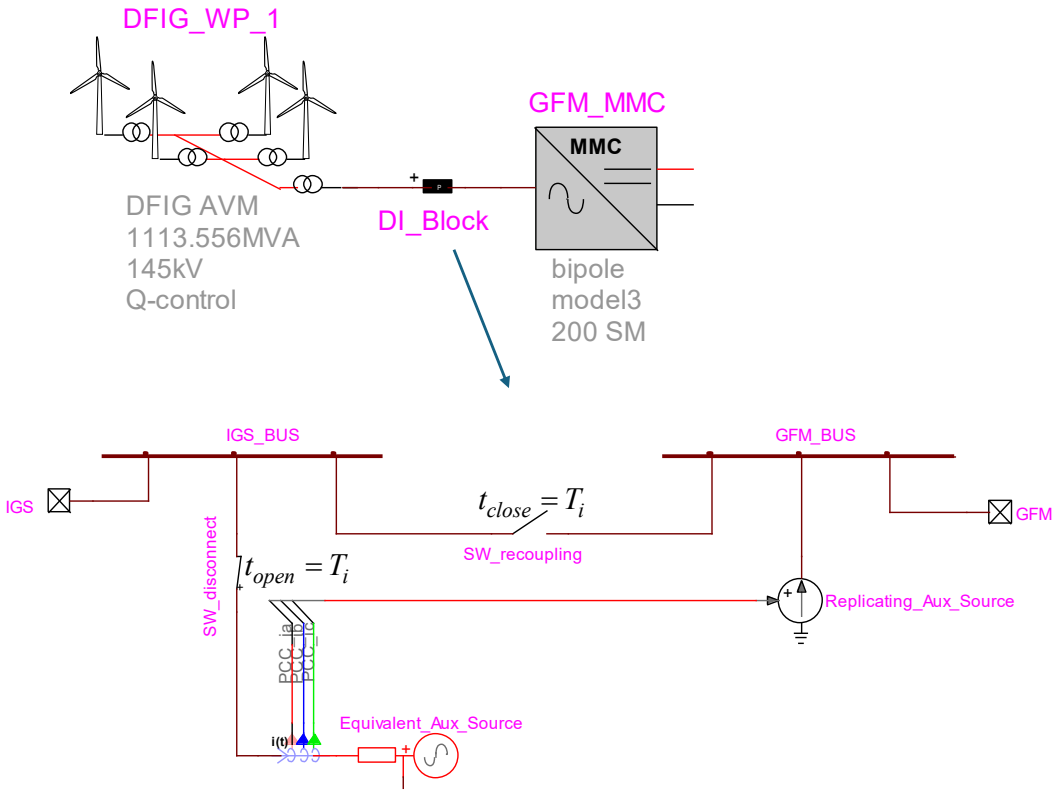

Figure 3.8 The DI implementation in EMTP®.

3.5 Performance evaluation

The DI method proposed in this study is implemented in EMTP® software [5], as explained in the section above, and tested on the CIGRE BM4 benchmark [4], as shown in Figure 3.9. This model of CIGRE MTDC benchmarks is selected as it focuses on collecting and integrating wind resources. The BM4 model combines three HVDC subnetworks:

- A monopolar point-to-point (P2P) link (Cm-D1 and Cm-D2).
- A five-terminal bipolar MTDC system (Cb-D3, Cb-D4, Cb-D6, Cb-D7, and Cb-D9).
- A four-terminal monopolar MTDC system (Cm-D5, Cm-D10, Cm-D12, and Cm-D13).

The DI initialization method is compared against both the OCISS method and the LFSI method described in Section 3.2.3. The components of BM4 are modeled as outlined in Table 3.1, where T_i represents the time required to disconnect the auxiliary sources from TDIS models (as detailed in Section 3.2.3). The T_i values are determined based on the default LFSI settings of each model in

EMTP®, which also remain consistent for the DI and the OCISS methods. Both simulation cases are available in the folder *"Chapter 3/"*, included in the supplementary material.

Table 3.1 Model types used in BM4

Device	Modelled by
MMC	Arm equivalent model (Model 3 in [40]), $T_i = 0.2\,s$
dc-dc converters	Ideal DC transformers
Wind parks	Aggregated DFIG models with controls, $T_i = 0.5\,s$
Electrical loads	Fixed impedances
Lines /cables	Wideband models [22]

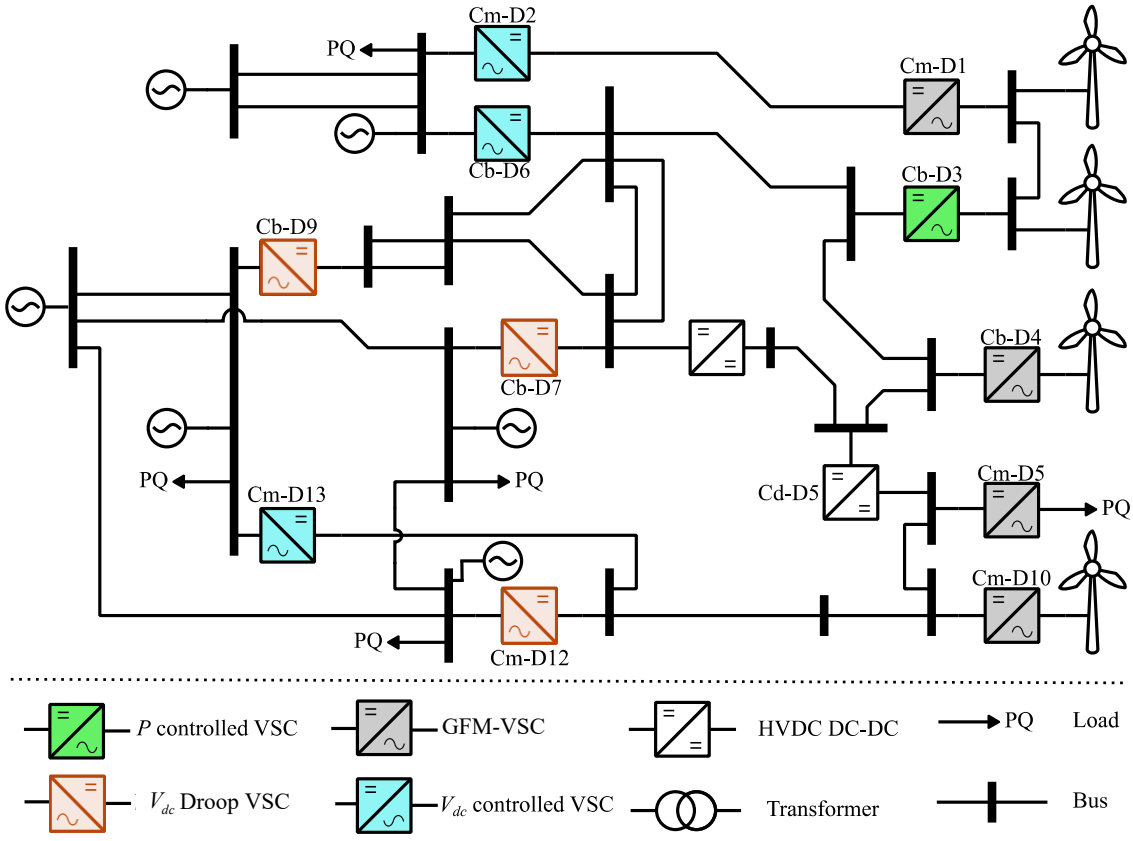

Figure 3.9 The CIGRE BM4 benchmark [4].

For the DI approach, initialization is applied exclusively to the GFM-VSC links connecting the islanded grids, as shown in Figure 3.10. The remaining system components, including other VSC types and wind parks, retain the default LFSI-based initialization embedded inside the model. All simulations use a 10 µs time-step, and initialization is considered complete when power and voltage deviations remain within ±1% of the LF results.

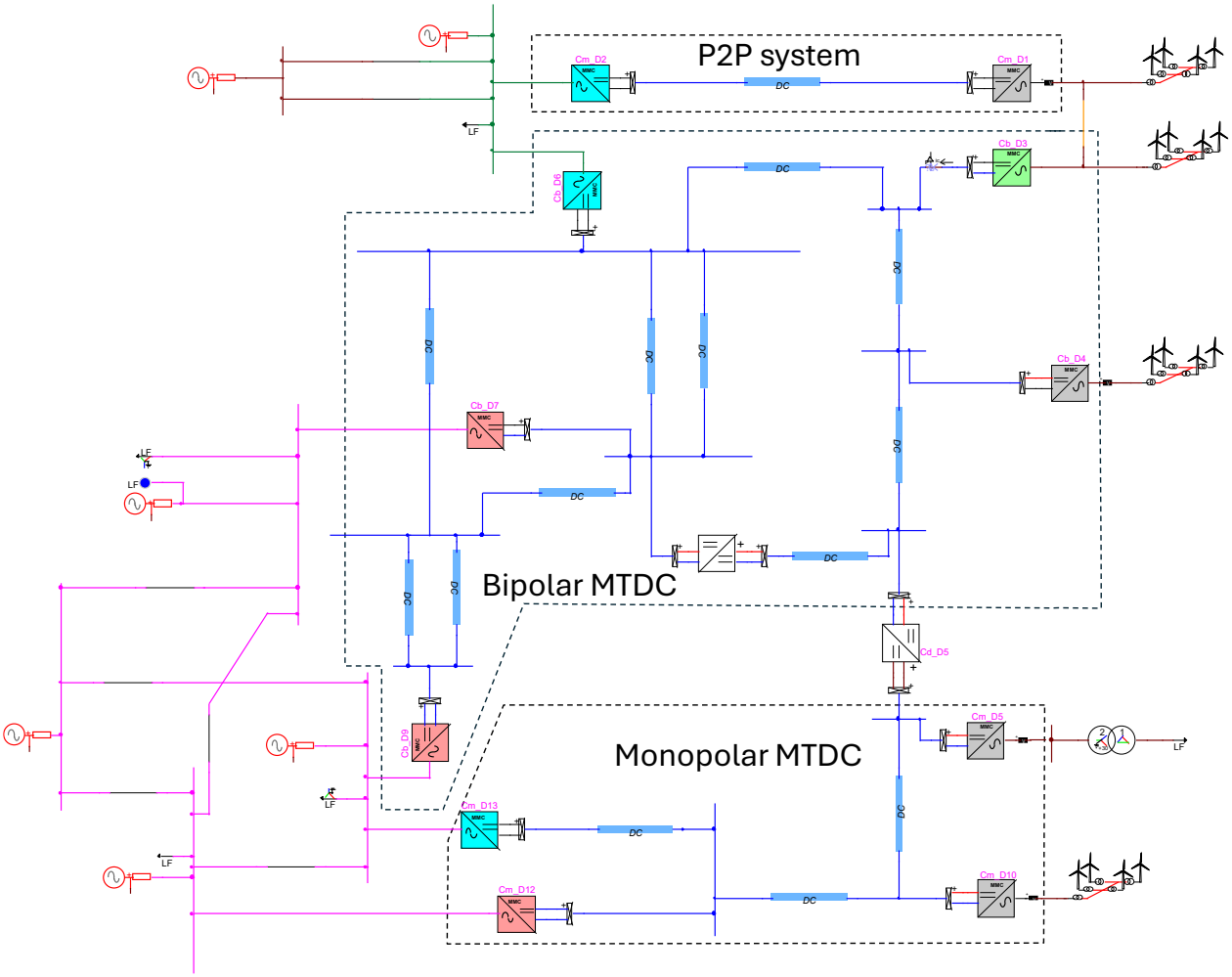

Figure 3.10 CIGRE BM4 [4] modeled in EMTP® with DI blocks on all GFM-MMCs.

3.5.1 Time-domain results and comparison

As CIGRE BM4 has three different types of subsystems: a P2P line, Bipolar MTDC, and a unipolar MTDC, the results are presented and discussed for each subsystem individually. The time-domain performance of the P2P system is illustrated in Figure 3.11. As shown in Figure 3.11 (a), the LFSI method initially ramps up the power of the Cm-D1 converter but settles at an incorrect steady-state operating point due to the influence of auxiliary sources applied to the wind park model, as the

control conflict that is explained in the section 3.2.4. Consequently, the V_{dc} controlled VSC (Cm-D2) in Figure 3.11 (b) receives inaccurate DC power, causing it to settle at an incorrect operating point during the T_i interval. Once T_i elapses and the auxiliary source is removed, the system enters a correction phase and gradually converges to the correct operating point.

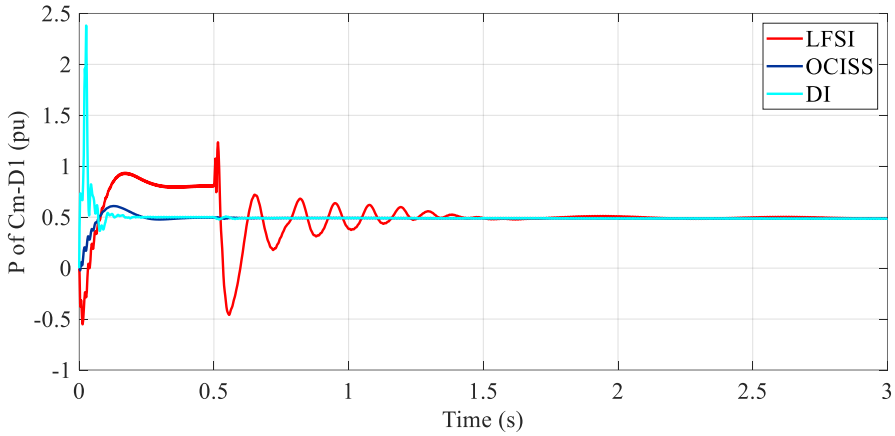

(a) P of the Cm-D1.

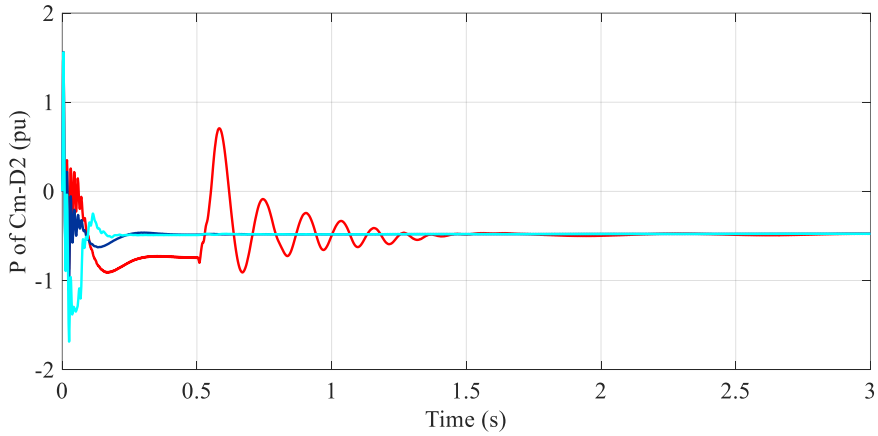

(b) P of the Cm-D2.

Figure 3.11 Initialization comparison for the monopolar P2P line of BM4.

Once the T_i period for the wind park elapses, the auxiliary sources are disconnected, allowing the GFM-VSC control to correct its operating point and reach steady-state. After which, Cm-D2 follows. The LFSI approach achieves steady-state within 1.45 s of simulation. However, both the OCISS and DI methods demonstrate significantly better performance, achieving steady-state conditions in 0.15 s and 0.3 s, respectively.

Figure 3.12, presents a sample of converter behaviours located within the bipolar MTDC subnetwork. As observed, the LFSI method requires a significantly longer time to reach steady-state. Specifically, the Vdc-controlled VSC (Cb-D6) in Figure 3.12.(b) takes 3.4 s to stabilize. This delay is primarily attributed to the interaction between the bipolar system and the monopolar system via the Cd-D5 DC-DC converter, which introduces power oscillations during initialization. In contrast, both the OCISS and DI methods demonstrate superior efficiency, stabilizing the system in a significantly shorter timeframe.

The initialization results for the monopolar system are presented in Figure 3.13. The GFM-VSC Cm-D5 is directly connected to an electrical load, meaning no auxiliary source is applied. However, in the LFSI approach, the influence of its own auxiliary source remains observable until 0.2 s. In contrast, both the DI and OCISS methods exhibit similar performance, successfully initializing the monopolar MTDC system within 0.4 s.

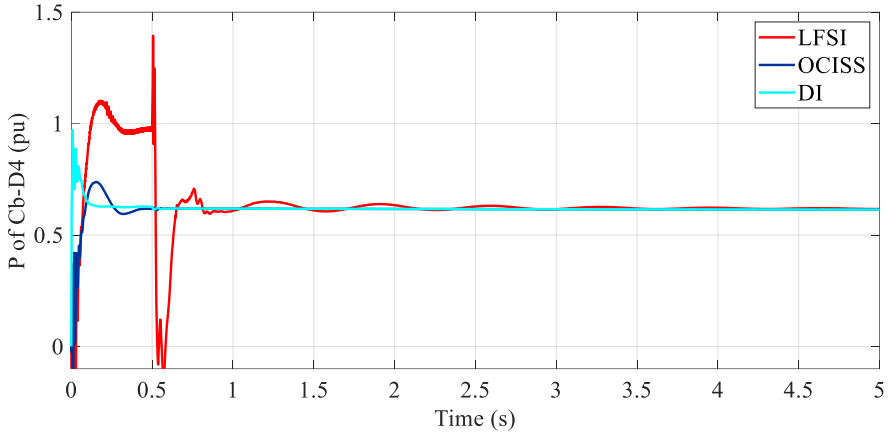

(a) P of Cb-D4

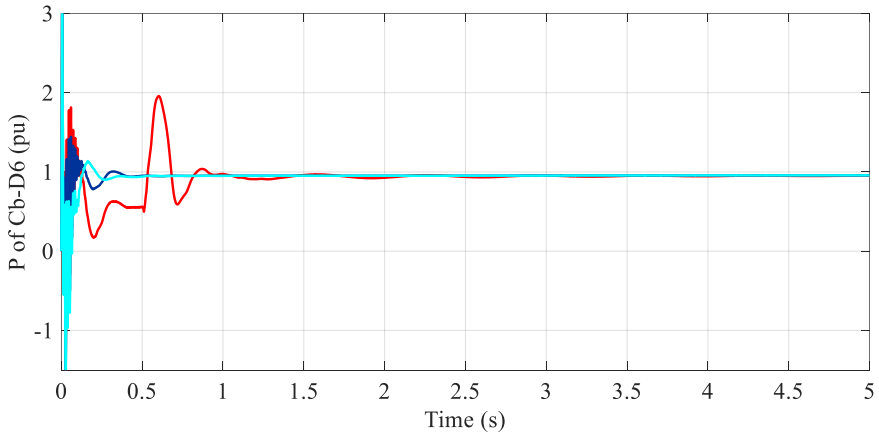

(b) P of Cb-D6

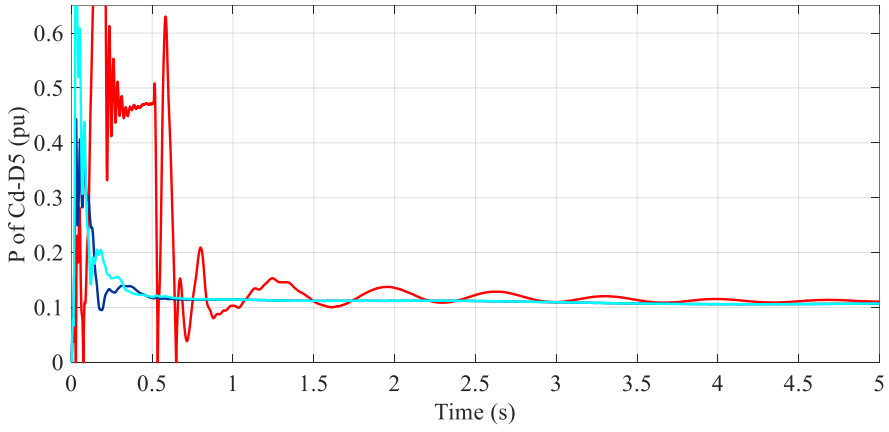

(c) P of Cd-D5

Figure 3.12 Initialization behaviors for the bipolar MTDC subnetwork of BM4.

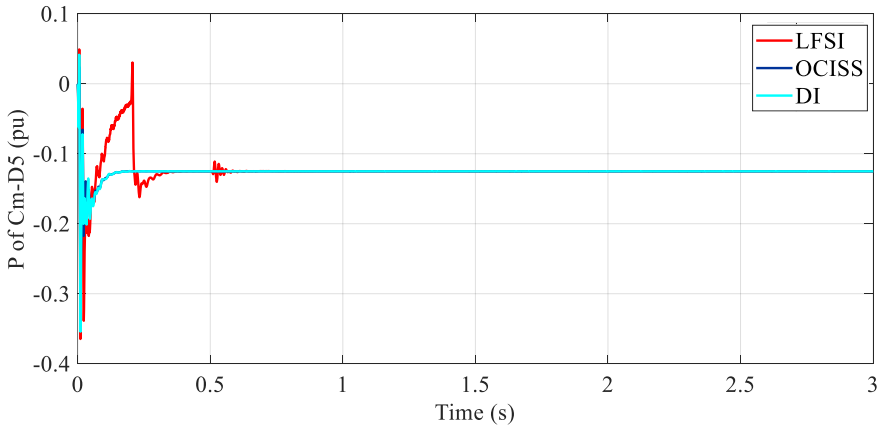

(a) P of Cm-D5

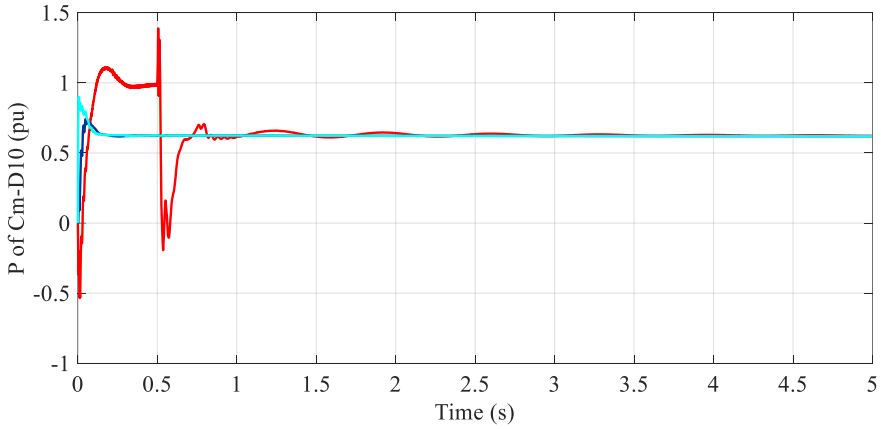

(b) P of Cm-D10

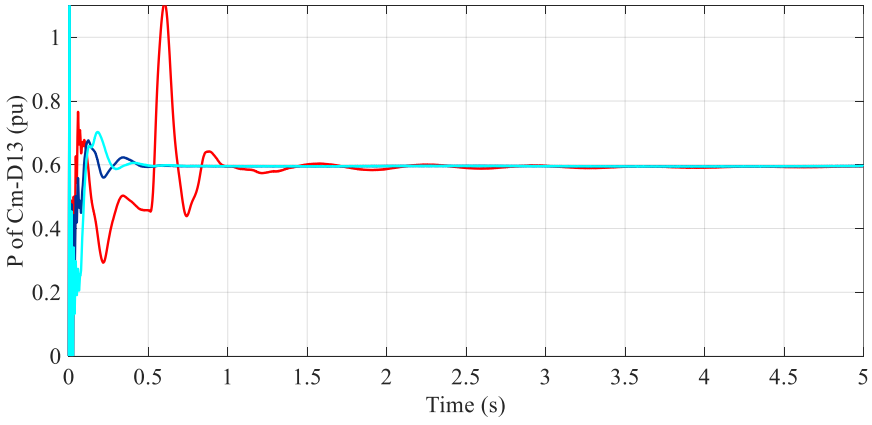

(c) P of Cm-D13

Figure 3.13 Initialization behaviors for the monopolar MTDC subnetwork of BM4.

Ultimately, the entire BM4 benchmark reaches steady-state with LFSI in approximately 3.4 s, whereas OCISS and DI showed comparable behavior, achieving steady-state within 0.5 s, which

can be seen as a significant improvement over LFSI. To analyze in depth, the computational details should be monitored and analyzed to gain a comprehensive understanding of all methods.

3.5.2 Computational time gains

Table 3.2 provides a comparative analysis of initialization time and CPU execution time for the LFSI, OCISS, and DI methods. The CPU time reflects the duration of the initialization phase, and the computing time gain quantifies the acceleration achieved by each method relative to LFSI.

In this table, the *CPU time* refers to the total wall-clock duration required to complete the initialization process, measured directly from the simulation platform for each method. The *computing time gain* is then calculated as the ratio of the CPU time of the baseline method (LFSI) to that of the alternative method. For example, $1714.8s / 249.9s \approx 6.9$, showing that DI achieves nearly a sevenfold acceleration compared to LFSI, with a similar value observed for OCISS.

Both OCISS and DI demonstrate a 6.9 times reduction in initialization time compared to LFSI, underscoring their superior efficiency. However, while both methods achieve comparable performance, DI stands out as the most practical approach, as it does not require accessing the models or model internal parameters, unlike OCISS. This makes DI the preferred method for efficiently initializing complex MTDC systems.

Table 3.2 Computational efficiency comparisons

Measure	**Initialization method**		
	LFSI	**DI**	**OCISS**
Initialization interval (s)	3.4	0.5	0.5
CPU time (s)	1714.8	249.9	248.4
Computing time gain	1	6.9	6.9

3.6 Conclusion

This chapter presented and analyzed two advanced initialization methods, Outer Control Initialization in Steady-State (OCISS) and Decoupling Interface (DI), for grid-forming voltage source converters (GFM-VSCs) in MTDC systems. While conventional load-flow-based initialization is effective for traditional power system components, it struggles with the complex control interactions of power electronic converters, particularly in islanded AC systems. LFSI, a widely used time-domain initialization method, was shown to introduce conflicts in GFM-VSC control loops, leading to prolonged transients and incorrect steady-state conditions.

The proposed OCISS method addresses this by explicitly initializing PI controller states using a steady-state solution, ensuring consistency with LF results. On the other hand, the DI approach provides a more generic and robust initialization technique, decoupling the GFM-VSC from its surrounding system during the startup phase. DI eliminates initialization conflicts, accelerates convergence, and enhances numerical stability.

Performance evaluations on the CIGRE BM4 benchmark demonstrated that both methods significantly outperform LFSI, reducing initialization time by a factor of 6.9. While OCISS is highly effective when model details are available, DI remains the most adaptable method, particularly for black-box converter models where internal parameters are inaccessible.

Given the effectiveness of DI, the next chapter will expand its application to a more general MTDC framework, integrating multiple converter types and addressing broader initialization challenges in large-scale MTDC networks.

CHAPTER 4 UNIFIED INITIALIZATION ALGORITHM OF MTDC MODELS: OFFLINE AND REAL-TIME APPLICATIONS

4.1 Introduction and background

Efficient initialization remains a critical factor in the simulation of large-scale MTDC networks, particularly when incorporating diverse converter types, control strategies, and black-box models. While the previous chapter focused on the initialization of GFM-VSCs, this chapter expands the scope to a generalized EMT simulation framework that accommodates a broader range of MTDC system configurations.

Traditional LF-based initialization methods, despite their effectiveness in conventional AC networks, face considerable challenges in complex MTDC grids. The presence of multiple converter types, such as grid-following VSCs (GFL-VSCs), LCCs, IBRs, and hybrid DC/DC converters, introduces diverse control constraints that must be properly handled. Additionally, black-box and grey-box models restrict access to internal control parameters, necessitating initialization strategies that do not rely on detailed model structures. In this work, the proposed framework only requires the AC–DC LF results and knowledge of the control mode of power converters, making it equally applicable to open and black-box models

To address these challenges, this chapter extends the Decoupling Interface (DI) method beyond GFM-VSCs, establishing a unified initialization framework applicable to diverse MTDC configurations. Previous works, such as [10], have proposed initialization methods for large AC–DC systems, including black-box models. However, these approaches primarily focus on the AC side and rely on Thevenin equivalents for system components, a process that is computationally demanding and difficult to generalize for large-scale MTDC networks. In contrast, the proposed framework fully integrates AC–DC initialization within the DI approach, ensuring a seamless and computationally efficient startup process, even when internal model parameters are inaccessible.

The proposed framework is designed to:

- Support various converter types by adapting DI methodology for different control modes.
- Enable black-box model initialization without requiring detailed internal parameters.
- Enhance stability and computational efficiency for large-scale EMT simulations.

The methodology is validated using CIGRE BM1 and BM7 benchmarks [4], demonstrating its capability to streamline initialization across heterogeneous MTDC systems.

Beyond offline EMT simulations, this chapter also explores the extension of DI to real-time applications. Real-time simulation imposes additional constraints, such as strict execution time limits and the need for initialization techniques that minimize transient durations. Section 4.5 evaluates the DI method in a real-time simulation environment using the HYPERSIM® platform, assessing its ability to maintain computational efficiency and ensure rapid steady-state convergence. The results highlight DI's potential as a robust and scalable initialization method for large-scale MTDC systems under real-time constraints, offering a viable alternative to conventional load-flow-based techniques.

The following sections provide a detailed formulation of the extended DI method, implementation strategies, and performance evaluations, ensuring a scalable and adaptable initialization process for complex EMT studies.

4.2 Unified DI methodology

The main difference between the DI method presented in CHAPTER 3 and the unified DI, is the scope of application, the unified DI method is extended and adapted to all MTDC components, not only for the GFM. Therefore, although there are some similarities in the flow chart's main steps, each step has different contents and details.

The key distinction between the DI method presented in CHAPTER 3 and the unified DI method introduced here lies in their scope of application. The previous chapter focused exclusively on GFM-VSCs within MTDC systems, whereas the unified DI extends the methodology to all converter types and MTDC components, including grid-following VSCs, LCCs, hybrid DC/DC converters, and IBRs. While the overall initialization sequence (decoupling, auxiliary sources, and reconnection) follows the same high-level structure, the specific procedures within each step differ significantly depending on the component type and control strategy. This ensures that the unified DI framework is scalable and adaptable to heterogeneous MTDC networks.

The DI method, as illustrated in Figure 4.1, is structured to systematically divide the system into distinct subsystems, where each subsystem contains only one TDIS. These subsystems are isolated through appropriate decoupling sources, ensuring that each TDIS operates independently until

reaching its steady-state conditions. Once the steady-state conditions are achieved, the subsystems are gradually reconnected by removing the auxiliary sources, facilitating a seamless transition back to the coupled system. This approach eliminates manual intervention by allowing the integration of interfacing sources directly within the simulation models.

The following subsections outline the DI initialization process in detail.

4.2.1 Decoupling

All system components are categorized into two groups: TDISs and Initialized Subsystems (ISSs). Subsystems containing power converters, such as IBRs with intricate control mechanisms, are designated as TDISs. Conversely, ISSs include components that can be initialized directly from the steady-state solution, such as transmission lines, transformers, and synchronous machines with their respective control systems.

The decoupling process occurs at PCC, as shown in Figure 4.2, Here, power converters such as VSCs and their corresponding IBRs (e.g., wind turbines) are assigned to distinct TDISs (highlighted in grey), while the remaining system elements form the ISS group. This classification ensures that components with high control complexity are effectively isolated during initialization, blocking initialization transient from passing to other components and mitigating potential conflicts between their transient behavior and the rest of the network.

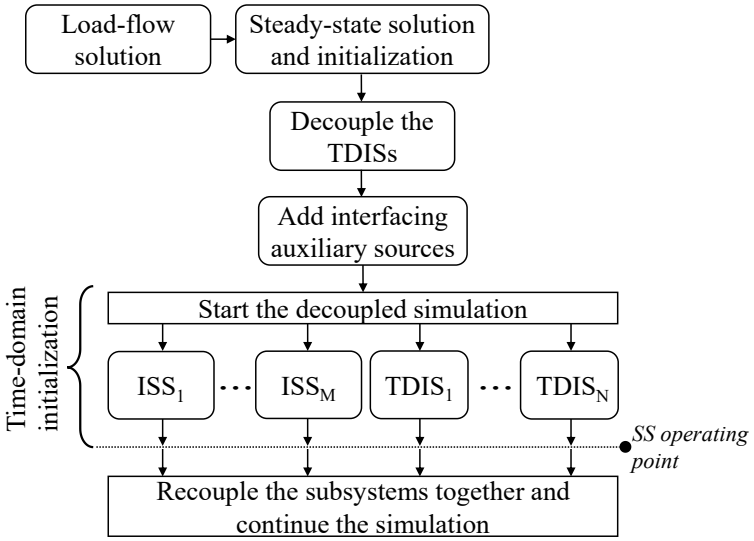

Figure 4.1 The procedure of unified DI initialization.

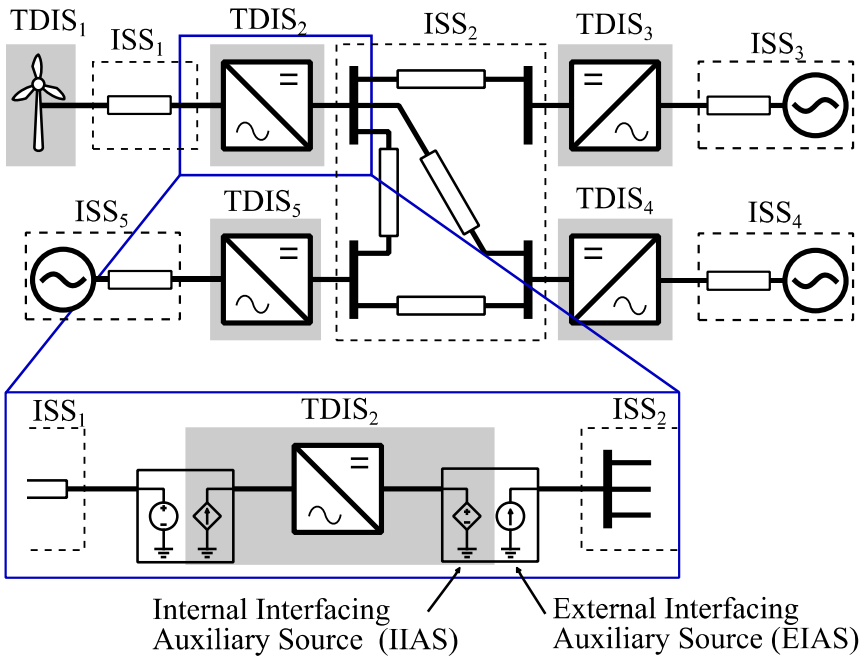

Figure 4.2 Decoupled MTDC system.

4.2.2 Adding interfacing auxiliary sources

To maintain steady-state conditions during initialization, Interfacing Auxiliary Sources (IASs) are introduced at each decoupling point. These auxiliary sources are categorized into two types:

- Internal IAS (IIAS): Represented by a dependent source, this type of IAS dynamically adjusts based on system interactions.
- External IAS (EIAS): An independent source that enforces steady-state conditions using predefined constraints from the LF solution.

The EIAS plays a crucial role in sustaining the steady-state state of ISSs, ensuring that these components remain stable while the adjacent TDISs are initialized. The appropriate EIAS type is determined based on the LF constraints, as summarized in Table 4.1.

All EIAS phasors are derived from the LF results to maintain consistency with the system's initial conditions.

IASs are particularly vital in cases where ISSs must provide consistent boundary conditions to their corresponding TDISs. Their correct implementation prevents unwanted transients and ensures a smooth transition to time-domain simulation.

Table 4.1 EIAS type selection

Side	LF constraints		EIAS
DC	V_{dc}		DC voltage source
	I_{dc}, P_{dc}, or $\hat{P}$		DC current source
AC	δ	V	AC voltage source
	P or $\hat{P}$	Q, V, or $\hat{Q}$	AC current source

4.2.3 Decoupled simulation and recoupling

Once decoupling is complete, the system progresses to the time-domain simulation phase. During this phase:

- All ISSs retain their steady-state conditions.
- Each TDIS undergoes a controlled transition toward steady-state by ramping its internal variables.
- The initialization process ensures that TDIS variables evolve from a consistent initial state rather than abrupt, undefined conditions.

After all TDISs achieve their steady-state conditions within a predefined tolerance, the recoupling phase begins. At this stage:

- IASs are removed, restoring the original network topology.
- TDISs and ISSs are seamlessly reconnected to form the complete MTDC system.

This structured approach minimizes initialization transients, ensuring a stable and computationally efficient transition from steady-state analysis to full EMT simulation.

4.3 Internal interfacing auxiliary source selection

The control systems of IBRs often rely on several variables measured at the PCC. While some of these variables are explicitly controlled, others are utilized internally for auxiliary calculations. These latter variables, referred to as disturbance variables, play a crucial role in the initialization process.

Since the performance of the control system depends on the accuracy of these disturbance variables, they must reach their steady-state values as quickly as possible. However, in many cases, these variables exhibit slow dynamic behavior, as they reflect the external system's transient

response. Their delayed convergence can introduce initialization inconsistencies, prolonging the system's initialization period.

To overcome these challenges, this section proposes a methodology for selecting IIASs based on disturbance variables. The objective is to accelerate the response of the outer control loop, typically the slowest control component, by ensuring that TDISs receive an accurate replica of steady-state values for disturbance variables. This is achieved using a dependent source, which replicates the expected steady-state behavior and stabilizes the initialization process.

By employing this approach, the outer control dynamics of the TDIS align more closely with the intended steady-state conditions, reducing transient response complexity and expediting the system's transition to a stable operating state.

4.3.1 Determination of disturbance variables

To effectively identify the relevant disturbance variables for a given control mode, the error expression of the outer control loop can be formulated concerning the manipulated control variables. This provides a systematic framework for determining which variables influence initialization stability and accuracy.

A more detailed analysis of this procedure is presented for VSCs and their common control modes, as illustrated in Figure 4.3. Additionally, a sensitivity analysis is performed for grid-connected converters, allowing a comparative assessment of how the outer control response differs from the original uninitialized case.

It is important to emphasize that this framework does not require direct access to the converter's internal control equations. In practice, the only information required is the specified control mode (e.g., P, V_{dc}, GFM,..etc), which is always available even for black-box vendor models. As a rule of thumb, once the control mode is known, the corresponding disturbance variable can be directly identified, regardless of whether the internal control structure is exposed or hidden. The derivations in this section therefore serve as illustrative examples based on typical control implementations, while the overall framework remains general and applicable across both open and black-box models.

4.3.1.1 P-Controlled VSC initialization

The P-VSC control configuration is widely employed in MTDC systems, where the d-axis regulates active power, while the q-axis manages either voltage magnitude or reactive power. The schematic representation of this control structure is provided in Figure 4.4.

Typically, P-VSCs incorporate either a DC voltage limiter to maintain voltage within acceptable thresholds or a droop control mechanism for power-sharing among multiple converters. However, these two control strategies are mutually exclusive, only one can be applied at a time.

In the subsequent demonstrations, the following assumptions have been considered:

- The positive power flow direction is from DC to AC side.
- The VSC is lossless $P_{ac} = P_{dc} = P$.
- The control system uses vector control, i.e., $v_q = 0$.
- The current control is very fast, and the current matches its reference immediately $i_d^{ref} = i_d$.

From these assumptions, the expressions of P, Q, and AC–DC power balance are given by

$$P = v_d i_d + v_q i_q = v_d i_d = v_d i_d^{ref} \tag{0.21}$$

$$Q = v_q i_d - v_d i_q = -v_d i_q = -v_d i_q^{ref} \tag{0.22}$$

$$\left| v_d i_d^{ref} \right| = \left| V_{dc} I_{dc} \right| \tag{0.23}$$

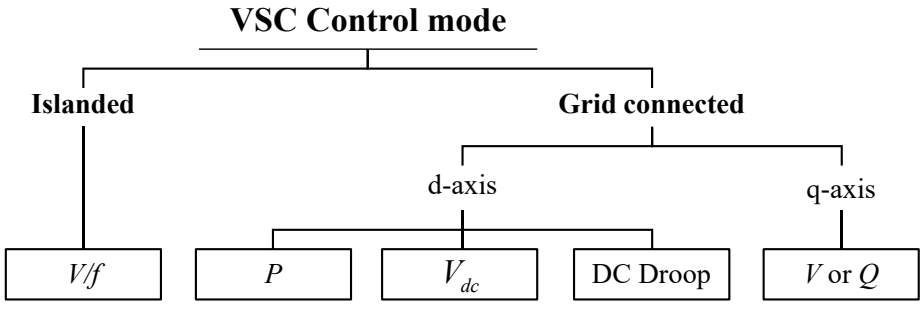

Figure 4.3 The common VSC control modes.

A basic control schematic for the P-VSC is illustrated in Figure 4.4. In this scheme, the d-axis channel governs active power *P*, whereas the q-axis channel manages either the AC voltage

magnitude $|V_{ac}|$ or the reactive power Q. Typically, this control strategy is complemented by a Vdc-limiter [2] to maintain the DC voltage within its permissible range. Alternatively, a droop control mechanism may be introduced when coordinating multiple P-VSCs, allowing power-sharing adjustments by modifying reference values. However, it is important to note that a P-VSC can operate with either the Vdc-limiter or droop control, but not both simultaneously.

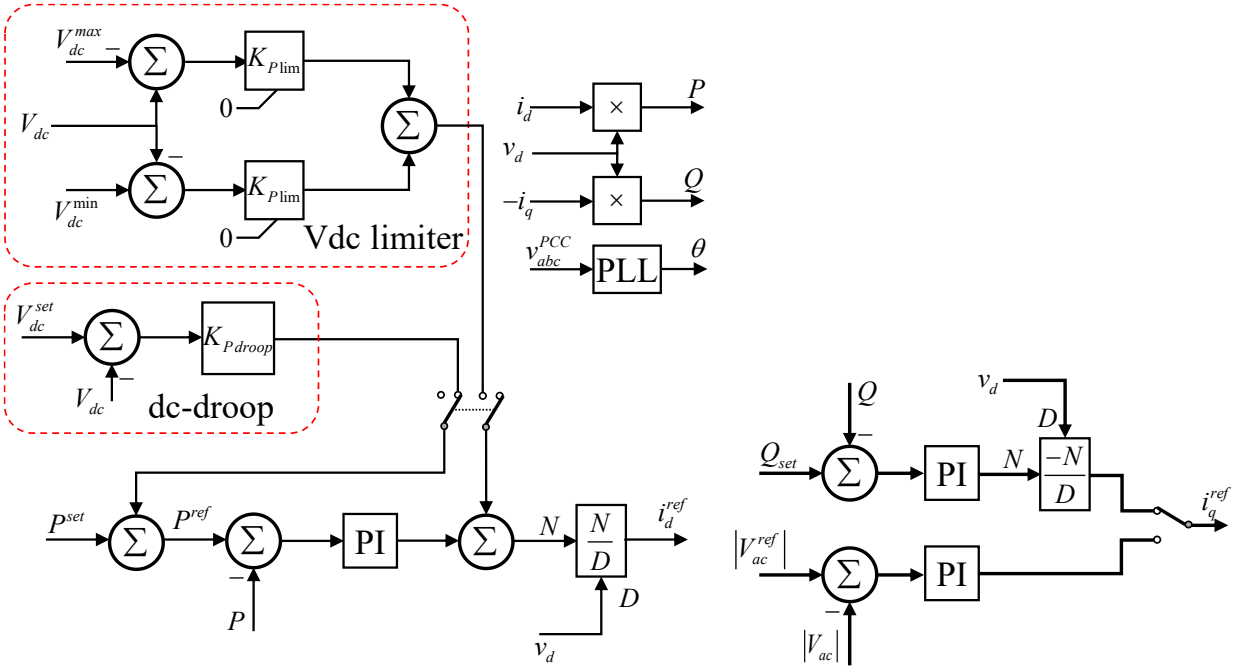

(a) d-axis (b) q-axis

Figure 4.4 Outer control schematic of P-VSC.

In Figure 4.4.(a), the active power reference is compared with the measured value, and the error is processed by a PI controller to generate the reference d-axis current i_d^{ref}. Similarly, the q-axis loop in Figure 4.4.(b) compares either the reactive power or AC voltage magnitude with their setpoints, and the PI controller produces the reference current i_q^{ref}. Both loops operate within a dq frame established by the PLL, while the optional Vdc-limiter and DC droop functions adjust the active power reference when the DC voltage deviates from nominal. In practice, these control loops are implemented with additional details in EMT simulation tools. To illustrate this correspondence, Figure 4.5 shows the actual EMTP® implementation of the P-controlled MMC.

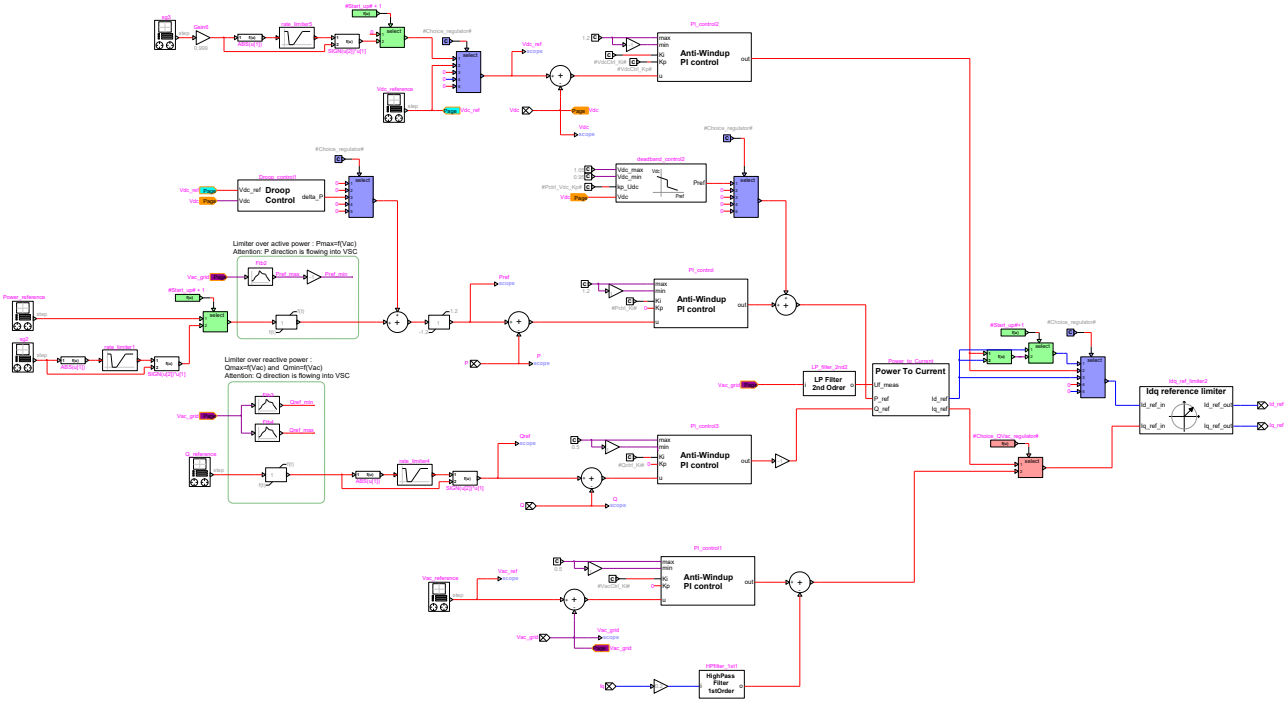

Figure 4.5 Outer control of grid-connected VSCs as modeled in EMTP®.

Diving into the details, as depicted in Figure 4.4.(a), the manipulated variables (outputs) of the system are the direct and quadrature components of the reference current, i_d^{ref} and i_q^{ref}, respectively. Applying the previously established equations (0.21) and (0.22), the error expressions for the manipulated variables are formulated as follows:

$$\Delta P = P^{set} - v_d i_d^{ref} \tag{0.24}$$

$$\Delta Q = Q^{set} + v_d i_q^{ref} \tag{0.25}$$

These expressions remain valid under the assumption that the influence of DC droop control or Vdc-limiter is negligible. Notably, the only variable appearing in the control input-output relationship that is not directly regulated by the converter is v_d. Consequently, v_d serves as the disturbance variable in this simplified control loop.

When the DC droop control mechanism in Figure 4.4.a s activated, equation (0.24) modifies to:

$$\Delta P = \left[P^{set} + f_{droop}\left(V_{dc}\right) \right] - v_d i_d^{ref} \tag{0.26}$$

Here, $f_{droop}(V_{dc})$ denotes the functional dependency on DC voltage. Consequently, both v_d and V_{dc} should be considered disturbance variables in this control scenario. Similarly, when utilizing an activated Vdc-limiter, both v_d and V_{dc} influence the control behavior.

To ensure accurate initialization, the IIAS placed on the left side of the VSC in Figure 4.2 should be selected as a dependent voltage source, replicating the waveform of v_{abc}^{ss}. Meanwhile, the IIAS on the right side should be assigned to a steady-state value, represented as V_{dc}^{ss}, where the superscript 'SS' signifies that it corresponds to the system's steady-state condition. The selection of IIAS sources is adaptable across different TDIS types that exhibit similar outer control behaviors. For instance, AC-side IIAS configurations can be applied effectively to wind and PV parks, whereas DC-side IIAS configurations can be specifically tailored for PV arrays.

To evaluate the impact of the selected IIASs on the initialization speed, an analytical sensitivity assessment is conducted for the P-VSC control mode.

Utilizing equations (0.21) and (0.22), the sensitivity of the manipulated variables to the controlled variable is expressed as:

$$\frac{di_d^{ref}}{dP} = \frac{1}{v_d}\left(1 - \frac{P}{v_d}\frac{dv_d}{dP}\right) \tag{0.27}$$

$$\frac{di_q^{ref}}{dQ} = -\frac{1}{v_d}\left(1 - \frac{Q}{v_d}\frac{dv_d}{dQ}\right) \tag{0.28}$$

where di_d^{ref}/dP represents the speed of response (i.e., initialization rate). From equations (0.27) and (0.28), it is evident that the AC-side system dynamics are dictated by the derivatives dv_d/dP and dv_d/dQ, respectively. These derivatives exhibit positive slopes, which contribute to reducing the ramping time of the outer control. By implementing the selected IIASs, the dependent AC voltage source maintains v_d at its steady-state value, v_d^{ss} sets $dv_d/dP = 0$, ensuring that the outer control sensitivity remains fixed at $di_d^{ref}/dP = 1/v_d^{ss}$. Consequently, the outer control response becomes linear and accelerates initialization, improving upon the original ramping behavior [9].

4.3.1.2 Vdc-controlled VSC (Vdc-VSC)

The control schematic for the Vdc-VSC is illustrated in Figure 4.6. This control mode is primarily used as a DC slack bus, regulating the DC voltage to maintain system stability. Similar to the P-VSC, the controlled outputs in this scheme are the current reference components, i_d^{ref} and i_q^{ref} . For the d-axis, applying the AC–DC power balance equation from (0.23) results in the following error expression:

$$\Delta Vd_{dc} = V_{dc}^{ref} - V_{dc} = V_{dc}^{ref} - \frac{v_d i_d^{ref}}{I_{dc}} \tag{0.29}$$

The q-axis control structure follows the same principles as in the P-VSC case, where the error term is derived as a function of the manipulated variable, as previously expressed in (0.25). In equation (0.29), both v_d and I_{dc} serve as disturbance variables, influencing the system's response. Consequently, in the IIAS framework depicted in Figure 4.2, the left-side dependent source is assigned to v_{abc}^{ss}, while the right-side dependent source is allocated to I_{dc}^{ss}.

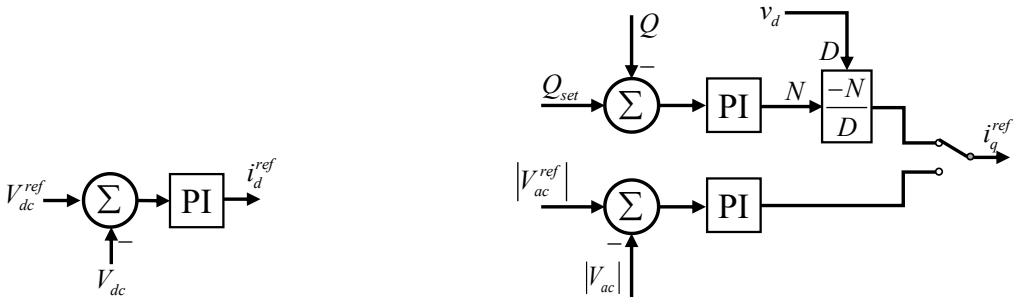

(a) d-axis (b) q-axis

Figure 4.6 Outer control schematic of Vdc-VSC.

To assess the impact of the selected IIASs on initialization speed, equation (0.23) can be utilized to derive the expression for the manipulated variable i_d^{ref} :

$$i_d^{ref} = \frac{V_{dc} I_{dc}}{v_d} \tag{0.30}$$

From equation (0.30), the sensitivity of i_d^{ref} to variations in the controlled variable V_{dc}, is expressed as:

$$\frac{di_d^{ref}}{dV_{dc}} = \frac{I_{dc}}{v_d} + \frac{V_{dc}}{v_d}\frac{dI_{dc}}{dV_{dc}} - \frac{V_{dc}I_{dc}}{v_d^2}\frac{dv_d}{dV_{dc}} \tag{0.31}$$

Further refinement leads to:

$$\frac{di_d^{ref}}{dV_{dc}} = \frac{I_{dc}}{v_d} + \frac{V_{dc}}{v_d}\frac{dI_{dc}}{dV_{dc}} - \frac{V_{dc}I_{dc}}{v_d^2}\frac{dv_d}{dP}\frac{dP}{dV_{dc}} \tag{0.32}$$

The first term, (I_{dc}/v_d), represents the linear response of the Vdc-VSC outer control. The second term accounts for the DC-side dynamics, which influences the outer control response. Notably, the term dI_{dc}/dV_{dc} exhibits a negative slope, thereby reducing the initialization speed. The third term encapsulates the combined effects of AC and DC dynamics. Since dv_d/dP and dP/dV_{dc} exhibit positive slopes, they further contribute to a reduction in response speed.

By applying the DI initialization, the IIASs will effectively fix I_{dc} and v_d at their steady-state values, ensuring that dI_{dc}/dV_{dc} , dv_d/dP , and dP/dV_{dc} approach zero. Consequently, the outer control behavior becomes linear, enabling rapid ramping of the Vdc-VSC to its steady-state operating point.

4.3.2 Grid forming VSC (V/f-VSC)

The V/f-VSC control mode is predominantly utilized in MTDC grids to integrate passive loads or weak AC networks. The control schematic for this mode is depicted in Figure 4.7. In this scheme, the d-axis voltage regulates the AC voltage, while an oscillator maintains the frequency stability.

The manipulated variable in this configuration is E_d^{ref} , which represents the internal reference voltage, while $|V_{ac}|$ denotes the magnitude of the AC voltage at the PCC. A high-pass filter (HPF) is typically incorporated to dampen high-frequency components and improve control stability [143]. To connect the abstract control description with its practical realization, Figure 4.8 illustrates the EMTP® implementation of the V/f-VSC outer control used in the MMC models.

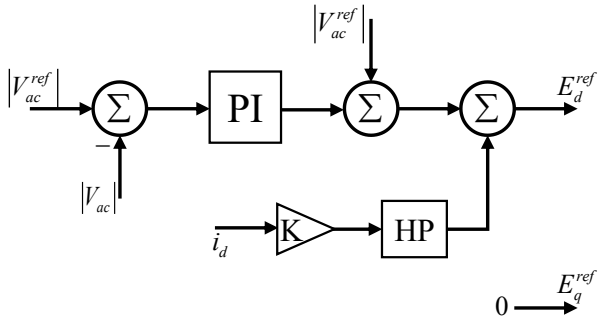

Figure 4.7 Outer control for V/f-VSC.

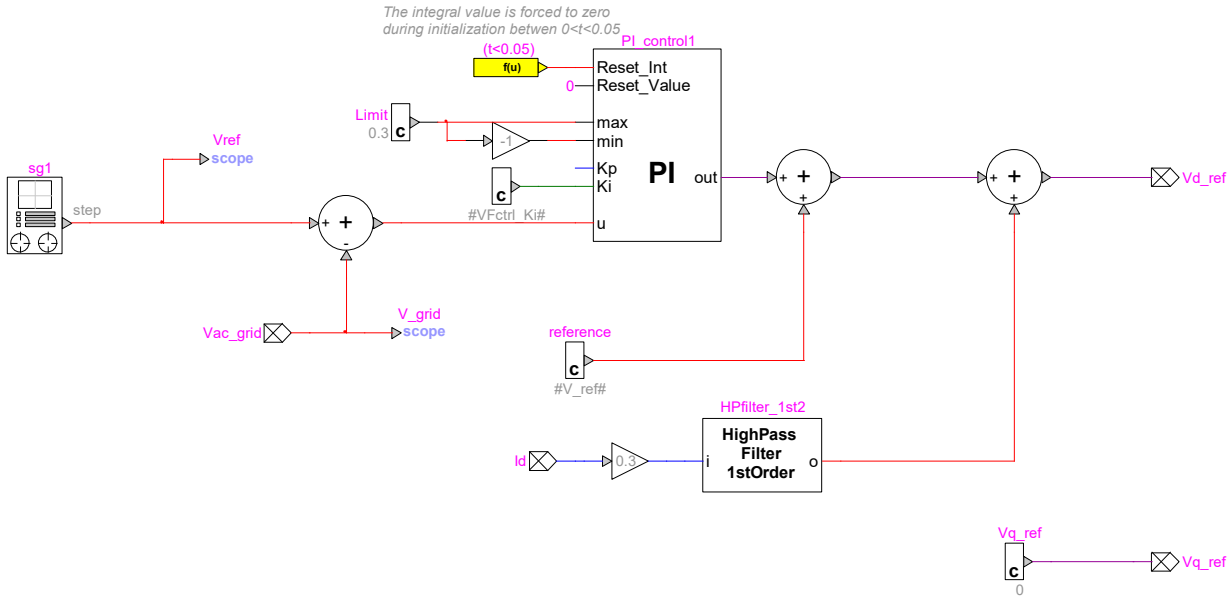

Figure 4.8 V/f-VSC outer control as modeled in EMTP®.

The subsequent analyses and demonstrations are conducted in phasor domain. To establish the governing equations, Kirchhoff's Voltage Law (KVL) is first applied to the converter's AC side:

$$V_d + jV_q = E_d^{ref} - (I_d + jI_q)\vec{Z}_{eq} \tag{0.33}$$

where $\vec{Z}_{eq}$ represents the equivalent impedance of VSC at the AC side, encompassing the transformer impedance and the equivalent arm inductance. Using this formulation, the magnitude of the AC voltage can be written as:

$$|V_{ac}| = |V_d + jV_q| = |E_d^{ref} - (I_d + jI_q)\vec{Z}_{eq}| \tag{0.34}$$

Finally, utilizing (0.34), the error expression in terms of the manipulated variable becomes:

$$\Delta|V_{ac}| = |V_{ac}|^{ref} - \left|E_d^{ref} - (I_d + jI_q)\vec{Z}_{eq}\right| \tag{0.35}$$

Since neither i_d nor i_q influence the DC side, they are identified as the disturbance variables in this outer control scheme. Given that no DC-side variables affect this control mechanism, the IIASs should interface i_{abc}^{ss} on the AC side and either I_{dc}^{ss} or V_{dc}^{ss} on the DC side. However, V_{dc}^{ss} is the preferred choice since it is actively utilized in the modulation processes, leading to a slightly improved performance [9, 126].

4.3.3 Ramping speed comparison with the Thevenin method

This section evaluates the impact of dI_{dc}/dV_{dc}, from equation (0.32), on the initialization speed of TDISs. The proposed IIAS-based approach is compared against a ramp-up technique that incorporates a Thevenin equivalent method, as described in [10]. This approach, referred to as the Thevenin Equivalent Approach (TEA), introduces a unified auxiliary circuit to facilitate TDIS decoupling from the rest of the system.

Under TEA, the Vdc-VSC is isolated from a point-to-point HVDC system, as depicted in Figure 4.9 (a), and compared with the DI-based approach proposed in this chapter, Figure 4.9 (b). From Figure 4.9 (a), applying Kirchhoff's Voltage Law (KVL) to the DC side yields:

$$V_{th} - I_{dc}Z_{th} = V_{dc} \tag{0.36}$$

The relationship for dI_{dc}/dV_{dc} can then be derived as:

$$\frac{dI_{dc}}{dV_{dc}} = \frac{-1}{Z_{th}} \tag{0.37}$$

Substituting this into the equation (0.32) while considering $dv_d/dP = 0$, since in this test case, the AC part is connected to an ideal source representing an infinite bus, the sensitivity expression becomes:

$$\frac{di_d^{ref}}{dV_{dc}} = \frac{I_{dc}}{v_d^{ss}} - \frac{V_{dc}}{v_d^{ss}}\frac{1}{Z_{th}} \tag{0.38}$$

This equation highlights that the sensitivity depends on two variables, V_{dc} and I_{dc}.Assuming a lossless operation, the AC–DC VSC power is given by:

$$P = v_d^{ss} i_d^{ref} = V_{dc} I_{dc} \tag{0.39}$$

Rearranging for I_{dc}:

$$I_{dc} = \frac{V_{th} - V_{dc}}{Z_{th}} = \frac{V_{th} - V_{dc} + (V_{dc}^{ss} - V_{dc}^{ss})}{Z_{th}} \tag{0.40}$$

The term $(+V_{dc}^{ss} - V_{dc}^{ss})$ is introduced to simplify the expression. Since V_{th} and Z_{th} are constants, I_{dc} is approximately equal to I_{dc}^{ss} when $V_{dc} \approx V_{dc}^{ss}$. Thus, equation (0.40) can be rewritten as:

$$I_{dc} = I_{dc}^{ss} + \frac{V_{dc}^{ss} - V_{dc}}{Z_{th}} \tag{0.41}$$

By combining (0.39) and (0.41), we obtain::

$$v_d^{ss} i_d^{ref} = V_{dc} \left(I_{dc}^{ss} + \frac{V_{dc}^{ss} - V_{dc}}{Z_{th}} \right) \tag{0.42}$$

Differentiating equation (0.42) gives:

$$\frac{di_d^{ref}}{dV_{dc}} = \frac{I_{dc}^{ss}}{v_d^{ss}} + \frac{-2V_{dc} + V_{dc}^{ss}}{Z_{th} v_d^{ss}} \tag{0.43}$$

From this, it can be observed that the sensitivity di_d^{ref} / dV_{dc} in the TEA method varies with V_{dc}. In contrast, as discussed in (0.32), the DI-based IIAS stabilizes this sensitivity at a constant value:

$$\frac{di_d^{ref}}{dV_{dc}} = \frac{I_{dc}^{ss}}{v_d^{ss}} \tag{0.44}$$

(a) Thevenin auxiliary circuit. (b) DI's IIAS

Figure 4.9 Ramping Vdc-VSC test with Thevenin auxiliary circuit and the DI's IIAS.

Figure 4.10 compares the sensitivities of (0.43) and (0.44), showing that the TEA-based approach experiences a deceleration in response speed as the system reaches its steady-state. On the other

hand, the DI method, with its IIAS-based initialization, simplifies implementation by eliminating the need to compute individual Thevenin equivalents, thereby significantly reducing computational overhead. Furthermore, the DI method improves the overall TDIS outer control initialization process.

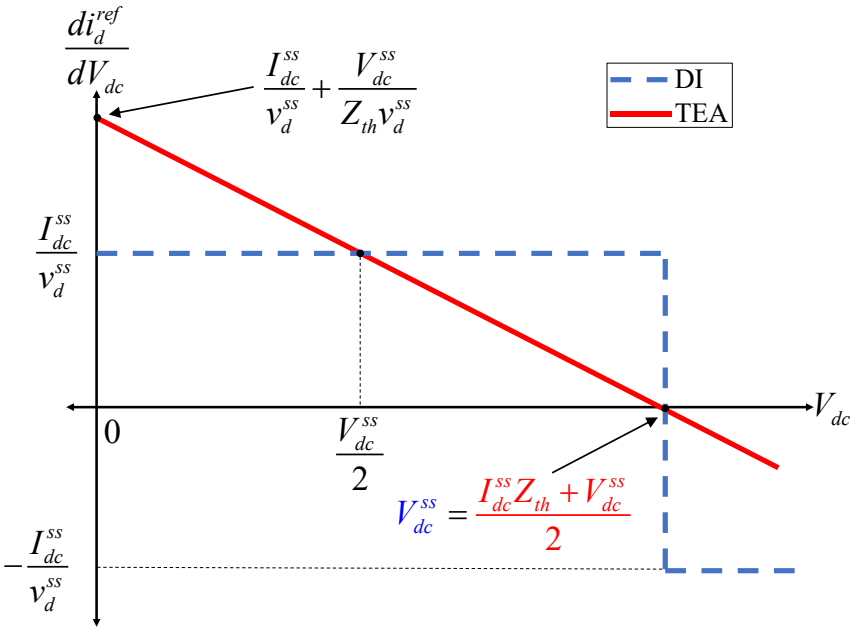

Figure 4.10 Outer control sensitivity comparison of Vdc-VSC.

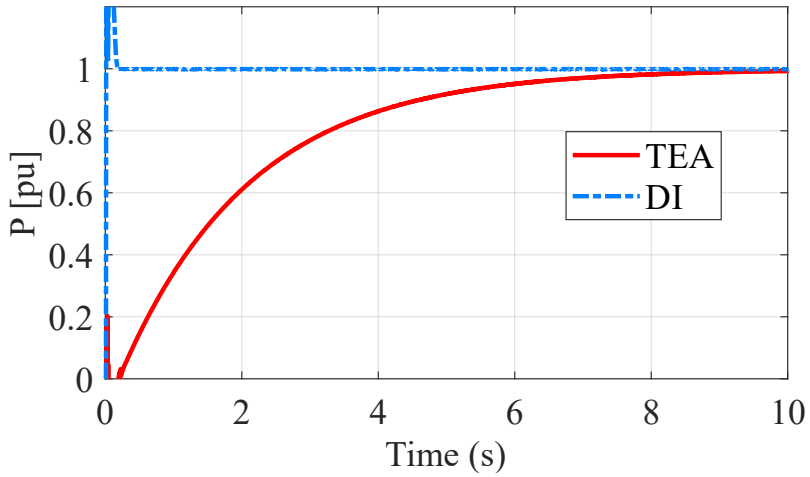

Figure 4.11 Vdc-VSC ramp-up comparison of TEA and DI's IIAS in time-domain.

A direct time-domain comparison of both approaches is presented in Figure 4.11, with test parameters obtained from the point-to-point HVDC line in [111]. The results demonstrate that the DI-based IIAS enables the Vdc-VSC to achieve initialization 50 times faster than the TEA method.

4.4 Performance evaluation

The proposed DI method has been implemented EMTP® [5] and tested on MTDC grid benchmarks proposed by CIGRE [141]. The implementation utilizes a dedicated library, where each control mode and LF constraint is encapsulated within a predefined block. The DI block is constructed by integrating IIAS, EIAS, and switching mechanisms necessary for the decoupling and recoupling processes. Through scripting, the LF results are automatically mapped to the auxiliary sources and other relevant simulation parameters. Consequently, the DI method can be seamlessly applied at the PCC with a simple drag-and-drop operation, making it compatible with any EMT-based simulation tool.

The selected benchmark systems encompass a variety of network scales and complexities. As illustrated in Figure 4.12, the largest test case, BM7, incorporates multiple sub-benchmarks (BM1–BM4) [141]. BM7 therefore covers monopolar and bipolar HVDC systems, both VSC- and LCC-based. The bipolar configuration relies on ground return without a DMR. The BM1 model corresponds to the first quarter of BM7, as highlighted in Figure 4.12, and serves as a standalone benchmark. Among these, BM1 and BM7 have been chosen as representative cases for medium- and large-scale MTDC networks. The corresponding system models are detailed in Table 4.2.

Table 4.2 Model types used in BM7

Device	Modelled by
Electrical sources and grid equivalents	Detailed synchronous machines with controls & some ideal voltage sources
MMC	Arm equivalent model
LCC	Detailed model with thyristors
DC-DC converters	Front-to-front MMCs and ideal DC transformers
Wind parks	Aggregated DFIG models with controls
PV parks	Aggregated models, some with controls
Electrical loads	Fixed impedances
Lines /cables	Wideband models

As listed in Table 4.2, wind parks are represented by aggregated DFIG models available in EMTP®. The mechanical dynamics are captured by a two-mass shaft system, which includes initialization routines to align the rotor and shaft states with the load-flow solution. In addition, the DFIG models feature built-in initialization for critical control components such as the PLL, ensuring stable

synchronization at startup. This DFIG model with integrated initialization is consistently employed in all methods and test scenarios, providing a uniform representation of wind parks throughout the study.

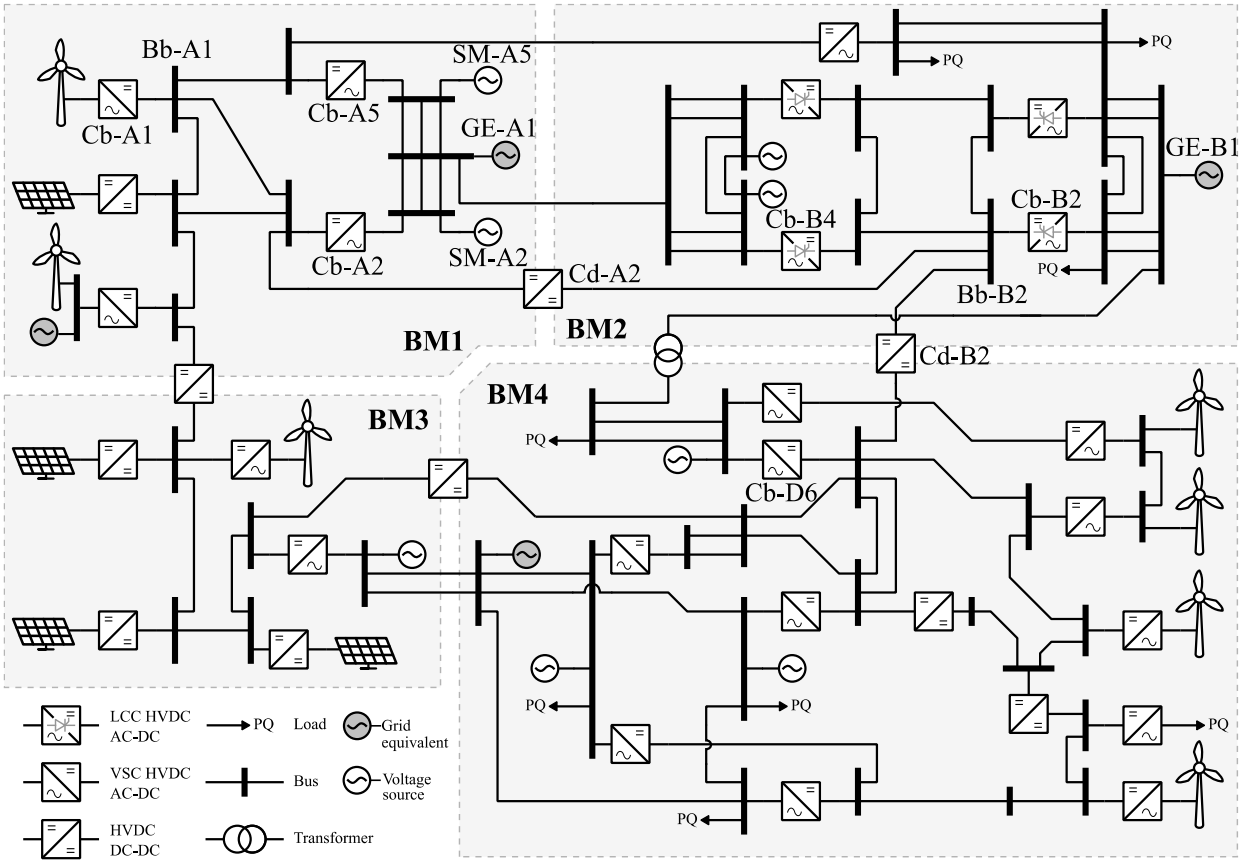

Figure 4.12 CIGRE BM7 benchmark including BM1–BM4.

The DI initialization method is benchmarked against the LFSI technique, as described in Section 3.2.3. Both methods are implemented within EMTP® to ensure a direct comparison. The initialization process is considered complete when the system reaches steady-state, defined by power and voltage deviations remaining within 1% of the LF results.

4.4.1 Implementing the proposed method in EMT software

To demonstrate the applicability of the proposed DI method, the EMT implementation is organized as a modular workflow that allows seamless integration with existing simulation models. Each DI block is encapsulated within a predefined subcircuit, enabling direct placement at the point of common coupling without requiring modifications to the main system model. As illustrated in Figure 4.13, DI blocks are positioned on both the AC and DC sides of the converter. Although the method is implemented and tested in EMTP®, its structure is generic and can be applied in any EMT-type simulation platform, since it only relies on basic circuit elements such as controlled sources and switches.

From the starting of simulation till the recoupling instant (T_i), the auxiliary sources are connected to enforce the load-flow solution, after which the original network elements are reconnected in a controlled manner. The value of T_i is selected based on the expected settling time of the controlled converter, typically determined from prior knowledge of its dynamic response. As discussed in CHAPTER 3, this time can also be obtained automatically by monitoring the settling behavior of the TDIS during the decoupled simulation phase.

The detailed realization of the AC-side DI block is shown in Figure 4.14.(a) and (b), while the corresponding DC-side implementations are provided in Figure 4.15.(a) and (b).

By construction, the same DI library can be reused across different control modes, providing flexibility for a wide range of operating scenarios. In practice, the method allows users to initialize complex MTDC test cases, such as CIGRE BM1 and BM7, through a straightforward drag-and-drop operation. Once the DI blocks are placed, the remainder of the process is automatic, reducing modeling effort and setup time. This makes the method particularly well suited for large-scale EMT studies and for benchmarking against alternative initialization schemes

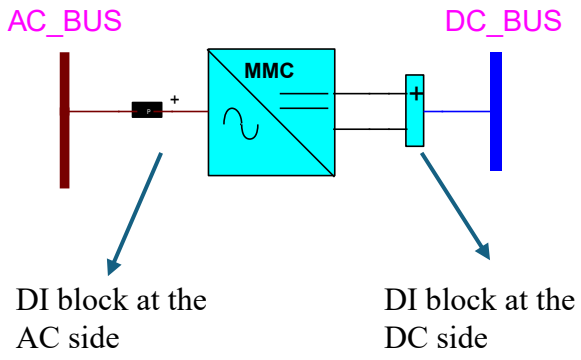

Figure 4.13 The unified DI method implementation in EMTP®

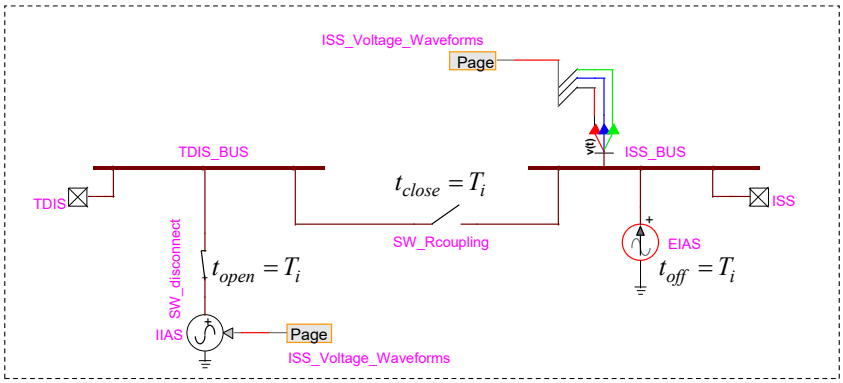

(a)

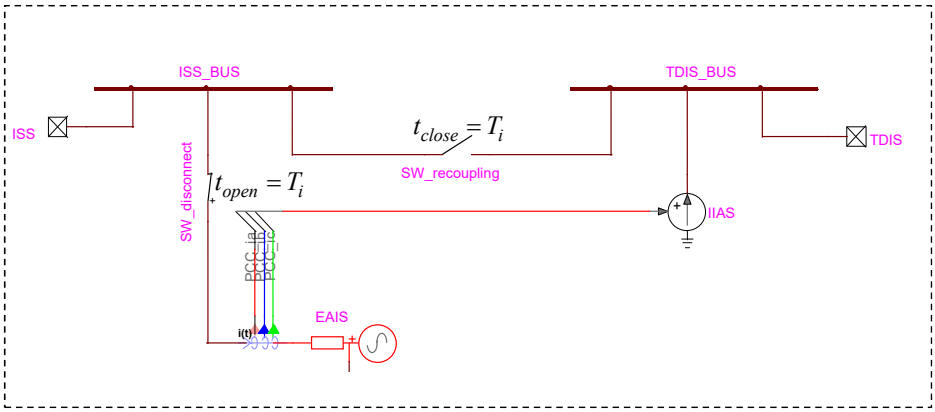

(b)

Figure 4.14 DI block for AC side: (a) P-constraint, (b) V-constraint..

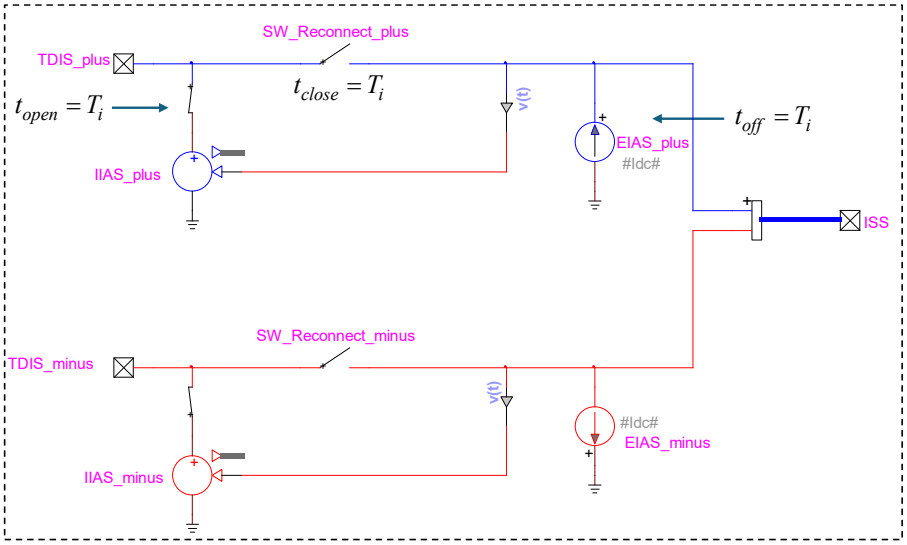

(a)

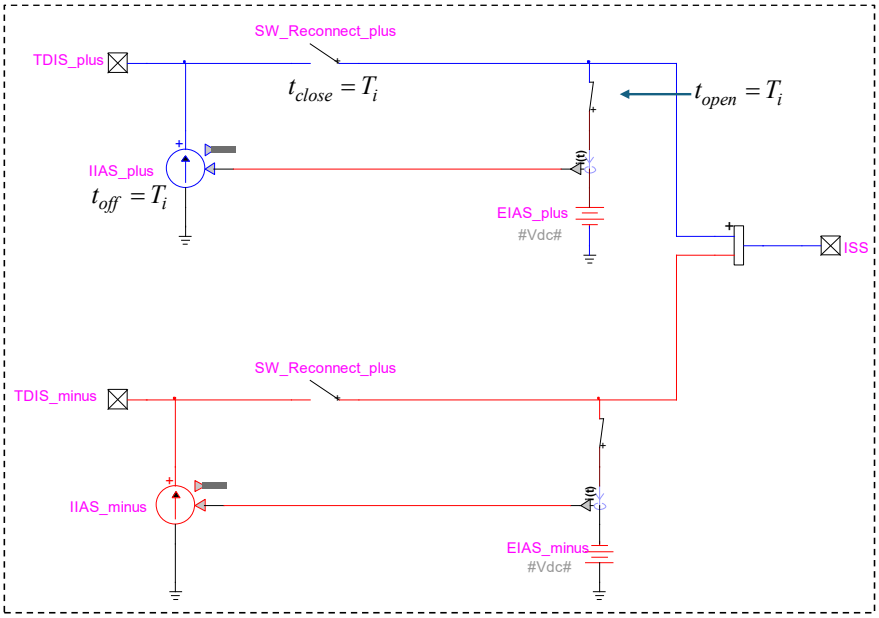

(b)

Figure 4.15 DI block for DC side: (a) P-constraint, (b) V-constraint.

4.4.2 CIGRE BM1 initialization results

The BM1 system is partitioned into seven TDISs and four ISSs for initialization. Figure 4.16 shows a screenshot of modelling CIGRE BM1 in EMTP® with DI blocks inserted for each TDIS on AC and DC sides. This simulation case is available in the folder *"Chapter 4/BM1/"*, included in the supplementary material.

As illustrated in Figure 4.17, the DI method successfully initializes the system in under 0.3 s, whereas the LFSI method requires 0.9 s to achieve steady-state. A key difference appears in the synchronous machines: although they start from their correct steady-state conditions, startup transients from the converters propagate through the AC side and excite the machines. Under LFSI, this interaction prolongs the machine settling time to about 9 s before a new steady-state is reached.

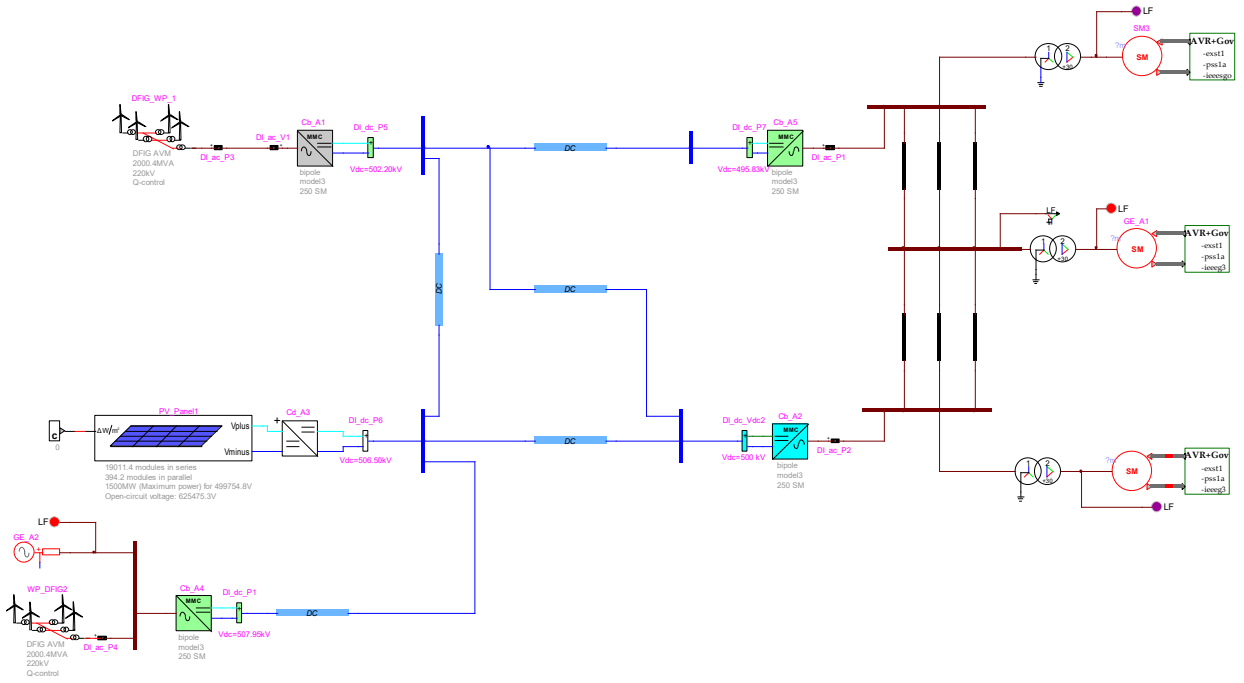

Figure 4.16 CIGRE BM1 modeled in EMTP® with DI blocks at AC and DC sides.

Figure 4.17 and Figure 4.18 compare the initialization performance of V/f-VSC (Cb-A1) and Vdc-VSC (Cb-A2) for both methods. The results indicate a significant improvement when applying DI, particularly in reducing initialization transients. However, for P-VSC (Cb-A5), the gain from DI over LFSI is negligible. This observation aligns with the sensitivity expression in (0.27), which shows that P-VSC initialization speed is influenced by dv_d/dP, a factor linked to the strength of the AC network.

In BM1, Cb-A5 is connected to a robust AC grid via SM-A5, which has a 4 GW capacity. This leads to an almost negligible sensitivity (dv_d/dP), ensuring that LFSI achieves fast initialization in this case.

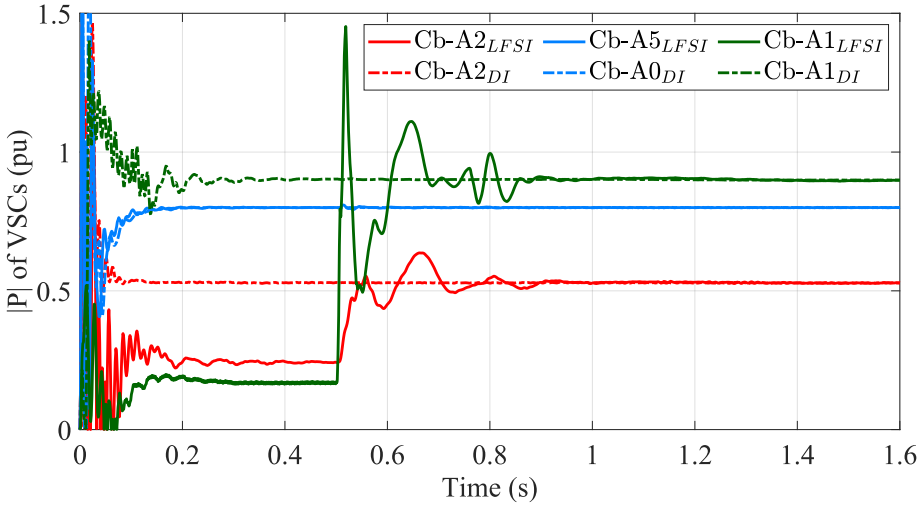

Figure 4.17 Initialization comparisons for the VSCs, BM1 case.

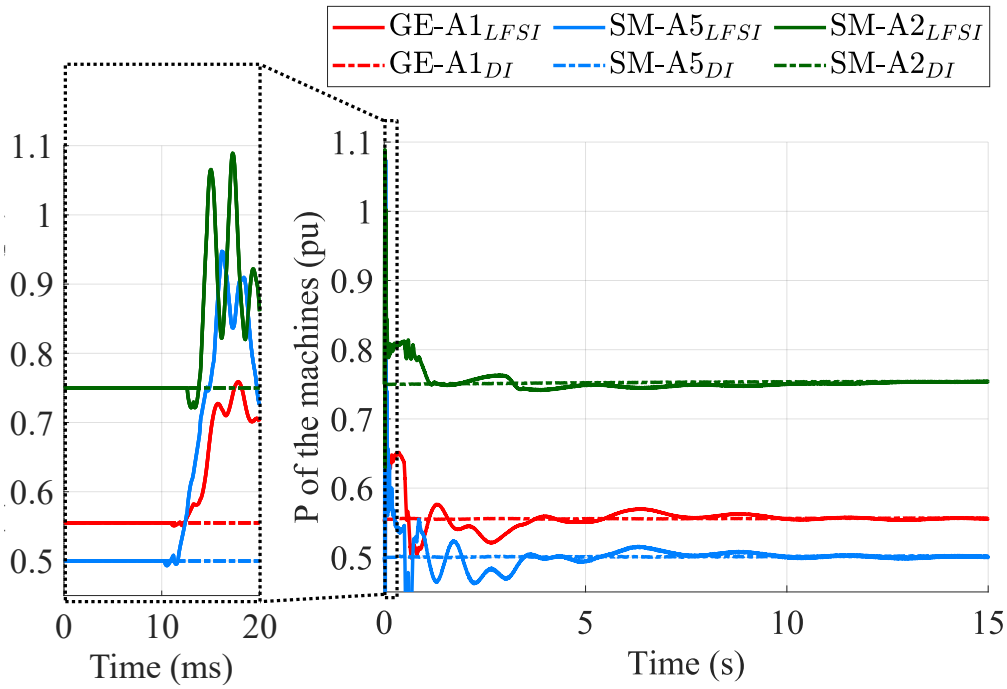

Figure 4.18 Initialization comparisons for the machines, BM1 case.

Regarding the AC components in BM1, synchronous machines are directly initialized in EMTP® from LF, meaning they are treated as ISSs in the DI method. Consequently, both initialization

techniques ensure that synchronous machines start from the same steady-state condition between 0 to 10 ms. However, a key distinction arises in the DC subsystem initialization.

Under LFSI, transients in the DC part propagate and impact the synchronous machines through Cb-A5 and Cb-A1 VSCs. These disturbances trigger electromagnetic transients, which eventually transition into electromechanical oscillations. Due to this phenomenon, oscillations persist for an extended period before fully settling.

In BM1, Cb-A5 is connected to a robust AC grid via SM-A5, which has a 4 GW capacity. This leads to an almost negligible sensitivity (dv_d/dP), ensuring that LFSI achieves fast initialization in this case.

Regarding the AC components in BM1, synchronous machines are directly initialized in EMTP® from LF, meaning they are treated as ISSs in the DI method. Consequently, both initialization techniques ensure that synchronous machines start from the same steady-state condition between 0 to 10 ms. However, a key distinction arises in the DC subsystem initialization.

Under LFSI, transients in the DC part propagate and impact the synchronous machines through Cb-A5 and Cb-A1 VSCs. These disturbances trigger electromagnetic transients, which eventually transition into electromechanical oscillations. Due to this phenomenon, oscillations persist for an extended period before fully settling. On the other hand, the DI approach prevents these interactions. Consequently, the machines start and preserve their steady-state operating points.

4.4.3 CIGRE BM7 initialization results

The BM7 benchmark consists of 44 VSCs, making its initialization a complex and computationally demanding task. Figure 4.19 shows a screenshot of modelling CIGRE BM7 in EMTP® with DI blocks inserted for each TDIS on AC and DC sides. This simulation case is available in the folder *"Chapter 4/BM7/",* included in the supplementary material.

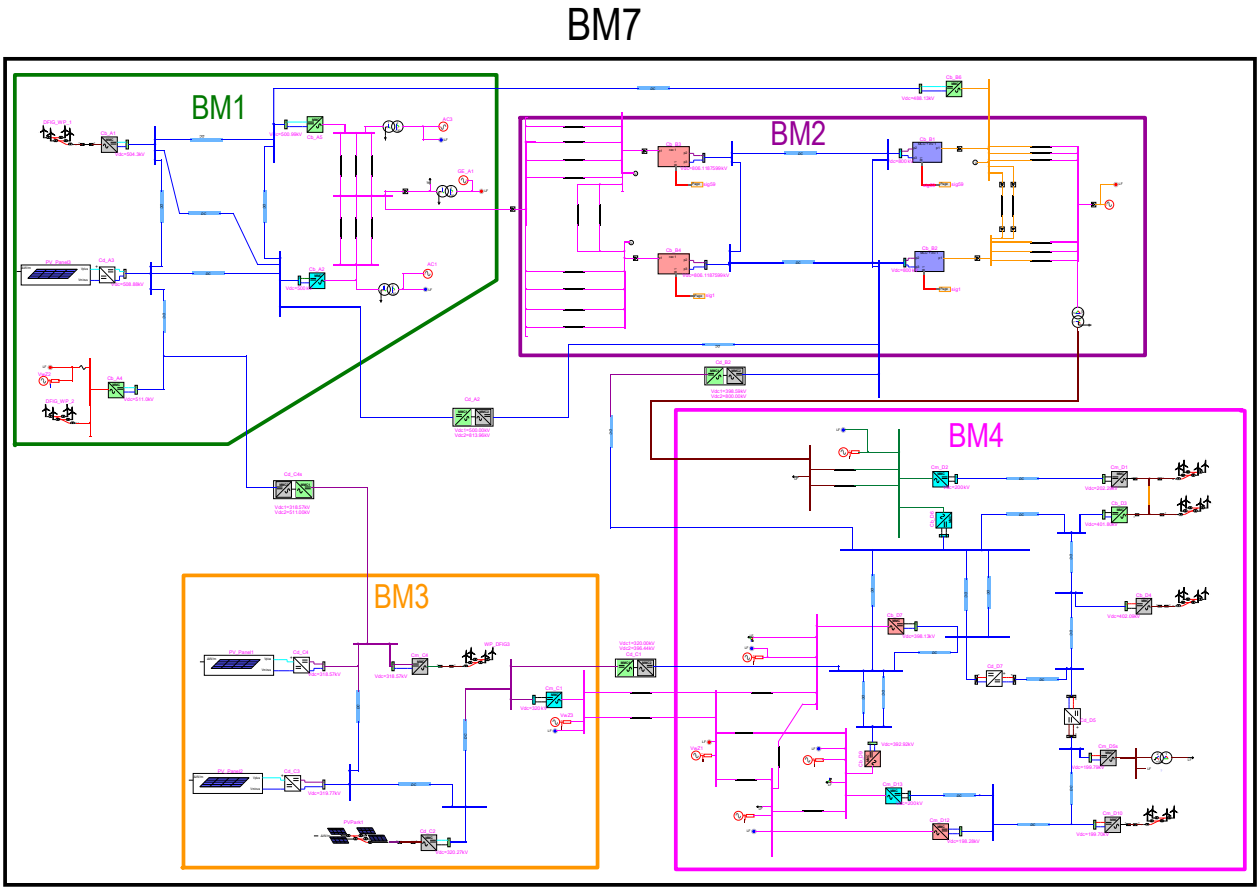

Figure 4.19 CIGRE BM7 modeled in EMTP® with DI blocks at AC and DC sides.

As depicted in Figure 4.20 and Figure 4.21, the LFSI method fails to correctly initialize BM7. This failure is attributed to the presence of multiple converter types and control interactions across both AC and DC networks, which complicate system stabilization.

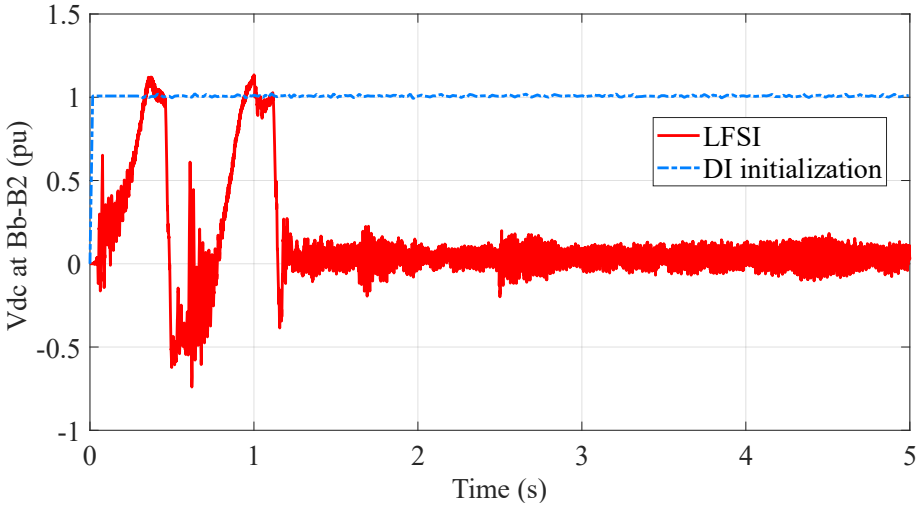

Figure 4.20 Initialization comparisons of V_{dc} at LCC inverter, Original BM7 case.

Conversely, the DI method successfully initializes BM7, achieving the correct steady-state operating point as verified by time-domain simulations. It is crucial to emphasize that the initialization procedure must not alter the steady-state solution of a stable system. The successful initialization using DI confirms that incorrect initialization could lead to significant time-domain transients, potentially delaying or even preventing the system from converging to its correct steady-state as determined by the LF solution.

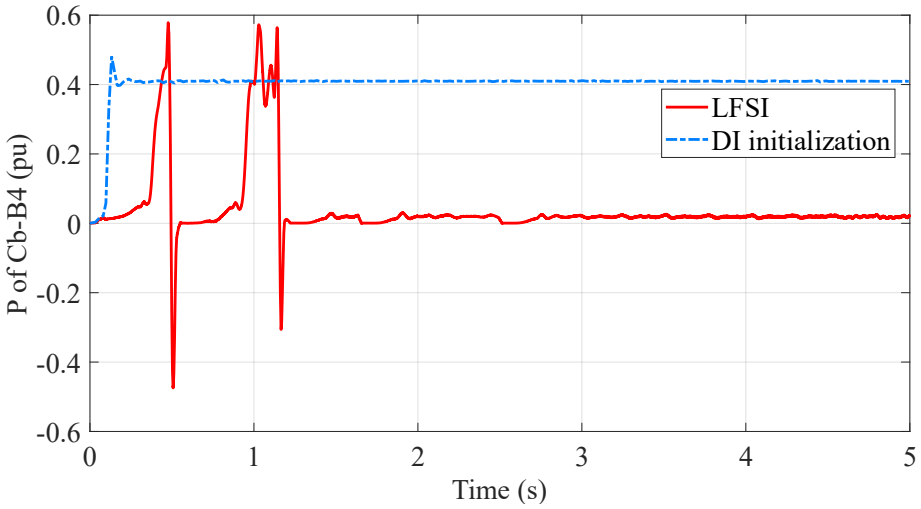

Figure 4.21 Initialization comparisons of P at LCC rectifier, original BM7 case.

To facilitate a reasonable LFSI-based initialization for BM7 in EMTP®, the CIGRE benchmark authors [4] introduced modifications to the model. However, these modifications caused

discrepancies between the steady-state operating points obtained from LF and time-domain simulations. Specifically, based on AC–DC LF results, the DC-DC converters (Cd-A2 and Cd-B2) collectively provide a 2.5 GW LCC network (BM2). However, in time-domain simulation, these components contribute zero power, leading to inconsistencies in initialization.

To enable a fair comparison between DI and LFSI, specific adjustments were made to stabilize LFSI, including:

- Replacing synchronous machines with ideal voltage sources.
- Sequentially initializing BM2's LCCs: LCCs are first started independently, reaching steady-state at 1 s, after which BM1 and BM4 are reconnected through Cd-A2 and Cd-B2 converters.
- Limiting the ramping rate of the DC-DC converters to 5 pu/s when reconnecting LCC with BM1 and BM4.

With the DI method, none of these modifications are required. The BM7 system is naturally partitioned into 39 TDISs and 16 ISSs under DI. The slowest simulation behaviors are illustrated in Figure 4.22 and Figure 4.23, where LFSI-based initialization transients persist until 3.6 s, whereas DI achieves steady-state in only 0.3 s.

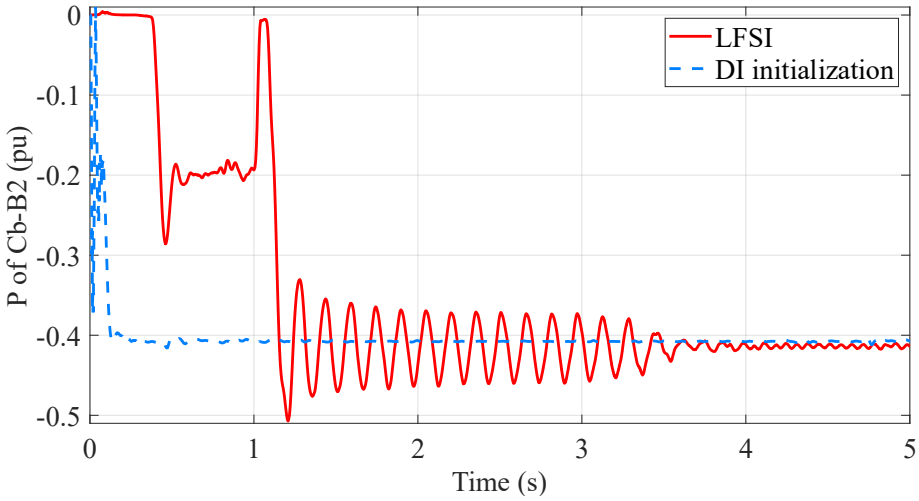

Figure 4.22 Initialization comparisons of P at LCC rectifier modified BM7 case.

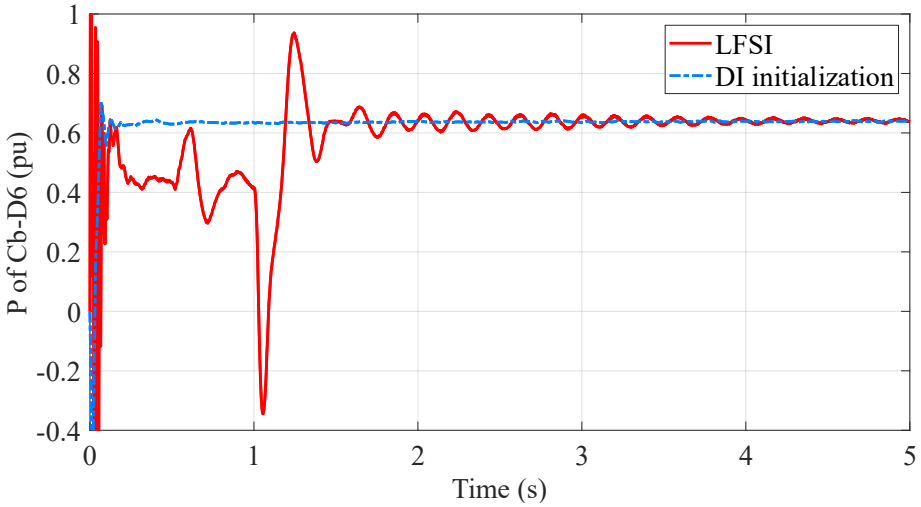

Figure 4.23 Initialization comparisons of Cb-D6's Power, modified BM7 case.

4.4.4 Computational time gains

Table 4.3 presents a comparison of the initialization and CPU execution times for LFSI and DI methods. The initialization time gain G_{init} is defined as the ratio of LFSI to DI execution times:

$$G_{init} = t_{\mathrm{LFSI}} / t_{\mathrm{DI}} \tag{0.45}$$

where t_{LFSI} and t_{DI} represent the CPU times of the LFSI and DI methods, respectively. This metric quantifies the computational efficiency improvements achieved by DI over LFSI.

As shown in Table 4.3, BM1 and BM7 (modified version) were successfully initialized using DI, whereas LFSI failed to initialize BM7 in its original form. In BM1, LFSI required 9 s of simulation time, while DI achieved steady-state in just 0.3 s, leading to an impressive speedup of 20.3 times. Similarly, in the modified BM7 case, DI reduced the initialization time to 0.3 s, compared to 3.6 s required by LFSI, resulting in a 16-fold improvement.

Regarding CPU execution time, LFSI required 170.9 s for BM1 and 659.4 s for the modified BM7, whereas DI drastically reduced these times to 8.4 s and 41.1 s, respectively. The DI method not only achieves a faster transition to steady-state but also significantly reduces computational overhead, making it a more scalable and efficient approach for initializing large MTDC systems.

Table 4.3 Computational efficiency, DI method versus LFSI

Measure	Initialization method	BM1	BM7	BM7*
Simulation interval (s)	LFSI	9	Failed to initialize	3.6
	DI	0.3	0.3	0.3
CPU time (s)	LFSI	170.9	Failed to initialize	659.4
	DI	8.4	52.7	41.1
Time gain G_{init}	DI	20.3	-	16

*Modified BM7 system model

4.5 Application of the DI method in real-time simulation

Although real-time simulation environments operate in strict synchronization with the real clock, initialization of large-scale MTDC systems within them may still be slow if not properly managed. This challenge is particularly evident when the system includes multiple converter-based devices and IBRs, whose control interactions can cause prolonged transients before steady-state is reached. While users may tolerate short delays during initialization, excessive waiting times can hinder scenario-based testing and reduce the effectiveness of analysis in real-time environments.

More critically, improper or prolonged initialization may lead to incorrect operating points or unstable behaviour. In complex hybrid AC–DC systems, for example, transients introduced during startup can activate protection schemes or trigger the disconnection of sensitive components, such as wind turbines. Such failures not only compromise the validity of the simulation but can also interrupt HIL experiments or delay controller tuning procedures.

To address these limitations, this section demonstrates how the DI method can be effectively extended to real-time applications. The method's ability to isolate subsystems and mitigate transients enables stable and rapid initialization, making it well-suited for real-time testing of MTDC systems under realistic and demanding operating conditions.

The DI method is evaluated using a modified version of the CIGRE BM1 benchmark system shown in Figure 4.24. In this variant, the simplified AC equivalent is replaced with a detailed two-area power system. Two-area systems are widely used as benchmark models for small-signal and transient stability studies, since they introduce inter-area oscillations and multiple synchronous machine dynamics. This addition increases the realism and complexity of the test case, providing

a more stringent benchmark for assessing initialization methods under real-time simulation constraints. The system is modeled and simulated using HYPERSIM®.

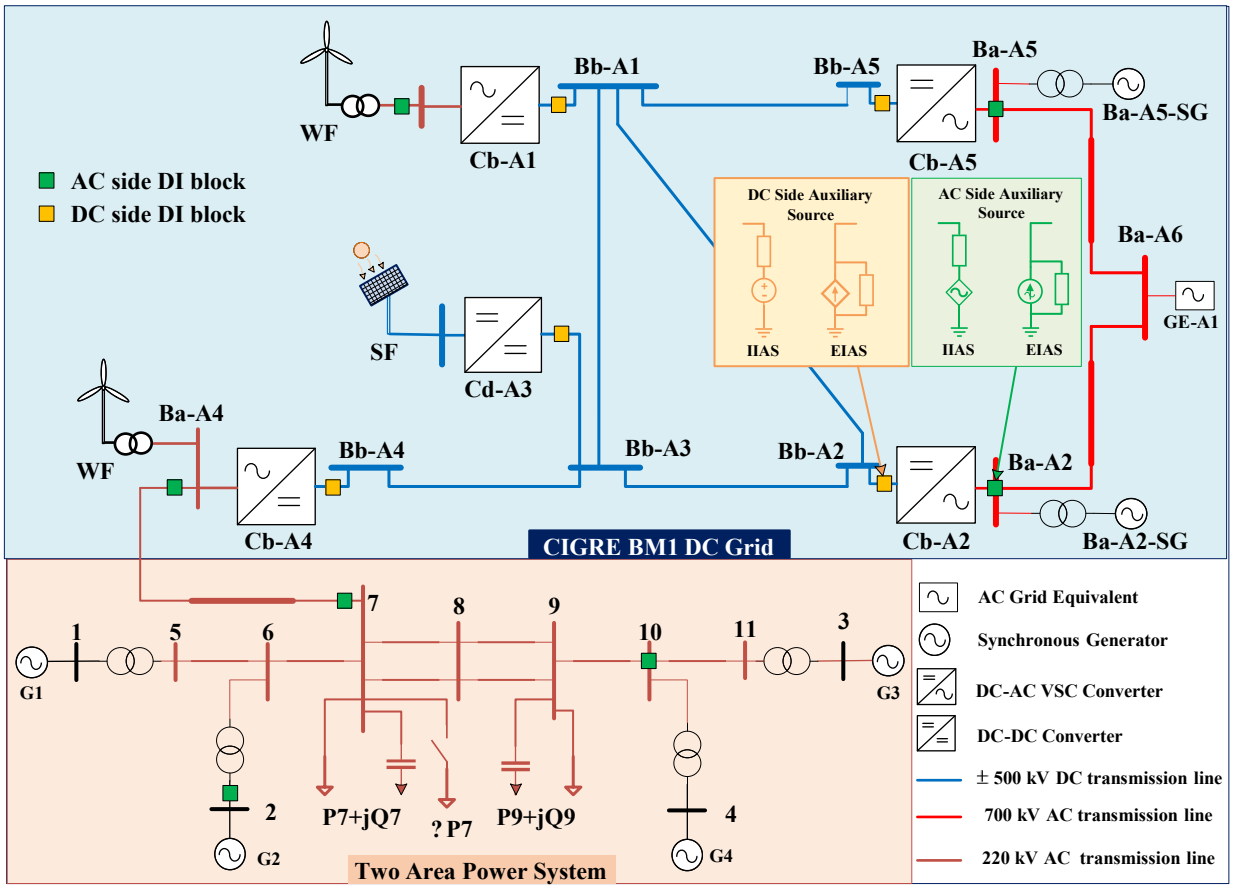

Figure 4.24 Modified CIGRE BM1 with a two-area power system

The DI methodology was implemented using controlled voltage and current sources to emulate the auxiliary sources used in the decoupled phase. Controlled switches were used to isolate subsystems and manage the transition back to the original topology during the recoupling step. The recoupling was programmed to occur at t = 5 s, once the monitored subsystems reached predefined steady-state criteria.

The system components used in the real-time simulation reflect the diversity of elements present in MTDC networks. These include Vdc-controlled and P-controlled MMC-based VSCs, wind and PV parks, and synchronous machines with their respective controls. Specific configurations and models used are summarized inTable 4.4. The two-area AC grid, added to increase complexity, is detailed in Table 4.5 and reflects realistic long-distance interconnection scenarios.

Table 4.4 Model types used in BM1

Device	Modelled by
Electrical sources and grid equivalents	Detailed synchronous machines with controls & some ideal voltage sources
MMC	Arm equivalent model (model 3)
DC-DC converters	Front-to-front MMCs and ideal DC transformers
Wind parks	Aggregated DFIG models with controls
PV parks	Aggregated models, some with controls
Electrical loads	Fixed impedances
Lines /cables	Wideband models
Simulation time-step	50 μs

Table 4.5 Two area power system specifications

Synchronous Generators			**Loads**			**Lines**	
Label	**Active power (MW)**	**Reactive power (MVAR)**	**Label**	**Active power (MW)**	**Reactive power (MVAR)**	**Label**	**Length (km)**
G1	700	185	Load 7	P7= 967 ΔP7=400	QL=100 QC= 387	5-6	25
						6-7	10
G2	700	235				7-8	110
						8-9	110
G3	719	176	Load 9	P9=1767	QL=100 QC=537	9-10	10
						10-11	25
G4	700	202				7-Ba-B4	50

To assess the performance of the DI method in the real-time environment, it is compared against the Partial Steady-State Initialization (PSSI) method, which is commonly used in some commercial platforms. The PSSI method first performs a conventional AC load-flow to initialize synchronous machines, passive elements, and other components that can be directly solved from steady-state equations. More challenging devices, such as converters, HVDC links, IBRs, or black-box models, are left uninitialized, and a time-domain simulation is then executed until the residual transients naturally dissipate. This approach is efficient and widely adopted for conventional AC systems, where the main part of the network is properly initialized from LF and the remaining uninitialized portion is not significant. However, in large-scale MTDC networks, the situation is different: a substantial share of the system consists of converters and IBRs with complex dynamics, making PSSI less effective. In such cases, prolonged convergence times, sometimes exceeding 100 s, can occur, and transients may propagate into sensitive components. These limitations underscore the

need for alternative methods, such as the DI approach, which provides direct control over subsystem interactions during initialization.

To illustrate the comparative performance between DI and PSSI, Figure 4.25 to Figure 4.31 present the initialization waveforms for several key components of the system. Figure 4.25 and Figure 4.26 shows the active and reactive power of the Vdc-controlled VSC (Cb-A2), which reflects transients from other parts of the network. The DI method suppresses these disturbances effectively, achieving a smooth transition, while the PSSI method results in prolonged oscillations.

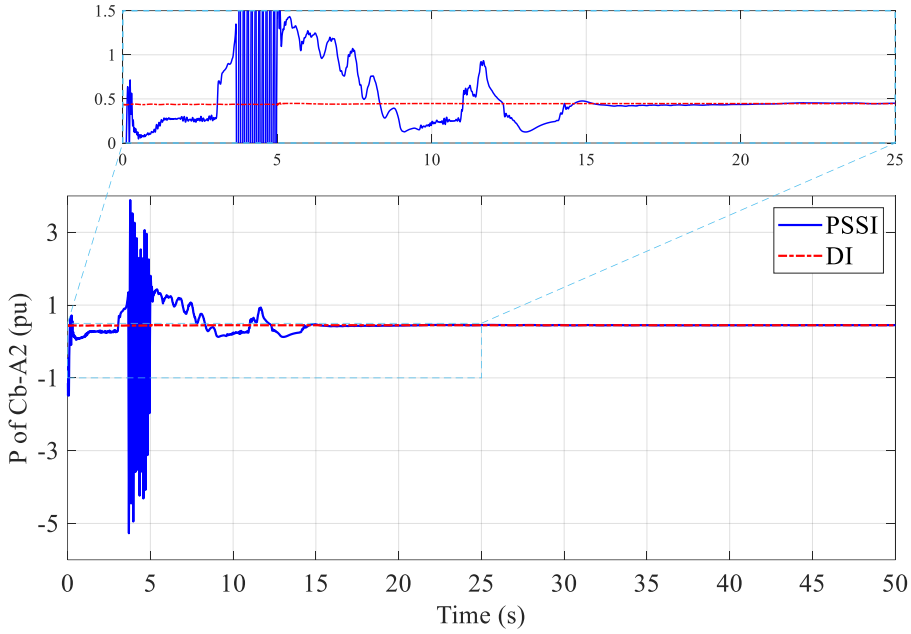

Figure 4.25 Bus Cb-A2 Active power.

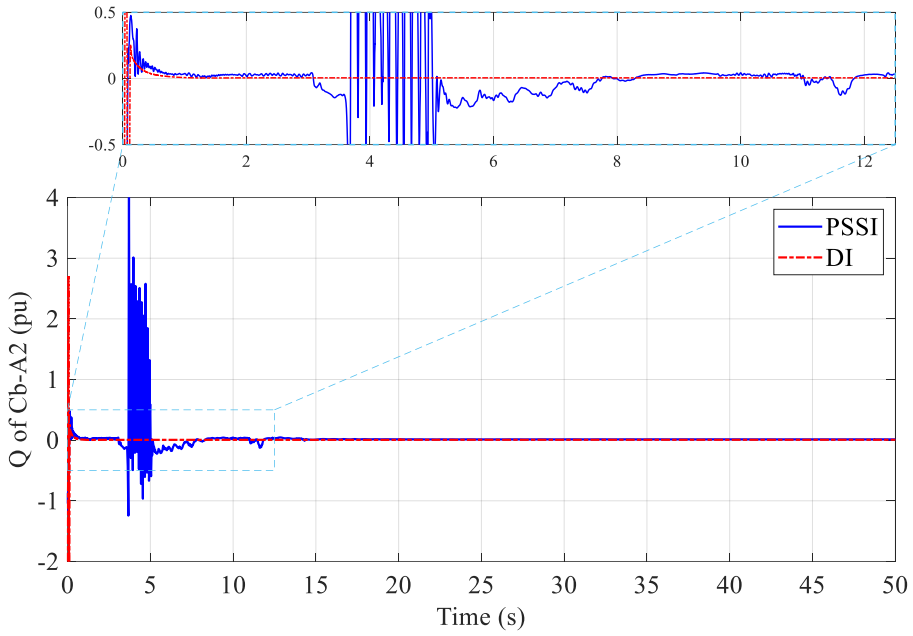

Figure 4.26 Bus Cb-A2 Reactive power.

Figure 4.27 and Figure 4.28 highlight the performance of a P-controlled VSC (Cb-A4), showing similarly improved stability and faster steady-state with DI. Because all VSCs either regulate or interact with the DC link, their collective initialization dynamics are effectively reflected in the DC voltage profile. Figure 4.29 illustrates this behavior at bus Cb-A2, where the voltage trajectory serves as a holistic indicator of system-wide convergence. Any mismatch in control response, instability, or delayed subsystem behavior becomes immediately apparent in this signal, making it a valuable metric for evaluating initialization strategies. With the DI method, the system transitions smoothly to steady-state, and the recoupling event at t = 5 s is clearly identifiable without disturbance. In contrast, the PSSI method exhibits a pronounced voltage overshoot, underscoring the DI method's superior capability to maintain voltage stability and ensure controlled initialization.

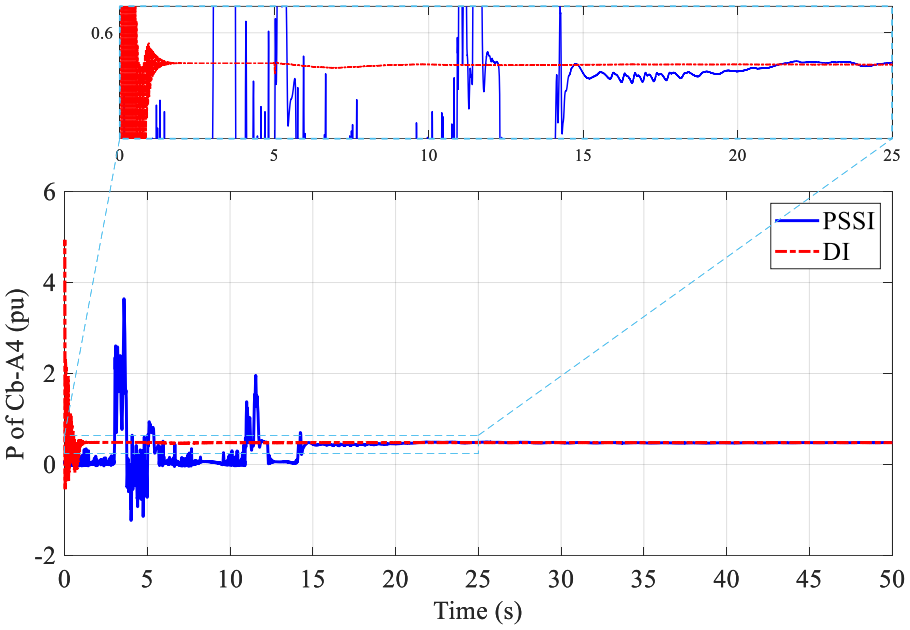

Figure 4.27 Cb-A4 converter's Active power

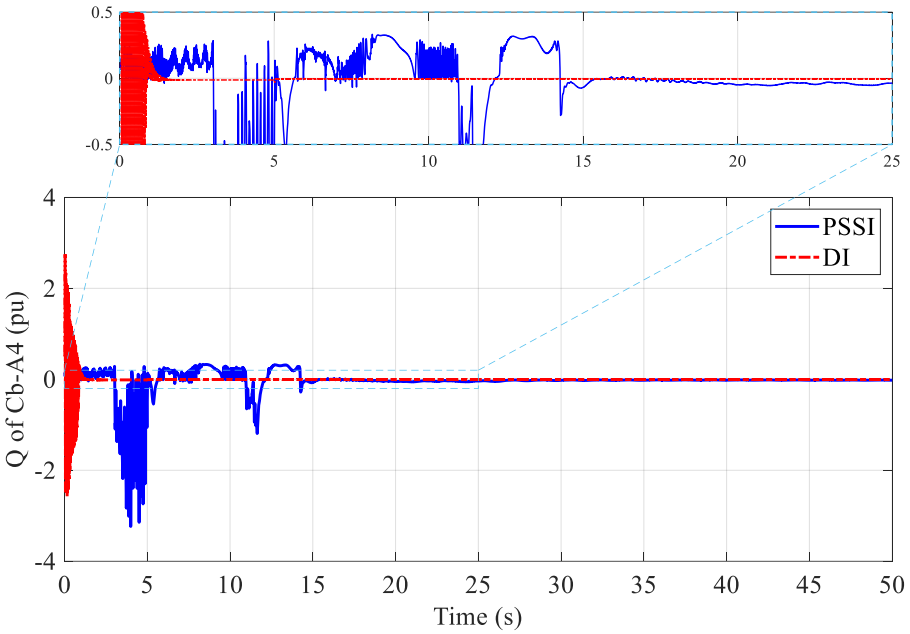

Figure 4.28 Cb-A4 converter's Reactive power

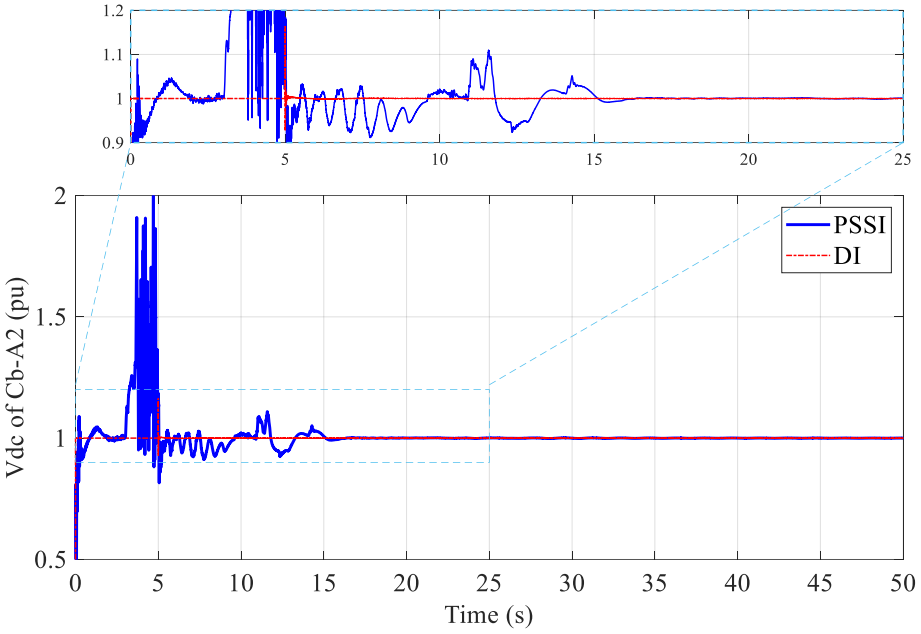

Figure 4.29 DC voltage at bus Cb-A2

Figure 4.30 and Figure 4.31 illustrate the initialization behavior of the synchronous generator G2, which operates as the slack bus in the two-area system. Under the PSSI method, the generator experiences substantial active and reactive power oscillations that persist for nearly 100 s. These oscillations not only highlight the prolonged settling time but also reflect the propagation of disturbances from the DC side into the AC grid during initialization. In contrast, the DI method ensures a smooth startup, with the generator quickly stabilizing at its steady-state power levels within a few seconds and exhibiting minimal overshoot. This clearly demonstrates the DI method's ability to decouple subsystems effectively and protect critical components from cross-area transients during the initialization phase.

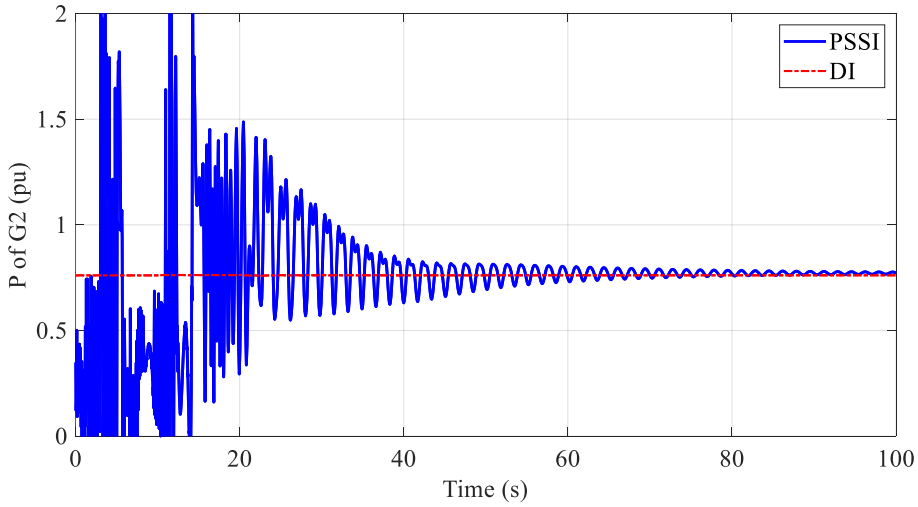

Figure 4.30 G4 (a) Active power (b) Reactive power

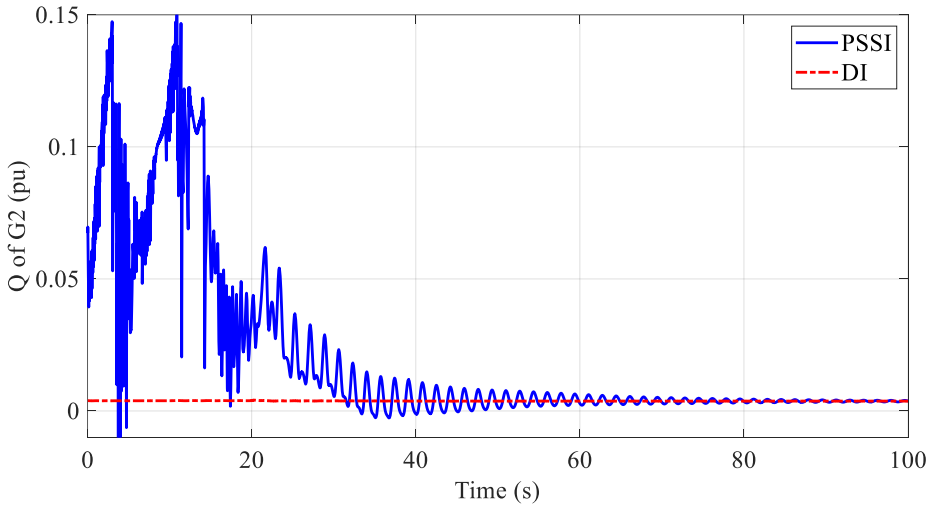

Figure 4.31 G4 (a) Active power (b) Reactive power

4.6 Conclusion

This chapter introduced the DI method, a novel initialization approach designed to enhance both computational efficiency and stability in large-scale MTDC systems. By leveraging load-flow results, the DI method effectively initializes complex control systems while mitigating interactions between subsystems, ensuring a rapid and precise transition to steady-state in time-domain simulations. Unlike traditional techniques, DI does not rely on access to internal control structures, making it especially suitable for black-box models and varied converter control modes.

The performance of the DI method was evaluated using the CIGRE BM1 and BM7 benchmarks within an EMT simulation framework. The results showed that DI drastically reduced initialization time compared to the LFSI method, achieving speedup factors of 20.3 and 16 for BM1 and BM7, respectively. Moreover, DI successfully addressed initialization failure scenarios encountered in BM7, which could not be stabilized using LFSI due to complex converter interactions and system nonlinearities.

To further demonstrate the practicality and adaptability of the DI method, this chapter also presented its extension to real-time simulation environments. Using a modified version of the BM1 benchmark featuring a two-area AC system, the DI method was implemented in a real-time simulation platform. It significantly outperformed the Partial Steady-State Initialization (PSSI) method by achieving complete system convergence within 5 s, compared to over 100 s with PSSI. The DI method also mitigated large transients during recoupling and protected sensitive components, such as wind farms and synchronous generators, from unstable behaviors and protection-triggered disconnections.

The robustness, flexibility, and scalability of the DI framework make it a promising candidate for initializing modern hybrid AC–DC systems in both offline and real-time EMT simulations. However, analysis of DI performance revealed that the initialization of certain inverter-based resources, particularly DFIG-based wind parks, constitutes the main bottleneck due to their relatively slow convergence toward steady-state conditions. Consequently, further enhancement of DI initialization speed could be achieved by specifically targeting and accelerating DFIG initialization. This topic will be explored in detail in the following chapter, which introduces a dedicated strategy for expediting the initialization of DFIG-based wind parks to further enhance overall system initialization performance.

CHAPTER 5 HYBRID INITIALIZATION STRATEGY FOR DFIG-WP MODELS

5.1 Introduction and background

As demonstrated in CHAPTER 4, the DI method significantly enhances the initialization speed and stability of large-scale MTDC systems. Nevertheless, one remaining challenge arises in the initialization of DFIG wind park (DFIG-WP) models. These models tend to require the longest initialization times among system components, typically up to 0.3 s of simulation interval, thereby limiting the overall efficiency gains of the DI methodology.

To address this challenge, this chapter introduces a novel hybrid initialization method specifically designed for DFIG-WP simulation models. The Hybrid Decoupling Interface (HDI) method combines the strengths of the conventional DI method with a non-iterative steady-state calculation of a strategically selected subset of critical control equations. Leveraging LF results, this hybrid approach efficiently initializes both electrical and control variables, significantly expediting the DFIG-WP initialization process without compromising stability or accuracy.

Implemented and evaluated within EMTP®, using only external components and scripts, the HDI method demonstrates substantial computational improvements, achieving up to a 100 times reduction in initialization time compared to conventional methods. Furthermore, it maintains compatibility with aggregated and detailed WP models, making it highly versatile for practical applications and compatible with commercial wind turbine packages. This chapter presents the HDI strategy, including its theoretical basis, practical implementation, and comprehensive performance validation through case studies.

5.2 Overview of initialization burden in DFIG models

The DFIG-WP model, shown in Figure 5.1 (a) features a complex hierarchical control system. It can be categorized into three main control loops:

- Turbine mass model.
- WP controller.
- DFIG bridge controllers.

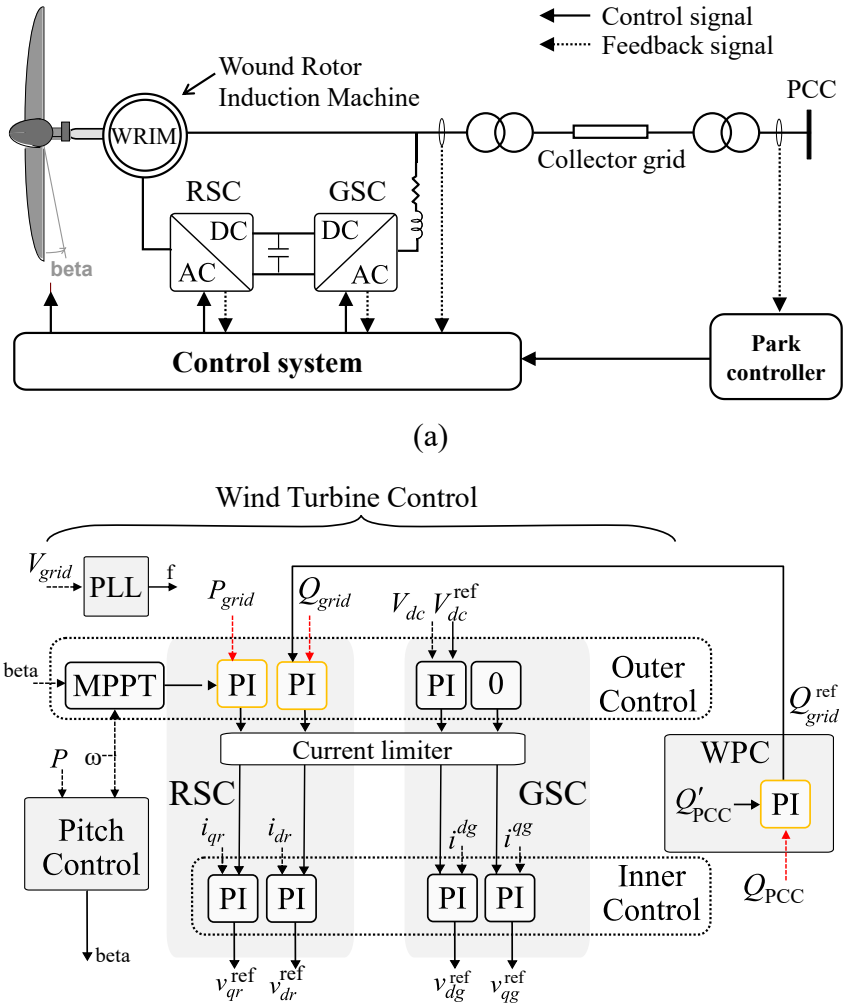

Figure 5.1 Aggregated DFIG-WP model: (a) power layout, (b) control architecture.

The turbine mass model [144] is the slowest among the three, as it represents the mechanical dynamics of the generator. Its correct initialization is essential since errors can lead to torque-speed mismatch, prolonged transients, or even simulation failure. In EMTP®, this loop is initialized reliably using steady-state analysis, obtained during the second stage of the LF-based initialization procedure, as depicted in Figure 3.1.

The WP controller (WPC) governs the reactive power or voltage at the PCC. Acting as the master control loop of the WP, it defines the reactive power reference for the converter bridge controllers. Due to its supervisory role, the WPC has extremely slow dynamics and is often left uninitialized in the steady-state stage. Instead, it converges gradually through time-domain simulation, the last

step in Figure 3.1. While this strategy is sufficient for small-scale or simplified systems, it often results in prolonged convergence times or instability in large-scale or detailed EMT models.

The converter bridge control, comprising the Rotor Side Converter (RSC) and Grid Side Converter (GSC), poses the most significant initialization challenge. These controllers typically implement cascaded control loops, as shown in Figure 5.1.(b). Fast inner current control loops regulate the d–q axis currents. Outer loops then supervise higher-level objectives such as DC-link voltage, active power, or reactive power. In parallel, synchronization modules such as PLLs provide the rotating reference frame needed by the controllers. Stable operation requires precise coordination among these elements. However, standard LF-based initialization provides only terminal voltage and current phasors, which are insufficient to determine internal controller states such as integrator values, feedforward terms, or the memory states of PI controllers.

Without proper initialization, the converter bridge may produce inaccurate reference signals or unstable control actions during simulation startup. This manifests as electromagnetic transients, leading to long convergence times or, in some cases, numerical instability and simulation failure. For this reason, converter bridge initialization is typically deferred to the time-domain stage of the LF-based procedure, as described earlier in Section 3.2 and illustrated in Figure 3.1.

As demonstrated later in this chapter, the proposed hybrid initialization approach mitigates this issue by eliminating the need to initialize each controller loop individually. Instead, it strategically combines partial steady-state initialization with selective decoupling, enabling a fast and stable startup even in detailed EMT models.

5.3 The proposed HDI method

The proposed method consists of two main steps. First, the DI technique is applied internally within the wind turbine model at selected locations, as detailed in this section. Second, a targeted steady-state initialization is performed for key control components to prevent incorrect behavior during startup; this is presented in the following section.

5.3.1 Wind-turbine decoupling

As previously discussed, the converter bridge control is composed of multiple cascaded control loops (Figure 5.1.(b)), each with distinct time constants. These dynamic layers create significant challenges during initialization, particularly when interacting with the machine model.

To mitigate such transients, the DI method, presented in CHAPTER 4, is applied internally within the DFIG schematics. The internal insertion of DI blocks suppresses startup oscillations, prevents unwanted interactions between control loops and the power circuit, and accelerates the time-domain initialization. Two critical spots are identified for the decoupling, corresponding to the main sources of interaction during startup:

- Spot 1 – AC-side decoupling at location A (Figure 5.2):

The machine–converter block is first isolated from the rest of the power system by inserting a DI block at location A. At this point, an AC DI block is used with P and Q constraints, as described in Section 4.3.1.1. This confines the initialization process to a localized segment, preventing dynamic interaction between the machine–converter set and the external grid.

- Spot 2 – (Optional) DC-side decoupling at location B:

The coupling between the machine and the converter bridge is the second source of transients. A DC DI block is inserted at location B, applied across the DC link to address this. In this setup, the RSC and GSC are treated as two separate converters, one constrained with P_{dc} and the other with V_{dc}. Each converter is decoupled using a standard DI block, as outlined in CHAPTER 4.

In this specific configuration (special case), the two DC DI blocks are directly connected, without any intervening lines or components. Thus, the dependent sources mimic the behavior of the independent ones. To simplify the setup, the dependent sources can be removed entirely and replaced with independent ones. This yields a simplified schematic, as shown in Figure 5.3, which is applicable in this special case. By decoupling at location B, the RSC is seen as part of the rotor, while the GSC can be seen as a shunt-connected converter.

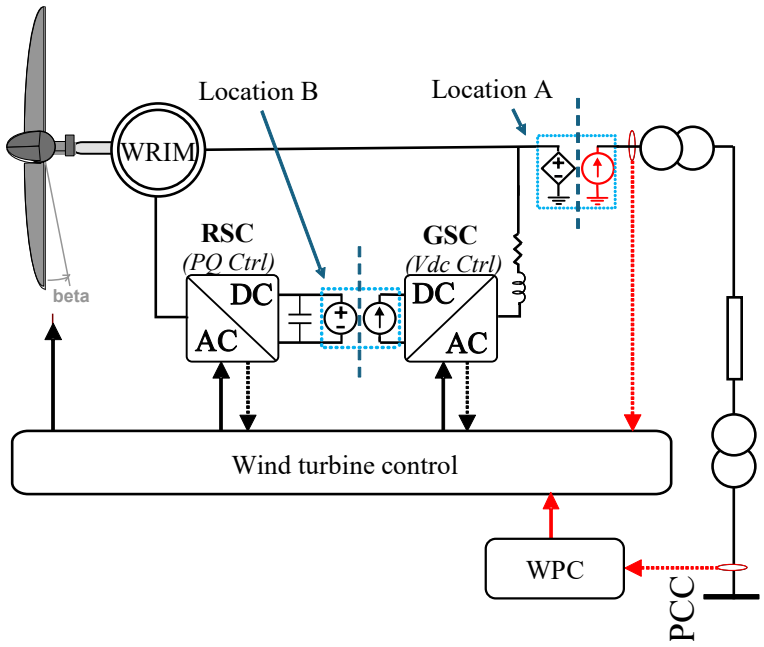

Figure 5.2 The proposed decoupling locations within the DFIG model.

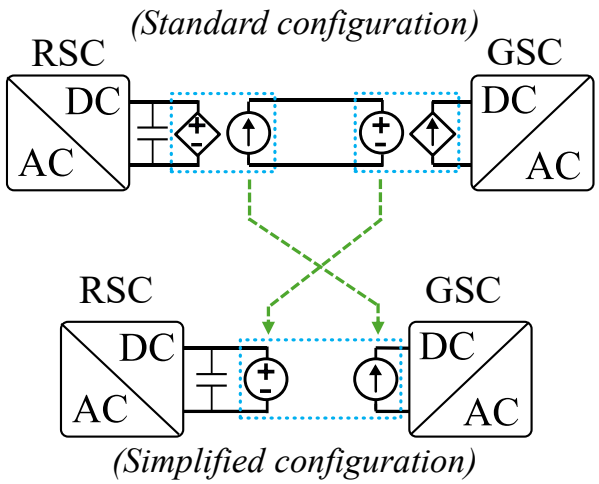

Figure 5.3 Simplified DI configuration within DFIG converter bridge.

However, according to the test cases, both the RSC and GSC were fast enough that decoupling at location B had no measurable impact. Thus, decoupling at location B is offered as an optional step for systems where the RSC or GSC exhibit slow dynamics. This step is not employed in the current work to maintain simplicity.

5.3.2 Other considerations

Applying the DI technique internally, as described above, effectively suppresses the sources of initialization transients. However, the DI method was originally designed for black-box models,

where it is typically applied only at the PCC. This restriction stems from the requirement that the entire control system must remain within the initialization framework, referred to as the TDIS in Section 4.2.1.

If control elements are located within the initialized part of the DI block, ISS, as explained in Section 4.2.1, a critical limitation arises. Specifically, when a controller's feedback signal is sourced from within the ISS, it becomes identical to its setpoint, resulting in a zero-error signal. This condition effectively “freezes” the controller output at an incorrect value, preventing the control loop from functioning as intended.

In our case, internal application of the DI method results in some feedback signals falling within the ISS, as illustrated in Figure 5.2. In particular, at location A, the initialized region includes feedback paths (highlighted in red) that belong to active control loops. Their presence within the ISS corrupts the initialization of the associated controllers. Figure 5.1. (b) highlights the three affected PI controllers, which are:

- The WPC.
- The outer active power controller of the RSC.
- The outer reactive power controller of the RSC.

These controllers rely on fixed feedback signals during initialization, preventing them from responding as intended. In other words, this setup disables both the WPC and the outer loops of the RSC controller during the initialization phase.

To overcome this issue, we propose a hybrid DI approach that incorporates a partial steady-state calculation to support the correct initialization of these vulnerable controllers. This method restores proper control behavior without requiring full-time-domain convergence. The technical details of this hybrid strategy are presented in the following section.

5.4 Partial steady-state control initialization

This section presents simplified initial condition calculations for selected controllers. Here, the focus is on simplified and approximated initialization, as any small discrepancies are expected to be corrected during the subsequent time-domain simulation.

The targeted control modules are the controllers whose feedback signals reside within the ISS and are thus prone to freezing when the DI method is applied internally. In this work, only three

controllers meet this criterion: the WP controller and the RSC's outer active and reactive power controllers, since the steady-state initialization is applied only to a subset of the WP controller loops.

5.4.1 WPC

The WPC, shown in Figure 5.1. (b), requires explicit initialization, as it receives Q_{PCC} as a feedback signal from the PCC. By inserting a decoupling interface at Location A in Figure 5.2, the PCC becomes part of the ISS created by the red current source.

The WPC regulates the reactive power exchanged at the PCC by computing a reactive power reference for the stator side of each DFIG unit. To initialize this controller, the reference output must be set to match the stator's steady-state reactive power, which is derived from the LF solution:

$$H_{WP} = Q_S \tag{0.46}$$

Where H_{WP} is the initial condition of WPC and Q_S is the reactive power at the stator of the machine. Therefore, WPC can be directly initialized from the LF solution.

5.4.2 RSC's outer control q-axis channel

The q-channel of the RSC controller, shown in Figure 5.1. (b), regulates the grid-side active power (P_{grid}), by computing the reference value of the rotor q-axis current (I_{qR}^{ref}). Consequently, this PI controller can be initialized by determining the steady-state value of I_{qR}^{ref} . Where P_{grid} is measured at the location shown in Figure 5.4.

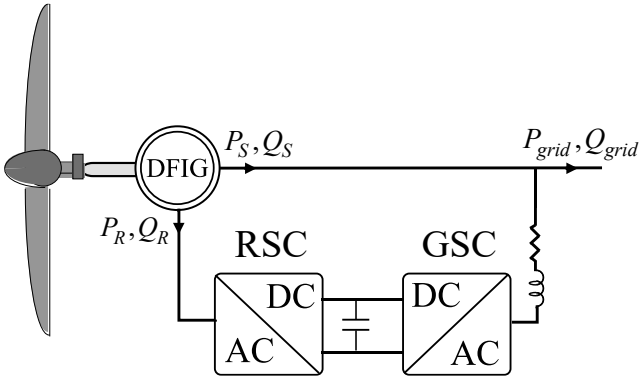

Figure 5.4 DFIG wind turbine schematic.

Since the control is based on vector-oriented principles, the active power injected by the rotor side of the machine (P_R) can be written as:

$$P_R = -V_{qR} I_{qR} \tag{0.47}$$

Where V_{qR} and I_{qR} are the q-axis rotor voltage and current, respectively. All quantities are expressed hereafter in pu. Under steady-state conditions, the reference current value at the q-axis (I_{qR}^{ref}) can be set equal to the actual rotor *q*-axis current:

$$I_{qR}^{ref} = I_{qR} = -\frac{P_R}{V_{qR}} \tag{0.48}$$

Using the generic DFIG relationships from [144], the rotor active power can be expressed as a function of the grid-side power P_{grid} :

$$P_R = -sP_S \tag{0.49}$$

where *s* denotes the machine's slip. The stator-side active power (P_S) is expressed as:

$$P_S = \frac{P_{grid}}{1-s} \tag{0.50}$$

Substituting (0.49) and (0.50) into (0.48) gives:

$$P_R = \frac{-sP_{grid}}{1-s} \tag{0.51}$$

To simplify the expression, we approximate $V_{qR} \approx sV_S$ in steady-state conditions, where V_S is the stator voltage. This is valid when rotor quantities are referred to the stator side. Then (0.48) can be substituted in (0.51) and rewritten in terms of I_{qR}^{ref} as:

$$H_{RSCq} = I_{qR}^{ref} = \frac{P_{grid}}{V_s\left(1-s\right)} \tag{0.52}$$

where H_{RSCq} represents the initial value that should be set to the PI controller. Note that this approximation assumes all rotor quantities are referred to the stator side.

5.4.3 RSC's outer control d-axis channel

The d-channel of the RSC controls the reactive power at the grid side (Q_{grid}). The outer control of this channel finds the reference value of the rotor d-axis current (I_{dR}^{ref}). Consequently, this PI controller can be initialized by determining the steady-state value of I_{dR}^{ref}.

This formula is derived in [145] as

$$Q_s = \left(\frac{\omega \lambda_{ds}}{L_{ls} + L_M} \right) \left(\lambda_{ds} - L_m I_{dR} \right) \tag{0.53}$$

In this expression, ω denotes the synchronous electrical angular frequency, λ_{ds} is the stator d-axis flux linkage, L_{ls} represents the stator leakage inductance. The term L_M refers to the magnetizing inductance in the dq frame, while L_m denotes the mutual inductance between the stator and the rotor circuits.

In steady-state, all machine variables in this formula are time-invariant [145] and can be written as:

$$Q_s = K_1 + K_2 I_{dR}^{ref} \tag{0.54}$$

where K_1 and K_1 are constants. More details can be found in [145]. Finally, the initial condition of the PI controller (RSC's outer - d-axis controller) can be written as:

$$H_{RSCd} = I_{dR}^{ref} = K_3 + K_4 Q_s \tag{0.55}$$

These machine constants can be either calculated using (0.53) or can be obtained practically by a simple test.

5.5 Implementation in EMT software

The proposed method can be implemented in any EMT-type software using the same steps described earlier. First, the P-constrained DI block, Figure 4.14.(a), is inserted at Location A of the DFIG model shown in Figure 5.2. Figure 5.5 provides a screenshot of the DFIG wind-turbine model in EMTP, highlighting the location where the DI block is added.

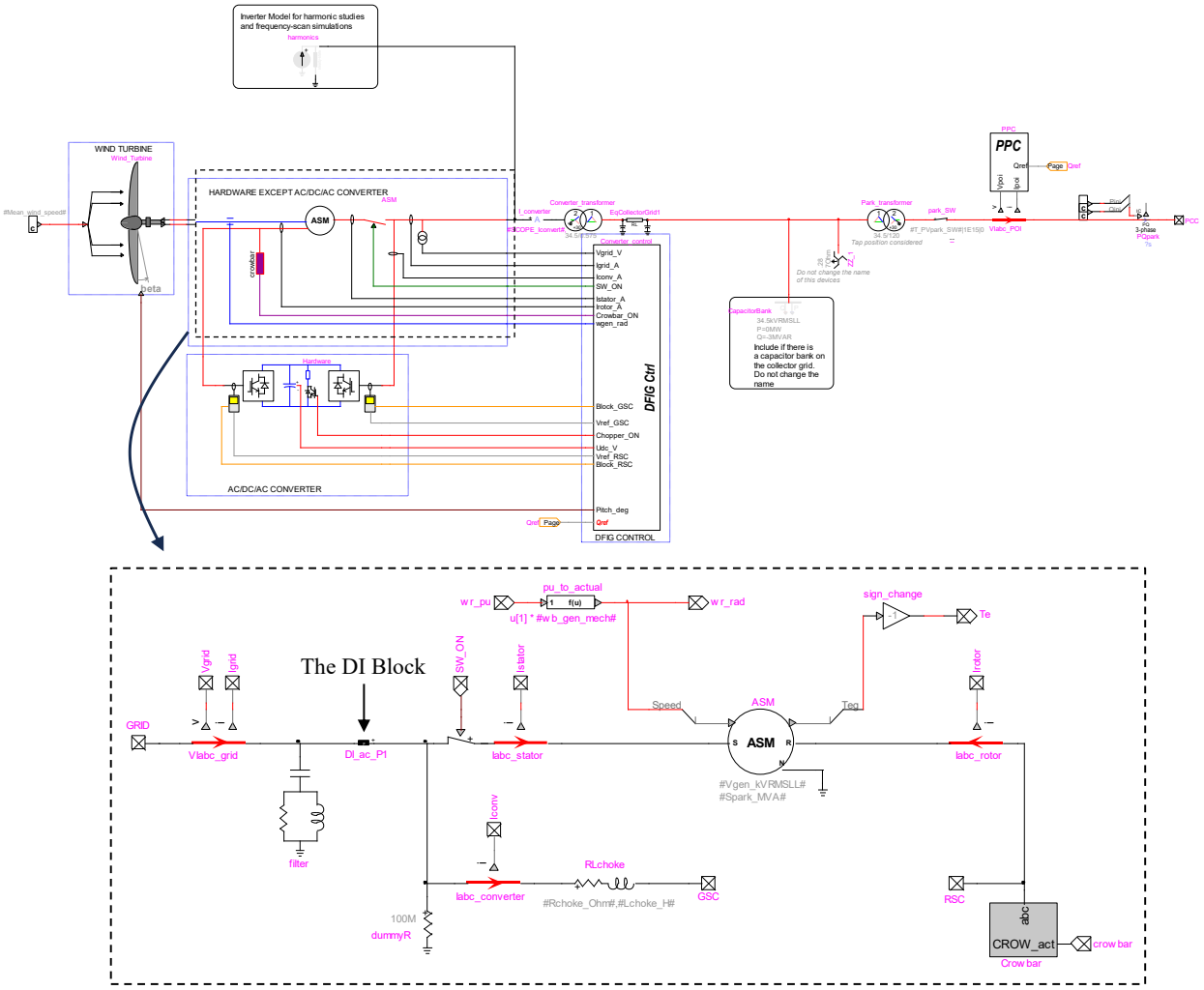

Figure 5.5 EMTP® schematic of DFIG model with DI at machine terminals.

Secondly, the three selected PI controllers described in Sections 5.4.1-5.4.3 are initialized by assigning their initial values according to (0.46), (0.52), and (0.55) as shown in Figure 5.6. These values are automatically computed using scripting.

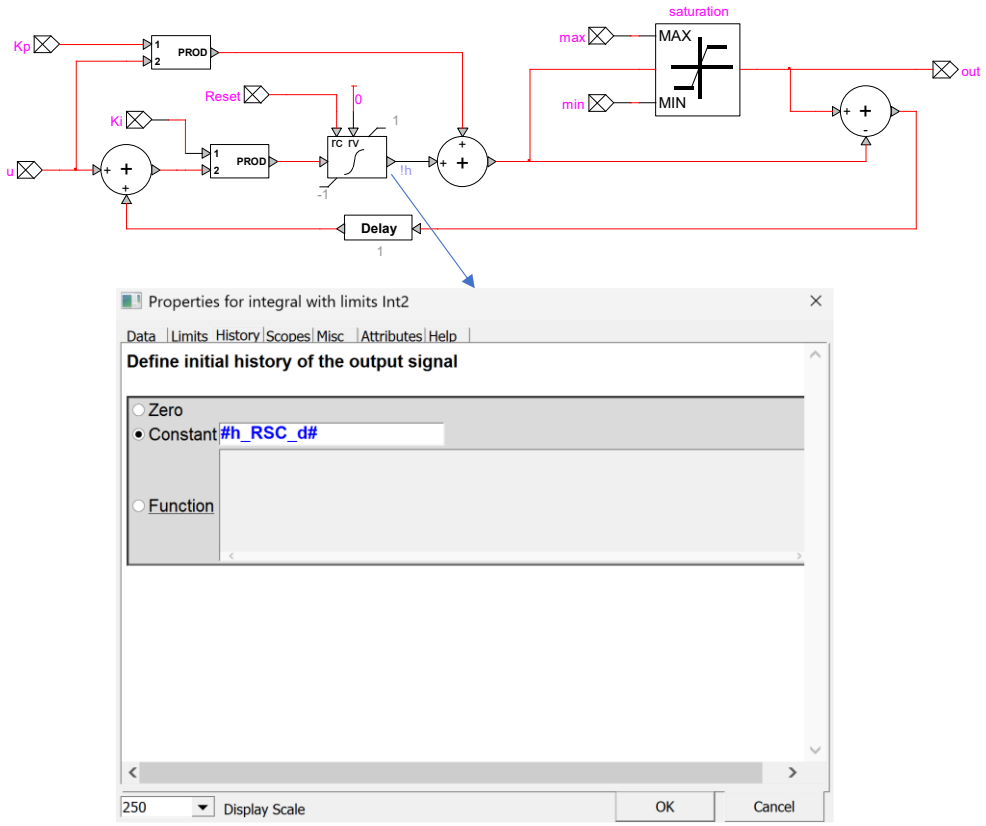

Figure 5.6 EMTP® PI controller showing LF-based integral initialization.

5.6 Performance evaluation

This section evaluates the performance of the proposed initialization method by comparing it to a conventional LF-based initialization approach used as a baseline. The comparison focuses on two key aspects, namely the simulation interval required to reach steady-state convergence and the total CPU runtime.

To assess the effectiveness of the proposed method, two test cases were considered based on the EPRI system in Figure 5.7 from EMTP® software:

- A. Test Case 1: A simplified WP system using an aggregated DFIG model.
- B. Test Case 2: A large-scale WP composed of 45 individual DFIG units grouped into three feeders.

In both cases, the simulations are conducted using the EMTP® software [5], with an Average Value Model for converters. The simulations use a 50 µs time step, and a steady-state condition is defined

as the point at which waveform variations remain within 1% of the LF reference values. All cases are executed on an Intel(R) Core (TM) i7-13800H processor, ensuring consistent computational conditions for performance comparison. Both simulation files are provided in the folder *"Chapter 5/"*, included in the supplementary material.

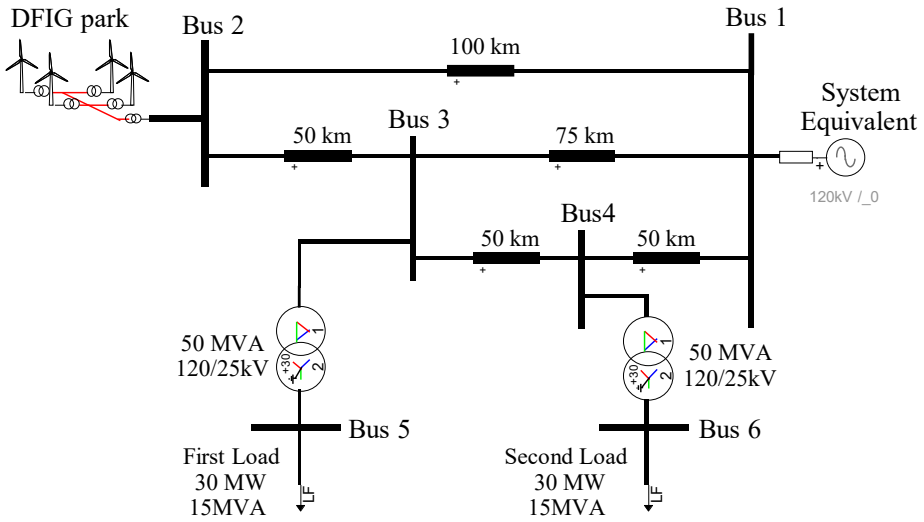

Figure 5.7 Single-line diagram of EPRI benchmark system.

Further simulation and modeling details, including the number of nodes, control devices, and model configurations, are summarized in Table 5.1

Table 5.1 Simulation and model details for test cases I and II.

Simulation detail/ model	**Test case 1**	**Test case 2**
WP model	Aggregated WP	Detailed WP
Control structure	Aggregated control	Individual control system per wind turbine
Collector system	Aggregated equivalent PI line	detailed system using PI lines (Figure 5.10)
Simulation nodes	12	122
Control devices	122	12121
Time-step (µs)	50	
Electrical source model	Voltage sources with impedance	
Transmission line model	Constant parameter model	
Simulation interval	Until steady-state is reached (1% criterion)	

5.6.1 Test case 1: 120 kV system with aggregated DFIG park model

The 120-kV/60-Hz EPRI benchmark system, using an aggregated DFIG-WP model, is simulated to study the independent impact of initialization strategies on simplified models. Its topology is shown in Figure 5.7 [146]. In the baseline LFSI method, an auxiliary source is connected at the PCC during the early stage of simulation and disconnected at t=0.5 s. The measurement setup is illustrated in Figure 5.8, where active and reactive power are recorded at two locations: LFSI_External (PCC, including the auxiliary injection) and LFSI_WP Internal (measured inside the wind-park model). For steady-state assessment, the same criterion as in the previous chapters is applied, namely, within ±1% of the LF results.

In contrast, all auxiliary sources are removed earlier in the proposed HDI method, with recoupling triggered at t=0.15 s. Figure 5.9 presents the active and reactive power at the PCC for both methods. The times to reach steady state are 0.65 s and 0.15 s for LFSI and HDI, respectively, corresponding to 3.76 s and 0.92 s of computation time. From an EMT perspective, HDI achieves a fourfold reduction in computational cost while maintaining stability. A summary is given in Table 5.2.

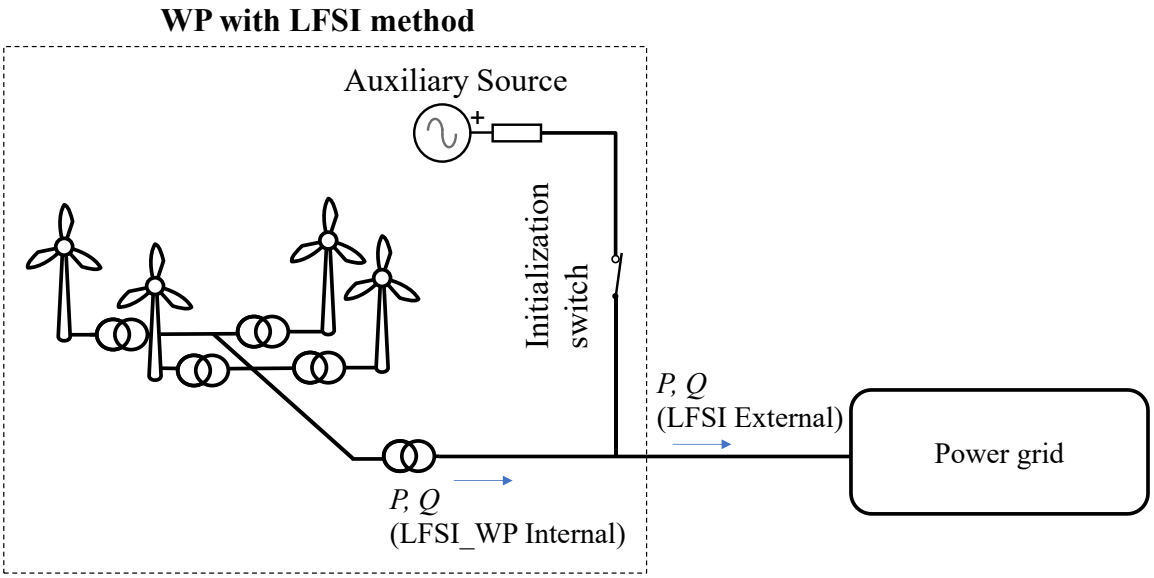

Figure 5.8 Measurement points for active/reactive power under LFSI initialization.

Table 5.2 Comparison of LFSI and HDI methods from a computational perspective

Test Case	Initialization method	Simulation interval (s)	Computation time (s)
1	LFSI	0.65	3.76
	HDI	0.15	0.92
2	LFSI	12.67	6760 (≈**1.87** hours)
	HDI	0.15	78.6 (≈**1.3** minute)

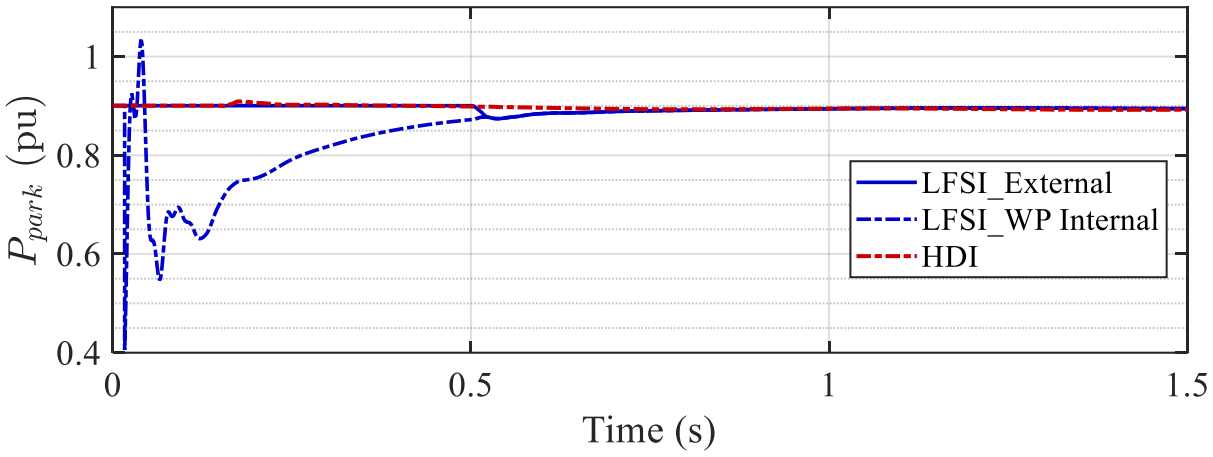

(a)

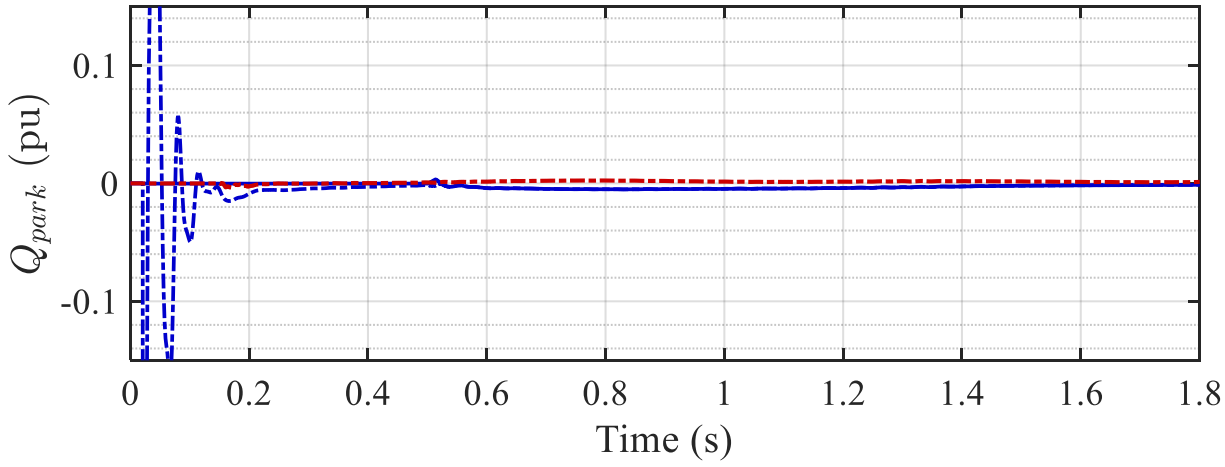

(b)

Figure 5.9 Park-level results, test 1: (a) P at PCC, (b) Q at PCC, LFSI vs HDI.

5.6.2 Test case 2: 120 kV system with detailed DFIG park model

This test case evaluates the proposed initialization strategy on a fully detailed DFIG-WP model. This test case is taken from EMTP®. The system comprises 45 individual DFIG units, connected to the PCC transformer through three feeders containing 18, 12, and 15 turbines, respectively. The layout of the WP, including the internal feeder configuration and transformer connections, is shown in Figure 5.10.

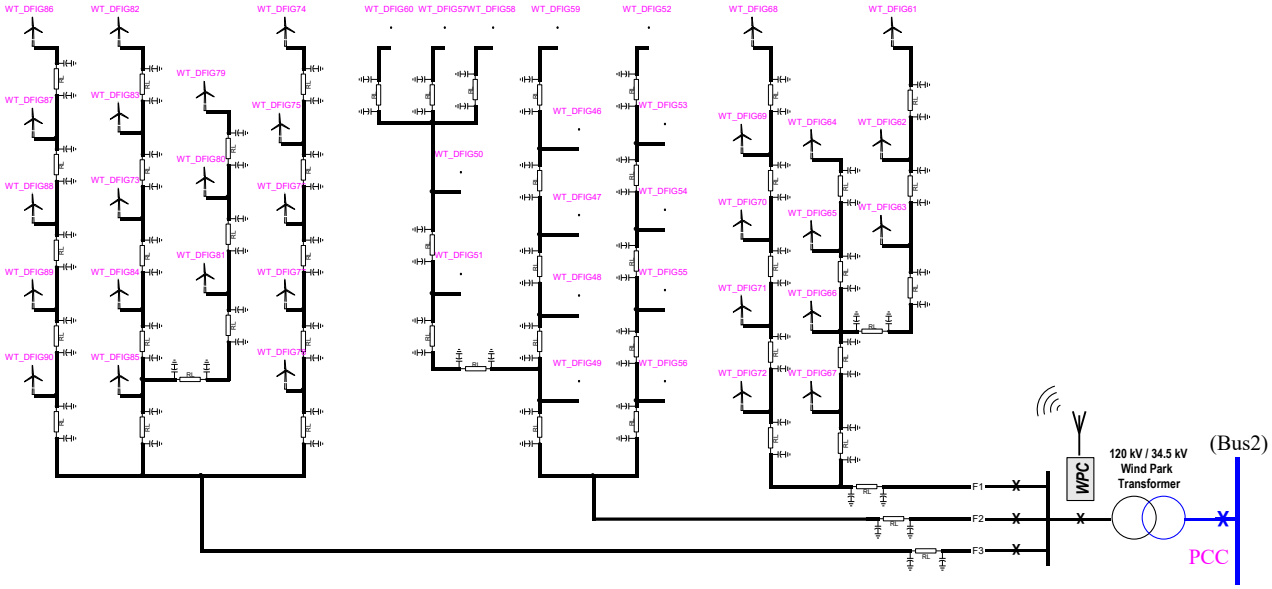

Figure 5.10 Test 2: single-line diagram of detailed DFIG-WP (three feeders, 45 turbines).

In both the LFSI and proposed HDI methods, initialization is applied individually to each wind turbine, ensuring full electrical decoupling and preventing machine-to-machine interactions during startup. However, the two methods differ fundamentally in how they handle the initialization of internal controller states, particularly in DFIG outer loops responsible for regulating active and reactive power.

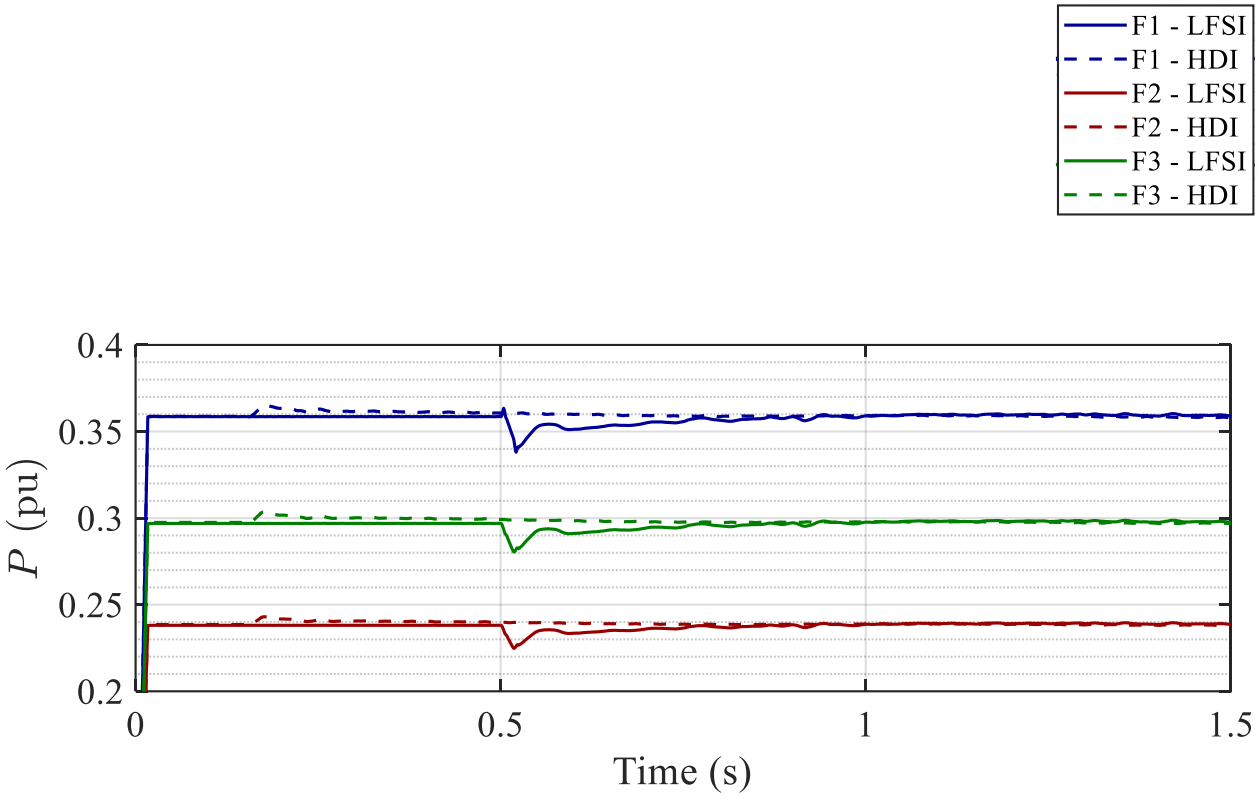

(a)

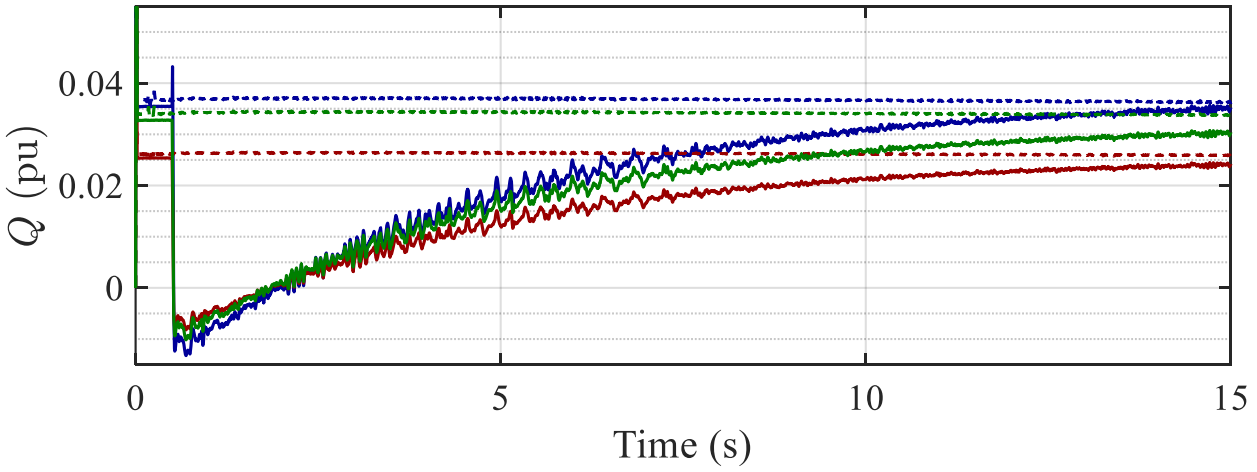

(b)

Figure 5.11 Feeder-level results, test 3: (a) P, (b) Q across feeders, LFSI vs HDI.

The impact of these differences can be observed at the feeder and WP levels. Figure 5.11 presents the initialization performance for each feeder, showing the active and reactive power responses under both methods. Notably, both LFSI and HDI start from the same steady-state operating point, consistent with the LF solution. However, in the LFSI case, once the auxiliary sources are

disconnected at $t = 0.5\ s$, the effects of improper controller initialization begin to surface. The absence of pre-initialized values for the WP and the d-axis current references within each DFIG leads to control mismatches and uncoordinated responses across feeders.

Each feeder exhibits distinct reactive power transients under LFSI, ranging from steep overshoots to prolonged drifts, as the controllers attempt to recover and stabilize in the time domain. These discrepancies are especially amplified in feeders located farther from the PCC, where the electrical distance further challenges the system's ability to self-correct.

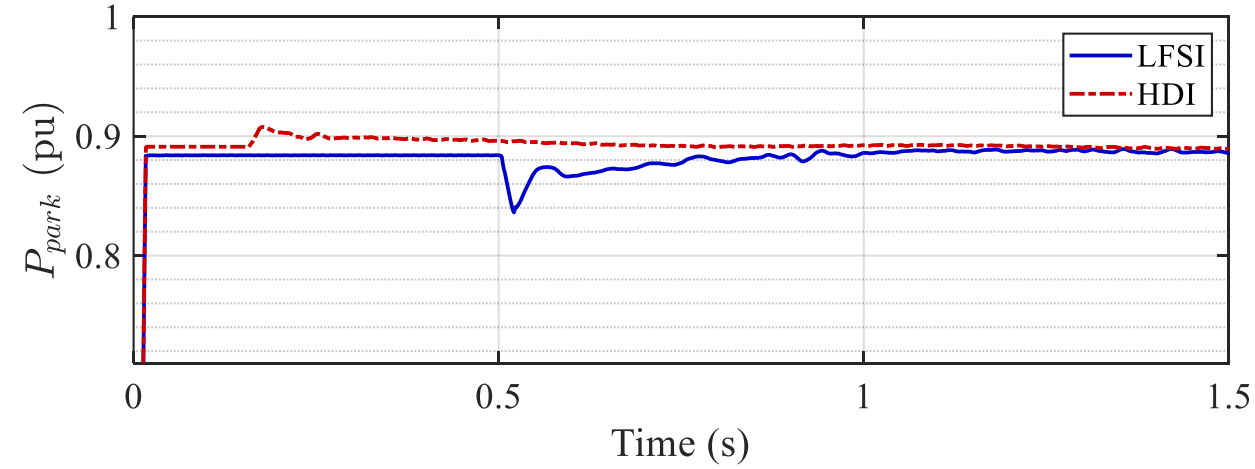

(a)

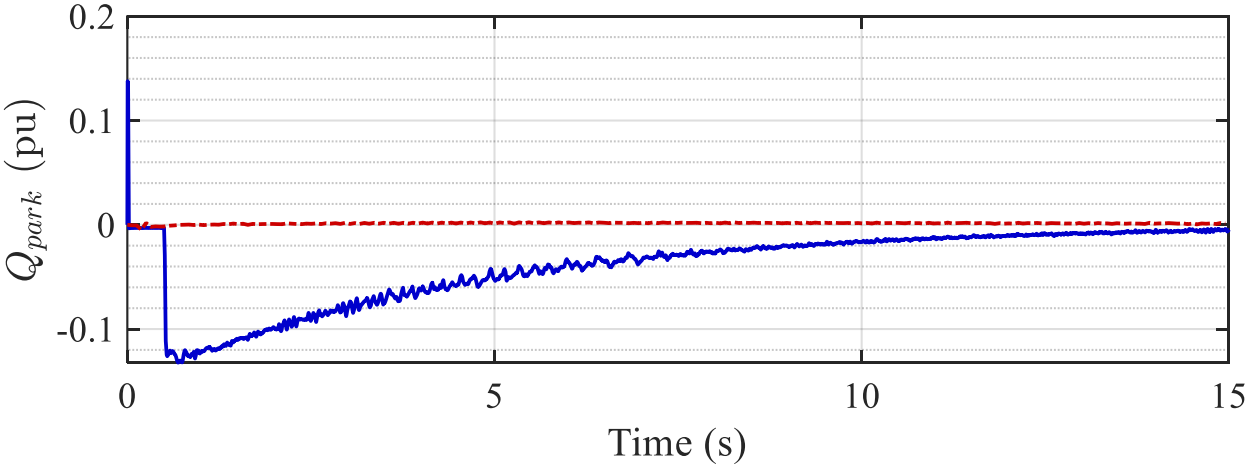

(b)

Figure 5.12 Park-level results, test 3: (a) P at PCC, (b) Q at PCC, LFSI vs HDI.

In contrast, the HDI method, through its partial steady-state initialization, ensures consistent internal control states from the outset. As a result, all feeders exhibit fast, coordinated, and smooth convergence of reactive power, regardless of their location in the network.

Figure 5.12 illustrates the overall system response. Subfigure (a) shows the total active and reactive power at the PCC under both initialization methods, with the response consistent with the behavior observed in the aggregated test case (Test Case 1). Subfigure (b) highlights a more pronounced difference in reactive power convergence. Under LFSI, the response is characterized by delayed settling exceeding 12 s, accompanied by visible oscillations and slow ramping. This slow response is due to improper initialization of the d-axis current controllers and the WPC. While the initial conditions were consistent with the LF solution, the absence of correctly initialized control states causes reactive power to deviate significantly as the system evolves dynamically.

In contrast, the HDI method ensures stable operation, matching the behavior of the aggregated system, and reaches steady-state within a 0.15 s simulation interval. As summarized in Table 5.2, the CPU times corresponding to these initialization intervals are 6760 s and 78.6 s for LFSI and HDI, respectively, representing a nearly 100 times improvement in computational speed.

5.7 Conclusion

This chapter presented a hybrid initialization method for DFIG-based wind parks (WPs), combining decoupling interfaces with partial steady-state control initialization. The approach specifically targets controllers affected by the internal DI application, including the WPC and the outer loops of the RSC. By selectively initializing key PI controllers and applying DI only at critical points, the proposed method achieves fast and stable simulation startup.

Case studies demonstrated that the hybrid method significantly improves initialization accuracy and reduces computational burden. In aggregated and detailed test systems, the method consistently reduced the simulation interval required to reach steady-state and achieved up to 100 times reduction in computational time compared to traditional LFSI. The results confirm that the proposed strategy offers a robust, scalable solution for initializing large-scale WP EMT models.

CHAPTER 6 ADAPTING AND EVALUATING ACCELERATION TECHNIQUES TO MTDC SIMULATION MODELS

6.1 Introduction and background

As HVDC and MTDC systems continue to grow in complexity, the computational demands of their EMT simulations increase accordingly. While some acceleration methods are specifically tailored to HVDC applications, many of the most impactful techniques are general-purpose, aimed at enhancing EMT performance across a broad range of power system models. This chapter focuses on the application and evaluation of such generic acceleration strategies within HVDC and MTDC simulation contexts.

One effective approach is Transmission Line-Based Parallelization (TLP), which exploits the inherent propagation delays in transmission lines to partition the network into decoupled subsystems that can be simulated concurrently [92]. TLP has demonstrated strong potential for enabling distributed simulation without compromising accuracy.

A key finding of this chapter is that control systems constitute a major share of the computational burden in HVDC simulations. To address this, two control-oriented acceleration methods are investigated. The first is Control System Parallelization (CtrlP), which distributes control computations across multiple processors. This includes implementations based on the Functional Mock-up Interface (FMI), allowing modular and scalable simulation of complex control architectures [147].

Beyond parallel execution, modifying the control system solution method itself offers further opportunities for performance improvement. Conventional control solvers often rely on a sequential approach that introduces artificial one-time-step delays to break feedback loops. Although this technique is not mathematically rigorous, it can still provide acceptable results in some cases, particularly with small integration time steps. However, in large-scale systems dominated by IBRs and power electronics, it may introduce numerical instabilities. Such stability issues, particularly in sensitive control subsystems, have been documented in [148].

To overcome this limitation, simultaneous solvers using Jacobian-based iterations have been proposed to eliminate these delays [148]. However, the computational cost of iterative Jacobian methods can become prohibitive when scaling up to large MTDC networks. As a more efficient

alternative, non-iterative Jacobian (NIJ) approaches [148] have been developed, using linearization at each time step to resolve feedback interactions without iteration. While NIJ achieves a good trade-off between accuracy and performance, further efficiency gains can be obtained through reduced Jacobian formulations which lower computational demands while maintaining numerical robustness [149]. To that end, Optimized Sequential Control Solvers (OSeqCtrl) have been introduced [150], specifically targeting systems with dense control structures. These solvers enhance computational efficiency by selectively optimizing the order and execution of control tasks, demonstrating significant simulation speedups without compromising numerical stability. They do not require user intervention and should be used with caution.

This chapter evaluates the performance of TLP, CtrlP, and OSeqCtrl, which have been proposed in the literature. In this work, the methods are not re-developed but rather applied and systematically assessed in the context of MTDC systems. Each technique is first tested, profiled, and analyzed on a small-scale point-to-point HVDC model, then applied to the InterOPERA benchmark system [138], which serves as a representative large-scale MTDC network. Furthermore, hybrid approaches that combine both network-level and control-level acceleration techniques are explored to assess their combined benefits.

6.2 Parallel computing

6.2.1 Transmission Line based Parallelization, TLP

In large-scale EMT simulations, network parallelization leverages the natural decoupling effect of transmission lines, where propagation delays allow different network segments to be simulated in parallel. This approach can significantly reduce the computational burden.

In [92], the FMI is used as an interoperability standard with a master-slave configuration to create a co-simulation setup of multiple simulation instants. This allows parallel execution of decoupled subsystems using transmission line propagation delays. Therefore, it is particularly effective for networks involving long transmission lines and multiple IBRs, where the computational load can be offloaded across parallel simulation instances. The communication protocol for synchronizing parallel instances is established using low-level primitives. This setup enables efficient and scalable simulations without compromising accuracy.

6.2.1.1 Performance evaluation

The TLP technique introduced in [92] is applied to the test system modelled using EMTP® [5] as illustrated in Figure 6.1. The benchmark model features a bipolar MMC-based point-to-point HVDC link, incorporating two MMCs for the collection and export of offshore wind power. A detailed description of the system components and simulation parameters is provided in Table 6.1.

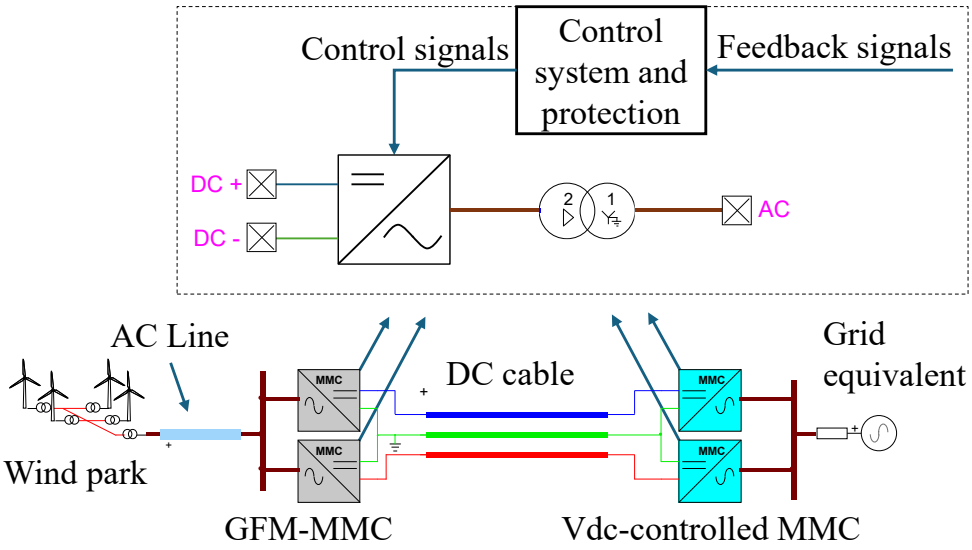

Figure 6.1 Bipolar point-to-point HVDC test system.

The system is partitioned into three subsystems using the existing transmission lines as natural decoupling boundaries. As shown in Figure 6.2, the system is decoupled using master–slave FMI configurations, implemented with Functional Mock-up Units (FMUs). Each FMU is simulated in parallel on a dedicated CPU core within EMTP® [5].

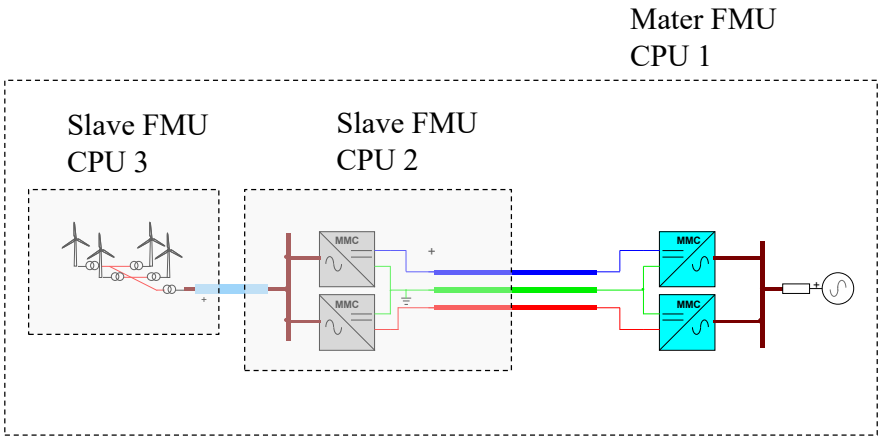

Figure 6.2 TLP application on the HVDC system in Figure 6.1.

Simulations were executed on an Intel® Xeon® Gold 6258R processor. The computational performance is summarized in Table 6.2, which compares the TLP-enhanced simulation to the default serial execution (Ser). Both configurations employ the same control solver in EMTP®, which implements the Non-Iterative Jacobian (NIJ) method [5]; thus, the simulations are labeled as TLP_NIJ and Ser_NIJ, respectively.

Table 6.1 Simulation and model details for the HVDC system in Figure 6.1.

Aspect		**Details**
Component model	**Grid equivalents**	Voltage sources with impedance
	MMC	Generic 401-level, half-bridge, arm equivalent model (Model 3) [141]
		GFM-MMC operates in V/f control mode. More details about V/f and Vdc-control can be found in [2].
	Wind parks	Generic aggregated DFIG models with controls.
		Contains 1200 wind turbines, 1.5 MW each.
	Lines /cables	Wideband models [22]
		DC cable: 70 km, ±640 kV
Simulation details	**Total number of simulation nodes**	318
	Total number of control devices	3617
	Simulation interval (s)	10
	Time-step (µs)	50

Decoupling the system using TLP allows the simultaneous execution of control and power system tasks across processors. This intrinsic parallelism yields significant gains in computational efficiency. Notably, the control system experiences the most pronounced improvement, with a speedup factor of 2.1 compared to Ser_NIJ. The power system solution also benefits, achieving a speedup factor of 1.5. Since the control system accounts for approximately 87% of the total simulation time, its acceleration is the primary driver of overall performance, culminating in a total simulation speedup factor of 2.0. The accuracy of TLP is thoroughly validated in Section 6.4.2.

The results highlight that TLP is especially effective in systems where control computations dominate. However, its potential impact can be even greater in models where the power system equations constitute a more significant portion of the load. Given the current control-heavy computational profile, the following sections focus on further accelerating the control system solution to unlock additional performance gains.

Table 6.2 Computational performance comparison, TLP

Equations	Ser_NIJ simulation time (s)	TLP_NIJ simulation time (s) 3 CPUs	Speedup factor
Power system	27.1	18.1	1.5
Control system	188.5	87.7	2.1
Total simulation	215.6	105.8	2.0

6.2.2 Control system parallelization, CtrlP

While the TLP method proves highly effective in systems rich in transmission lines, it is often insufficient on its own for achieving optimal performance in large-scale EMT simulations, particularly when control systems introduce a substantial computational burden. In both compact and large-scale HVDC networks, solving control system equations, especially those associated with IBRs, represents a major share of the overall simulation cost. As a result, accelerating the control system solution becomes essential for enhancing simulation efficiency. This chapter focuses on generic IBR models.

An effective strategy for addressing this challenge is the parallel execution of control systems, as explored in [147] using a co-simulation-based framework. EMT simulators typically alternate between solving power system and control system equations, introducing a one-step time lag between the two domains. In MTDC systems, control architectures are often modular and repetitive. For example, each MMC in Figure 6.1 hosts an identical control system. Because these control modules operate independently at each discrete time step, their solutions can be parallelized across multiple CPU cores. Assigning each control instance to a dedicated processor (e.g., using four CPUs) allows the workload to be distributed effectively, resulting in a noticeable reduction in simulation time. This same principle applies to IBR systems composed of multiple units.

To facilitate applying this concept, [147] proposes the use of the FMI standard within a master-slave architecture. In this configuration, each control module is encapsulated as a slave FMU, with a central master responsible for coordinating synchronization across simulation steps.

Some IBRs also feature internally decoupled control branches, which opens further opportunities for parallelization. For example, the DFIG model in Figure 6.3 includes separate control loops for

the RSC, GSC, and pitch control. These branches can be simulated in parallel to improve performance. However, to maintain balanced CPU usage, it may be advantageous to group the more computationally demanding RSC and GSC controls together, as illustrated in Figure 6.3.(b). This ensures a more even distribution of the computational load across available processors.

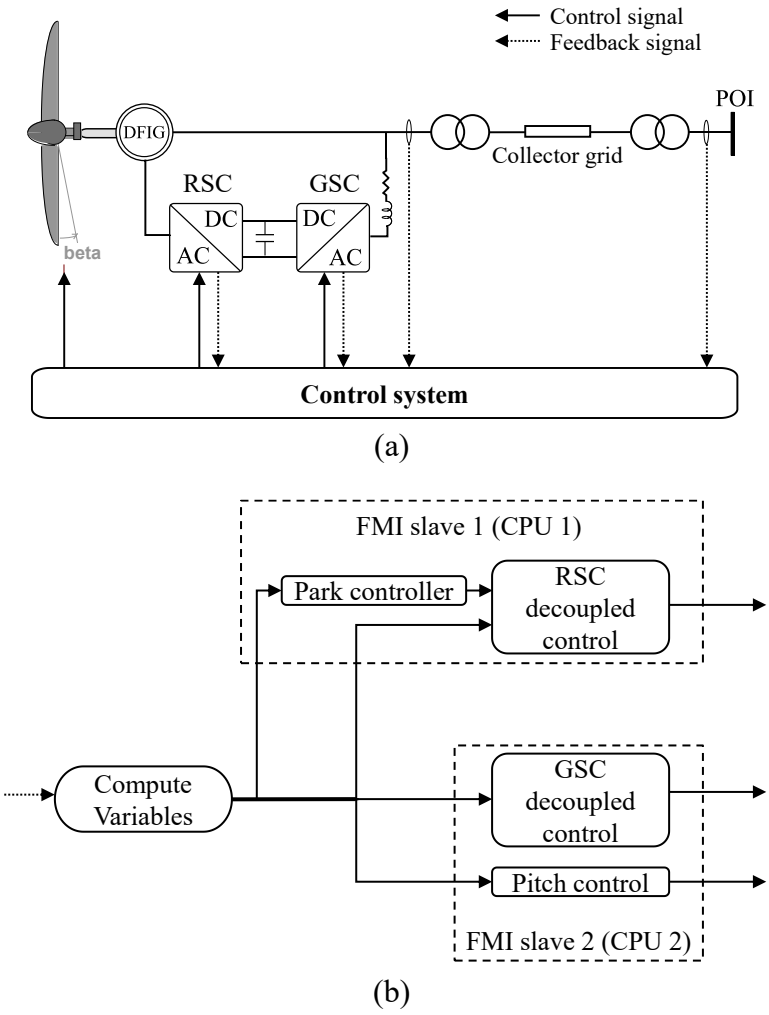

Figure 6.3 (a) DFIG model and its (b) Control system.

6.2.2.1 Performance evaluation

The effectiveness of the CtrlP approach is evaluated using the system shown in Figure 6.1 within the EMTP® simulation environment [5]. In this setup, the control systems of each MMC converter are assigned to separate CPU cores, while the wind park controller is partitioned and distributed across two slave FMUs. This parallel configuration utilizes a total of six CPU cores, with all simulations employing EMTP®'s default (NIJ) control solver [148].

As reported in Table 6.3, CtrlP delivers a substantial boost in computational performance. The control system runtime is reduced dramatically, from 188.5 s to 37.5 s, representing a 5.02 speedup in control-related computations. This improvement directly translates into a significant reduction in overall simulation time, which drops from 215.6 s in the serial NIJ case (Ser_NIJ) to just 64.6 s with CtrlP. This results in a total simulation speedup of 3.33 across the six-core setup. The accuracy of the CtrlP implementation is confirmed through validation in Section 6.4.2.

Table 6.3 Computational performance comparison, CtrlP

Equations	Ser_NIJ simulation Time (s)	CtrlP simulation Time (s) 6 CPUs	Speedup factor
Power system	27.1	27.1	1.00
Control system	188.5	37.5	5.02
Total simulation	215.6	64.6	3.33

6.3 Optimized control solvers

As shown in the previous sections, control systems represent a major source of computational overhead in EMT simulations. Their complexity and the presence of nonlinear feedback loops make them particularly demanding, often creating a bottleneck that limits overall simulation speed. Although both TLP and CtrlP offer substantial performance gains, the control solution process itself remains a limiting factor, underscoring the need for further optimization.

To address this, reduced Jacobian matrix techniques have been proposed in [149], along with an enhanced version introduced in [150], both of which significantly improve computational efficiency without compromising time-step accuracy. In particular, [150] presents also an optimized sequential control strategy, referred to as SEQ+DFSOpt, which minimizes artificial delays and their impact on accuracy through improved ordering of the control solution process. In this work, this technique is referred to as OSeqCtrl.

The OSeqCtrl method is evaluated in the following section. It delivers substantial performance gains while maintaining acceptable accuracy across the test cases used in this study. However, because its accuracy is not universally guaranteed, especially in systems with highly sensitive control dynamics, OSeqCtrl is best applied as an optional or localized solution, where its use can be targeted to specific subsystems or regions.

6.3.1 Performance evaluation

To assess the performance of OSeqCtrl, it is applied to the system shown in Figure 6.1, with results summarized in Table 6.4. The table compares the computational performance of the standard serial NIJ approach (Ser_NIJ) against OSeqCtrl, breaking down the CPU times spent solving both control and power system equations.

The results demonstrate dramatic improvements. OSeqCtrl reduces the control system computation time by a factor of 14.7 compared to NIJ, effectively reducing the control system's share of the total simulation time to just 30%. This substantial reduction leads to an overall simulation speedup of 5.4, all achieved using a single CPU. The method's accuracy is confirmed in Section 6.4.2, supporting its viability as a high-performance control solver for EMT applications.

Table 6.4 Computational performance comparison, OSeqCtrl

Equations	Ser_NIJ simulation time (s)	Ser_OSeqCtrl Simulation time (s) 1 CPU	Speedup factor
Power system	27.1	27.1	1
Control system	188.5	12.8	14.7
Total simulation	215.6	39.9	5.4

6.4 Evaluation on large-scale MTDC system

This section assesses the performance of the previously discussed acceleration techniques in the context of a large-scale MTDC network. The evaluation is conducted using the InterOPERA system [138], a benchmark topology developed under a European-funded initiative aimed at ensuring interoperability among multi-vendor HVDC grids and supporting the integration of renewable energy sources.

For this study, Variant 1 of the InterOPERA system, titled "Meshed Offshore Grid for Wind Export", is selected as the test case. As illustrated in Figure 6.4, the system includes five bipolar MMC converters connected through a meshed DC transmission network. This layout is designed to efficiently gather and deliver power from offshore wind farms to onshore terminals, offering a practical and technically relevant scenario for evaluating both HVDC grid control strategies and EMT simulation acceleration methods.

The system is implemented and simulated in EMTP® [5], and its configuration and parameters are detailed in Table 6.5.

Table 6.5 Simulation and model details for InterOPERA Variant 1

Aspect		Details
Component model	**Grid equivalents**	Voltage sources with impedance
	MMC	Generic 401-level, half-bridge, arm equivalent model (Model 3) [141]
		Offshore stations operate in V/f control mode [2]
		Onshore stations operate in DC Droop control mode [138].
	Wind parks	Generic aggregated DFIG models with controls.
		Contains 1200 wind turbines, 1.5 MW each.
	Lines /cables	Wideband models [22].
	Loads	Fixed impedance.
Simulation details	**Total number of simulation nodes**	1016
	Total number of control devices	9754
	Simulation interval (s)	10
	Time-step (µs)	50

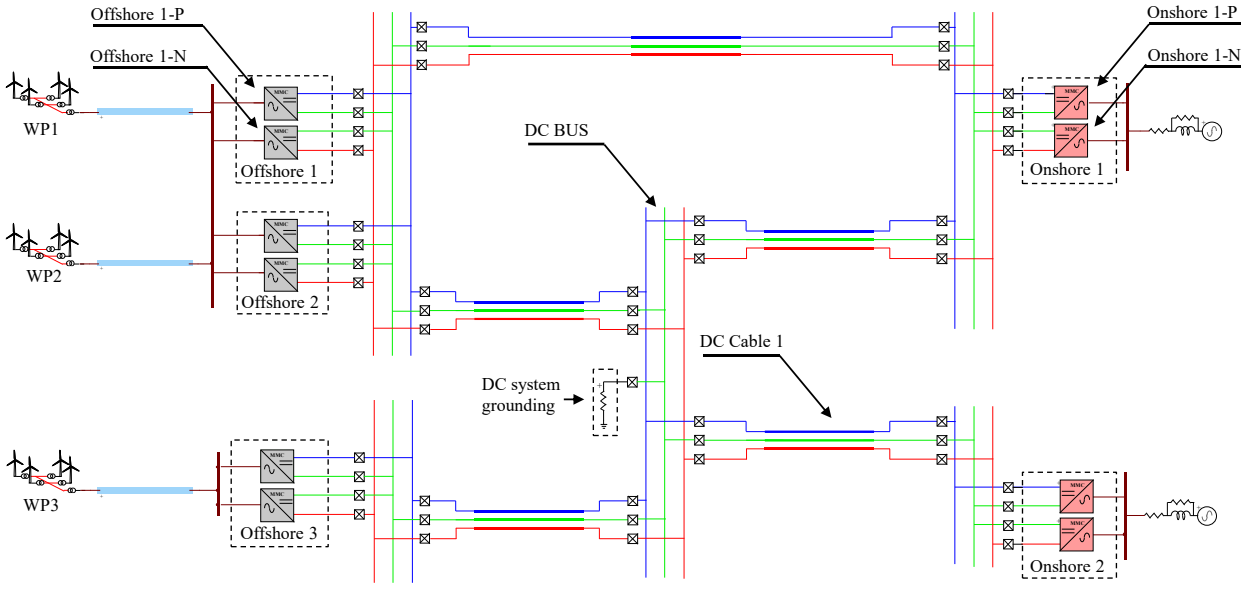

Figure 6.4 InterOPERA's Variant 1 test system schematic

6.4.1 Computing time gains

This section evaluates the simulation speed improvements achieved by the proposed acceleration strategies. Simulations were performed on an Intel® Xeon® Gold 6258R processor. Initially, the three core methods, TLP_NIJ, CtrlP, and Ser_OSeqCtrl, are assessed individually and compared against the baseline case, Ser_NIJ. Following that, two hybrid configurations are introduced:

- TLP+CtrlP, which integrates the TLP and CtrlP techniques using the NIJ solver, and
- TLP_OSeqCtrl, which combines TLP with the optimized OSeqCtrl solver.

In the TLP_NIJ setup, the system (as illustrated in Figure 6.4) is distributed across 8 CPU cores with the following allocation:

- Wind parks: 3 CPUs.
- DC network: 1 CPU.
- MMCs: 4 CPUs (Note: Offshore 1 and Offshore 2 MMCs share a single CPU, due to the absence of a decoupling transmission line delay between them.)

As shown in Table 6.6, TLP_NIJ delivers a significant performance boost, reducing simulation time by a factor of 5.6.

The CtrlP method parallelizes the control system across 16 CPUs, allocating 10 CPUs for the MMC controllers and 6 for the wind park controllers, maintaining the same structure discussed in Section 6.2.2. This configuration achieves a 4.33 times speedup, as indicated in Table 6.6.

Replacing the NIJ solver in the serial baseline with OSeqCtrl, i.e., in the Ser_OSeqCtrl setup, results in a 4.13 reduction in CPU time, despite utilizing only one CPU, highlighting the solver's efficiency.

The hybrid approaches provide even greater acceleration:

- TLP+CtrlP, using 24 CPUs and combining both parallelization techniques with the NIJ solver, achieves a 7.23 speedup.
- The most effective configuration, TLP_OSeqCtrl, leverages both the system-level parallelization of TLP and the solver-level optimization of OSeqCtrl. This setup, running on 8 CPUs, achieves the highest acceleration factor of 23.65, offering the most substantial reduction in total simulation time by minimizing both interdependencies and solver delays.

Table 6.6 Performance evaluation of simulation techniques

Simulation technique	Number of CPUs	CPU time (s)	Acceleration factor
Ser_NIJ (Ref)	1	615.6	-
TLP_NIJ	8	109.9	5.60
CtrlP	16	142.1	4.33
Ser_OSeqCtrl	1	149.2	4.13
TLP+CtrlP	24	85.2	7.23
TLP_OSeqCtrl	8	26.0	23.65

6.4.2 Error analysis

To assess the accuracy of the proposed acceleration methods, a DC fault scenario is simulated on the InterOPERA system (Figure 6.4) using EMTP® [5]. Detailed simulation parameters are provided in Table 6.7. The fault event is cleared by tripping the affected pole of DC Cable 1.

Table 6.7 Key parameters of the fault simulation scenario

Parameter	Details
Fault Resistance (Ω)	1
Fault location	Mid-point of DC cable 1, tagged in Figure 6.4. (Positive pole)
Fault type	Pole to ground
Fault instant (s)	0.8
Fault clearing time (ms)	5
Time-step (µs)	10

Figure 6.5 presents the DC fault current contributions, specifically, the I_{dc} values from Onshore 1-P and Onshore 2-P, for both the baseline (Ser_NIJ) and all accelerated configurations. Additionally, Figure 6.6 displays the corresponding DC voltage (V_{dc}) at the Onshore 1-P terminal. All evaluated techniques closely replicate the transient behavior of the baseline case, demonstrating a high degree of accuracy.

To better observe any discrepancies, both figures include zoomed-in plots of the fault's initial moments, where differences are typically most pronounced. Across all methods, the results confirm minimal deviation from the reference solution.

Notably, as shown in Figure 6.6, switching from NIJ to OSeqCtrl introduces no observable deviation: the responses of Ser_NIJ and Ser_OSeqCtrl are identical, as are those of TLP_NIJ and

TLP_OSeqCtrl. Among all configurations, the setups involving TLP, namely TLP_NIJ, TLP_OSeqCtrl, and TLP+CtrlP, exhibit slightly higher, yet still negligible, deviations compared to the other methods.

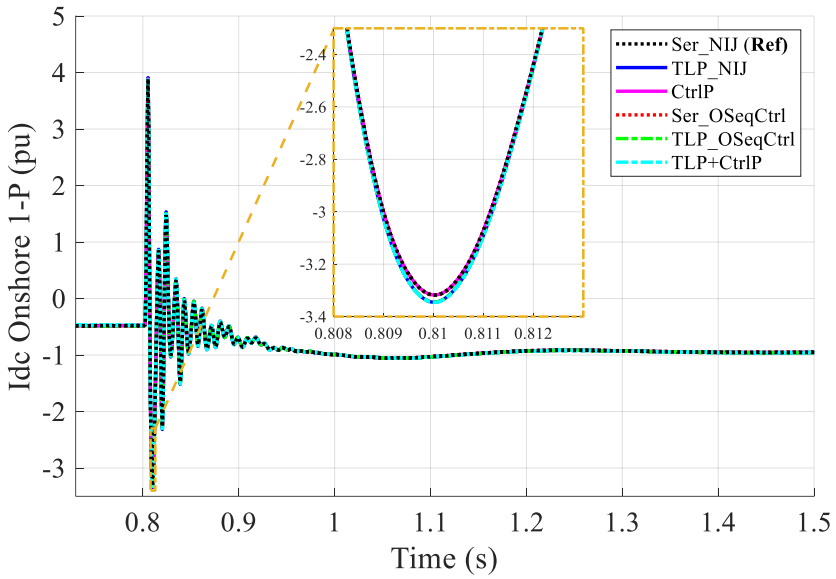

(a)

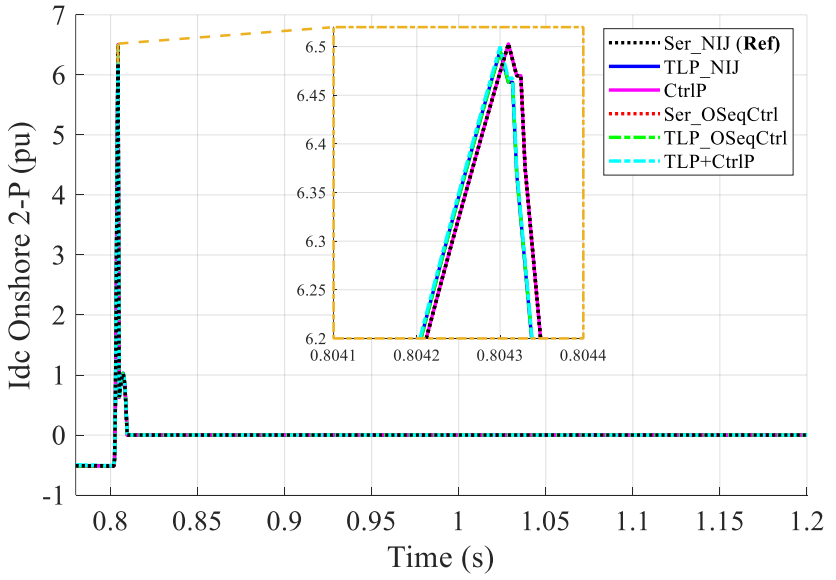

(b)

Figure 6.5 DC fault current from onshore converters: (a) Onshore 1-P, (b) Onshore 2-P.

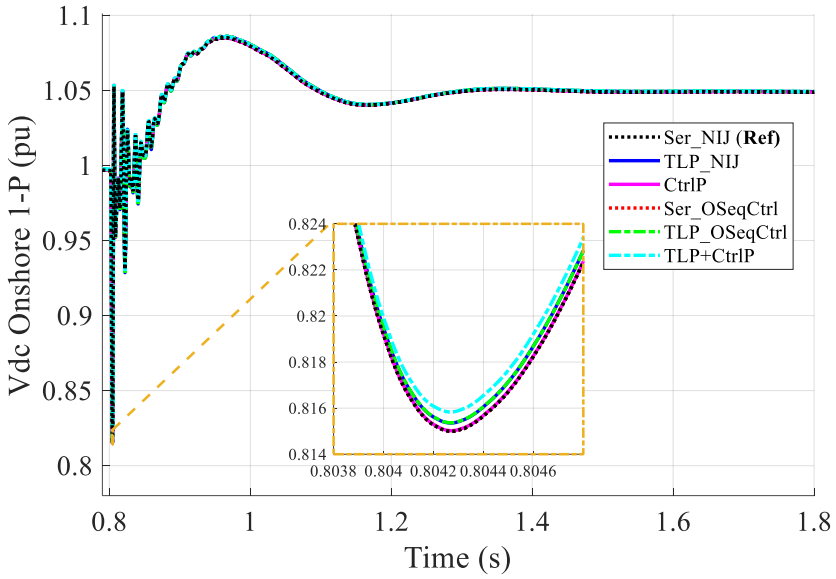

Figure 6.6 DC voltage response at Onshore 1-P terminals (V_{dc}) during the fault event.

6.5 Conclusion

This chapter presented a comprehensive evaluation of three acceleration techniques for EMT simulation of HVDC systems: TLP, CtrlP, and the OSeqCtrl. These methods were assessed based on their achievable performance gains, with simulations conducted on both a compact HVDC test system and the large-scale InterOPERA MTDC benchmark.

In the small-scale system, each method yielded notable improvements: TLP achieved a speedup of up to 2.0, CtrlP reached 3.33, and OSeqCtrl provided the highest speedup of 5.4 on a single CPU. However, the scalability of each technique varied. The number of decoupling transmission lines inherently limited TLP's performance, while CtrlP offered better scalability at the cost of increased CPU usage. OSeqCtrl delivered significant gains with minimal hardware requirements but requires careful use due to potential accuracy limitations in certain cases.

On the large-scale InterOPERA system, all methods demonstrated even greater performance improvements. TLP reached a speedup of 5.6, CtrlP 4.33, and OSeqCtrl 4.13. To further enhance simulation speed, two hybrid strategies were tested. The most effective was the TLP_OSeqCtrl configuration, which combined system-level and solver-level acceleration to achieve a maximum speedup of 23.65.

All proposed techniques maintained high fidelity, as verified through detailed DC fault simulations. These findings confirm the potential of combining network and control-level acceleration strategies to significantly improve the efficiency of EMT simulations for large-scale HVDC systems.

CHAPTER 7 CONCLUSION

7.1 Summary of dissertation

This dissertation focuses on advancing electromagnetic transient (EMT) simulation practices for large-scale hybrid AC–DC systems, particularly Multi-Terminal DC (MTDC) networks. The research addresses two critical challenges that currently limit the practicality of EMT simulations for future power systems: the lack of robust initialization techniques suited to complex systems with generic or black-box IBR models. The main target of this work was on MTDC systems, but its results are also applicable to other generic and arbitrary systems.

The work begins with a review of MTDC system components and their modeling aspects, highlighting the challenges posed by the widespread integration of inverter-based resources (IBRs), offshore wind parks (WPs), and the adoption of modular multilevel converters (MMCs). The computational burden introduced by detailed power electronic converters and nonlinear control structures forms the foundation for the subsequent research developments.

The first major contribution is the development of a hybrid AC–DC load-flow methodology that balances simplicity, versatility, and the ability to handle complex hybrid AC–DC configurations. Most existing EMT platforms generally lack flexible AC–DC load-flow (LF) solvers for initialization of time-domain computations, often providing only conventional AC LF tools. Moreover, most existing AC–DC LF algorithms suffer from severe limitations, such as an inability to accurately handle systems with multiple Vdc-controlled converters or hybrid combinations involving both DC droop and Vdc-controlled. To address these gaps, a hybrid method is proposed, combining an adapted Newton-based multiphase AC LF solver for both AC and DC networks with a fixed-point iterative approach. The proposed method supports a wide range of control modes, including P-control, Vdc-control, DC droop-control, and V/f control, and introduces novel extensions such as adaptive droop characteristics. Special emphasis is placed on enabling the initialization of unbalanced hybrid grids and supporting systems with multiple interacting Vdc-regulated VSC terminals.

Building upon the load-flow framework, the dissertation then focuses on one of the most challenging aspects of EMT initialization: the steady-state initialization of Grid-Forming Voltage Source Converters (GFM-VSCs). GFM-VSCs actively regulate AC voltage and frequency, making their startup particularly sensitive to initial conditions. A dedicated initialization methodology is

developed, which involves a steady-state resolution of outer control loops and the introduction of a subsystem decoupling approach called the Decoupling Interface (DI) method. This method effectively isolates GFM-controlled subsystems, enabling stable and accurate initialization even in complex or islanded configurations.

Following the successful demonstration of the DI concept for GFM-VSCs, the method is generalized into a unified initialization framework applicable to broader MTDC systems. The generalized DI approach supports black-box models, accommodates various converter types and control modes, and ensures fast and robust initialization across hybrid AC–DC grids. Validation on industry benchmark systems confirms the method's ability to reduce initialization time and improve simulation stability significantly.

Further contributions extend the application of the DI method to real-time simulation environments. A real-time-compatible variant of the DI initialization strategy is proposed and validated through real-time simulation software. By suppressing startup transients and minimizing initialization delays, the method facilitates efficient real-time EMT simulations, demonstrating significant time savings compared to conventional startup procedures.

Recognizing that DFIG-based wind parks present a major bottleneck in the initialization of large-scale MTDC systems, this dissertation proposes the Hybrid Decoupling Interface (HDI) method to expedite time-domain initialization for DFIG models. The HDI strategy is specifically tailored for the initialization of DFIG wind parks, which typically suffer from slow convergence using conventional EMT techniques. By combining selective steady-state initialization of critical control channels with internal DI-based subsystem decoupling, the HDI method significantly improves convergence speed while maintaining stability and accuracy. This targeted approach enables practical and robust EMT initialization even for highly detailed commercial wind park models.

Finally, this dissertation investigates unconventional acceleration methods for EMT simulation and evaluates their applicability, feasibility, and effectiveness for HVDC systems and MTDC networks. Each method is first studied individually, with performance assessments conducted on both small-scale HVDC systems and large-scale MTDC networks. Furthermore, hybrid strategies combining multiple acceleration techniques are proposed and demonstrated, highlighting their potential to achieve substantial simulation speedups without compromising accuracy. These

findings contribute to advancing scalable and efficient EMT simulation practices for complex future power systems.

7.2 List of publications

Journal publications

1. **A. Allabadi**, J. Mahseredjian, K. Jacobs, S. Dennetière, I. Kocar, and T. Ould-Bachir, "Initializing Large-Scale Multi-Terminal HVDC Systems Using Decoupling Interface," in *IEEE Transactions on Power Delivery*, vol. 39, no. 3, pp. 1600-1609, June 2024, doi: 10.1109/TPWRD.2024.3373657.
2. **A. Allabadi**, J. Mahseredjian, K. Jacobs, S. Dennetière, I. Kocar, and T. Ould-Bachir, "Initializing EMT models of grid forming VSCs in MTDC systems," *Electric Power Systems Research*, vol. 235, p. 110674, 2024, https://doi.org/10.1016/j.epsr.2024.110674, (https://www.sciencedirect.com/science/article/pii/S0378779624005601).
3. **A. Allabadi**, J. Mahseredjian, A. Abusalah, S. Dennetière, I. Kocar, and T. Ould-Bachir, " Acceleration strategies for EMT Simulation of HVDC systems," status: Accepted for publication *in Electric Power Systems Research*, 2025.
4. **A. Allabadi**, J. Mahseredjian, S. Dennetière, I. Kocar, and T. Ould-Bachir, " A Novel Hybrid AC–DC Load-Flow Algorithm for EMT Software," Status: To be submitted to IEEE Transactions on Power Delivery, 2025
5. **A. Allabadi**, J.A. Ocampo Wilches, J. Mahseredjian, I. Kocar, and T. Ould-Bachir, " A Novel Hybrid Initialization Method for DFIG Wind Park Simulation Models," Status: To be submitted to IEEE Transactions on Power Delivery, 2025

Conference publications

6. **A. Allabadi**, S. Satish Kumar, J. Mahseredjian, J. Paez Alvarez, W. Li, and J. N. Paquin, "Initializing real-time simulation models of MTDC systems," in CIGRE Canada 2024, Wennipig, Manitoba, 28-31 Oct 2024.

7.3 Future work

While this dissertation addresses key challenges in EMT simulation and initialization of MTDC systems, several directions remain open for future exploration:

- **Full Newton-Based Load-Flow Algorithm:** The present hybrid AC–DC load-flow relies on a Newton formulation for the AC network and a fixed-point method for the DC grid. A natural extension is to develop a unified Newton-based solver for the entire AC–DC system, which could improve convergence robustness, particularly in large-scale or weakly meshed MTDC networks.
- **Extension to Diverse Grid-Forming Controls:** The initialization framework can be further enhanced by accommodating a wider range of GFM control strategies, such as droop control, virtual synchronous machine, or combined Vdc–V/f modes. This would expand the applicability of the proposed methods to converter-dominated grids with heterogeneous control philosophies.
- **Digital-Twin-Based Models for EMT:** Detailed models of devices such as MMCs and other IBRs impose significant computational costs. Future work could investigate the development of reduced-order or data-driven digital twin models that replicate the dynamic behavior of these devices with high fidelity. Embedding such twins into EMT platforms offers a promising avenue to accelerate simulations without sacrificing accuracy.

REFERENCES

[1] P. Christensen, G. K. Andersen, M. Seidel, S. Bolik, S. Engelken, T. Knueppel, A. Krontiris, K. Wuerflinger, T. Bülo, and J. Jahn, "High penetration of power electronic interfaced power sources and the potential contribution of grid forming converters," 2020.

[2] "Guide for the Development of Models for HVDC Converters in a HVDC Grid," *CIGRE Technical Brochure,* vol. 604, 2014.

[3] D. Jovcic, *High voltage direct current transmission: converters, systems and DC grids*. John Wiley & Sons, 2019.

[4] W. G. B. 71, "DC grid benchmark models for system studies," *CIGRE Technical Brochure,* vol. 804, 2020.

[5] J. Mahseredjian, S. Dennetière, L. Dubé, B. Khodabakhchian, and L. Gérin-Lajoie, "On a new approach for the simulation of transients in power systems," *Electric power systems research,* vol. 77, no. 11, pp. 1514-1520, 2007.

[6] J. Peralta, H. Saad, S. Dennetière, J. Mahseredjian, and S. Nguefeu, "Detailed and averaged models for a 401-level MMC–HVDC system," *IEEE Transactions on Power Delivery,* vol. 27, no. 3, pp. 1501-1508, 2012.

[7] H. Saad, J. Peralta, S. Dennetiere, J. Mahseredjian, J. Jatskevich, J. Martinez, A. Davoudi, M. Saeedifard, V. Sood, and X. Wang, "Dynamic averaged and simplified models for MMC-based HVDC transmission systems," *IEEE transactions on Power delivery,* vol. 28, no. 3, pp. 1723-1730, 2013.

[8] A. Stepanov, *Modeling of direct current grid equipment for the simulation and analysis of electromagnetic transients*. Ecole Polytechnique, Montreal (Canada), 2020.

[9] A. Allabadi, J. Mahseredjian, K. Jacobs, S. Dennetière, I. Kocar, and T. Ould-Bachir, "Initializing Large-Scale Multi-Terminal HVDC Systems Using Decoupling Interface," *IEEE Transactions on Power Delivery,* 2024.

[10] Y. Liu, Y. Song, L. Zhao, Y. Chen, and C. Shen, "A general initialization scheme for electromagnetic transient simulation: towards large-scale hybrid AC-DC grids," in *2020 IEEE Power & Energy Society General Meeting (PESGM)*, 2020: IEEE, pp. 1-5.

[11] A. Allabadi, S. Satish Kumar, J. Mahseredjian, J. Paez Alvarez, W. Li, and J. N. Paquin, "Initializing real-time simulation models of MTDC systems," in *CIGRE Canada 2024*, Wennipig, Manitoba, 28-31 Oct 2024.

[12] *IEC TS 63291-1:High voltage direct current (HVDC) grid systems and connected converter stations - Guideline and parameter lists for functional specifications - Part 1: Guideline*, IEC, Geneva, Switzerland, 2023.

[13] *IEC TS 63291-2: High voltage direct current (HVDC) grid systems and connected converter stations - Guideline and parameter lists for functional specifications - Part 2: Parameter lists*, IEC, Geneva, Switzerland, 2023.

[14] M. Goertz, S. Wenig, S. Beckler, C. Hirsching, M. Suriyah, and T. Leibfried, "Analysis of cable overvoltages in symmetrical monopolar and rigid bipolar HVDC configuration," *IEEE transactions on power delivery,* vol. 35, no. 4, pp. 2097-2107, 2019.

[15] S. Dennetière and A. Bacon, "HVDC-VSC Newsletter," 2022.

[16] Y. Yu, Y. Gan, Q. Xin, F. Rojas, J. M. Silva, and F. Garcia, "Research on Insulation Coordination Design for±600kV Bipolar HVDC Transmission Line with Dedicated Metallic Return in Chile," in *2024 IEEE International Conference on DC Technologies and Systems (DCTS)*, 2024: IEEE, pp. 1-6.

[17] A. Armeni, M. Semenyuk, C. Plet, L. Kitzing, M. González, A. G. Arnklit, L. Dall, L. Winther, L. L. Lyck, and S. Funk, "D12. 5 Deployment Plan for Future European offshore Grid Development. Short-Term Project–Bornholm Island CleanStream Energy Hub," 2021.

[18] S. ANHAUS, P. DÜLLMANN, L. OSTERKAMP, T. TSO, G. G. I. France, and C. GONZALEZ, "2024 Paris Session."

[19] I. Arrambide, "Applications on power systems using HVDC-VSC technology," *RE&PQJ,* vol. 23, no. 4, pp. 162-167, 2025.

[20] J. Cabañas Ramos, M. Moritz, N. Klötzl, C. Nieuwenhout, W. Leon Garcia, I. Jahn, D. Kolichev, and A. Monti, "Getting ready for multi-vendor and multi-terminal hvdc technology," *Energies,* vol. 17, no. 10, p. 2388, 2024.

[21] InterOPERA. "Project Publications." https://interopera.eu/publications/ (accessed 2025).

[22] I. Kocar and J. Mahseredjian, "Accurate frequency dependent cable model for electromagnetic transients," *IEEE Transactions on Power Delivery,* vol. 31, no. 3, pp. 1281-1288, 2015.

[23] "DC-DC converters in HVDC grids and for connections to HVDC systems," 2021, vol. 827. [Online]. Available: https://www.e-cigre.org/publications/detail/827-dc-dc-converters-in-hvdc-grids-and-for-connections-to-hvdc-systems.html

[24] D. Jovcic and H. Zhang, "Dual channel control with DC fault ride through for MMC-based, isolated DC/DC converter," *IEEE Transactions on Power Delivery,* vol. 32, no. 3, pp. 1574-1582, 2017.

[25] "Control methodologies for direct voltage and power flow in a meshed HVDC grid," 2017, vol. 699. [Online]. Available: https://www.e-cigre.org/publications/detail/699-control-methodologies-for-direct-voltage-and-power-flow-in-a-meshed-hvdc-grid.html

[26] P. Pourbeik, "Grid Integration and Dynamic Impact of Wind Energy [Book Reviews]," *IEEE Power and Energy Magazine,* vol. 11, no. 2, pp. 91-92, 2013.

[27] D. Wu, G.-S. Seo, L. Xu, C. Su, L. Kocewiak, Y. Sun, and Z. Qin, "Grid integration of offshore wind power: Standards, control, power quality and transmission," *IEEE Open Journal of Power Electronics,* vol. 5, pp. 583-604, 2024.

[28] K. Sun, W. Yao, C. Yan, and J. Wen, "Impedance modeling and analysis of medium-frequency oscillation caused by VSC-HVDC connected to local weak grid and DFIG-based wind farms," *Frontiers in Energy Research,* vol. 9, p. 693903, 2021.

[29] B. Shao, S. Zhao, Y. Yang, B. Gao, and F. Blaabjerg, "Sub-synchronous oscillation characteristics and analysis of direct-drive wind farms with VSC-HVDC systems," *IEEE Transactions on Sustainable Energy,* vol. 12, no. 2, pp. 1127-1140, 2020.

[30] F. Ryder, C. Stairs, G. Breuer, and J. Fink, "The New Brunswick Electric Power Commission Solid State HVDC Asynchronous Tie Installation," in *Proceedings of the American Power Conference*, 1970, vol. 32, pp. 866-875.

[31] T. Horigome, K. Kurokawa, K. Kishi, and K. Ozu, "A 100-kV thyristor converter for high-voltage dc transmission," *IEEE Transactions on Electron Devices,* vol. 17, no. 9, pp. 809-815, 1970.

[32] J. Cochrane, M. Emerson, J. Donahue, and G. Wolf, "A survey of HVDC operating and maintenance practices and their impact on reliability and performance," *IEEE transactions on power delivery,* vol. 11, no. 1, pp. 514-518, 1996.

[33] J. Arrillaga, *High voltage direct current transmission* (no. 29). Iet, 1998.

[34] M. Bahrman, D. Martin, and G. Sweezy, "Quebec-New England Phase II HVDC Transmission System Part II. Multi-terminal Control Strategy for Dynamic Performance," in *CIGRÉ Symposium on AC/DC Transmission Interaction and Comparisons*, 1987.

[35] P. Sun, F. Arraño-Vargas, H. R. Wickramasinghe, and G. Konstantinou, "Benchmark models for HVDC systems and DC-grid studies," in *2019 9th International conference on power and energy systems (ICPES)*, 2019: IEEE, pp. 1-6.

[36] K. Eriksson, "Operational experience of HVDC Light/sup TM," in *Seventh International Conference on AC-DC Power Transmission*, 2001: IET, pp. 205-210.

[37] U. Axelsson, "Gotland HVDC Light transmission-world's first commercial small scale DC transmission," in *Proc. of CIRED Conference in Nice, France, May*, 1999.

[38] B. Railing, J. Miller, G. Moreau, J. Wasborg, Y. Jiang-Häfner, and D. Stanley, "The directlink VSC-based HVDC project and its commissioning," *Proc. Session 2002 Cigre,* pp. 14-108, 2002.

[39] A. Nakagawa, Y. Yamaguchi, K. Watanabe, and H. Ohashi, "Safe operating area for 1200-V nonlatchup bipolar-mode MOSFET's," *IEEE transactions on electron devices,* vol. 34, no. 2, pp. 351-355, 2005.

[40] H. Saad, S. Dennetière, J. Mahseredjian, P. Delarue, X. Guillaud, J. Peralta, and S. Nguefeu, "Modular multilevel converter models for electromagnetic transients," *IEEE Transactions on Power Delivery,* vol. 29, no. 3, pp. 1481-1489, 2013.

[41] Y. Li, "Arm inductance and sub-module capacitance selection in modular multilevel converter," 2013.

[42] S. Debnath, J. Qin, B. Bahrani, M. Saeedifard, and P. Barbosa, "Operation, control, and applications of the modular multilevel converter: A review," *IEEE transactions on power electronics,* vol. 30, no. 1, pp. 37-53, 2014.

[43] K. Jacobs, S. Heinig, D. Johannesson, S. Norrga, and H.-P. Nee, "Comparative evaluation of voltage source converters with silicon carbide semiconductor devices for high-voltage direct current transmission," *IEEE Transactions on Power Electronics,* vol. 36, no. 8, pp. 8887-8906, 2021.

[44] T. Abedin, M. S. H. Lipu, M. A. Hannan, P. J. Ker, S. A. Rahman, C. T. Yaw, S. K. Tiong, and K. M. Muttaqi, "Dynamic modeling of hvdc for power system stability assessment: A review, issues, and recommendations," *Energies,* vol. 14, no. 16, p. 4829, 2021.

[45] A. Beddard, M. Barnes, and R. Preece, "Comparison of detailed modeling techniques for MMC employed on VSC-HVDC schemes," *IEEE Transactions on Power Delivery,* vol. 30, no. 2, pp. 579-589, 2014.

[46] W. Z. El-Khatib, J. Holboell, and T. W. Rasmussen, "Efficient modelling of a modular multilevel converter," in *2013 48th International Universities' Power Engineering Conference (UPEC)*, 2013: IEEE, pp. 1-6.

[47] U. N. Gnanarathna, A. M. Gole, and R. P. Jayasinghe, "Efficient modeling of modular multilevel HVDC converters (MMC) on electromagnetic transient simulation programs," *IEEE Transactions on power delivery,* vol. 26, no. 1, pp. 316-324, 2010.

[48] J. Xu, C. Zhao, W. Liu, and C. Guo, "Accelerated model of modular multilevel converters in PSCAD/EMTDC," *IEEE Transactions on Power Delivery,* vol. 28, no. 1, pp. 129-136, 2012.

[49] H. J. Kim, S. Jung, F. Mosallat, and K. Hur, "Validation for compatible modular multilevel converter models using PSCAD/EMTDC," in *2013 IEEE PES Asia-Pacific Power and Energy Engineering Conference (APPEEC)*, 2013: IEEE, pp. 1-6.

[50] K. Strunz and E. Carlson, "Nested fast and simultaneous solution for time-domain simulation of integrative power-electric and electronic systems," *IEEE Transactions on Power Delivery,* vol. 22, no. 1, pp. 277-287, 2006.

[51] A. Stepanov, H. Saad, U. Karaagac, and J. Mahseredjian, "Spurious power losses in modular multilevel converter arm equivalent model," *IEEE Transactions on Power Delivery,* vol. 35, no. 1, pp. 205-213, 2019.

[52] J. Xu, A. M. Gole, and C. Zhao, "The use of averaged-value model of modular multilevel converter in DC grid," *IEEE Transactions on Power Delivery,* vol. 30, no. 2, pp. 519-528, 2014.

[53] J. Freytes, L. Papangelis, H. Saad, P. Rault, T. Van Cutsem, and X. Guillaud, "On the modeling of MMC for use in large scale dynamic simulations," in *2016 Power Systems Computation Conference (PSCC)*, 2016: IEEE, pp. 1-7.

[54] A. Beddard, C. Sheridan, M. Barnes, and T. Green, "Improved accuracy average value models of modular multilevel converters," *IEEE Transactions on Power Delivery,* vol. 31, no. 5, pp. 2260-2269, 2016.

[55] H. Yang, Y. Dong, W. Li, and X. He, "Average-value model of modular multilevel converters considering capacitor voltage ripple," *IEEE Transactions on Power Delivery,* vol. 32, no. 2, pp. 723-732, 2016.

[56] H. Zhang, D. Jovcic, W. Lin, and A. J. Far, "Average value MMC model with accurate blocked state and cell charging/discharging dynamics," in *2016 4th International Symposium on Environmental Friendly Energies and Applications (EFEA)*, 2016: IEEE, pp. 1-6.

[57] A. Beddard and M. Barnes, "Modelling of MMC-HVDC systems–an overview," *Energy Procedia,* vol. 80, pp. 201-212, 2015.

[58] R. Li, L. Xu, and D. Guo, "Accelerated switching function model of hybrid MMCs for HVDC system simulation," *IET Power Electronics,* vol. 10, no. 15, pp. 2199-2207, 2017.

[59] F. B. Ajaei and R. Iravani, "Enhanced equivalent model of the modular multilevel converter," *IEEE Transactions on Power Delivery,* vol. 30, no. 2, pp. 666-673, 2014.

[60] N. Ahmed, L. Ängquist, S. Norrga, A. Antonopoulos, L. Harnefors, and H.-P. Nee, "A computationally efficient continuous model for the modular multilevel converter," *IEEE Journal of Emerging and Selected Topics in Power Electronics,* vol. 2, no. 4, pp. 1139-1148, 2014.

[61] J. A. Ansari, C. Liu, and S. A. Khan, "MMC based MTDC grids: A detailed review on issues and challenges for operation, control and protection schemes," *IEEE Access,* vol. 8, pp. 168154-168165, 2020.

[62] C. Gavriluta, J. I. Candela, J. Rocabert, A. Luna, and P. Rodriguez, "Adaptive droop for control of multiterminal DC bus integrating energy storage," *IEEE Transactions on Power Delivery,* vol. 30, no. 1, pp. 16-24, 2015.

[63] Z. P. Cheng, Y. F. Wang, Z. W. Li, and J. F. Gao, "DC voltage margin adaptive droop control strategy of VSC-MTDC systems," *The Journal of Engineering,* vol. 2019, no. 16, pp. 1783-1787, 2019.

[64] M. Zhang, J. Ding, Y. Cai, and H. Wang, "Research on control strategy of MMC-MTDC system based on improved droop control," in *Journal of Physics: Conference Series*, 2019, vol. 1176, no. 6: IOP Publishing, p. 062011.

[65] M. Aragüés-Peñalba, A. Egea-Alvarez, S. G. Arellano, and O. Gomis-Bellmunt, "Droop control for loss minimization in HVDC multi-terminal transmission systems for large offshore wind farms," *Electric Power Systems Research,* vol. 112, pp. 48-55, 2014.

[66] S. Sayed and A. Massoud, "Optimal DC voltage control in multi-terminal HVDC network: Modeling and scenarios," in *2019 IEEE 9th Symposium on Computer Applications & Industrial Electronics (ISCAIE)*, 2019: IEEE, pp. 86-91.

[67] L. Harnefors, N. Johansson, L. Zhang, and B. Berggren, "Interarea oscillation damping using active-power modulation of multiterminal HVDC transmissions," *IEEE Transactions on Power Systems,* vol. 29, no. 5, pp. 2529-2538, 2014.

[68] A. A. Taffese, A. G. Endegnanew, S. D'Arco, and E. Tedeschi, "Power oscillation damping with virtual capacitance support from modular multilevel converters," *IET Renewable Power Generation,* vol. 14, no. 5, pp. 897-905, 2020.

[69] F. Yan, P. Wang, X.-P. Zhang, J. Xie, X. Li, C. Tang, and Z. Zhao, "Coordinated start-up control and inter-converter oscillations damping for MMC-HVDC grid," *IEEE Access,* vol. 7, pp. 65093-65102, 2019.

[70] *IEC 62747:Amendment 1 - Terminology for voltage-sourced converters (VSC) for high-voltage direct current (HVDC) systems*, IEC, Geneva, Switzerland, 2019.

[71] H. A. Saad, "Modélisation et simulation d'une liaison HVDc de type VSC-MMC," École Polytechnique de Montréal, 2015.

[72] Q. Tu and Z. Xu, "Impact of sampling frequency on harmonic distortion for modular multilevel converter," *IEEE Transactions on Power Delivery,* vol. 26, no. 1, pp. 298-306, 2010.

[73] N. Ahmed, L. Ängquist, and H.-P. Nee, "Continuous modeling of open-loop control based negative sequence current control of modular multilevel converters for HVDC transmission," in *2013 15th European Conference on Power Electronics and Applications (EPE)*, 2013: IEEE, pp. 1-10.

[74] A. Abur and H. Singh, "Time domain modeling of external systems for electromagnetic transients programs," *IEEE transactions on power systems,* vol. 8, no. 2, pp. 671-679, 1993.

[75] B. Gustavsen, "Computer code for rational approximation of frequency dependent admittance matrices," *IEEE Transactions on Power Delivery,* vol. 17, no. 4, pp. 1093-1098, 2002.

[76] B. Gustavsen and A. Semlyen, "Application of vector fitting to state equation representation of transformers for simulation of electromagnetic transients," *IEEE transactions on power delivery,* vol. 13, no. 3, pp. 834-842, 1998.

[77] B. Gustavsen and A. Semlyen, "Rational approximation of frequency domain responses by vector fitting," *IEEE Transactions on power delivery,* vol. 14, no. 3, pp. 1052-1061, 1999.

[78] J.-H. Hong and J.-K. Park, "A time-domain approach to transmission network equivalents via Prony analysis for electromagnetic transients analysis," *IEEE transactions on power systems,* vol. 10, no. 4, pp. 1789-1797, 1995.

[79] A. Ibrahim and M. Salama, "Frequency dependent network equivalent algorithm for AC power systems," in *Proceedings of 1996 Canadian Conference on Electrical and Computer Engineering*, 1996, vol. 2: IEEE, pp. 639-642.

[80] A. Ramirez, "Vector fitting-based calculation of frequency-dependent network equivalents by frequency partitioning and model-order reduction," *IEEE Transactions on Power Delivery,* vol. 24, no. 1, pp. 410-415, 2008.

[81] C. Tian, H. Zhao, J. Diao, and B. Li, "Electromagnetic and electromechanical hybrid simulation based on mosaik framework," in *2020 IEEE/IAS Industrial and Commercial Power System Asia (I&CPS Asia)*, 2020: IEEE, pp. 887-891.

[82] D. N. Hussein, M. Matar, and R. Iravani, "A wideband equivalent model of type-3 wind power plants for EMT studies," *IEEE Transactions on Power Delivery,* vol. 31, no. 5, pp. 2322-2331, 2016.

[83] P. Sowa and D. Zychma, "Dynamic equivalents in power system studies: A review," *Energies,* vol. 15, no. 4, p. 1396, 2022.

[84] "Reliability Guideline Recommended Practices for Performing EMT System Studies for Inverter-Based Resources," NERC, 2024. [Online]. Available: https://www.nerc.com/comm/RSTC_Reliability_Guidelines/Reliability_Guideline_Recommended_Practices_for_EMT_Studies_for_IBR_Approved.pdf

[85] C. Yue, X. Zhou, and R. Li, "Node-splitting approach used for network partition and parallel processing in electromagnetic transient simulation," in *2004 International Conference on Power System Technology, 2004. PowerCon 2004.*, 2004, vol. 1: IEEE, pp. 425-430.

[86] C. Liu, Y. Hou, H. Dong, Y. Lv, X. Wang, and C. Su, "Parallel multi-rate simulation scheme for modular multilevel converter-based high-voltage direct current with accurate simulation

of high-frequency characteristics and field programmable gate array-based implementation," *High Voltage,* vol. 10, no. 1, pp. 17-31, 2025.

[87] R. Yao, Q. Chen, H. Bai, C. Liu, T. Liu, Y. Luo, and W. Yang, "A Multi-Rate Simulation Strategy Based on the Modified Time-Domain Simulation Method and Multi-Area Data Exchange Method of Power Systems," *Electronics,* vol. 13, no. 5, p. 884, 2024.

[88] M. Armstrong, J. R. Martí, L. R. Linares, and P. Kundur, "Multilevel MATE for efficient simultaneous solution of control systems and nonlinearities in the OVNI simulator," *IEEE Transactions on Power Systems,* vol. 21, no. 3, pp. 1250-1259, 2006.

[89] J. Mahseredjian, B. Bruned, and A. Abusalah, "Compensation Method, Diakoptics and MATE," *IEEE Access,* 2025.

[90] B. Bruned, J. Mahseredjian, S. Dennetière, J. Michel, M. Schudel, and N. Bracikowski, "Compensation method for parallel and iterative real-time simulation of electromagnetic transients," *IEEE Transactions on Power Delivery,* vol. 38, no. 4, pp. 2302-2310, 2023.

[91] A. Abusalah, O. Saad, J. Mahseredjian, U. Karaagac, and I. Kocar, "Accelerated sparse matrix-based computation of electromagnetic transients," *IEEE Open Access Journal of Power and Energy,* vol. 7, pp. 13-21, 2019.

[92] M. Ouafi, J. Mahseredjian, J. Peralta, H. Gras, S. Dennetière, and B. Bruned, "Parallelization of EMT simulations for integration of inverter-based resources," *Electric Power Systems Research,* vol. 223, p. 109641, 2023.

[93] A. Stepanov, J. Mahseredjian, H. Saad, and U. Karaagac, "Parallelization of MMC detailed equivalent model," *Electric Power Systems Research,* vol. 195, p. 107168, 2021.

[94] T. Ould-Bachir, H. Saad, S. Dennetière, and J. Mahseredjian, "CPU/FPGA-based real-time simulation of a two-terminal MMC-HVDC system," *IEEE Transactions on Power Delivery,* vol. 32, no. 2, pp. 647-655, 2015.

[95] H. Saad, T. Ould-Bachir, J. Mahseredjian, C. Dufour, S. Dennetière, and S. Nguefeu, "Real-time simulation of MMCs using CPU and FPGA," *IEEE Transactions on Power Electronics,* vol. 30, no. 1, pp. 259-267, 2013.

[96] H. Saad, S. Dennetière, J. Mahseredjian, T. Ould-Bachir, and J. P. David, "Simulation of Transients for VSC-HVDC Transmission Systems Based on Modular Multilevel Converters," *Transient Analysis of Power Systems: Solution Techniques, Tools and Applications,* pp. 317-359, 2015.

[97] X. Ma, C. Yang, X.-P. Zhang, Y. Xue, and J. Li, "Real-time simulation of power system electromagnetic transients on FPGA using adaptive mixed-precision calculations," *IEEE Transactions on Power Systems,* vol. 38, no. 4, pp. 3683-3693, 2022.

[98] Z. Yu, Y. Chen, Y. Song, and S. Huang, "Comparison of parallel implementations of controls on GPU for transient simulation of power system," in *2016 35th Chinese Control Conference (CCC)*, 2016: IEEE, pp. 9996-10001.

[99] H. Gao, Y. Chen, Y. Xu, Z. Yu, and L. Chen, "A GPU-based parallel simulation platform for large-scale wind farm integration," in *2014 IEEE PES T&D Conference and Exposition*, 2014: IEEE, pp. 1-5.

[100] D. Shu, Y. Wei, V. Dinavahi, K. Wang, Z. Yan, and X. Li, "Cosimulation of shifted-frequency/dynamic phasor and electromagnetic transient models of hybrid LCC-MMC DC grids on integrated CPU–GPUs," *IEEE Transactions on Industrial Electronics,* vol. 67, no. 8, pp. 6517-6530, 2019.

[101] R. Hassani, J. Mahseredjian, T. Tshibungu, and U. Karaagac, "Evaluation of time-domain and phasor-domain methods for power system transients," *Electric Power Systems Research,* vol. 212, p. 108335, 2022.

[102] W. Wu, P. Li, X. Fu, Z. Wang, J. Wu, and C. Wang, "GPU-based power converter transient simulation with matrix exponential integration and memory management," *International Journal of Electrical Power & Energy Systems,* vol. 122, p. 106186, 2020.

[103] W. Nzale, J. Mahseredjian, I. Kocar, X. Fu, and C. Dufour, "Two variable time-step algorithms for simulation of transients," in *2019 IEEE Milan PowerTech*, 2019: IEEE, pp. 1-6.

[104] A. Stepanov, J. Mahseredjian, U. Karaagac, and H. Saad, "Adaptive modular multilevel converter model for electromagnetic transient simulations," *IEEE Transactions on Power Delivery,* vol. 36, no. 2, pp. 803-813, 2020.

[105] M. Cai, H. Gras, J. Mahseredjian, E. Rutovic, and A. El-Akoum, "Functional mock-up interface-based approach for parallel and multistep simulation of electromagnetic transients," *IEEE Transactions on Power Delivery,* vol. 33, no. 6, pp. 2978-2988, 2018.

[106] A. Benigni, A. Monti, and R. A. Dougal, "Latency-based approach to the simulation of large power electronics systems," *IEEE transactions on power electronics,* vol. 29, no. 6, pp. 3201-3213, 2013.

[107] C. Deml and P. Turkes, "Fast simulation technique for power electronic circuits with widely different time constants," *IEEE Transactions on Industry Applications,* vol. 35, no. 3, pp. 657-662, 1999.

[108] S. Subedi, M. Rauniyar, S. Ishaq, T. M. Hansen, R. Tonkoski, M. Shirazi, R. Wies, and P. Cicilio, "Review of methods to accelerate electromagnetic transient simulation of power systems," *IEEE Access,* vol. 9, pp. 89714-89731, 2021.

[109] D. Athaide, J. Qin, and Y. Zou, "Matlab/simulink-based electromagnetic transient-transient stability hybrid simulation for electric power systems with converter interfaced generation," in *2019 IEEE Texas Power and Energy Conference (TPEC)*, 2019: IEEE, pp. 1-6.

[110] M. Cai, J. Mahseredjian, I. Kocar, X. Fu, and A. Haddadi, "A parallelization-in-time approach for accelerating EMT simulations," *Electric Power Systems Research,* vol. 197, p. 107346, 2021.

[111] A. Stepanov, H. Saad, U. Karaagac, and J. Mahseredjian, "Initialization of modular multilevel converter models for the simulation of electromagnetic transients," *IEEE Transactions on Power Delivery,* vol. 34, no. 1, pp. 290-300, 2018.

[112] J. A. Ocampo-Wilches, J. Mahseredjian, K. Jacobs, A. G. Pavani, and H. Xue, "Comprehensive Full-Scale Converter Wind Park Initialization for Electromagnetic Transient Studies," *IEEE Transactions on Power Delivery,* 2025.

[113] J. A. Ocampo-Wilches, A. Ramirez, K. Jacobs, J. Mahseredjian, and A. G. Pavani, "Full-Control Initialization of Photovoltaic Park Models for Electromagnetic Transient Simulations," in *IECON 2024-50th Annual Conference of the IEEE Industrial Electronics Society*, 2024: IEEE, pp. 1-8.

[114] J. Slootweg, H. Polinder, and W. Kling, "Initialization of wind turbine models in power system dynamics simulations," in *2001 IEEE Porto Power Tech Proceedings (Cat. No. 01EX502)*, 2001, vol. 4: IEEE, p. 6 pp. vol. 4.

[115] T. J. Aprille and T. N. Trick, "Steady-state analysis of nonlinear circuits with periodic inputs," *Proceedings of the IEEE,* vol. 60, no. 1, pp. 108-114, 1972.

[116] M. Nakhla and F. Branin Jr, "Determining the periodic response of nonlinear systems by a gradient method," *International Journal of Circuit Theory and Applications,* vol. 5, no. 3, pp. 255-273, 1977.

[117] B. Perkins, J. Marti, and H. Dommel, "Nonlinear elements in the EMTP: steady-state initialization," *IEEE Transactions on Power Systems,* vol. 10, no. 2, pp. 593-601, 2002.

[118] X. Lombard, J. Mahseredjian, S. Lefebvre, and C. Kieny, "Implementation of a new harmonic initialization method in the EMTP," *IEEE Transactions on Power Delivery,* vol. 10, no. 3, pp. 1343-1352, 2002.

[119] J. Mahseredjian, U. Karaagac, S. Dennetière, H. Saad, and A. Ametani, "Simulation of electromagnetic transients with EMTP-RV," in *Numerical Analysis of Power System Transients and Dynamics*: IET, 2015, pp. 103-134.

[120] S. Li, T. A. Haskew, K. A. Williams, and R. P. Swatloski, "Control of DFIG wind turbine with direct-current vector control configuration," *IEEE transactions on Sustainable Energy,* vol. 3, no. 1, pp. 1-11, 2011.

[121] M. Tsili and S. Papathanassiou, "A review of grid code technical requirements for wind farms," *IET Renewable power generation,* vol. 3, no. 3, pp. 308-332, 2009.

[122] Y. Coughlan, P. Smith, A. Mullane, and M. O'Malley, "Wind turbine modelling for power system stability analysis—A system operator perspective," *IEEE Transactions on power systems,* vol. 22, no. 3, pp. 929-936, 2007.

[123] I. Kocar, U. Karaagac, J. Mahseredjian, and B. Cetindag, "Multiphase load-flow solution and initialization of induction machines," *IEEE Transactions on Power Systems,* vol. 33, no. 2, pp. 1650-1658, 2017.

[124] I. Kocar, J. Mahseredjian, U. Karaagac, G. Soykan, and O. Saad, "Multiphase load-flow solution for large-scale distribution systems using MANA," *IEEE Transactions on power delivery,* vol. 29, no. 2, pp. 908-915, 2013.

[125] J. A. Martinez and J. Mahseredjian, "Load flow calculations in distribution systems with distributed resources. A review," in *2011 IEEE power and energy society general meeting*, 2011: IEEE, pp. 1-8.

[126] A. Allabadi, J. Mahseredjian, K. Jacobs, S. Dennetière, I. Kocar, and T. Ould-Bachir, "Initializing EMT models of grid forming VSCs in MTDC systems," *Electric Power Systems Research,* vol. 235, p. 110674, 2024.

[127] J. Mahseredjian, "Simulation des transitoires électromagnétiques dans les réseaux électriques," 2007.

[128] J. Mahseredjian, "Multiphase load-flow method," course notes, Comportement des réseaux électriques, 2007.

[129] N. Rashidirad, J. Mahseredjian, I. Kocar, U. Karaagac, and O. Saad, "Mana-based load-flow solution for islanded ac microgrids," *IEEE Transactions on Smart Grid,* vol. 14, no. 2, pp. 889-898, 2022.

[130] N. Rashidirad, J. Mahseredjian, I. Kocar, and U. Karaagac, "Unified MANA-based load-flow for multi-frequency hybrid AC/DC multi-microgrids," *Electric Power Systems Research,* vol. 220, p. 109313, 2023.

[131] Z. Javid, U. Karaagac, and I. Kocar, "MANA formulation based load flow solution for DC distribution networks," *IEEE Transactions on Circuits and Systems II: Express Briefs,* vol. 70, no. 7, pp. 2590-2594, 2023.

[132] A. A. Hamad, M. A. Azzouz, and E. F. El Saadany, "A sequential power flow algorithm for islanded hybrid AC/DC microgrids," *IEEE Transactions on Power Systems,* vol. 31, no. 5, pp. 3961-3970, 2015.

[133] A. Alvarez-Bustos, B. Kazemtabrizi, M. Shahbazi, and E. Acha-Daza, "Universal branch model for the solution of optimal power flows in hybrid AC/DC grids," *International Journal of Electrical Power & Energy Systems,* vol. 126, p. 106543, 2021.

[134] W. Lambrichts and M. Paolone, "General and unified model of the power flow problem in multiterminal AC/DC networks," *IEEE Transactions on Power Systems,* 2024.

[135] M. M. Rezvani and S. Mehraeen, "Unified AC-DC load flow via an alternate AC-equivalent circuit," *IEEE Transactions on Industry Applications,* vol. 57, no. 6, pp. 5626-5635, 2021.

[136] J. Renedo, A. A. Ibrahim, B. Kazemtabrizi, A. Garcia-Cerrada, L. Rouco, Q. Zhao, and J. Garcia-Gonzalez, "A simplified algorithm to solve optimal power flows in hybrid VSC-based AC/DC systems," *International Journal of Electrical Power & Energy Systems,* vol. 110, pp. 781-794, 2019.

[137] InterOPERA. "D2.1-Functional requirements for HVDC grid systems and subsystems " https://interopera.eu/wp-content/uploads/files/deliverables/20250417-D2.1-Functional-requirements-for-HVDC-grid-systems-and-subsystems.pdf (accessed 2025).

[138] InterOPERA. "D3.1-Multi-vendor Interoperability Process and Demonstration Definition " https://www.ready4dc.eu/wp-content/uploads/files/230331_D31_Draft_White_Paper_WG3.pdf (accessed 2025).

[139] K. Jacobs, H. Saad, and S. Dennetière, "Modelling of semiconductor losses of the modular multilevel converter in EMTP," in *2016 IEEE 17th Workshop on Control and Modeling for Power Electronics (COMPEL)*, 2016: IEEE, pp. 1-8.

[140] *IEC 62751-2:Power losses in voltage sourced converter (VSC) valves for high-voltage direct current (HVDC) systems – Part 2: Modular multilevel converters*, IEC, Geneva, Switzerland, 2014.

[141] W. G. B4.57, "Guide for the Development of Models for HVDC Converters in a HVDC Grid," CIGRE techniqcal Brochur, 2014, vol. 604.

[142] J. A. Martinez-Velasco, *Power system transients: parameter determination*. CRC press, 2017.

[143] L. Zhang, "Modeling and control of VSC-HVDC links connected to weak AC systems," KTH, 2010.

[144] V. Vittal and R. Ayyanar, "Grid integration and dynamic impact of wind energy'ser," *ed: Kluwer international series in engineering and computer science: Power electronics & power systems,* 2012.

[145] M. Singh and S. Santoso, "Dynamic models for wind turbines and wind power plants," National Renewable Energy Lab.(NREL), Golden, CO (United States), 2011.

[146] A. Haddadi, I. Kocar, U. Karaagac, J. Mahseredjian, and E. Farantatos, "Impact of renewables on system protection: wind/PV short-circuit phasor model library and guidelines for system protection studies," *EPRI, Palo Alto, CA, USA, Tech. Rep. 3002008367,* 2016.

[147] M. Cai, J. Mahseredjian, U. Karaagac, A. El-Akoum, and X. Fu, "Functional mock-up interface based parallel multistep approach with signal correction for electromagnetic transients simulations," *IEEE Transactions on Power Systems,* vol. 34, no. 3, pp. 2482-2484, 2019.

[148] J. Mahseredjian, L. Dube, M. Zou, S. Dennetière, and G. Joos, "Simultaneous solution of control system equations in EMTP," *IEEE Transactions on Power Systems,* vol. 21, no. 1, pp. 117-124, 2006.

[149] C.-F. Mugombozi, J. Mahseredjian, and O. Saad, "Efficient computation of feedback-based control system equations for electromagnetic transients," *IEEE transactions on Power delivery,* vol. 30, no. 6, pp. 2501-2509, 2015.

[150] B. Bruned, J. Mahseredjian, S. Dennetière, and N. Bracikowski, "Optimized reduced Jacobian formulation for simultaneous solution of control systems in Electromagnetic Transient simulations," *IEEE Transactions on Power Delivery,* vol. 38, no. 5, pp. 3366-3374, 2023.